Title

Mapping structural deformations in moiré materials using diffraction-based electron microscopy

Author

Van Winkle, Madeline

Publication Date

2024

Peer reviewed|Thesis/dissertation

Mapping structural deformations in moiré materials using diffraction-based electron microscopy

by

Madeline Van Winkle

A dissertation submitted in partial satisfaction of the

requirements for the degree of

Doctor of Philosophy

in

Chemistry

in the

Graduate Division

of the

University of California, Berkeley

Committee in charge:

Professor D. Kwabena Bediako, Chair
Professor Peidong Yang
Professor Alex Zettl

Spring 2024

Abstract

Mapping structural deformations in moiré materials using
diffraction-based electron microscopy

by

Madeline Van Winkle

Doctor of Philosophy in Chemistry

University of California, Berkeley

Professor D. Kwabena Bediako, Chair

Moiré superlattices, formed by vertically stacking atomically thin van der Waals layers with a slight interlayer rotation and/or lattice constant difference, are a powerful platform for modulating the physicochemical behavior of two-dimensional solids. While the optical, electronic, and magnetic properties of moiré materials can be intentionally tuned by changing the extent of crystallographic mismatch between constituent layers, structural perturbations such as lattice reconstruction, strain, and disorder also have a substantial impact on observed behavior. Therefore, directly measuring intrinsic structural deformations in moiré superlattices, learning how to dynamically deform moiré structures, and efforts toward correlative structure–property measurements are critical to understanding and controlling the emergent properties of these unique materials.

In this dissertation, Chapter 1 first provides an introductory overview of recent developments in the field of two-dimensional materials and how the properties of these materials can be modified, including through construction of moiré superlattices. This discussion is followed by a comprehensive look at the fundamentals of moiré engineering, the role that structural deformations play in affecting moiré properties, and the appeal of a diffraction-based imaging approach for linking the structure of moiré architectures to observed properties and current theoretical models. Chapter 2 then describes the development of Bragg interferometry, a 4D-STEM-based imaging methodology for mapping moiré structures, and the insights afforded by the methodology regarding the spontaneous lattice deformations driving reconstruction in twisted bilayer graphene, the effects of these deformations on flat band formation, and the impact of extrinsic heterostrain on reconstruction-induced strain fields. Chapter 3 explores the extension of Bragg interferometry to transition metal dichalcogenide (TMD) systems, providing evidence of distinct reconstruction mechanisms in twisted

bilayer TMDs and heterobilayer TMDs. The compatibility of Bragg interferometry with different heterostructure geometries is also exploited to illuminate the effects of encapsulation layers on in-plane and out-of-plane reconstruction. Chapter 4 demonstrates the application of Bragg interferometry to functional devices for the first time, specifically for mapping the spatial arrangement of polar stacking domains in twisted trilayer WSe_2. This information is then complemented by operando dark-field TEM imaging that uncovers a variety of electric field-driven structural responses in different twisted trilayer polytypes. Lastly, Chapter 5 provides a summary of the reported work and an outlook for future endeavours.

To my great grandfather

Whose legacy inspired me to become a scientist

Contents

Acknowledgments

Having reached the final step toward earning my Ph.D., there are many people that I must thank for their tremendous support and contributions over the past six years.

First and foremost, I thank my Ph.D. advisor, Prof. Kwabena Bediako, for his guidance and encouragement throughout all of the stages of my graduate school journey. During my time in his research group, he has consistently challenged me to maximize my potential not only as a scientist but also as a writer, speaker, and mentor. His enthusiasm for science and dedication to the success of his students is truly admirable, and I am incredibly grateful for all of the knowledge, skills, tips and tricks I have learned from him over the years.

I would also like to thank all of the Bediako Lab members with whom I have gotten to ride the graduate school rollercoaster with. Samra Husremović, Jonathon Nessralla, Valerie McGraw, Matt Erodici, Zhizhi Kong, Ted Zhang, and Dr. Yun Yu experienced the lab's earliest days and the beginning of the COVID pandemic with me. Those first couple of years were the toughest for me personally, but we found light and shared many great laughs through it all. I thank all of them for being great colleagues and friends. To the newer members who joined us since – Dr. Lilia Xie, Isaac Craig, Oscar Gonzalez, Sonal Maroo, Shannon Fender, Garrett Hegel – your presence has brightened my time in the group even more and I know the lab will continue to flourish in your hands. I would also like to acknowledge all of the talented undergraduate students who I had the opportunity to work with during my time at Berkeley, in particular Elijah Sherratt, Nikita Dowlatshahi, Nikta Khaloo, and Mrinalni Iyer.

None of my work would have been possible without the help of the fantastic electron microscopists I have interacted with. In particular, thank you to Dr. Justin Ondry who first showed me the basics of TEM operation on the Alivisatos Group's instrument, and to Dr. Karen Bustillo, who spent month after month teaching me how to use the microscopes at NCEM and figuring out the parameters for Bragg interferometry with me. Thank you also to Dr. Colin Ophus, Dr. Jim Ciston, Dr. Rohan Dhall, and Chengyu Song from NCEM, Dr. Reena Zalpuri and Dr. Danielle Jorgens from UC Berkeley's Electron Microscope Lab, and Dr. Berit Goodge, Dr. Ellis Kennedy, and Dr. Catherine Groschner for all of the fundamental and technical microscopy knowledge they have shared with me. Together they have given me the wings for the next stage of my scientific career. I would also like to give a shoutout to the staff at UC Berkeley's Marvell Nanolab, in particular Dr. Allison Dove, Dr. Ryan Rivers, and Dave Taosaka, for their support on the nanofabrication component of my research, which was essential in the final phase of my project.

I have been extremely fortunate to work with many wonderful collaborators during these past several years. Nathanael Kazmierczak and Isaac Craig are both brilliant scientists, and Bragg interferometry would not have come to fruition without their impressive mathematical prowess and coding expertise. I greatly appreciate their

years of dedication to these projects. In addition to everyone mentioned above, I also thank Dr. Stephen Carr, Dr. Medha Dandu, and Dr. Hamish Brown for their important contributions to the work shown in this dissertation.

Last but not least, I must not forget all of those who guided and inspired me in the years before I arrived at Berkeley. My high school chemistry teacher, Mr. Kaufman, and my undergraduate professors and mentors, Prof. Joe Reczek, Dr. Bryan Kaehr, Prof. Jordan Katz, Prof. Steven Olmschenk, Dr. Alexis de la Cotte, and Prof. Arjun Yodh, were invaluable to my growth as a scientist and gave me the critical foundation I needed for success in a graduate program. Most of all thank you to my family, friends, and my partner, Yusuph, for their unwavering support through everything.

Chapter 1

Introduction

1.1 Tuning the properties of two-dimensional van der Waals materials

The past several decades have seen rapid advances in the field of nanoscience and nanotechnology. The vigor of the field comes as no surprise considering the rich diversity and tunability of nanomaterial properties and the corresponding widespread utility of these systems for various applications. Stemming from the Greek word *nanos*, which means dwarf, nanoscience is centered on the design, modification, and study of structures on the atomic to nanometer (< 100 nm) length scale, and nanotechnology involves the associated assembly, processing, and application of these structures. Although nanomaterials have been embedded in society for quite some time, with the earliest evidence of colloidal nanoparticles in dichroic glass dating back to the 4th century[1], the idea of nanoengineering was formally proposed by American physicist Richard Feynman in 1959. In his well-known lecture, titled "There's Plenty of Room at the Bottom", Feynman pondered possibilities such as writing all 24 volumes of the Encyclopedia Brittanica on the head of a single pin, miniaturizing computers and circuits, and building molecules atom-by-atom while also pointing out the challenges in materials characterization and manipulation that must be overcome in order to realize these visions[2]. Since then, nanomaterials have been extensively explored for use in areas ranging from (opto)electronic devices[3–5] to energy storage[6,7] and medicine[8,9], driven by crucial developments in advanced electron microscopy and scanning probe methods for imaging structures down to the atomic limit[10–12], lithographic tools for nanoscale patterning[13,14], and synthetic schemes for producing nanostructures in an ever-growing list of morphologies[15,16], among many others.

Two-dimensional (2D) van der Waals (vdW) compounds comprise one major class of nanomaterials that has garnered immense interest during this period. The era of experimental research on 2D materials research largely began in 2004 when Konstantin Novoselov and Andre Geim from the University of Manchester discovered that

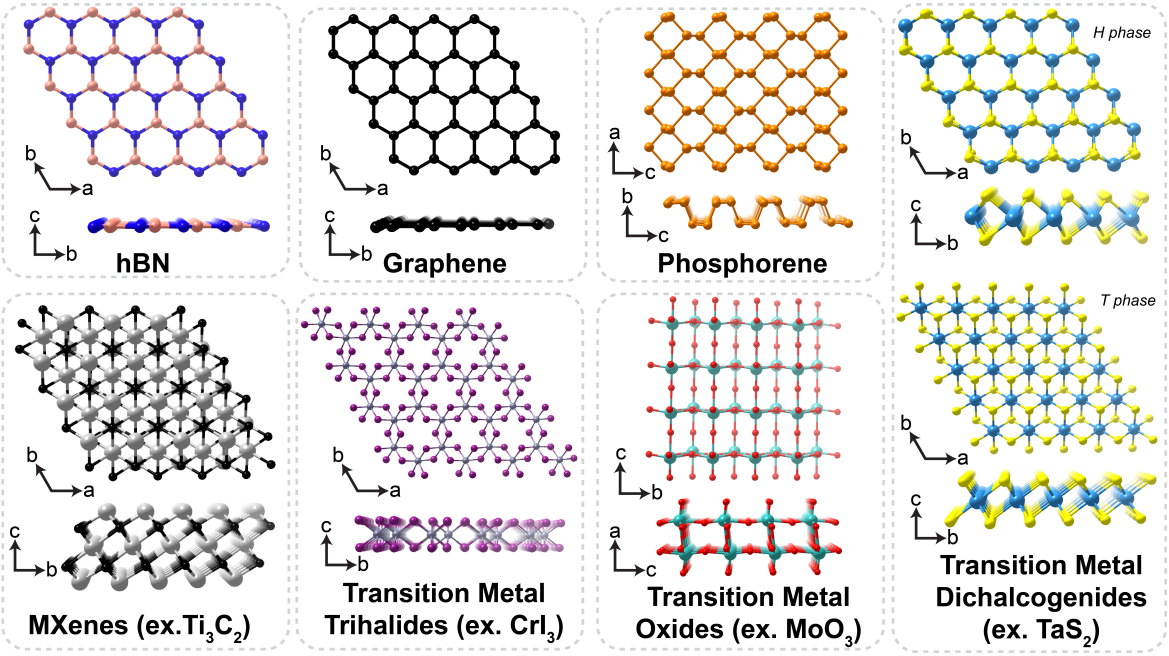

Figure 1.1: Monolayer crystal structures of some common vdW materials.

bulk (that is, three-dimensional) graphite crystals, which consist of vertically-stacked layers of carbon held together by weak interlayer vdW forces, could be repeatedly exfoliated (peeled apart) using tape until a single atomic layer had been isolated[17]. These monolayer carbon sheets, called graphene, contain a covalently-bound hexagonal network of sp^2-hybridized carbon atoms and, intriguingly, display exceptional electronic mobility[17], thermal conductivity[18], and mechanical strength[19]. As of today, the library of vdW materials that can be isolated in 2D sheets (via mechanical exfoliation, solvent-assisted exfoliation, bottom-up growth, etc.) has substantially grown to include hexagonal boron nitride (hBN), transition metal dichalcogenides (TMDs), MXenes, transition metal trihalides, and 2D oxides, to name a few[20,21] (Fig. 1.1). The materials in this group have electrical conductivities ranging from insulating to metallic regimes at room temperature[20,21] and can exhibit a range of exotic physical phenomena (often at lower temperatures) including superconductivity[22,23], charge density wave formation[24,25], and (anti-)ferromagnetism[19,26,27]. Due to their wide selection of (opto)electronic and magnetic properties, coupled with a high surface-to-volume ratio, compatibility with silicon-based device schemes and electrostatic gating, and good mechanical durability, 2D vdW materials are being actively studied as candidates for low-power electronics[17,28–31], next-generation catalysts and battery components[32–34], flexible sensors[35], and more.

One of the most exciting features of 2D vdW materials is that their properties can be readily tuned in a myriad of ways. Varying the number of stacked layers in the

vdW crystal is one common route for controlling the material properties. For example, the band gap of semiconducting vdW materials[36–38] and electronic phase transition temperatures of many 2D compounds[39,40] can both be modulated in this way due to a combination of alterations in interlayer interactions with changing thickness and the relevance of quantum confinement effects in the 2D limit. The optical contrast of 2D sheets placed on a reflective substrate, such as SiO_2/Si wafers, is also layer-dependent due to interference effects as visible light is absorbed by the nanothick crystal and then reflected back by the substrate, enabling assignment of material thickness using optical microscopy[41]. A second approach to manipulating the properties of 2D vdW materials is the fabrication of heterostructures via vdW heteroepitaxy[21,42]. This process consists of stacking or growing various atomic sheets on top of one another, akin to building a tower of LEGO blocks but without any constraints on the rotational alignment of the individual components, a key consideration that we will discuss further. VdW materials exfoliate cleanly with no dangling bonds on the surface of the 2D layers, yielding heterostructures with atomically precise interfaces between constituent layers[28,42]. The emergent properties of a given heterostructure are not always a simple compilation of the properties of the individual layers but can also depend on the interactions of the stacked materials across these interfaces, enabling access to phenomena that would not be observed in the isolated compounds[43–45]. Other strategies that have exhibited clear effects on measured properties include chemical doping and/or intercalation[46–48], incorporation of defects/vacancies[49–51], using an electrostatic or ionic liquid gate to fine-tune carrier density[17,48,52–54], and strain engineering[49,55,56]. Lastly, a relatively new method for tailoring the properties of 2D vdW compounds is the construction of moiré superlattices. The remaining sections of this Chapter detail the fundamentals of moiré engineering and the close connection between structure and observed properties in these systems, motivating the body of work presented in this dissertation.

1.2 A deep dive into moiré engineering

In general, overlaying two patterns with similar but inequivalent periodicities causes an interference effect called a moiré pattern. On an atomic scale, the same principle applies when two similar crystalline lattices with a small lattice constant difference and/or rotational misalignment are vertically stacked. The resulting structure, called a moiré superlattice, contains a spatially varying atomic stacking order with a much larger periodicity than that of the underlying atomic lattices (Fig. 1.2). This periodicity (λ) can be modelled by the following expression:

$$\lambda = \frac{(1+\delta)a}{\sqrt{2(1+\delta)(1-cos(\theta_m))+\delta^2}} \tag{1.1}$$

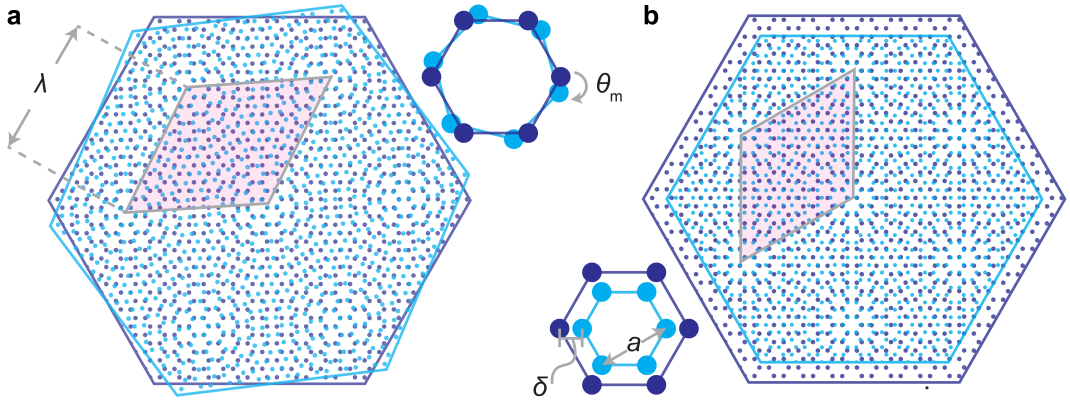

Figure 1.2: Illustrations of moiré superlattices formed by **a,** a rotation (θ_m) and **b,** a lattice constant difference (δ) between two overlaid atomic lattices. a is the atomic lattice constant. Insets between the two panels depict the atomic lattices.

where a is the smaller lattice constant, θ_m is the moiré twist angle, and δ is the lattice mismatch between the two materials[57]. Early reports showed the presence of nanoscale moiré superlattices in graphite crystals containing naturally folded/rotated layers[58–60]. Many studies have also demonstrated the generation of moiré superstructures in epitaxially grown 2D films due to interference effects between the lattice of the film and that of the substrate[61–64]. More recently, the fabrication of moiré heterostructures through vdW heteroepitaxy has made it possible to deterministically control the moiré periodicity (through precise control of θ_m) and to study moiré physics in a wide variety of material combinations, illuminating the unique behavior that can emerge in these systems and giving rise to an entire field of solid state physics – *twistronics*. The main classes of moiré materials and their properties are highlighted below.

1.2.1 Graphene-based moirés

Theoretical predictions of the manifestation of exotic physical phenomena in moiré materials began with graphene-based moirés. To understand the insight afforded by these studies, it is useful to first consider the electronic band structure of a single layer of graphene. Given real space lattice vectors describing the hexagonal graphene lattice, $\mathbf{a_1}$ and $\mathbf{a_2}$ (Equation 1.2, Fig. 1.3a), one can use a tight-binding model to derive the dispersion relationship for the two electronic bands corresponding to the π bonding and anti-bonding interactions between the C p_z orbitals[65,66], as shown in Equation 1.3 and Fig. 1.3b. We focus on the p_z orbitals because they are positioned out-of-plane and will therefore be most relevant when considering electronic interactions between stacked layers.

$$\mathbf{a_1} = \frac{a}{2}(\sqrt{3}, 1) \quad , \quad \mathbf{a_2} = \frac{a}{2}(\sqrt{3}, -1) \tag{1.2}$$

$$E_{\pm}(\mathbf{k}) = \pm t\sqrt{1 + 4cos\left(\frac{\sqrt{3}a}{2}k_x\right)cos\left(\frac{a}{2}k_y\right) + 4cos^2\left(\frac{a}{2}k_y\right)} \tag{1.3}$$

Here, E is energy defined relative to the Fermi energy, $\mathbf{k} = (k_x, k_y)$ is a wave vector in the Brillouin zone, t is the energy for electron hopping between nearest neighbors on the same sublattice, and a is the graphene lattice constant (2.46 Å). Based on this dispersion relation, the K and K' points, located at the corners of the Brillouin zone (Equation 1.4, Fig. 1.3c), are of particular importance.

$$K = \frac{2\pi}{a}\left(\frac{1}{\sqrt{3}}, \frac{1}{3}\right) \quad , \quad K' = \frac{2\pi}{a}\left(\frac{1}{\sqrt{3}}, -\frac{1}{3}\right) \tag{1.4}$$

Referring to Equation 1.3, one finds that at these specific positions, $E(\mathbf{k}) = 0$ for both the π and π^* bands, causing them to meet at a sharp point (Fig. 1.3b,d). Further, in the vicinity of these positions (highlighted by the gray box in Fig. 1.3d), there is

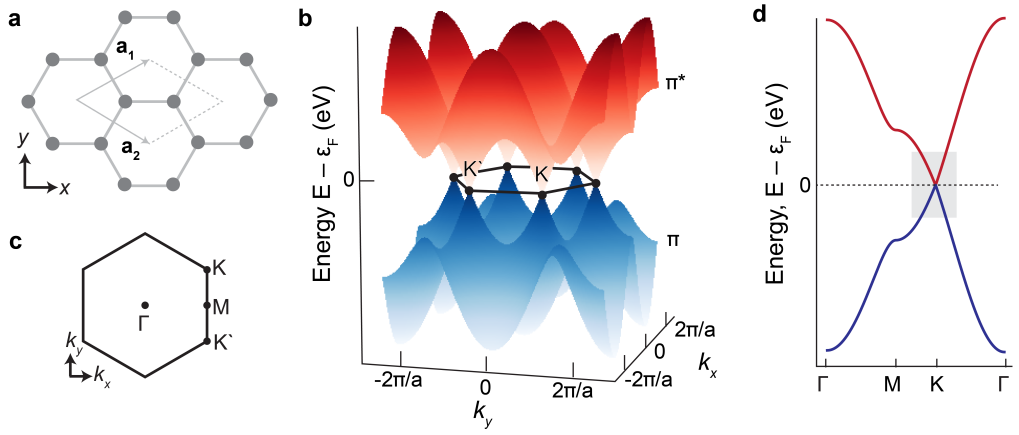

Figure 1.3: a, Atomic lattice of a graphene monolayer. Dashed lines outline the two-atom unit cell, defined by vectors $\mathbf{a_1}$ and $\mathbf{a_2}$. **b,** 3D and **d,** 2D representations of the π and π^* bands in an undoped graphene monolayer, obtained from the relationship given in Equation 1.3. ε_F is the Fermi energy. Dirac cones are located at the corners of the Brillouin zone, which is outlined in black in **b** and illustrated in further detail in **c**. The gray box in **d** highlights the linear dispersion near one of six Dirac points.

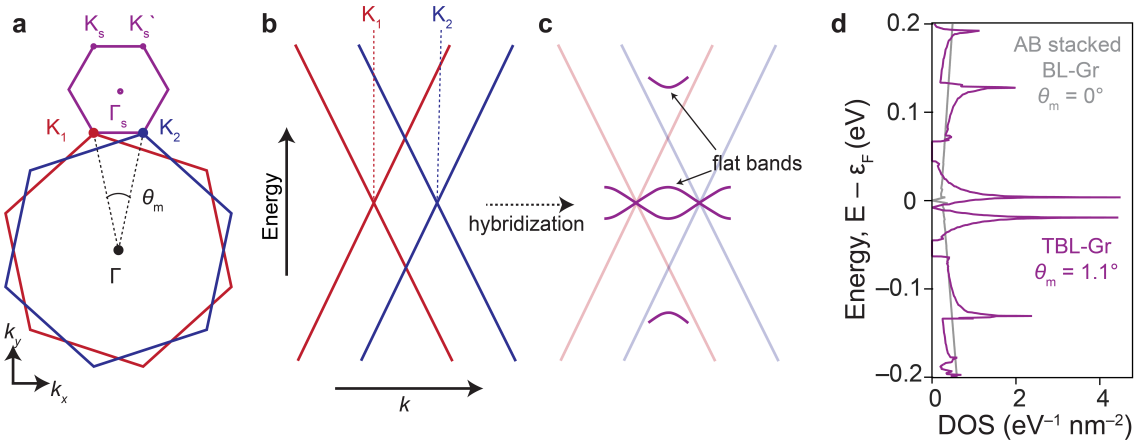

Figure 1.4: **a,** Brillouin zones for two graphene monolayers (shown in red and blue), offset by a twist angle of θ_m. The resulting mini Brillouin zone is shown in purple (subscript s represents the superlattice). **b,** 2D representation of the Dirac cones for graphene layers 1 and 2, offset by θ_m. **c,** Corresponding illustration of hybridization of the bands from the two layers, yielding flattened hybridized bands (purple). Transparent outlines of the original Dirac cones are shown in the background for comparison. **d,** Calculated density of states (DOS) profiles for TBL-Gr near the largest predicted magic angle (purple) compared to an untwisted AB (Bernal)-stacked bilayer graphene (BL-Gr, gray). Peaks are observed in the DOS profile for TBL-Gr at the flat band energies. ε_F is the Fermi energy. Panels **a,d** were adapted with permission from Yu, Y. et al. *Nat. Chem.* **14**, 267–273 (2020). Copyright 2022 by Springer Nature.

a linear relationship between E and $\mathbf{k}$:

$$\begin{aligned} E_{\pm}(\mathbf{k}) &\approx \pm\frac{\sqrt{3}ta}{2}|\mathbf{k}| \\ &= \pm v_F\hbar|\mathbf{k}| \end{aligned} \tag{1.5}$$

where v_F is the Fermi velocity (equivalent to $\sqrt{3}ta/2\hbar$). All together, this results in the formation of a Dirac cone structure at each K and K' point (also called the Dirac points) (Fig. 1.3b,d).

This unique band structure already yields many interesting electronic properties in isolated monolayer graphene, such as the possession of massless Dirac fermions[67]. However, when another monolayer of graphene is then placed on top of the first with a small interlayer rotation, the Dirac cones from the two layers become offset in k space by an amount that is directly proportional to the moiré twist angle (Fig. 1.4a,b), which also has very distinctive effects. These offset Dirac cones define the K and K' points of a mini Brillouin zone generated by the presence of the longer

lengthscale moiré periodicity (Fig. 1.4a). Consequently, the electronic bands from the two graphene sheets fold into this mini Brillouin zone where they can hybridize due to interlayer electronic interactions, producing a new band structure distinct from that of the individual graphene monolayers[68–71] (Fig. 1.4c).

The nature of this band hybridization in the mini Brillouin zone is dependent on the moiré twist angle; as a result, one can tune the electronic properties of the system by modulating θ_m. Calculations have shown that interlayer coupling in the twisted system causes the Fermi velocity (i.e., the slope of E vs $\mathbf{k}$) around the Dirac points to renormalize[68–71]. For a given value of for a given θ_m, the ratio between the Fermi velocity in the twisted (v_F^*) and untwisted (v_F) graphene bilayer can be expressed as[71]:

$$\frac{v_F^*}{v_F} = \frac{1 - 3\alpha^2}{1 + 6\alpha^2} \tag{1.6}$$

where $\alpha = w/v_F k_{\theta_m}$ with w as the interlayer hopping energy (set to 110 meV in Ref. [71]) and k_{θ_m} as the wave vector between the Dirac points of the two layers (i.e., the vector between K_1 and K_2 in Fig. 1.4a). For relatively small values of α (meaning larger twist angles, 10–30°), this equation simplifies to[68–72]:

$$\frac{v_F^*}{v_F} = 1 - 9\alpha^2 \tag{1.7}$$

In this large twist regime, there is relatively weak electronic coupling between layers; therefore, the Dirac cones remain intact at the corners of the mini Brillouin zone while the slope of the cones monotonically decreases as θ_m decreases[68–70,72]. On the other hand, at larger α (smaller twist angles, $< 10°$), electronic coupling strengthens. Notably, in this regime, Bistritzer and MacDonald found that v_F^* anomalously equals 0 at a series of specific twist angles (referred to as "magic angles"): 1.05°, 0.5°, 0.35°, 0.24°, and 0.2°[71]. In the smaller twist regime, a band gap also opens at the points where the Dirac cones from the two layers overlap due to increasing interlayer electron tunneling and corresponding hybridization of the π/π^* orbitals[70,73]. Taken together, these models proposed that the Fermi velocity renormalization and gap opening would lead to the generation of increasingly flat, isolated electronic bands in twisted bilayer graphene (TBL-Gr) as θ_m decreased[68–70,72] (Fig. 1.4c), with particularly flat bands appearing at the magic angles[71].

Flat bands are typically associated with the emergence of strongly correlated electronic states (for example, superconducting phases[74]). This is due to the fact that, when bands are very narrow, the Coulombic energy between electrons becomes more prominent than their kinetic energy, which is proportional to v_F[75]. In addition, in the energy range near the flat bands there is a high density of electronic states (DOS, Fig. 1.4d), defined as the number of states per unit energy, which further enhances these electron–electron interactions[74,75]. With this in mind, the theoretical predictions outlined above spurred great experimental interest in the flat band-driven physical

phenomena of twisted bilayer graphene and, more generally, in the electronic properties of graphene-based moiré matter. Some of the first experimental reports on a 2D vdW moiré heterostructure provided evidence of massless Dirac fermions[57] and a Hofstadter butterfly effect[76] in superlattices formed between monolayer hBN and monolayer graphene, which have a lattice constant difference of only 1.9%. Unconventional superconductivity[77,78], correlated insulating states[78,79], and ferromagnetism[80] have all been observed in TBL-Gr with θ_m near the largest magic angle, $1.05 \pm 0.1°$. Correlated phases also persist in twisted graphene multilayers (twisted trilayers and quadlayers[81–84], twisted double bilayers[85], etc.).

Beyond physics, the presence of flat bands also plays an important role in tuning the electrochemical activity of the moiré surface[34]. It has been shown that aligning the flat band energy (and therefore the peak in electronic DOS) of TBL-Gr with the redox potential of a particular chemical species in solution leads to a substantial enhancement in the rate of charge transfer between the moiré electrode and the molecule[86]. A similar effect has also been observed on twisted trilayer graphene surfaces; however, here there is the added complexity of variations in how the DOS from the hybridized bands is distributed across the three layers based on the two twist angles present, which also impacts the charge transfer kinetics at the electrode–electrolyte interface[87].

1.2.2 TMD-based moirés

Exploring vdW materials beyond graphene, moiré engineering has also been applied to TMD-based systems, with a strong focus on H-phase Group VI TMDs (MX_2 with M = Mo, W and X = S, Se, Te). These particular materials are direct band gap semiconductors in the monolayer limit[36,37] with parabolic conduction and valence band edges at the K and K' points[88] rather than the linear Dirac cone structure observed in monolayer graphene. Applying a similar concept of band hybridization in the mini Brillouin zone of a twisted TMD bilayer, calculations again predict the formation of flat bands near the Fermi level[89–91] (Fig. 1.5a). However, the actual mechanism of flat band formation is quite different between graphene and TMDs. Namely, in TMD-based moirés, flat band formation is largely attributed to the considerable variation in interlayer spacing throughout the superlattice, which occurs due to repulsion between the out-of-plane chalcogen p_z orbitals. The corrugation of the equilibrium structure produces an inhomogeneous interlayer hybridization that localizes charge carriers and produces the flattened bands[92].

The presence of a band gap and parabolic nature of the band edges near the K and K' points in the isolated layers also predisposes TMD-based moirés to hosting narrower bands after hybridization, which ultimately loosens the constraints on the twist angles at which flat bands occur[93]. Rather than having a list of discrete magic angles where correlated electronic states are expected, twisted bilayer TMDs are predicted to have a continuous range of magic angles, with substantial band flattening

starting around $\theta_m < 7°$ and the emergence of very flat bands (with a similar bandwidth to the flat bands in magic angle TBL-Gr[92]) around $\theta_m < 3.5°$[89–92]. Indeed, this has been experimentally realized, with a correlated insulating state and potential superconducting phase observed in TBL-WSe_2 for θ_m ranging from 4–5°[93] as well as the observation of flat bands in TBL-WSe_2 with $\theta_m = 3°$ using scanning tunneling spectroscopy[94]. Correlated insulating states and Wigner crystals, a crystalline phase of electrons driven by strong interactions, have also been reported in heterobilayer systems[95,96] (that is, moirés formed by two different TMDs with a small lattice constant mismatch).

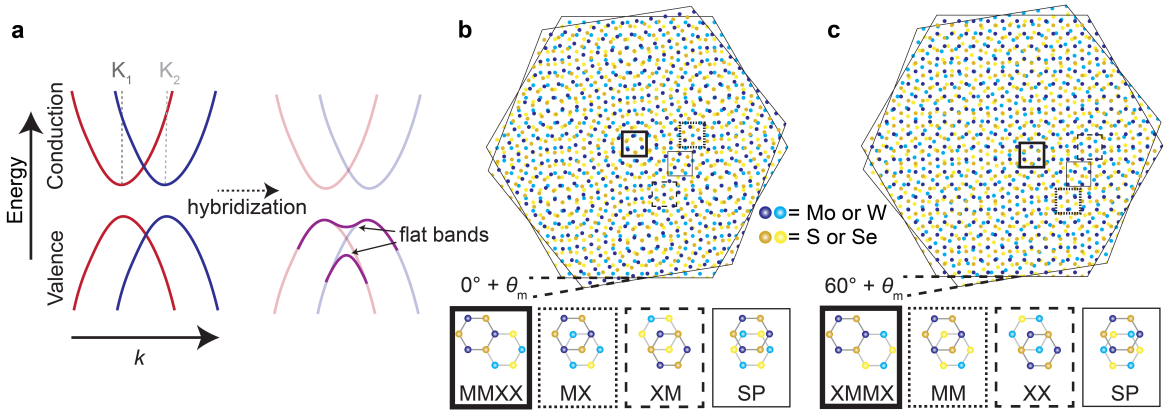

Figure 1.5: a, Illustration of band hybridization in a semiconducting twisted bilayer TMD. **b,c,** Schematics of parallel (near 0°, **b**) and anti-parallel (near 60°, **c**) twisted bilayer TMD configurations, with corresponding top-down views of the distinct sets of interlayer stacking orders found in each moiré shown underneath.

For TMD-based moirés it is also important to distinguish between the parallel (P) and anti-parallel (AP) stacking of the TMD monolayers. Unlike graphene, which has inversion symmetry, TMD monolayers are not symmetric with respect to inversion. Consequently, stacking the TMD monolayers near 0° (P) and near 180° (or 60°, AP) yields two distinct superlattices with different sets of atomic stacking sequences sampled in each (Fig. 1.5b,c). Both configurations can host flat bands; however, band flattening occurs primarily near the valence band edge in the P structure, while the AP structure has flat bands that are both narrower than in the P structure and are found at both the conduction and valence band edges. This is in part due to different spatial variations in interlayer hybridization in the two configurations[92]. Additional factors account for the other part, discussed in Section 1.3.

Many studies have also investigated the optical properties that arise in TMD-based moirés. As mentioned above, in these systems the extent of interlayer hybridization is inhomogeneous throughout the moiré unit cell. In turn, there is a variation in the band gap on the moiré length scale, meaning electrons and holes preferentially

localize in different stacking sites in the superlattice[92,97]. This enables the generation of intralayer moiré excitons[98] (bound exciton-hole pairs) upon optical excitation. In TMD heterobilayers, the conduction and valence band edges of the two layers are also staggered, which makes it possible for electrons and holes to also localize on different layers, producing interlayer moiré excitons[99,100]. Other more complex excitonic species, such as hybrid moiré excitons[101], moiré trions[102], and moiré exciton–polaritons[103] have been reported as well[97,104]. Uniquely, these moiré excitons are subject to different optical selection rules compared to typical excitons due to the presence of the moiré potential. As a result, multiple excitonic features have been observed in photoluminescence spectra for TMD moiré materials, in contrast to a single photoluminescence peak observed for monolayer TMDs[97,104].

1.2.3 Up and coming moiré materials

The vast majority of both theoretical and experimental work has focused on graphene- and TMD-based moiré structures, and these systems will also be the focus of the work in this dissertation. However, it is worth noting that studies on the properties of moirés comprised of other vdW materials have started to pop up in the last couple of years. For example, in 2023 Zhao et al. reported the fabrication of twisted $Bi_2Sr_2CaCu_2O_{8+\delta}$ (BSSCO) heterostructures[105]. BSSCO is a vdW material with a relatively high superconducting transition temperature ($\sim$ 87–90 K in bulk and $\sim$ 85–88 K in a monolayer)[106]. Uniquely, the twisted system (with a total thickness of $\sim$ 80 nm and θ_m near 45°) was found to exhibit spontaneous time-reversal symmetry breaking superconductivity, a rare type of unconventional superconductivity[105]. Recent studies have also shown how moiré engineering can be used to generate complex magnetic textures. In 2022 Xu et al. reported co-existing anti-ferromagnetic and ferromagnetic domains in twisted bilayer chromium triiodide (CrI_3) due to the presence of both rhombohedral (ferromagnetic) and monoclinic (anti-ferromagnetic) stacking orders in the moiré superlattice[107].

The incorporation of ions in the interstitial space between the layers of a moiré superlattice presents another opportunity to greatly diversify the range of potential moiré materials. Calculations suggest that, for dilute intercalation amounts, intercalants will preferentially cluster in particular regions of a moiré superlattice due to spatial variations in the local coordination environment[102,108]. This preferential clustering is predicted to affect the interlayer coupling of the layers in the intercalation sites[102,108] and to promote further band flattening[109], which may impact measured transport properties. One could also envision inducing spatially localized phase transitions, magnetic states, etc. in this way. While, experimentally, this concept has not been directly demonstrated in epitaxial vdW heterostructures, Zou et al. used atomic resolution electron microscopy to demonstrate similar regioselective ion exchange in naturally twisted biotite mica[110]. All of this is to say, the design of new moiré materials is just beginning.

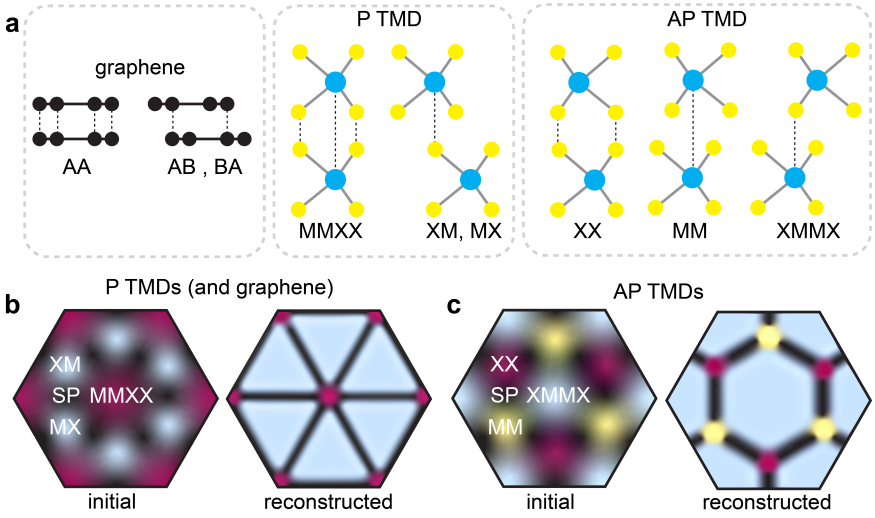

Figure 1.6: **a,** Side view illustrations of high and low energy stacking orders in graphene, P-stacked TMDs, and AP-stacked TMDs. AA, MMXX, and XX stacking orders have the highest interlayer energy. AB/BA, XM/MX, and XMMX stacking orders have the lowest energies. The MM stacking type is an intermediate case. Black dashed lines highlight positions where atoms in the two layers are directly aligned. **b,c,** Schematics depicting the formation of expanded low energy stacking regions due to lattice reconstruction. Similar relaxed structures are expected in P TMDs and graphene (**b**) while a different structure is expected in AP TMDs (**c**) based on the different stacking orders present in each superlattice, their spatial arrangements, and their relative energies.

1.3 Impacts of structural deformations in moirés

With a general understanding of moiré materials and their unique properties in hand, this section now discusses structural perturbations that can affect the observed behavior of these systems.

1.3.1 Lattice reconstruction effects

One of the primary types of structural deformations that occurs in moiré systems is lattice reconstruction. Lattice reconstruction is a process consisting of periodic local deformations in the layers comprising the moiré. This process occurs because of the differences in interlayer energy between the atomic stacking orders found throughout the superlattice[111–115]. In the case of TBL-Gr, AA-type sites have higher stacking energy than AB-type sites ($E_{AA} - E_{AB} = 3.44$ meV/Å^2) due to greater repulsion

between the π clouds of the two graphene layers (Fig. 1.6a)[112]. Similarly, in twisted bilayers of the Group VI TMDs discussed in Section 1.2.2 (e.g., H-phase MoS_2), sites with maximal overlap of the chalcogen p_z orbitals (MMXX sites in the P configuration and XX sites in the AP configuration) are higher in energy than sites where the chalcogens are staggered and there is instead more favorable overlap between the chalcogen p_z orbitals and transition metal d_{z^2} orbitals (XM or MX regions in the P configuration and XMMX regions in the AP configuration) (Fig. 1.6a)[92,114]. To lower the overall stacking energy, the layers spontaneously deform to increase (decrease) the total area of regions with the lowest (highest) stacking energy, forming extended low-energy domains as shown in Fig. 1.6b,c[111–115].

A few models have been proposed for how moiré reconstruction occurs on an atomic scale. In moirés formed by a rotational offset between lattices, reconstruction is predicted to occur through periodic rotations that either increase or decrease the local twist angle[89,111,112,116]. Given the inverse relationship between the twist angle θ_m and periodicity λ shown earlier in Equation 1.1, further increasing the local rotation reduces the size of a given region while decreasing local rotation has the opposite effect (Fig. 1.7a). On the other hand, in moirés formed by a lattice constant difference between layers (in the case of heterobilayers), reconstruction is predicted to occur through periodic changes in the local lattice mismatch[116–118]. Again referring to Equation 1.1, there is an inverse relationship between the lattice constant mismatch δ and λ (Fig. 1.7b). Therefore increasing the local mismatch between layers (meaning

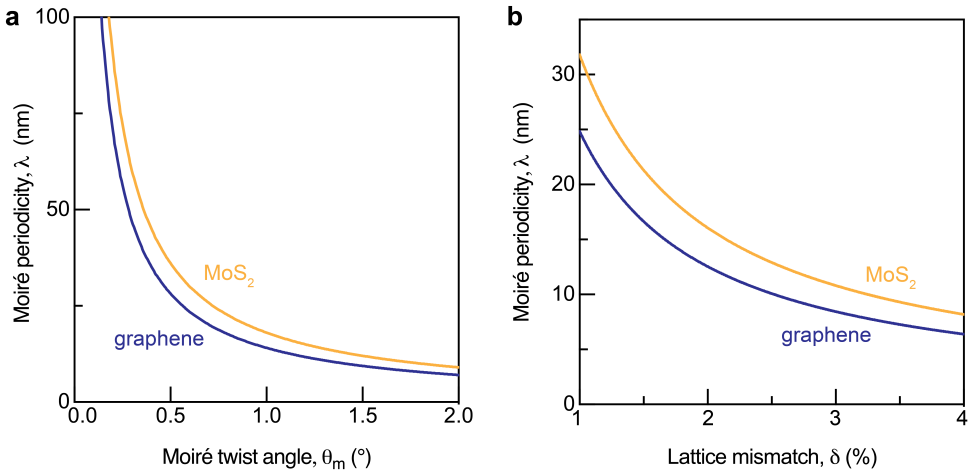

Figure 1.7: Plots illustrating the dependence of the moiré periodicity on **a,** twist angle and **b,** lattice mismatch, generated using Equation 1.1 with lattice constants of 0.246 nm and 0.315 nm for graphene and MoS_2, respectively. During lattice reconstruction, locally increasing (decreasing) θ_m or δ can similarly decrease (increase) the area of a particular stacking site.

the larger lattice expands slightly and the smaller lattice shrinks slightly) reduces domain size while decreasing the local mismatch increases domain size.

The energetic trade-off for lowering the total stacking energy through these local in-plane structural transformations is the introduction of intralayer strain. For twisted bilayers, simulations predict that there will be a shear-type strain in the boundaries between locally rotating stacking regions[92,111,112]. For heterobilayers, a volumetric strain is expected within the stacking domains[117,118]. Part of this strain can be relieved by additional out-of-plane corrugation, but an appreciable amount remains[89,111,117]. The final relaxed structure balances the reduction in stacking energy and gain in strain energy[92,112] and is therefore dependent on the geometry of the moiré pattern (dictated by the interlayer twist angle and lattice constant difference).

Ultimately, lattice reconstruction plays a crucial role in determining the properties of moiré systems and must be taken into account when modelling these structures and interpreting their emergent properties. For both graphene- and TMD-based moiré materials, reconstruction is expected to affect flat band formation. Notably, in TBL-Gr, calculations suggest that in-plane rotation-driven reconstruction suppresses flat band formation at all originally predicted magic angles except for the largest one around $1.05°$[113]. As discussed in Section 1.2, out-of-plane relaxation in TMD-based moirés creates an inhomogeneous interlayer hybridization pattern that increases the localization of charge carriers and spurs band flattening in both P and AP structures[89,92]. Exactly how the band gap varies throughout the superlattice depends on this interlayer hybridization; therefore the specific stacking sites where electrons and holes will localize and the strength of this localization are intertwined with out-of-plane deformation[89,92,119]. At the same time, generation of lateral strain from in-plane deformations is also crucial to consider in TMD moirés because strain further modifies the local band gap throughout the superlattice[92,119]. Theoretical studies propose that in-plane reconstruction strain in AP-stacked TMD moiré bilayers generates distinctive triangular potential wells in the superlattice that strongly confine charge carriers in quantum dot-like states, producing several isolated, ultraflat bands at the conduction and valence band edges. In contrast, this phenomenon does not occur in the P configuration based on its stacking energy landscape and corresponding reconstruction strain distribution. In this case, flat bands exist but are wider and only found near the valence band edge[92]. In addition to affecting flat band formation, the band gap modifications from both out-of-plane and in-plane reconstruction can substantially increase the depth of the moiré potential. For example, the predicted moiré potential depth in $WSe_2/MoSe_2$ increases from ~ 10 meV without reconstruction to up to ~ 300 meV when both out-of-plane and in-plane reconstruction are taken into account[119].

Knowledge of how lattice reconstruction impacts the band structure of moiré materials has helped to explain many experimental results. For example, reconstruction-driven suppression of flat bands in TBL-Gr at other predicted magic angles explains why correlated phases have only been experimentally observed in TBL-Gr with twist

angles around $1.05 \pm 0.1^{\circ}$[77,79,113]. The fact that reconstruction deepens the moiré potential in TMD systems leads to longer moiré exciton lifetimes and has enabled observation of these features with spectroscopc probes at higher temperatures than would be possible otherwise[120,121]. The observation of ultraflat bands in AP TBL-WSe_2 by scanning tunneling spectroscopy has also been explained by reconstruction effects[122].

1.3.2 Strain effects

As mentioned in the previous section, strain plays a critical role in affecting the properties of moiré materials. Strain effects can be split into two main categories: intrinsic strain arising from lattice reconstruction and extrinsic strain, or strain arising from external factors. Here we focus on extrinsic strain effects. In particular, uniaxial heterostrain, where one layer is slightly stretched relative to the other layer along one axis, has been predicted to have a substantial impact on the electronic bands in moiré systems. While the electronic structure of moiré materials has been shown to be relatively insensitive to moderate homostrains[123], where both layers are stretched in sync (Fig. 1.8b), a rather small heterostrain ($< 1\%$) can change the relative atomic positions in the two layers enough (Fig. 1.8c) to have clear effects on the interlayer hybridization and resulting band structure. For example, calculations on TBL-Gr with $\theta_m = 1.25^{\circ}$ indicate that even a 0.35% heterostrain can eliminate the Dirac points at the mini Brillouin zone corners and induce band flattening at other nearby energies[123]. Another theoretical study on TBL-Gr with $\theta_m \sim 1^{\circ}$ reported an increase in the energy gap between the conduction and valence flat bands with increasing heterostrain magnitude (from 0.1–0.7%), showing that heterostrain can be used as a tuning knob to control the energies at which peaks in the DOS profile (called van Hove singularities, VHS) occur[124]. In fact, it has been suggested that for TBL-Gr with $\theta_m \sim 0.75$–1.15°, near the largest magic angle, the energies of the VHS are even more sensitive to a small heterostrain than to the change in twist angle[124], highlighting strong competition between moiré engineering and strain engineering. Heterostrain is typically introduced unintentionally during the vdW heteroepitaxy process because the weak vdW forces between layers allow the layers to readily stretch independently of one another. However, intentional application of heterostrain has been proposed as a way to dynamically tune the electronic properties of moiré superlattices[125].

The flat bands in TMD-based moirés are purportedly less sensitive to heterostrain than graphene-based systems[126]. On the other hand, the fact that uniaxial heterostrain can effectively generate a one-dimensional (1D) moiré potential[127] leads to modulation of the energetic landscape for excitons and affects their overall behavior[128,129]. Bai et al. report that in $WSe_2/MoSe_2$ heterobilayers, unstrained samples exhibit circularly polarized excitonic features whereas samples containing uniaxial strain exhibit linearly polarized excitonic features[128].

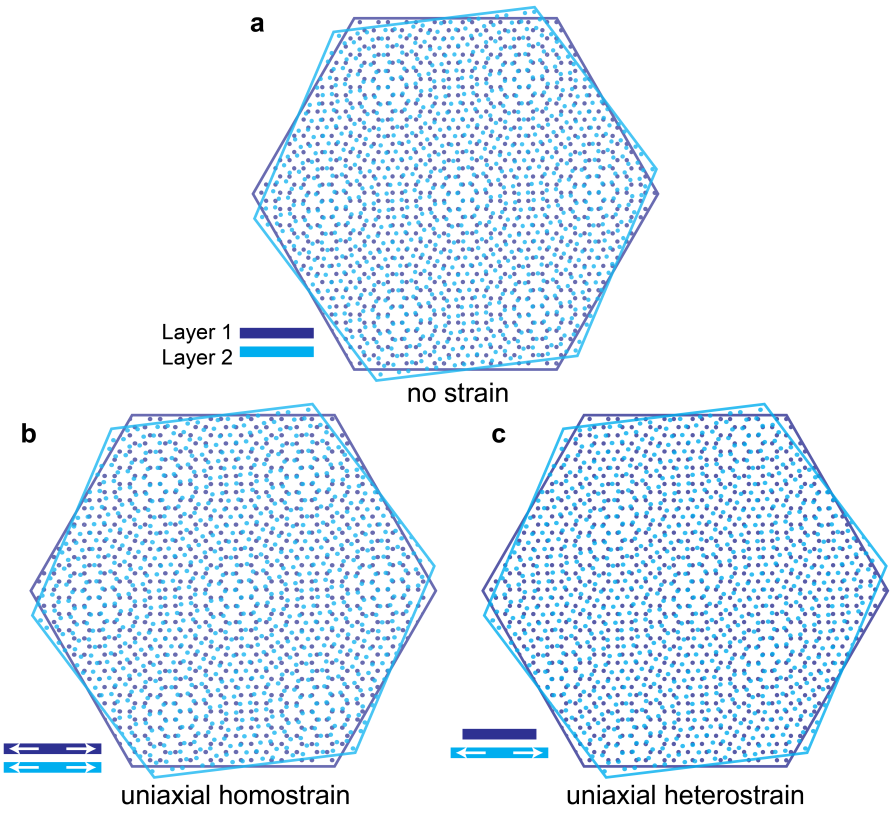

Figure 1.8: Schematics of **a,** an unstrained twisted bilayer compared to twisted bilayers with equivalent magnitudes of uniaxial **b,** homostrain and **c,** heterostrain. White arrows indicate the uniaxial straining axis.

1.3.3 Disorder effects

The last main category of structural perturbations that affects moiré systems is disorder. Disorder, such as twist angle disorder and strain disorder, is randomly introduced quite often during the sample fabrication process[130]. As a result, moiré devices tend to be quite inhomogeneous and there can be a lot of nano- to microscale variability from one device to the next. Given the strong dependence of observed optical and electronic properties on twist angle as well as strain, as discussed in the previous sections, the presence of disorder (typically variations of 0.1° for θ_m and 0.1–0.7% for heterostrain) presents experimental difficulties, particularly for the reproducibility of electronic transport behavior[130,131]. For example, Uri et al. reported that the presence of a gradually changing twist angle can effectively generate an in-plane electric field across a device, substantially affecting features in transport measurements for magic angle TBL-Gr[131]. Methods to controllably fabricate clean, ordered moiré heterostructures are actively being investigated[132,133]. Heterobilayers also tend to be

more homogeneous than twisted structures since the moiré periodicity is less sensitive to changes in lattice mismatch than twist angle (Fig. 1.7); this leads to more robust and reproducible correlated electronic phases in heterobilayers[130]. However, structural disorder is currently one challenge that still plagues the field of twistronics.

1.4 Structural characterization of moiré materials using diffraction-based imaging

1.4.1 Project goals

It is clear that the properties of moiré materials are governed by their structures, both through well-controlled parameters such as global twist angle and choice of materials, and through spontaneous or random perturbations such as lattice reconstruction, strain, and disorder. Detailed experimental characterization of moiré structures is then critical both for validating or modifying currently proposed structural models and for ultimately understanding and controlling the unique physics and chemistry offered by this class of 2D heterostructures. Based on this, the overarching goal of the work presented in this dissertation is two-fold. The first goal is to investigate the intrinsic structures of moiré materials, the spontaneous deformations that give rise to these structures, and how these structures can be systematically perturbed by external variables. The second is to develop imaging frameworks that are conducive to the study of a variety of moiré heterostructure geometries and can enable correlative structure–property measurements.

1.4.2 Background on the experimental approach

A variety of characterization methods have been employed for imaging moiré superlattices[113–115,134]. Out of the techniques that have been reported, dark-field transmission electron microscopy (DF-TEM), a diffraction-based technique, stands out as an approach that is particularly well-suited for imaging moiré superlattices stacked in multi-component heterostructures[113], enabling study of moiré samples with different arrangements (for example, encapsulated versus free-standing) and aligning with the second goal outlined above.

To understand how DF-TEM is used to observe moiré superlattices within a heterostructure, first consider the general principles of electron diffraction in a thin 2D crystal. As illustrated in Fig. 1.9a, when an incoming electron beam (a plane wave with wave vector $\mathbf{k}_{incident}$ oriented perpendicular to the sample) strikes the crystal, two things can occur. One possibility is that that the electron passes through the crystal with no change to its wave vector ($\mathbf{k}_{incident} = \mathbf{k}_{unscattered}$). The second possibility is that the electron is scattered due to interactions with the lattice. In the case of elastic scattering, where crystal momentum is conserved, the scattered and

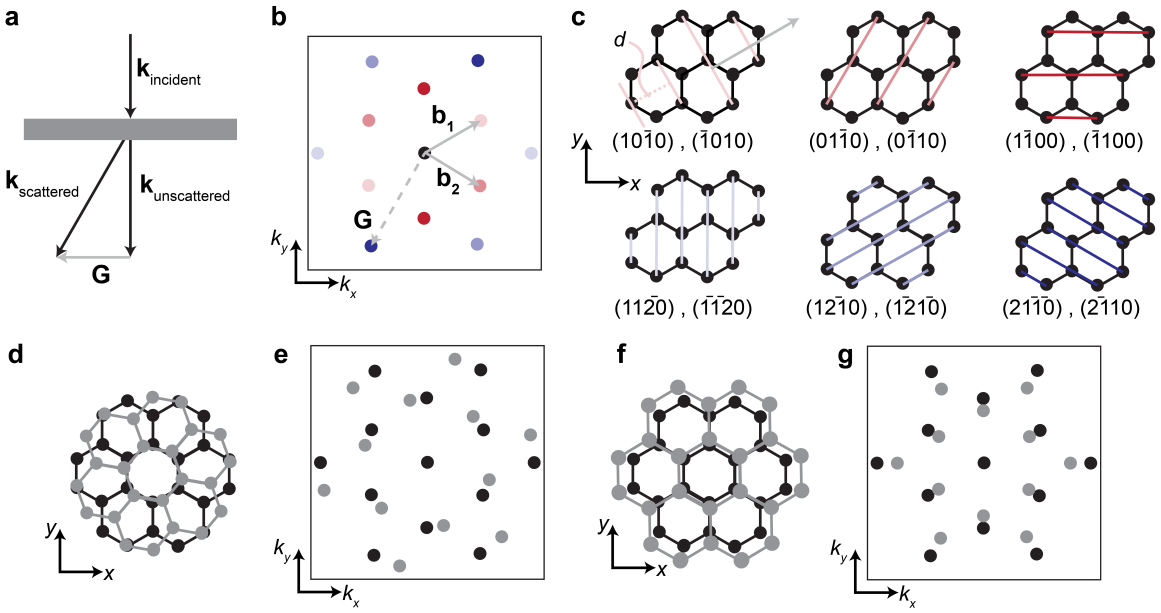

Figure 1.9: a, Schematic depicting the Laue condition for elastic scattering (Equation 1.8), which produces peaks in intensity in an electron diffraction pattern. **b,** Illustration of the first two rings of diffraction peaks for a hexagonal lattice. $\mathbf{b_1}$ and $\mathbf{b_2}$ are basis vectors defining reciprocal lattice vectors $\mathbf{G}$. **c,** Sets of lattice planes in real space corresponding to the diffraction peaks shown in **b**. The magnitude of $\mathbf{G}$ is inversely proportional to the periodicity d of the corresponding set of planes and is oriented perpendicular to these planes, as shown by the gray arrow. Equivalent Miller indices describing each set of planes are listed in the format $(hkil)$. $\bar{1} = -1$ and $\bar{2} = -2$. **d–g,** Schematics of the real space (**d,f**) and reciprocal space (**e,g**) structures with a rotation (**d,e**) and lattice constant mismatch (**f,g**) between layers.

unscattered wave vectors are related by the Laue condition:

$$\mathbf{G} = \mathbf{k}_{scattered} - \mathbf{k}_{unscattered} \tag{1.8}$$

where $\mathbf{G}$ is a reciprocal lattice vector. Points in reciprocal space where the Laue condition is met correspond to peaks in intensity, producing an electron diffraction pattern. An illustration of the first two rings of a diffraction pattern are shown in Fig. 1.9b for a prototypical hexagonal structure, which includes all of the materials studied in this dissertation (graphene, hBN, and TMDs). In Fig. 1.9b, $\mathbf{b_1}$ and $\mathbf{b_2}$ are reciprocal lattice basis vectors. All other $\mathbf{G}$ vectors are a linear combination of these basis vectors:

$$\mathbf{G}_{m,n} = m\mathbf{b_1} + n\mathbf{b_2} \tag{1.9}$$

In real space, each reciprocal lattice vector corresponds to a set of periodically spaced planes in the crystal lattice. Each $\mathbf{G}$ vector is oriented normal to a particular

set of planes (Fig. 1.9c) and has a magnitude

$$|\mathbf{G}| = \frac{2\pi}{d} \tag{1.10}$$

where d is the distance between planes. In the diffraction pattern, a particular diffraction peak position is then dependent on both the spacing and orientation of the corresponding set of planes in the real space lattice. For a hexagonal lattice, each set of planes is labeled with Miller indices $(hkil)$ where $h = m$, $k = n$, $i = -(m + n)$, and $l = 0$ for periodicities in the xy plane (Fig. 1.9c).

When a second hexagonal lattice is stacked on top of the first but with an interlayer twist (Fig. 1.9d), the planes in the two lattices are rotated in real space and, subsequently, the diffraction peaks are rotated by the same angle (Fig. 1.9e). Similarly, if a second material with a different lattice spacing is stacked on top of the first (Fig. 1.9f), the diffraction peaks are radially offset by an amount inversely proportional to the lattice mismatch (Fig. 1.9g). This azimuthal and/or radial offset of the diffraction peaks provides the foundation for DF-TEM imaging.

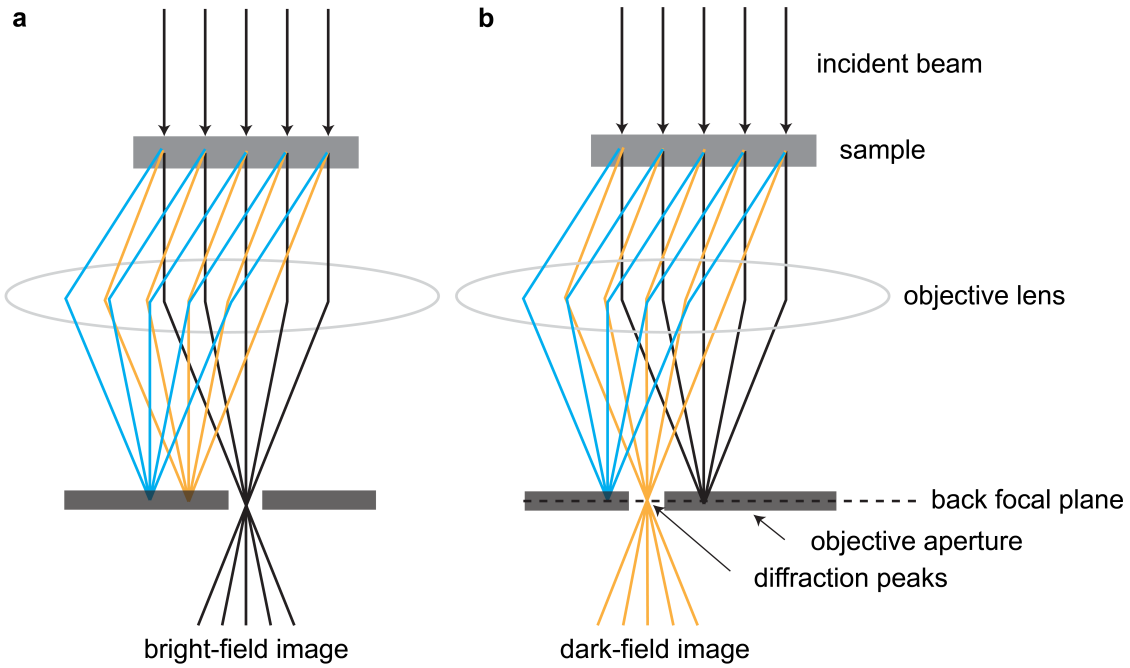

Figure 1.10: Ray diagrams describing formation of **a,** bright-field and **b,** dark-field TEM images.

A schematic of a typical bright-field (BF) TEM imaging setup is shown in Fig. 1.10a. The incident electron beam, widely spread over the sample, passes through the sample where the electrons are cleanly transmitted (black lines) or elastically scattered

(blue and yellow lines for electrons scattered by materials 1 and 2, respectively). These electrons are focused by an electromagnetic objective lens and converge into diffraction peaks in the back focal plane of the lens. By centering a physical aperture (the objective aperture) around the unscattered diffraction peak (the peak in the center of the pattern), one can block out signal from the scattered electrons and form what is called the bright-field image. On the other hand, by instead positioning the aperture to isolate one of the scattered peaks, a dark-field image is formed (Fig. 1.10b). In practice, this can be done by either moving the aperture itself, as shown in Fig. 1.10b, or by tilting the incident beam such that the diffraction peak of interest is centered in the objective aperture. The results shown in the following Chapters use the latter method.

With this picture in mind, it is now possible to see how DF-TEM can be used to isolate diffraction signal and form images from specific components of a vdW heterostructure. For example, moiré samples are often encapsulated with hBN to improve sample stability, and functional moiré devices may contain hBN and graphite slabs as a dielectric layer and electrical contacts, respectively. As long as these additional components are adequately offset in real space (either by a relatively large rotational misalignment, > 5–$10°$, or lattice mismatch, $> 10\%$), signal from the moiré layers, which are only marginally offset in real space, can be isolated to view the superlattice without extraneous contributions from the other layers.

It is important to note that the atomically thin nature of 2D materials in real space also gives their diffraction peaks an extended structure along the k_z axis in reciprocal space (Fig. 1.11a). The three-dimensional structure of these extended diffraction rods depends closely on stacking order, as shown for AA-, AB-, and BA-type stacking orders in bilayer graphene (BLG, Fig. 1.11b). Further, the measured intensity of each peak in the resulting diffraction pattern depends on the magnitude (width) squared of the diffraction rod at its intersection with the Ewald sphere (approximated as the black horizontal line in Fig. 1.11b), which can produce contrast between regions of a sample with different stacking orders. In cases where two stacking orders have the same diffraction intensities when the sample is perfectly horizontal in the xy-plane (that is, positioned on the [0001] zone axis), as in the case of AB- and BA-BLG, diffraction contrast can be obtained by tilting the sample so that the Ewald sphere intersects a different part of the diffraction rods (Fig. 1.11c). In the case of moiré superlattices, this tilt-induced diffraction contrast can be quite useful. For example, Yoo et al. distinguished AB and BA regions of hBN-encapsulated, reconstructed TBL-Gr superlattices in this way[113] (Fig. 1.11d,e).

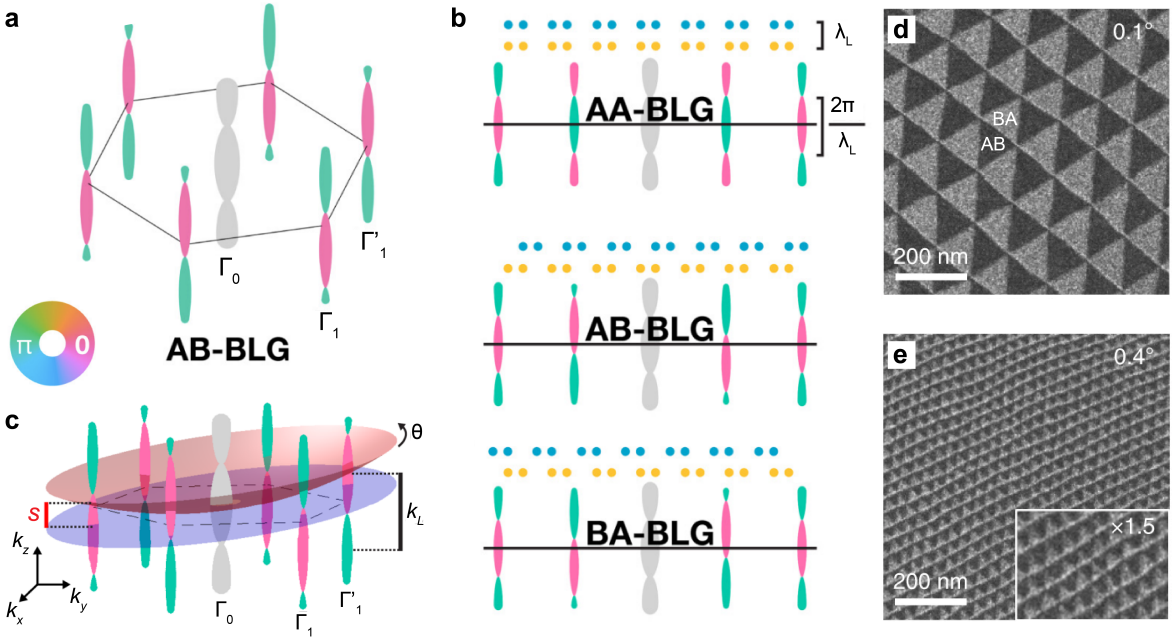

Figure 1.11: **a,** 3D structure of extended diffraction rods, shown for AB-stacked bilayer graphene (BLG). Rod color and width indicate phase and magnitude, respectively. **b,** Side view comparison of diffraction rod structures for three BLG stacking orders. The black line indicates the diffraction plane/the Ewald sphere in the absence of sample tilt, in which case this plane lies horizontal at $k_z = 0$. **c,** Effect of a non-zero sample tilt. The Ewald sphere is depicted in blue for an electron accelerating voltage of 200 keV (a standard TEM operating condition), and in red for an accelerating voltage of 0.3 keV (shown as an exaggeration). Panels **a**–**c** were reproduced with permission from Sung, S.H. et al. *Phys. Rev. Mater.* **3**, 064003 (2019). Copyright 2019 by the American Physical Society. **d,e,** DF-TEM images of TBL-Gr with $\theta_m = 0.1°$ (**d**) and 0.4° (**e**) showing how a sample tilt of $\sim 5°$ produces contrast between AB and BA domains. Panels **d,e** were reproduced with permission from Yoo, H. et al. *Nat. Mater.* **18**, 448–453 (2019). Copyright 2019 by Springer Nature.

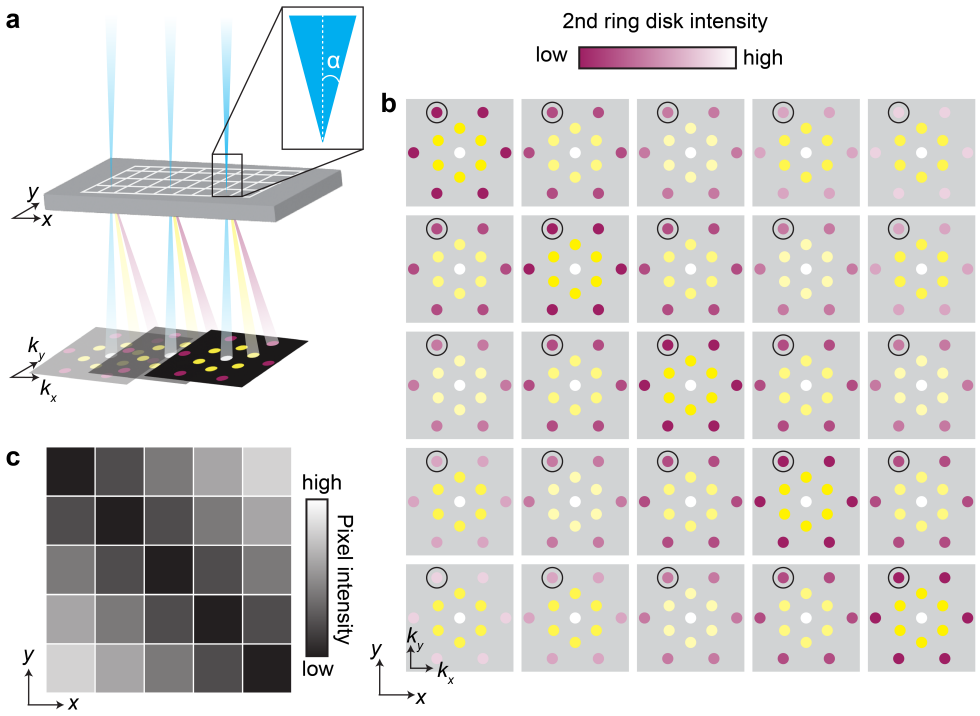

Figure 1.12: **a,** Schematic of a 4D-STEM experiment where a converged electron beam is rastered across a grid of positions (x,y) in the sample. The convergence angle of the beam (α) controls the diffraction disk diameter. **b,** Illustration of an array of CBED patterns acquired in a 4D-STEM scan. Integrating the intensity in a particular disk (circled in black) across the data set yields **c,** a virtual DF image where the intensity of each pixel corresponds to the integrated disk intensity for the local CBED pattern.

Dark-field images can also be generated using another diffraction-based technique called four-dimensional scanning transmission electron microscopy (4D-STEM)[135]. The efforts reported in this dissertation involve the first application of this imaging method to the characterization of moiré structures and will therefore be described in detail in Chapters 2–4. However, a brief summary of dark-field image generation from 4D-STEM is provided here. A typical 4D-STEM experiment is illustrated in Fig. 1.12a. Here, a converged electron beam is rastered through the sample and a convergent beam electron diffraction (CBED) pattern is collected at each beam position. The converged geometry of the beam causes the diffraction peaks to spread out into larger disks in the CBED pattern (Fig. 1.12b), and the size of the disk can be modified by changing convergence angle (α) of the beam. A virtual dark-field image can be constructed by integrating the intensity of the pixels within a given diffraction disk for each CBED pattern in the 4D-STEM scan, equivalent to

virtually placing an objective aperture. An illustration of this process is provided in Fig. 1.12b,c, where each pixel in the virtual DF image in Fig. 1.12c corresponds to the integrated disk intensity for the CBED pattern collected at that particular beam position. The advantage of generating a DF image using 4D-STEM rather than DF-TEM is that intensity information is simultaneously collected for all diffraction disks whereas DF-TEM requires separate image acquisition for each diffraction peak. A second advantage is that spreading the diffraction intensity out over more pixels (that is, into a disk rather than a sharp peak) makes it easier to control the imaging and acquisitions conditions such that the measured intensities are not saturated. 4D-STEM imaging can therefore be used for quantitative intensity measurements that reveal a wealth of structural information, as shown in the following Chapters. DF-TEM is still advantageous for faster image acquisition and over a larger field of view, which is highly beneficial for operando imaging, such as imaging during application of an external stimulus.

1.5 Overview of remaining chapters

This Chapter has highlighted the fundamental background of moiré engineering, the importance of drawing connections between theory, property measurements, and structural characterization of moiré materials, and the general utility of momentum-resolved diffraction-based electron microscopy for imaging moiré structures. Chapters 2–4 now detail the application of both DF-TEM and a new 4D-STEM-based methodology, Bragg interferometry, for the study of four different groups of moiré materials – twisted bilayer graphene, twisted bilayer MoS_2, MoS_2/WSe_2 heterobilayers, and twisted trilayer WSe_2. To start, Chapters 2 and 3 studies delve into measuring the spontaneous structural deformations that underlie lattice reconstruction in the twisted bilayer and heterobilayer systems. Chapter 4 then pivots to explore electric field-driven structural deformations in twisted trilayers that possess an interfacial polarization. Finally Chapter 5 summarizes the conclusions from this body of work and offers broader perspective on future directions.

Chapter 2

Interferometric imaging of lattice reconstruction in twisted bilayer graphene

Parts of this chapter were reproduced or adapted from: Kazmierczak, N.P.*, Van Winkle, M.*, Ophus, C., Bustillo, K.C., Carr, S., Brown, H.G., Ciston, J., Taniguchi, T., Watanabe, K. & Bediako, D.K. Strain fields in twisted bilayer graphene. *Nat. Mater.* **20**, 956–963 (2021). (*These authors contributed equally.)

Author Contributions: N.P.K., M.V.W., C.O., K.C.B., H.G.B. and D.K.B. conceived the study. M.V.W. designed and fabricated the samples. M.V.W., K.C.B. and J.C. developed the experimental methodology and acquired the 4D-STEM data. N.P.K., C.O. and H.G.B. created the data analysis code. S.C. carried out the band structure calculations and finite-element modelling. T.T. and K.W. provided the bulk hBN crystals. N.P.K. and M.V.W. processed the data. N.P.K., M.V.W. and D.K.B. analyzed the data and wrote the manuscript. All the authors contributed to the overall scientific interpretation and edited the manuscript.

2.1 Abstract

Van der Waals heteroepitaxy allows deterministic control over lattice mismatch or azimuthal orientation between atomic layers to produce long-wavelength superlattices. The resulting electronic phases depend critically on the superlattice periodicity and localized structural deformations that introduce disorder and strain. In this study we used Bragg interferometry to capture atomic displacement fields in twisted bilayer graphene with twist angles $< 2°$. Nanoscale spatial fluctuations in twist angle and uniaxial heterostrain were statistically evaluated, revealing the prevalence of intrinsic short-range disorder in moiré heterostructures. By quantitatively mapping strain

tensor fields, we uncovered two regimes of structural relaxation and disentangled the electronic contributions of constituent rotation modes. Further, we found that applied heterostrain accumulates anisotropically in saddle-point regions, generating distinctive striped strain phases. Our results establish the reconstruction mechanics underpinning the twist-angle-dependent electronic behavior of twisted bilayer graphene and provide a framework for directly visualizing structural relaxation, disorder and strain in moiré materials.

2.2 Introduction

Stacking two-dimensional (2D) van der Waals (vdW) bilayers with dissimilar lattice constants and/or slight rotational misalignment produces a moiré superlattice with a periodicity that is inversely related to the magnitude of the interlayer mismatch[75,136]. The moiré pattern superimposes a nanoscale periodic potential on the vdW material and can dramatically alter the electronic band structure of the system[71]. As such, moiré materials assembled from vdW layers are versatile platforms for designing electronic band structures[57,77,80,93,99,100,137–139]. For example, twisted bilayer graphene (TBL-Gr) displays a host of correlated electronic phases[75,77,80,137,138] associated with the formation of ultraflat electronic bands near an interlayer "magic" angle (MA) of 1.1°. However, the band structures of moiré materials are fragile and easily manipulated by small structural deformations in the superlattice. As discussed in Chapter 1, one of the most consequential structural modifications is an intrinsic intralayer lattice reconstruction process[111–115,140–143]. In TBL-Gr, this reconstruction introduces intralayer strain[111,142,144] and frustrates flat band formation at other theoretically predicted magic angles[71] below 1.1°. In addition, disorder from spatial variations in twist angle[131,145] and symmetry breaking due to extrinsic uniaxial heterostrain[123,124,146] strongly alter the observed electronic phases in magic-angle twisted bilayer graphene (MA-TBL-Gr).

Although visualizing the structure and strain fields of moiré materials is paramount to understanding and controlling emergent phases, directly mapping the reconstruction mechanics in these systems has been elusive. One challenge is the presence of hexagonal boron nitride (hBN) multilayers, typically used as capping layers in sample fabrication[77,80,137,138]. Various microscopy techniques have been used to image moiré bilayers[114,115,134,140,146], but these require the bilayer to be exposed or fully suspended. Conventional dark-field transmission electron microscopy (DF-TEM) can indirectly probe reconstruction in encapsulated samples[113], but remains limited in its ability to extract critical structural details near the MA. Although 2D strain tensors have been measured in lateral heterostructures[147], strain measurements in moiré materials have been restricted to determinations of one-dimensional (1D) strain[144] and uniaxial heterostrain[146].

This Chapter discusses the development of Bragg interferometry, an imaging methodology based on four-dimensional scanning transmission electron microscopy (4D-STEM)[135,148,149] that can be used to directly visualize the nanoscale deformations underlying spontaneous reconstruction in moiré systems. We demonstrate application of this technique for mapping the structure of TBL-Gr at high resolution, notwithstanding hBN capping layers, and quantifying localized 2D strain tensor fields in the moiré.

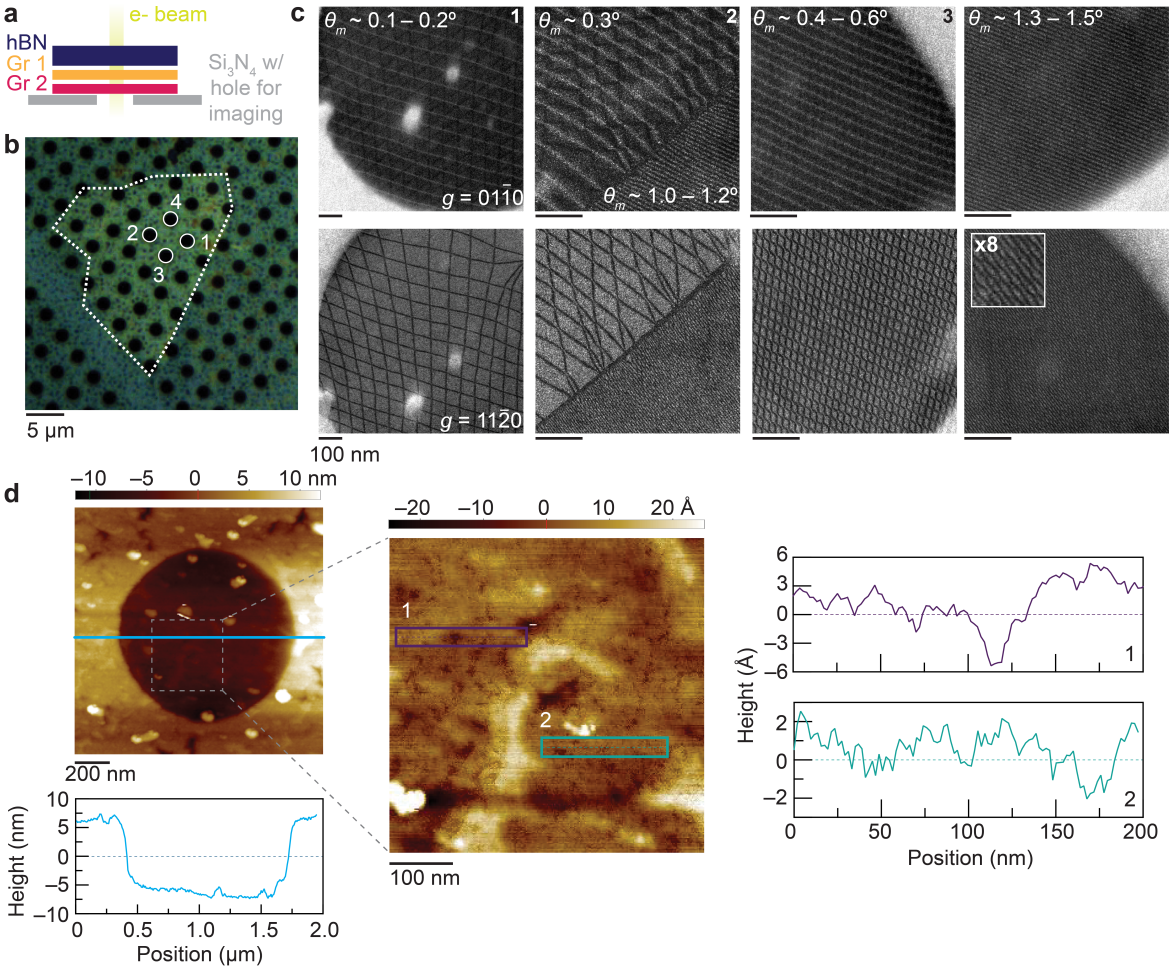

Figure 2.1: a,, Cross sectional schematic and **b,** optical micrograph of an hBN/TBL-Gr heterostructure (outlined in **b**) on a holey silicon nitride (Si_3N_4) TEM support. Locations used for imaging are labelled in **b c,** DF-TEM images of the regions labelled in **b**, obtained using the [01$\bar{1}$0] and [11$\bar{2}$0] graphene diffraction peaks, showing various twist angles (θ_m) in the different regions. **d,** Atomic force microscopy of the sample shown in **b,c**.

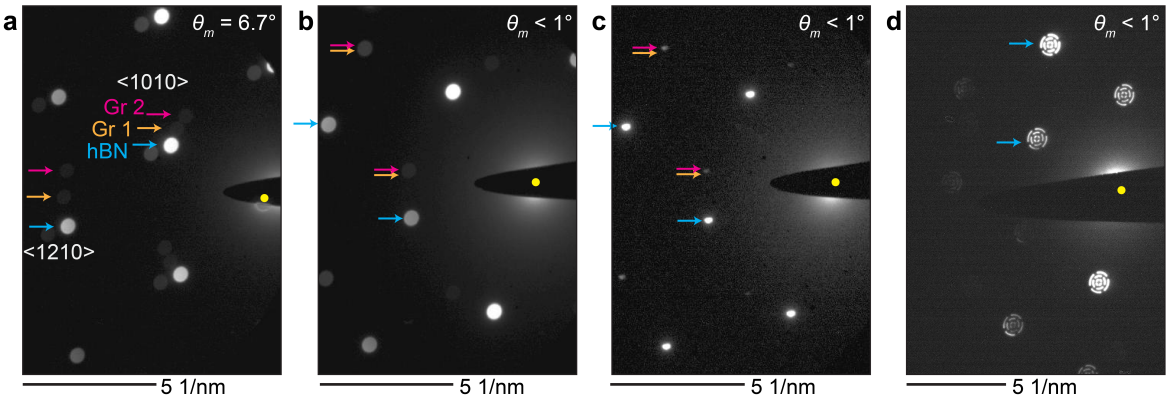

Figure 2.2: Initial exploration of imaging parameters for mapping strain in TBL-Gr. At a convergence semi-angle of 0.55 mrad, Bragg disk positions for the two graphene layers (marked by orange and pink arrows) could be distinguished at large twist angles (**a**) but not in the small twist angles of interest (**b**). Decreasing the convergence semi-angle further to 0.14 mrad (i.e., a nearly parallel beam) still could not resolve the two sets of graphene Bragg reflections (**c**). Only hBN Bragg disks (marked by blue arrows) were detectable when using a 10μm bullseye-patterned C2 aperture (**d**).

2.3 The development of Bragg interferometry

4D-STEM is a well-established technique for mapping structural transformations and deformations across a sample[135]. In a 4D-STEM experiment, a focused electron beam is rastered in a 2D array across a sample and a full convergent beam electron diffraction (CBED) pattern is collected at each probe position, yielding a 4D dataset. This technique is also often referred to as scanning nanobeam diffraction. Monitoring changes in the collected CBED patterns across a dataset yields rich information about variations in phase[150], crystallographic orientation[151], and strain[147,152], for example, throughout a material[135]. With this in mind, we set out to map the intrinsic structural deformations and 2D strain fields present in TBL-Gr using this technique.

TBL-Gr samples were fabricated with an encapsulating hBN layer using the tear-and-stack dry transfer method (Fig. 2.1a, see Section 11 for Experimental Details), introducing interlayer twist angles, θ_m, ranging from 0.1 to 1.6° between the graphene sheets. Since we found that samples produced using the tear-and-stack method are often inhomogeneous, we collected DF-TEM images of the prepared samples to identify regions of interest prior to 4D-STEM imaging. An optical micrograph of an exemplar hBN/TBL-Gr heterostructure and corresponding DF-TEM images are shown in Fig. 2.1b,c. Atomic force microscope images, presented in Fig. 2.1d, show that heterostructures were bent slightly over the edges of the holes in the TEM support, but were nearly flat over the majority of the regions of interest (the centers of the holes).

In the initial phase of this study, we attempted to calculate strain in the TBL-

Gr moiré using the conventional approach, which involves tracking changes in the diffracted Bragg disk positions (corresponding to changes in local lattice constant) across a dataset[135,147,152]. However, this method presented major challenges for the study of TBL-Gr samples because the large overlap between Bragg disks from the two graphene layers (due to the marginal twist angle between the lattices in real space) coupled with the low signal-to-noise ratio in the individual graphene Bragg disks precluded accurate registration of disk positions (Fig. 2.2a–c). We tried to overcome this challenge by using a patterned bullseye aperture, which produces bullseye shaped Bragg disks in the diffraction pattern to enable more precise recognition of Bragg disk centers[153]. However, in our samples the use of a patterned aperture substantially reduced the measured diffraction intensity in the graphene Bragg disks even further to the point where the disks were not detectable over the noise threshold (Fig. 2.2d).

In light of this, we developed Bragg interferometry, which is also based on 4D-STEM but utilizes diffraction intensities rather than disk positions to map moiré structures (Sections 2.4 and 2.5) and to measure their intralayer strain fields (Sections 2.6–9). Figure 2.3a shows a schematic of the experiment. Overlapping Bragg disks from the two graphene layers are discernible in Fig. 2.3b. We determined that the total intensity, I_j, in the overlapping region of the jth interfering Bragg disk pair corresponding to a graphene reciprocal lattice vector, $\mathbf{g}$, is given by:

$$I_j = A_j cos^2(\pi \mathbf{g}_j \cdot \mathbf{u}) \tag{2.1}$$

Here, $\mathbf{u} = (u_x, u_y)$ is the local displacement vector from an atom in the first graphene layer to the nearest atom in the same sublattice in the second graphene layer and A_j is a scaling factor representing the average number of pixel counts at maximum diffraction intensity (see Appendix, Section 1 for the full derivation). A collection of CBED patterns for a TBL-Gr sample are shown in Fig. 2.3c, illustrating the relationship between the interlayer displacement vector $\mathbf{u}$ and the intensity in the overlapping graphene Bragg disks.

2.4 Visualization of displacement maps

Using Equation 2.1, the arrangement of atomic stacking regions in the TBL-Gr layers is determined by measuring I_j for all $\langle 1010 \rangle$ and $\langle 2110 \rangle$ reflections and fitting a local $\mathbf{u}$ assignment for each pixel in the real space scan. An overview of this procedure is summarized here and in Fig. 2.4a,b; more information can be found in the Appendix, Section 2. First, the background scattering is fitted and removed from each CBED pattern to avoid biasing the Bragg disk intensities. Next, the overlap regions between each pair of $\langle 1010 \rangle$ and $\langle 1210 \rangle$ TBL-Gr Bragg disks are manually defined and all pixel intensity values in each region are summed, converting each CBED pattern into a 12-component vector. A displacement vector is then calculated by non-linear regression,

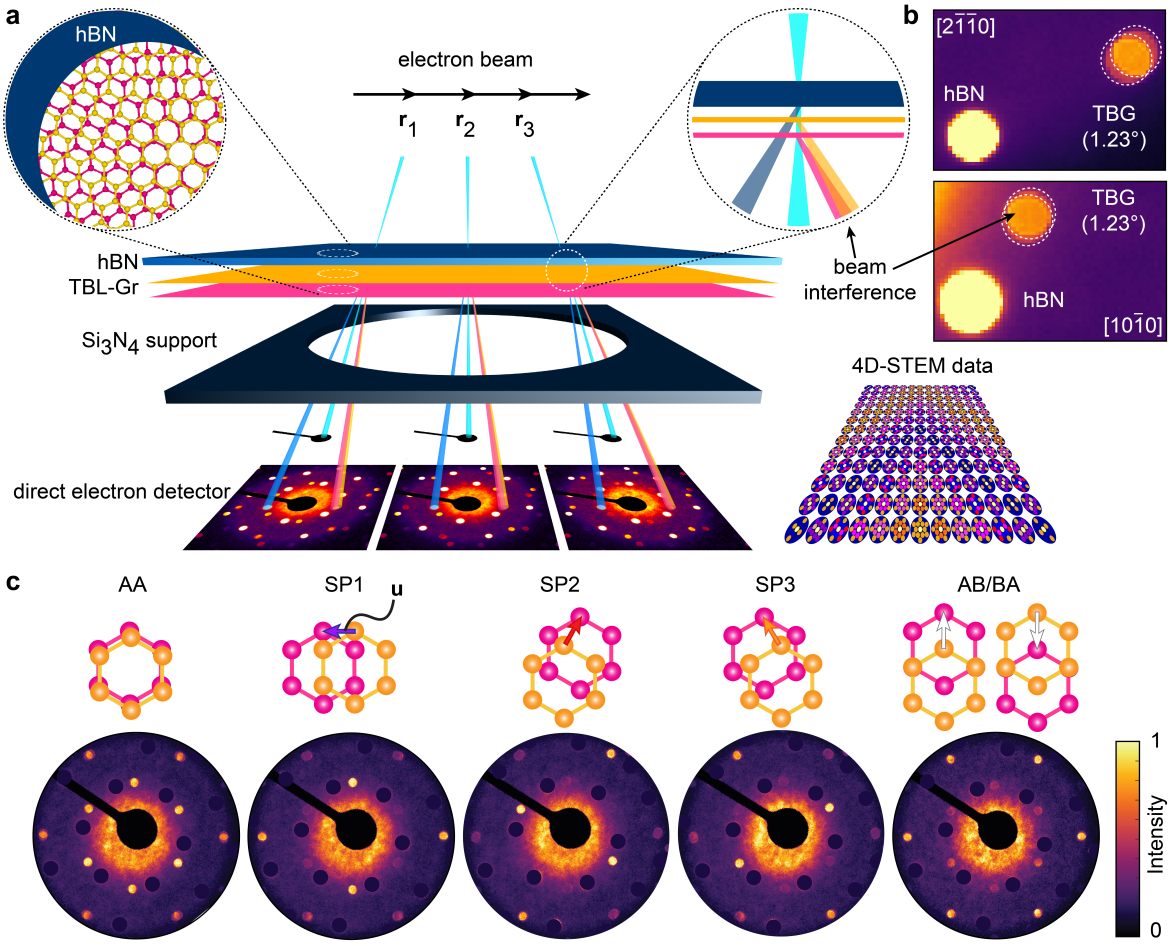

Figure 2.3: **a,** Schematic of 4D-STEM of an hBN/TBL-Gr heterostructure. Here $\mathbf{r_1}$, $\mathbf{r_2}$, and $\mathbf{r_3}$ refer to electron beam positions. **b,** Magnified images of the [2$\bar{1}\bar{1}$0] and [10$\bar{1}$0] hBN and graphene Bragg disks showing overlap between disks from azimuthally misaligned graphene layers. These images were produced by summing all of the CBED patterns within a 4D-STEM dataset to improve visibility of the graphene Bragg disks. **c,** High-symmetry bilayer graphene stacking orders with the corresponding displacement vectors (**u**) depicted with arrows. A representative CBED patterns is shown below each stacking type. hBN Bragg disks have been obscured for clarity in **c**

using Equation 2.1 as the fitting function. Although the prefactor coefficients A_j are not known a priori, they are also fitted by a multistep non-linear regression procedure, as discussed in Appendix, Section 2. Repeating the fit for each real space pixel (that is, each individual CBED pattern) produces the displacement maps shown in Fig. 2.4c. Note that this fitting process produces some bias due to the finite probe width, which can be later removed by a filter (see Appendix, Section 3 for details).

Figure 2.4c shows representative displacement vector maps for TBL-Gr samples with θ_m ranging from 0.16 to 1.37°. Each pixel depicts the local displacement vector according to the displacement-space half-hexagon shown in Fig. 2.4b. By using information from 12 Bragg disk pairs simultaneously, the displacement vector field provides a more comprehensive picture of the TBL-Gr structure than the DF-TEM images shown in Fig. 2.1c, allowing quantitative visualization of the reconstructed superlattice over many moiré wavelengths.

2.5 Geometric measurements and quantification of intrinsic disorder in TBL-Gr

Many details about the intrinsic moiré structure can be derived from the displacement maps. To start, we discuss how these maps enable a geometric analysis of the local variations in twist angle and heterostrain at the resolution of individual AB/BA domains. Local twist angle and heterostrain values were calculated using a model previously reported by Kerelsky et al.[146] (see Appendix, Section 8). To summarize, it is assumed that one layer of the TBL-Gr sample remains unstrained while the other bears uniaxial tensile heterostrain, ε_H, at some angle relative to the lattice. This model then provides three degrees of freedom for the distorted moiré geometry: the moiré angle θ_m, the heterostrain magnitude ε_H, and the angle of heterostrain application θ_h. By measuring the lengths of the three sides of each moiré triangle in the displacement maps, these three variables can be fit uniquely and plotted for the triangulated moiré geometry. Figure 2.5a,b exemplifies these analyses for the region shown in Fig. 2.4c with $\theta_m = 1.37°$. Mapping local θ_m for four ostensibly uniform samples near the MA, we found standard deviations to be approximately constant at around 0.03° (Fig. 2.5c). Likewise, mapping ε_H revealed an average ε_H of around 0.2% and standard deviations between 0.06 and 0.09% (Fig. 2.5d).

When quantifying structural disorder based on local changes in the moiré geometry, it is important to ensure that the variations observed do not arise simply from the uncertainty in the geometric fit of the AA sites (the vertices of the moiré unit cells). To this end, we performed bootstrapping[154] on three AA regions for $\theta_m = 1.37°$. The standard error of the AA region (x,y) coordinates was 0.08 nm. Numerical error propagation simulations show this corresponds to a standard deviation of about 0.01° in the calculated twist angle distribution arising from fitting error. As the measured θ_m

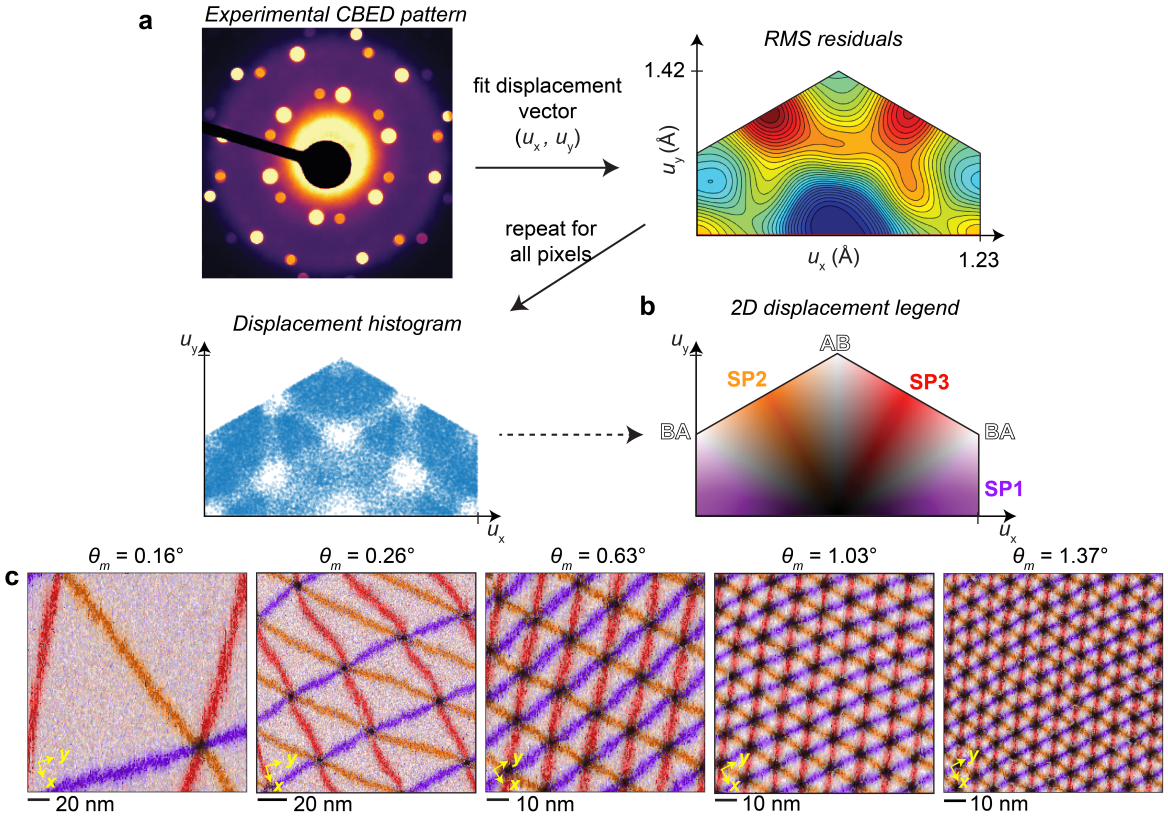

Figure 2.4: **a,** Schematic of the routine for fitting Bragg disk intensities, I_j, to local displacement vectors **u**. **b,** 2D hue–value colorization scheme used to produce the displacement maps shown in **c** from the fitted displacement vectors. The displacement vectors in **Fig. 2.3c** correspond to $\mathbf{u} = (u_x, u_y)$ displacement points in the half-hexagon and are colored accordingly, where the pixel hue and value correspond to the displacement vector direction and magnitude, respectively. **c,** Displacement field maps for TBL-Gr at various moiré twist angles, θ_m.

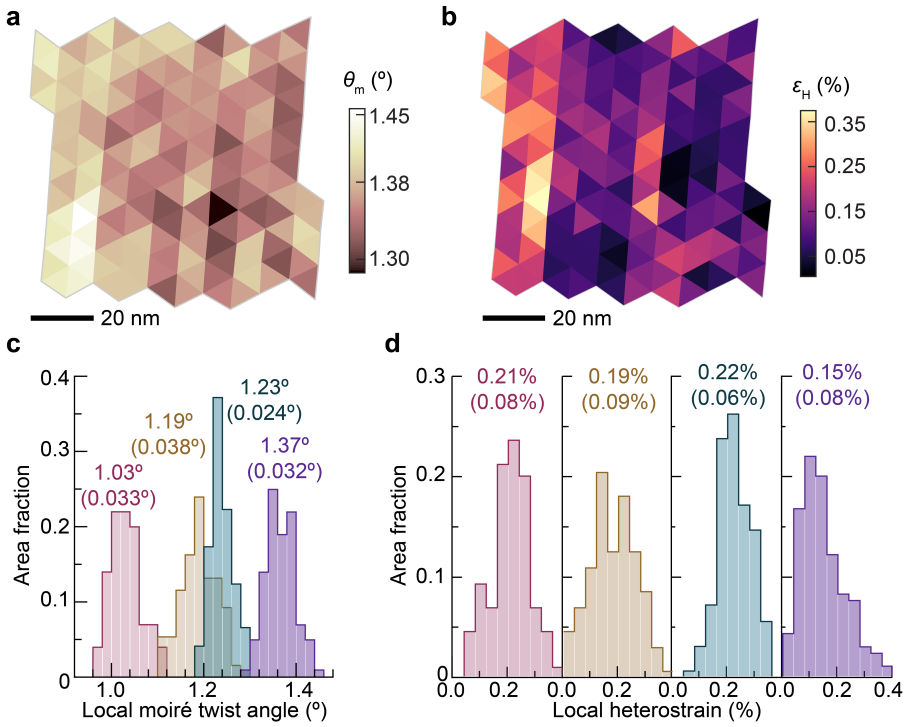

Figure 2.5: a,b, Maps of local twist angle θ_m (**a**) and uniaxial heterostrain ε_H (**b**) determined from AA-triangulated moiré domains over a region with an average twist angle of 1.37° (from the displacement map shown in **Fig. 2.4c**). **c,d,** Intrinsic local twist angle (**c**) and heterostrain (**d**) disorder for four 100 nm × 100 nm datasets of samples around the magic angle. Mean values are noted with standard deviations given in parentheses.

distribution standard deviations are in excess of this value, around 0.03° (Fig. 2.5c), we conclude that the observed twist angle disorder is a real effect. Furthermore, spatially-localized twist angle disorder is visible from the displacement maps. Analogous error propagation simulations show that AA registration uncertainty produces a heterostrain of 0.05% and a standard deviation of 0.026%. The non-zero value of heterostrain due to only AA registration uncertainty arises because the heterostrain triangulation model[146] is a biased estimator (that is, it is impossible to have a negative heterostrain value under this model, only positive heterostrains oriented in different directions can occur). Consequently, our measured heterostrain distributions could be systematically inflated, though we expect by $< 0.05\%$, given the above calculations. Again, since the experimental spread in heterostrain (0.06–0.09%, Fig. 2.5d) is about three times greater than what could be explained by AA registration error alone (0.026%), we can conclude this heterostrain disorder is likewise a real effect. Because the band structure is highly sensitive to supercell size and geometry[131,145],

the spatial fluctuations and distributions in both θ_m and ε_H that were resolved within these apparently homogeneous 100 nm × 100 nm regions may provide a gauge of the intrinsic short-range structural disorder to be expected from MA-TBL-Gr. The physical mechanism of the disorder remains unclear and requires further investigation.

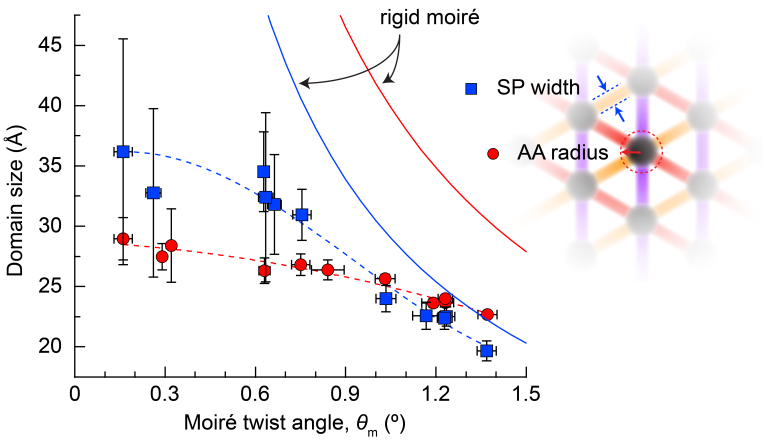

Figure 2.6: Domain size variation as a function of θ_m for measured samples (markers) and the simulated rigid moiré superlattice (solid lines). Vertical error bars represent 95% confidence intervals in domain size and horizontal error bars represent standard deviations of θ_m. Dashed lines are polynomial fits to the experimental data, drawn as visual guides to the overall trends.

These displacement maps also enable measurement of the geometric properties of the AA and saddle-point (SP) stacking regions (Fig. 2.6). The AA region radii were calculated by curve fitting the displacement amplitude to a 2D Gaussian function with equal variances and no correlation. Pixels with strong SP character were removed from the fit so as not to bias the background AB/BA displacement amplitude. The reported radii are for the circular level curve of the Gaussian at a displacement amplitude[140] of 0.71 Å. The SP region widths were calculated on the basis of the displacement vector angle with the origin before phase unwrapping. Each pixel was assigned an angle score between 0 (displacement angle equivalent to precise AB/BA stacking) and 1 (angle equivalent to precise SP stacking). The angle scores were interpolated perpendicularly to the boundary of the SP region, and the angle score threshold of 0.5 was used to determine the width of the SP region. Both AA and SP geometry fits were performed without TGV filtering of the data. The results of this analysis provide qualitative validation of trends previously predicted from multiscale modelling[142,143]. However, our measurements show larger AA region diameters and thinner SPs than those predicted from previous simulations, providing insights for future modelling.

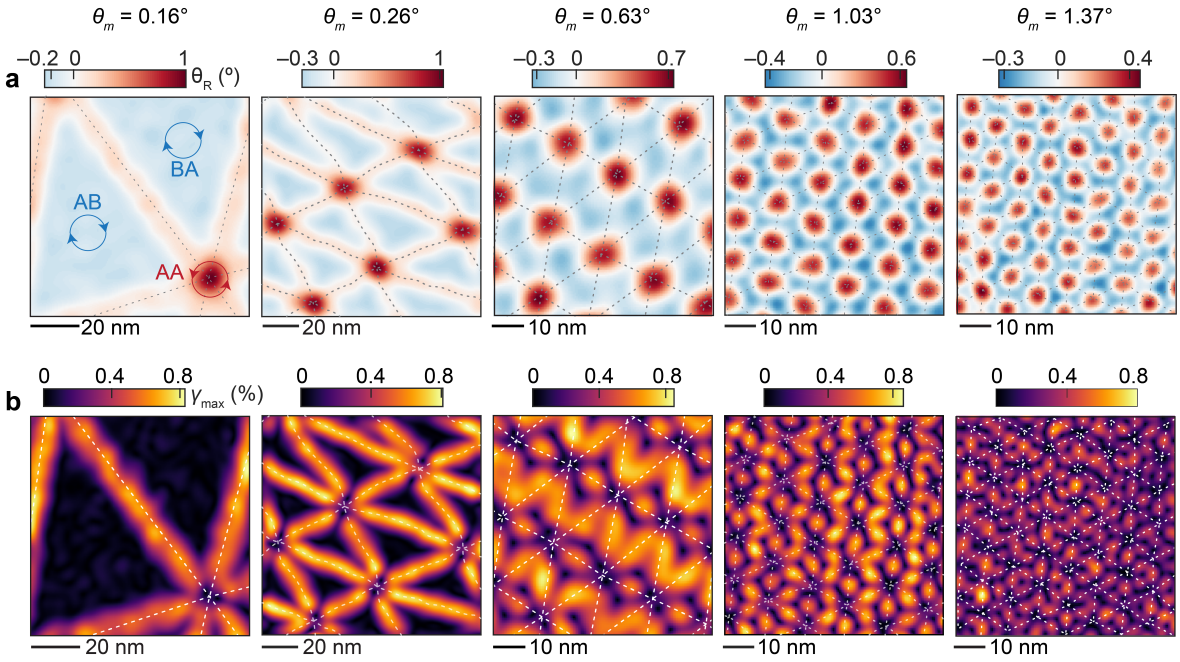

Figure 2.7: **a,** θ_R and **b,** γ_{max} maps for TBL-Gr with various values of θ_m. The overlaid dashed lines depict the moiré unit cell geometry from the displacement maps shown in **Fig. 2.4c**. The θ_R maps display the combined reconstruction rotation of both layers at each pixel and the γ_{max} maps represent the average strain per graphene layer at each pixel.

2.6 Strain field mapping

Since strain is a measure of the gradient of the displacement field[155,156], maps like those in Fig. 2.4c allow us to determine the complete 2D strain tensor describing all directions of in-plane deformation in TBL-Gr at each pixel as a function of θ_m (see Appendix, Sections 4–9 for more information). Consequently, we can measure both interlayer azimuthal rotations and intralayer deformation mechanics. The interlayer component is the total "fixed-body" rotation[155] field, θ_T, from which the local reconstruction rotation field, θ_R, can be determined by removing θ_m:

$$\theta_T = \theta_R + \theta_m \tag{2.2}$$

The maximum shear (also called principal shear) field, γ_{max}, provides the maximum amount of intralayer "engineering" shear strain in any direction experienced by the material[155,156]. Neither θ_R nor γ_{max} require definition of a local tensor coordinate system.

Figure 2.7 shows maps of θ_R (Fig. 2.7a) and γ_{max} (Fig. 2.7b) for several θ_m values. The maps of θ_R provide direct experimental evidence for a reconstruction mechanism predicted by theoretical studies[111,141–143] and indirectly suggested by electron diffraction data[113]: all maps display substantial positive θ_R in AA regions and negative θ_R in AB/BA domains. Positive θ_R^{AA} (rotation in the direction of θ_m) shrinks the area of the higher-energy AA regions; negative θ_R^{AB} (counteracting θ_m) brings the AB domains closer to commensurate, low-energy Bernal stacking. The effects of θ_m on rotational reconstruction can be visualized in regions of the sample possessing θ_m varying rapidly from 1.7 to 0.6° owing to a nearby tear in one of the graphene layers (Fig. 2.8). We plot θ_T instead of θ_R in Fig. 2.8 because of the variation in θ_m over the field of view.

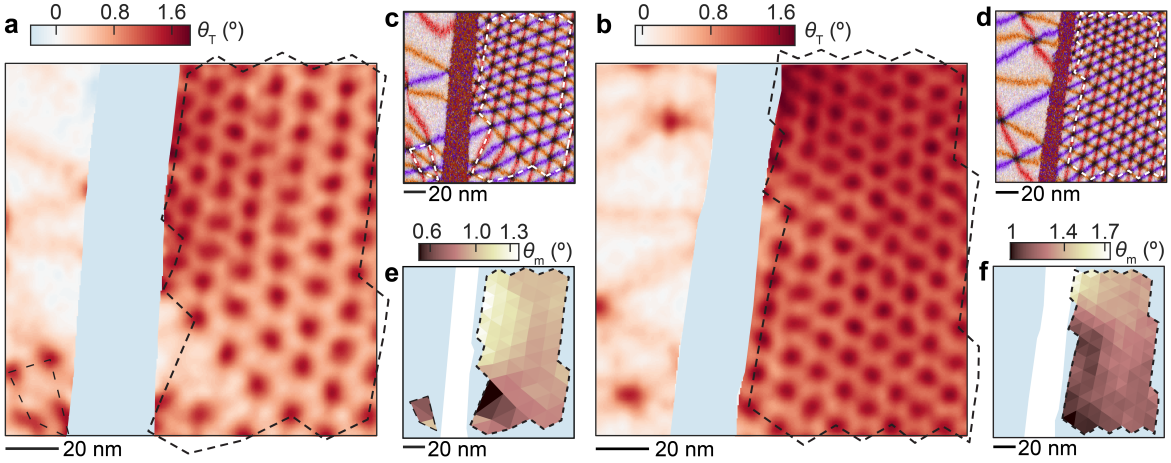

Figure 2.8: a,b, θ_T for two TBL-Gr regions in the vicinity of a tear in one of the graphene layers. **c,d,** Corresponding maps of the displacement fields and **e,f,** the moiré twist angle.

Figure 2.9 shows θ_T^{AA} and θ_R^{AA} as a function of θ_m based on 20 twist angle-homogeneous images and two additional datasets over regions with a nearby tear (from the regions shown in Fig. 2.8). The two types of dataset show excellent agreement, with greater precision from the homogeneous maps. As θ_m nears zero, θ_R^{AA} approaches a limiting value of approximately 1.2°. For $\theta_m < 0.5°$, reconstruction keeps approximately constant. Extrapolation of θ_R^{AA} to large θ_m suggests that the onset of reconstruction begins below $\theta_m \sim 2°$. We note that all reported twist angle-dependent strain and rotation trends were obtained through an region of interest (ROI)-based approach. Based on the geometry registration obtained during the displacement field unwrapping process (see Appendix, Section 4), masks were built by selecting all pixels within a given distance of the registration position. For the AA regions, all pixels within 1 nm of the AA center were included. For the SP regions (discussed later), all pixels within 1 nm of the line down the center of the region were

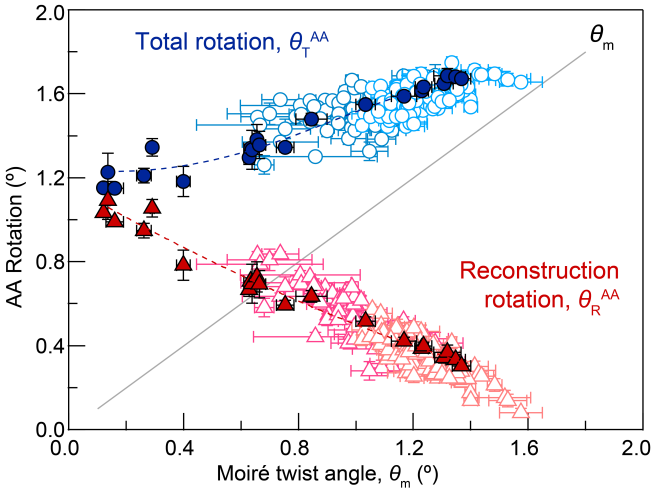

Figure 2.9: Total (blue, pale blue circles) and reconstruction (red, pink triangles) rotation in AA domains as a function of θ_m. The filled markers indicate average values obtained from homogeneous twist angle regions with a fields of view of $\geq$50 nm $\times$ 50 nm. The open markers indicate individual AA domains from two datasets with rapidly changing θ_m due to a nearby tear (**Fig. 2.8**). The solid line represents the moiré rotation. For the homogeneous regions, horizontal error bars represent standard deviations of the moiré angles, reflecting the distribution of all triangulated moiré unit cells within each dataset. Vertical error bars are 95% confidence intervals obtained from the variance across multiple domains measured within the image (for instance, multiple AA mask regions). For datasets acquired near a tear in one of the graphene layers, this approach cannot be followed because the twist angle is changing rapidly. Instead, each AA region is assigned an effective twist angle by averaging the triangulated moiré twist angles for all immediately adjacent moiré unit cells. Horizontal error bars are given as the standard deviation of these moiré angle values. Vertical error bars are given as the standard deviation of the quantity of interest for all pixels within the individual AA mask.

included, excepting a mask of variable size that prevented the AA region from being used. For the AB/BA domains, first the AA and SP regions were removed with wide masks, and then the remaining area was used as the AB region. Therefore, transitional pixels between two domains were not included in these calculations. Within each masked region, all pixels were averaged to produce the calculated value for that specific domain, and then all domains were averaged together to produce the single reported value for the dataset.

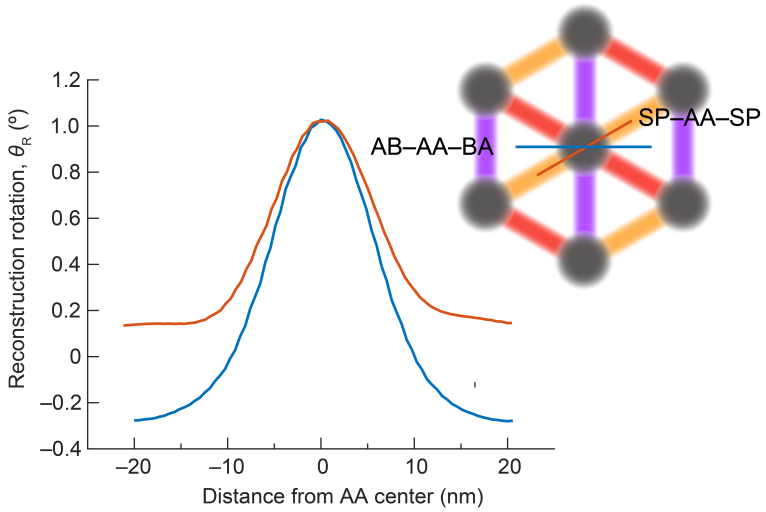

Figure 2.10: Variation in local reconstruction rotation across an AA region in a TBL-Gr sample with a moiré twist angle 0.26° via two paths shown in the inset schematic.

The maps of the rotational reconstruction mechanics in Fig. 2.7a explain the observed distribution of intralayer shear strain in Fig 2.7b. Despite the large rotational reconstruction taking place at all of the θ_m values sampled (Fig. 2.7a), γ_{max} decreases rapidly upon approaching the core of the AA region (Fig. 2.7b) due to the bivariate Gaussian radial profile of θ_R^{AA} (Fig. 2.10)[140,143]; near the center of the AA region, the approximately constant θ_R^{AA} produces no intralayer strain. For $\theta_m = 0.16°$ and 0.26°, the AB domains also exhibit no intralayer strain over an extended region (Fig. 2.7b), consistent with the constant θ_R^{AB} observed (Fig. 2.7a). Conversely, at twist angles near and greater than the MA θ_R^{AB} changes more rapidly through space (Fig. 2.7a), as extended Bernal domains have not formed. Consequently, intralayer strain in MA-TBL-Gr appears less localized than strain at smaller twist angles, relative to the moiré unit cell size. In general, the γ_{max} maps (Fig. 2.7b) show that the intralayer strain is largely localized at the SP for all values of θ_m, with peak values of γ_{max} exceeding 0.8%. Additionally, although some regions of the maximum shear strain maps for $\theta_m = 1.03°$ and 1.37° show nearly six-fold symmetric SP strain, other

regions display more striped features similar to that for the region with $\theta_m = 0.63°$ in Fig. 2.7b, an observation that we shall return to. The changing directions of the principal strain[156] axes (Fig. 2.11) reveal that reconstruction does not generate global strain.

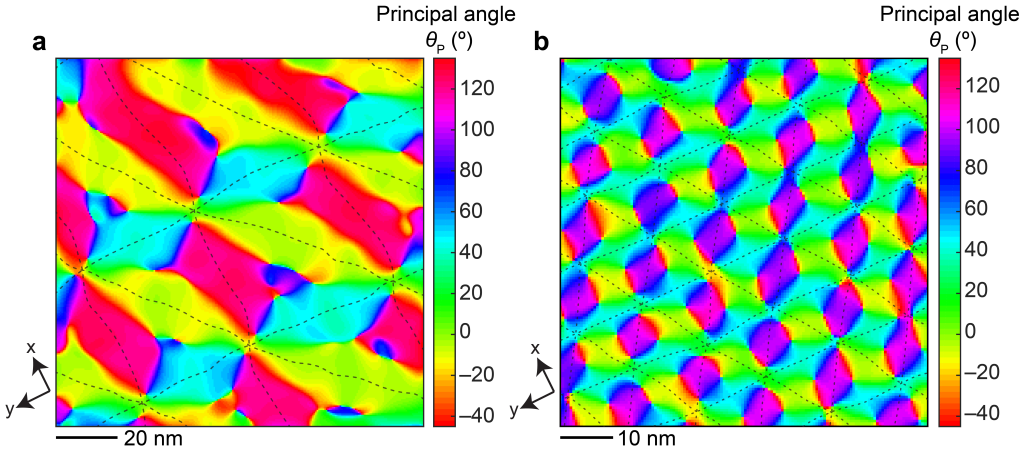

Figure 2.11: Orientation of the maximum principal strain component in two TBL-Gr samples with moiré twist angles of **a,** 0.26° and **b,** 1.03°. Overlaid dashed lines depict the moiré unit cell geometry from displacement maps, showing the strain direction is nearly uniform within each SP domain. Angles are computed relative to the positive x-axis displayed.

In addition to γ_{max}, SP strain can also be understood in terms of simple shear strain:

$$s_{yx} = \partial u_y / \partial x \tag{2.3}$$

$$s_{xy} = \partial u_x / \partial y \tag{2.4}$$

The quantity s_{yx}, used in previous 1D analysis of shear soliton walls[144], considers the displacement change parallel to a soliton wall[140,157]. Here, both s_{xy} and s_{yx} were directly obtained from our 2D strain measurements. Figure 2.12a shows that as θ_m decreases through the MA, s_{xy} is larger and increases more rapidly than s_{yx} until a maximum at around $\theta_m = 0.8°$, after which an inversion in s_{yx} and s_{xy} occurs at $\sim 0.5°$. The plot of γ_{max} versus θ_m shows that the average intralayer shear strain loading in MA-TBL-Gr is substantially greater than that suggested by s_{yx} or s_{xy} alone, and comparable to that at smaller θ_m, with a limiting mean γ_{max} of $\sim 0.7\%$. We note that the simple shear strain trends in s_{xy} and s_{yx} shown in Fig. 2.12a were obtained as averages over all three SP directions. For each SP direction, the s_{xy} and s_{yx} values were computed in the right-handed tensor coordinate system with the x-axis perpendicular to the SP direction and the y-axis parallel to the SP direction.

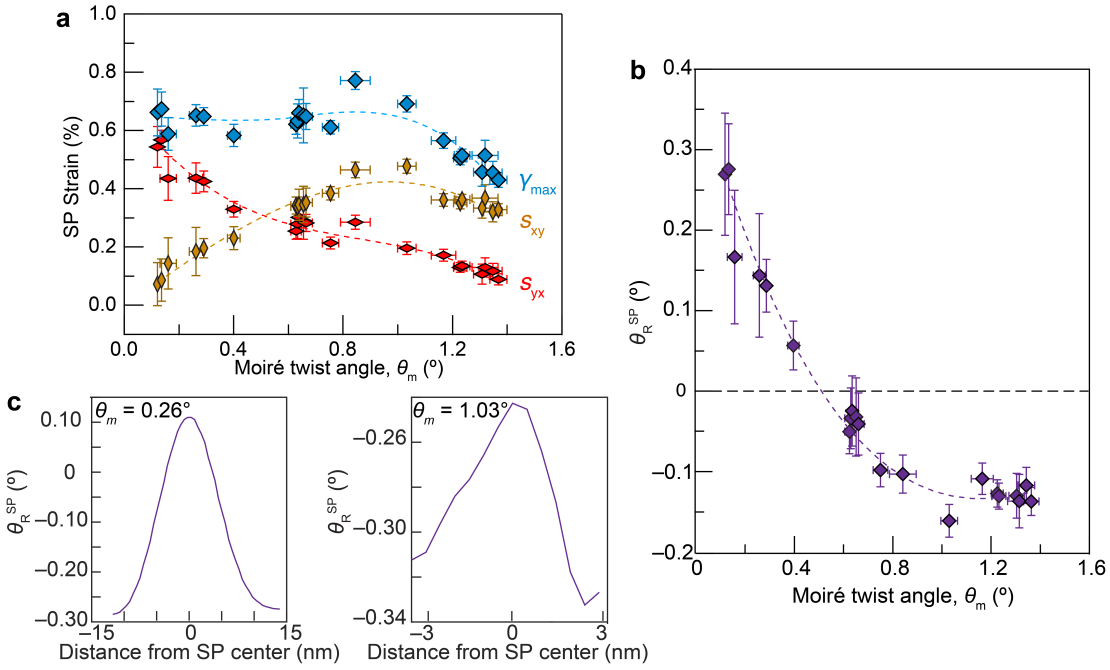

Figure 2.12: a, Three metrics for shear strain in SP domains (γ_{max}, s_{xy} and s_{yx}) as a function of θ_m. **b,** Local SP reconstruction rotation as a function of θ_m showing crossover in rotation direction near $\theta_m = 0.5°$. Horizontal error bars depict the standard deviations of moiré angles and vertical error bars depict 95% confidence intervals. The dashed line is a polynomial fit, drawn as a visual guide.

The magnitudes of s_{yx} and s_{xy} in the SP domains cross at $\theta_m = 0.5°$ because simple shear strain combines intralayer pure shear with interlayer fixed-body rotation (see Appendix, Section 6)[155]. Figure 2.12b shows plots of local rotation in the SP regions (θ_R^{SP}) as a function of θ_m. We see that θ_R^{SP} undergoes a sign change from negative to positive as θ_m decreases, consistent with the changing relative magnitudes of s_{yx} and s_{xy} in Fig. 2.12a. Plots of θ_R^{SP} as a function of distance from the center of the SP region (traversing the path AB $\rightarrow$ SP $\rightarrow$ BA) are shown in Fig. 2.12c for two regions with $\theta_m = 0.26°$ and $1.03°$, showing that the reconstruction rotation varies as a bell curve across the SP region in both cases but the change is much smaller for $\theta_m = 1.03°$ than $\theta_m = 0.26°$ due to weakening reconstruction. These plots also illustrate the sign change of θ_R^{SP} in the center of the SP region as θ_m varies.

Considering the AB/BA regions, Fig. 2.13a shows θ_R^{AB} as a function of θ_m. Although θ_R^{AB} is negative over the entire range of θ_m, it varies non-monotonically with θ_m, reaching a minimum value of $\theta_R^{AB} \sim -0.35°$ at $\theta_m \sim 0.8°$. Fully commensurate AB stacking is achieved for $\theta_m < 0.2°$, when $\theta_R^{AB} = -\theta_m$. Using these values of θ_R^{AB}, we calculated the induced displacement on each side of the AB boundary (that is,

near the SP regions). In the limit of $\theta_m < 0.2°$, AB reconstruction in TBL-Gr may be simplistically modelled as rotation of large fixed plates in the opposite direction of the moiré angle. As all AB plates rotate in the same direction, the boundary of any two plates experiences a shearing mechanic due to the reconstruction, leading to the observed concentration of γ_{max} in these regions. The displacement induced at such a boundary may be calculated geometrically using the moiré triangle side length $L = a/|\theta_m|$, where $a = 2.461$Å is the lattice constant of graphene. The distance from the center of the triangular AB domain to the boundary point is $a/2\sqrt{3}|\theta_m|$. Under the small angle approximation, the displacement arising from rotation of one AB domain is $|s| = r|\theta_R^{AB}| = a|\theta_{AB}|/(2\sqrt{3}|\theta_m|)$, where θ_R^{AB} is the reconstruction rotation in a single layer of graphene. The adjoining AB domain contributes an equal amount of displacement in the opposite direction. The total in-plane displacement in one layer of graphene at an AB/BA boundary is therefore $|u_{bound}| = 2|s| = a|\theta_R^{AB}|/(\sqrt{3}|\theta_m|)$. The induced displacement in a single layer of graphene is plotted according to this formula in Fig. 2.13b.

Notably, the shear-induced displacement on the AB boundary grows as θ_m decreases and accelerates for $\theta_m < 0.5°$, despite this diminution in the magnitude of θ_R^{AB}. To explore the physical significance of this trend, we first plot the displacement change both parallel (Δu_y) and perpendicular (Δu_x) to a line traversing a SP using the displacement maps from Fig. 2.4c. As shown in Fig. 2.13c,d for θ_m values of both 0.26° and 1.03°, Δu_y is negligible, indicating that the displacement in SP regions is of the shear type as expected[144]. Interestingly, Δu_x displays a sigmoidal profile for $\theta_m = 0.26°$ (Fig. 2.13c), but a linear profile for $\theta_m = 1.03°$ (Fig. 2.13d). The former is expected for a true shear-type soliton wall[144], while the latter is expected for a rigid moiré. The formation of soliton walls directly relates to the more rapid increase in induced displacement observed for $\theta_m < 0.5°$ in Fig. 2.13b.

We now rationalize the origin of these soliton walls. When traversing a shear soliton wall perpendicular to the direction of the wall, the total stacking order displacement change is $a/\sqrt{3}$. If the rotation in the two graphene layers is equal and opposite and all of the stacking order change is produced by AB reconstruction rotation, then there must be a simple shear displacement of $|u_{bound}| = a/(2\sqrt{3})$ in both the top and bottom layer to satisfy the soliton wall boundary condition. Equating this with the displacement formula derived in the previous paragraph, we have $a|\theta_{AB}|/(\sqrt{3}|\theta_m|) = a/(2\sqrt{3})$. This simplifies to just $|\theta_{AB}| = |\theta_m|/2$, which is also the angle at which the AB reconstruction exactly cancels out the moiré rotation to form commensurate Bernal-stacked AB domains. Indeed, as θ_m goes to zero, we see $|\theta_{AB}|$ approaching $|\theta_m|/2$ (Fig. 2.13a) and the induced displacement in the SP region of a single graphene layer approaching $a/(2\sqrt{3})$, about one-half the C–C bond length (Fig. 2.13b). Overall, this demonstrates that AB reconstruction not only improves the interlayer stacking energy, but it also produces the correct boundary displacement for thin soliton walls as θ_m decreases. This displacement change is sufficient to explain the formation of thin shear solitons in their entirety, indicating that reconstruction

rotations in AB domains are a mechanism for generating soliton walls.

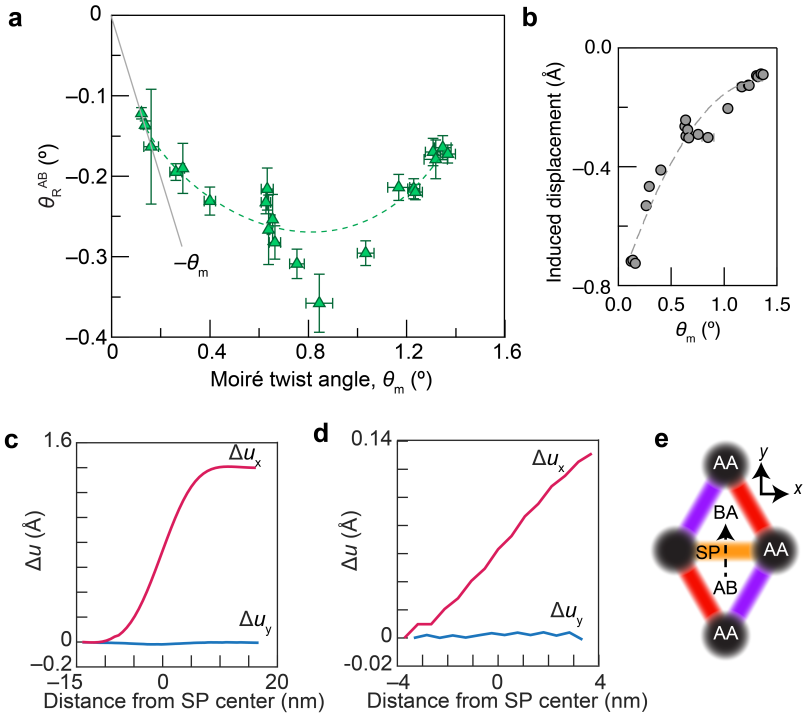

Figure 2.13: **a,** Local AB reconstruction rotation as a function of θ_m. The AB commensurability criterion $\theta_R^{AB} = -\theta_m$ (grey line) is met for $\theta_m < 0.2°$. Horizontal error bars depict the standard deviations of moiré angles and the vertical error bars depict 95% confidence intervals. The dashed line is a polynomial fit to the experimental data, drawn as a visual guide. **b,** Reconstruction-induced displacement on the boundary of two counter-rotating AB domains. **c,d,** Variation in displacement components, Δu_x and Δu_x, across an SP region in TBL-Gr samples with moiré twist angles of 0.26° (**c**) and 1.03° (**d**) from the datasets shown in **Fig. 2.4c**. An illustration of path followed in traversing across the SP region is shown in **e**, with the directions of the x- and y-axes labelled. Sigmoidal variation in displacement, as expected in a true shear soliton wall[144], is observed at $\theta_m = 0.26°$ (**c**) due to AB/BA-dominated reconstruction. Meanwhile, linear shear-induced displacement is observed at $\theta_m = 1.03°$ (**d**) due to weak AB reconstruction at this angle. The observed linear variation in displacement is due to the underlying moiré pattern.

2.7 Dual regimes of reconstruction mechanics in TBL-Gr

To explore how the twist angle-dependent trends in local strain and rotations impact the overall structure of TBL-Gr, Fig. 2.14a shows the extracted area percentages of different stacking orders. These stacking area trends were determined by partitioning the displacement vectors into three stacking order categories (AA, SP and AB/BA), as depicted in Fig. 2.14a (inset) and 2.14b. All displacement vectors with amplitude less than 0.71 Å were assigned to AA stacking[140], whereas the remaining vectors were assigned to whichever pure stacking order was closer in displacement space (AB/BA or SP). To avoid the influence of outliers, this calculation was performed on TGV-filtered data.

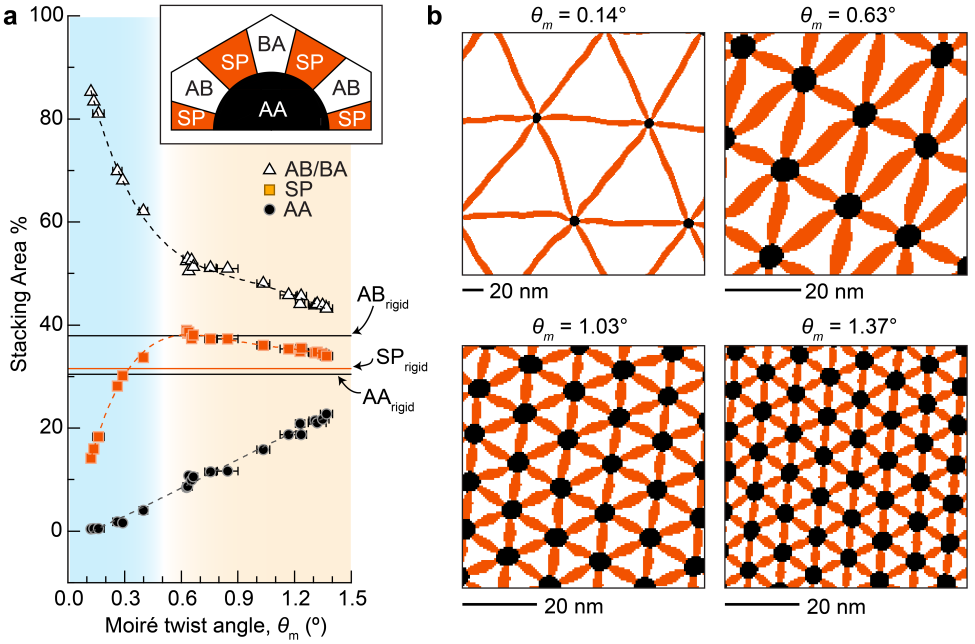

Figure 2.14: a, Variation of the relative stacking order areas with twist angle. The solid horizontal lines show the constant stacking area in the case of a rigid moiré (no reconstruction) for comparison. Horizontal error bars depict the standard deviations of moiré angles. **b,** Stacking assignments for regions with a series of representative moiré twist angles. Assignments were made using the three-category partition of displacement vectors shown in the inset of **a**.

We again find two regimes in the stacking area trends with a crossover point near $\theta_m = 0.5°$, the same angle where θ_R^{SP} changes sign (Fig. 2.12b) and the induced displacement in the SP regions increases more quickly (Fig. 2.13b). For $\theta_m > 0.5°$, the AA region fractions shrink steadily as θ_m decreases, driven by increasing θ_R^{AA}. In this

regime, as θ_m decreases, both the AB and SP areas increase, consistent with a dominant reconstruction process that does not distinguish between these arrangements. Conversely, the AB and SP areas diverge for $\theta_m < 0.5°$; the AB domains increase in size, whereas the SP regions decrease in relative area fraction, despite increasing in absolute width (Fig. 2.6) as they form true shear soliton walls bordering the AB domains at small angles. Even though the AA regions have approximately constant radii in this regime (Fig. 2.6), their area fraction continues to decrease because of the expanding moiré wavelength.

A second stacking area analysis was also conducted using a five-category partition to consider intermediate stacking categories (Fig. 2.15). Here, the AA region was divided into an inner AA region (displacement $|u| < 0.35$Å) and an outer AA region ($0.35 < |u| < 0.71$Å). In addition to the pure AB/BA and SP stacking orders, an "SP/AB transitional" stacking order was defined at exactly the average of the AB/BA and SP stacking order displacement vectors. All non-AA displacement vectors were assigned to the closest of these three stacking orders (Fig. 2.15a,c). We note that while there are several potential ways to define a five-category partition, this example serves as an illustration of the effect of intermediate stacking orders. As in Fig. 2.14a, the twist-angle-dependent stacking area percentage was analyzed (Fig. 2.15b). Between $\theta_m = 1.4°$ and $0.5°$, decreasing θ_m leads to a decrease in both the inner and outer AA stacking area percentage, while SP, AB/BA, and AB/SP transitional stacking areas each increase slightly. Below the critical angle of $\theta_m = 0.5°$, SP and AB/SP transitional stacking areas reverse trends and decrease in area percentage as the twist angle decreases, while AB/BA stacking increases sharply in area percentage. This behavior is the same as in the original partition in Fig. 2.14a, in which SP stacking area rose from $\theta_m = 1.4°$ to $0.5°$ and decreased below $\theta_m = 0.5°$, while AB/BA stacking rose modestly from $\theta_m = 1.4°$ to $0.5°$ and sharply below $\theta_m = 0.5$. This suggests that AA transitional stacking ("AA outer") diminishes as AA reconstruction takes place from $\theta_m = 1.4°$ to $0.5°$, while AB/SP transitional stacking diminishes as AB reconstruction takes place below $\theta_m = 0.5°$. These results are in agreement with intuitive expectations regarding reconstruction, and can be confirmed visually by examining the real-space stacking order assignment images (Fig. 2.15c). Overall, the same two regimes of reconstruction are visible regardless of the stacking partition employed.

To further understand these two reconstruction regimes we analyzed the reconstruction mechanics of TBL-Gr entirely through maps of simple shear strain (Fig. 2.16a,b) using local axis rotations (see Appendix, Section 7), establishing a conceptual picture of TBL-Gr reconstruction as an interplay between AA and AB/BA rotation (Fig. 2.16c). Again, positive θ_R^{AA} dominates for $\theta_m > 0.5°$ (Fig. 2.16c), and thus the primary simple shear is perpendicular to the SP region path between closely spaced AA regions ($s_{xy} > s_{yx}$ in Fig. 2.12a). Although AB counter-rotation does occur, the induced displacement change is minimal (Fig. 2.13b) because the moiré wavelength is small. Further, the SP fixed-body rotation produced by AA simple

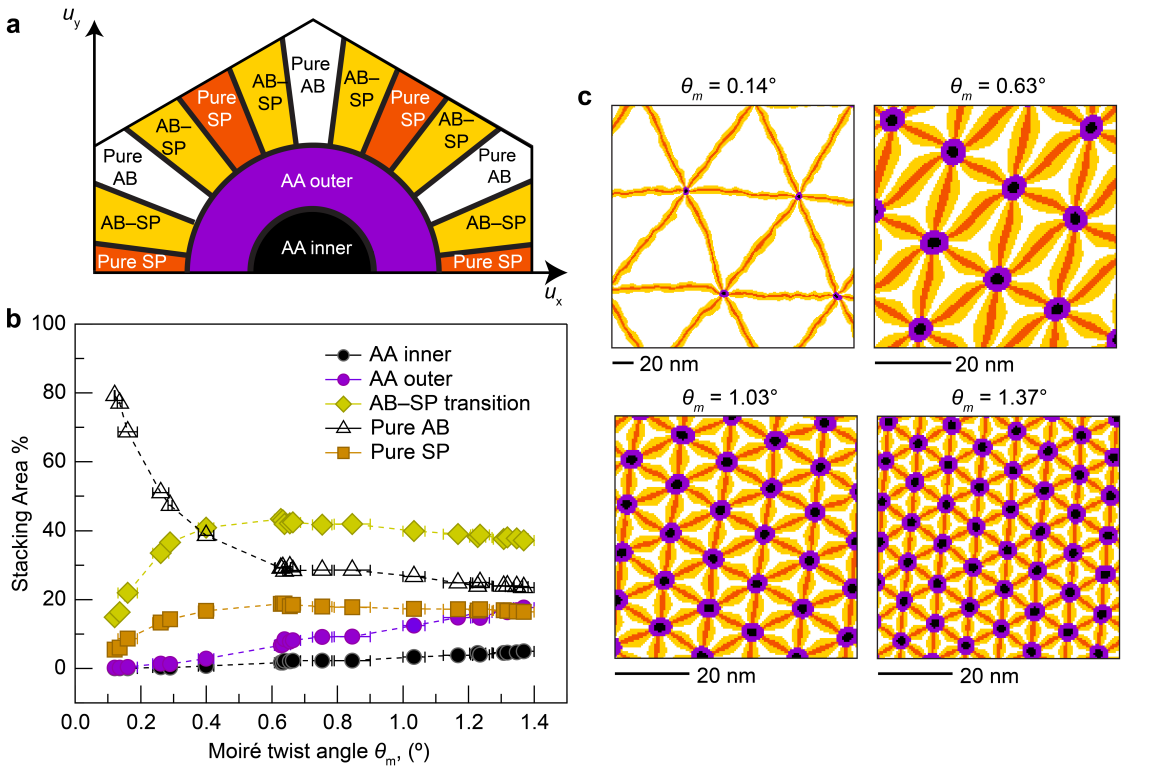

Figure 2.15: a, Schematic illustrating a five-category partition of the displacement space and **b,** corresponding plot of variation of the relative stacking order areas with twist angle. Horizontal error bars depict the standard deviations of moiré angles. **c,** Stacking assignments for regions with a series of representative moiré twist angles. Assignments were made using the five-category partition of displacement vectors shown in **a**.

shear is expected to be negative (Fig. 2.16c, right), explaining the observed negative θ_R^{SP} for $\theta_m > 0.5°$ (Fig. 2.12b). For $\theta_m < 0.5°$, θ_R^{AB} dominates. Because the AA rotation field decays quickly away from the AA core (Fig. 2.7a) and only a small θ_R^{AB} is required to counteract the small θ_m, θ_R^{AB} alone serves to maintain true soliton walls in this regime. Adjoining AB–BA domains rotating in the same direction (with negative θ_R^{AB}) generate dominant simple shear parallel to the soliton wall, demonstrating the case where $s_{yx} > s_{xy}$ in Fig. 2.12a and θ_R^{SP} is expected to be positive (Fig. 2.12b and Fig. 2.16c, left). When AA and AB simple shear forces are balanced in the SP domains, $\theta_R^{SP} = 0°$ because the SP experiences a pure shear force (Fig. 2.16c, center). This occurs near $\theta_m = 0.5°$, the critical angle separating the two regimes.

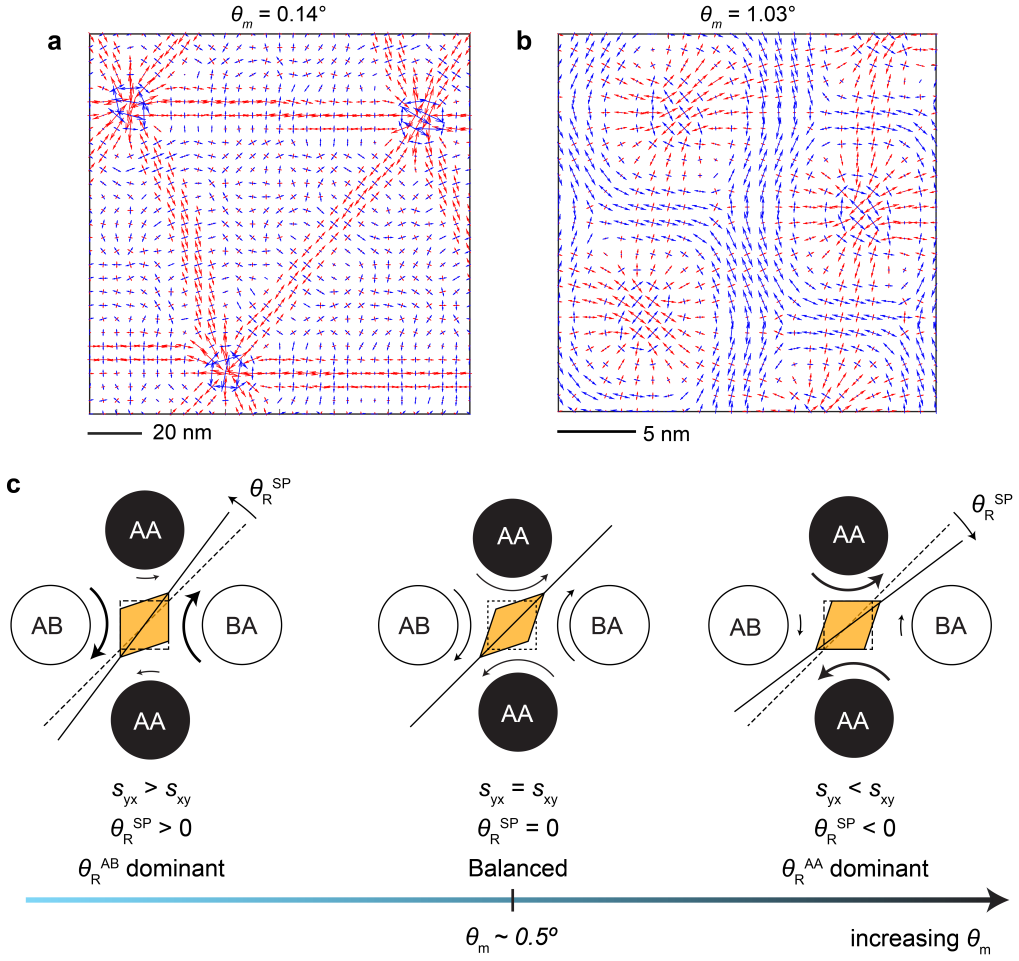

Figure 2.16: a,b, Simple shear decompositions for TBL-Gr at $\theta_m = 1.03°$ (**a**) and $0.14°$ (**b**). The red and blue arrows give the directions and relative magnitudes of the two simple shear components (see Appendix, Section 7). **c,** Schematic of the AA- and AB-dominated reconstruction regimes for TBL-Gr, explaining the observed changes in simple shear and SP reconstruction rotation.

2.8 Predicted effects of local rotations on electronic structure

The two-regime model provides a useful framework for examining the perturbation of the electronic structure by reconstruction and the destruction of ultraflat bands at smaller angles. We examined the effects of the two relaxation modes on the electronic structure of TBL-Gr using high-quality ab initio electronic tight-binding models[70] and a simple parameterized atomic reconstruction model based on our experimental strain maps, which allows selective implementation of θ_R^{AA}- or θ_R^{AB}-dominated reconstruction (see Appendix, Section 12 for details). We considered three values of θ_m: 0.35, 0.5 and 1.15°. $\theta_m = 0.5$ and 0.35° approximate the second and third magic angles predicted for a rigid (no reconstruction) TBL-Gr moiré[71]. For 0.35° (Fig. 2.17a), application of θ_R^{AB} alone removes the large number of low-energy bands and frames the lowest four by two pairs of neighbouring bands on each side, but in the process the extreme flatness is lost. In contrast, including only θ_R^{AA} retains band flatness, but does not remove as many low-energy bands. By including both rotations, a set of four nearly flat bands and two pairs of parabolic bands that touch the flattened bands at the Γ point emerge, reminiscent of the band structure of MA-TBL-Gr[71,113], albeit more dispersive in nature. At 0.5° (Fig. 2.17b), the results for the application of either θ_R^{AA} or θ_R^{AB} alone initially appear similar, although θ_R^{AB} noticeably produces more dispersive bands and θ_R^{AA} alone preserves some flatness. At 1.15° (Fig. 2.17c), θ_R^{AA} alone more closely replicates the flat band structure of the full reconstruction and opens gaps at the Γ point both above and below the flat band. It is impossible to exactly ascribe features of the doubly rotated band structure to individual rotation modes, but the trends observed in Fig. 2.17a–c imply that θ_R^{AA} helps define the flat low-energy modes, whereas θ_R^{AB} ensures that only four such bands exist at low energy and encourages a more dispersive band structure.

These qualitative observations of electronic modifications (Fig. 2.17a–c) arise because the band structure of TBL-Gr is predominantly described by the variation in interlayer electronic tunnelling over the moiré superlattice[71], which is highly sensitive to atomic reconstruction[158,159]. Figure 2.17d shows that the relative importance of θ_R^{AA} and θ_R^{AB} for interlayer tunnelling indeed changes with θ_m. At $\theta_m = 1.15°$, sole application of θ_R^{AA} yields better agreement of the calculated interlayer tunnelling with the fully reconstructed structure than pure θ_R^{AB}. For $\theta_m < 0.5°$, the converse is true, and at $\theta_m = 0.5°$, the influence of both rotations is almost balanced. This quantitative result agrees with qualitative comparisons between the full electronic interlayer tunnelling functions (see Appendix, Section 12). Thus, the relative contributions of the separate relaxation modes to the fully relaxed electronic structure (Fig. 2.17d) agree with our two-regime concept (Fig. 2.16c), providing the fundamental connection between the reconstruction-modified electronic band structures and our two-regime model developed from strain field mapping. This full-rotation

model also provides bands that are in good agreement with those obtained by realistic finite-element simulations, which relax the atomic structure self-consistently[141,143], but cannot interrogate the impact of individual rotation mechanics as permitted by our model.

2.9 Effect of heterostrain on reconstruction strain fields

Returning to the region in the vicinity of a tear (Fig. 2.8a), we estimated the uniaxial heterostrain (ε_H) over the field of view (Fig. 2.18a), revealing regions with nearly identical θ_m near the MA, but possessing ε_H varying between 0.1 and 1%. Figure 2.18b shows that MA-TBL-Gr regions with minimal ε_H (box 1) exhibit a fully six-fold symmetric strain pattern with localized, isolated pockets of shear strain on each individual SP. By contrast, regions with large ε_H (box 2) display striking striped features in γ_{max}. Additionally, SP shear strain fields are magnified both in value and in extent in the heterostrained region, suggesting that the extra strain loading from heterostrain localizes in the SP regions. We confirmed that the observed distortions are in fact due to heterostrain rather than a sample drift effect during data acquisition (see Appendix, Section 11).

Figure 2.18c captures the heterostrain-induced modification in a sample at $\theta_m = 0.63°$, where the regions are more zigzag in nature and the unstrained AB domains are consequently offset away from the shortened SP region angles. Finite-element relaxation simulations of heterostrained TBL-Gr (Fig. 2.18d, see Appendix, Section 12 for details) show excellent agreement with the experimentally extracted strain distributions and help to explain the formation of these quasi-1D strain features on geometric grounds. By changing the moiré cell geometry, heterostrain leads to a decrease in the angle between at least two pairs of SP regions, mandating a more rapid change in displacement. This 'displacement pinching' implies the need for a connected shear strain field in the decreased SP angle area to maintain reconstruction. Rather than shrinking or bending to avoid contact, the SP strain fields retain an approximately constant width under heterostrain, blending near the shortened SP region angles to break rotational symmetry and form striped regions. The tendency for TBL-Gr to generate this strain field rather than lessening reconstruction points to the importance of stacking energy over intralayer strain energy for driving reconstruction mechanics. This model also explains the observation of pronounced 1D striped regions in MA-TBL-Gr in comparison with TBL-Gr at smaller twist angles (Fig. 2.7b).

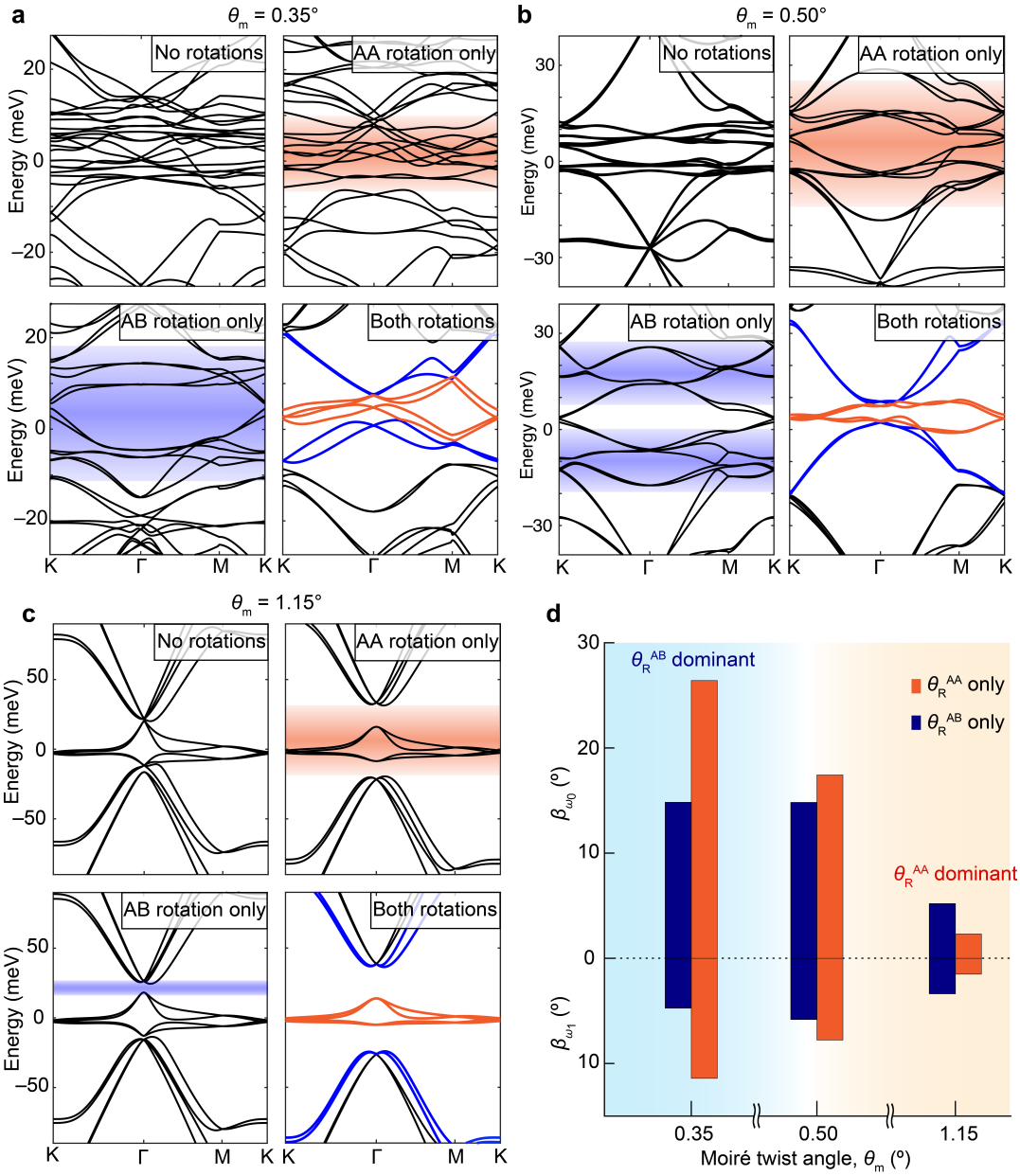

Figure 2.17: **a–c,** Calculated band structures for TBL-Gr at $\theta_m = 0.35°$ (**a**), 0.5° (**b**) and 1.15° (**c**) under various rotation assumptions. The band structure effects caused by AA (AB) rotation are highlighted in red (blue). **d,** The similarity in the ab initio calculated electronic interlayer scattering between the application of singular rotations (either θ_R^{AA} or θ_R^{AB}) and the full reconstruction (both θ_R^{AA} and θ_R^{AB}) is indicated by the generalized 'angle' β. A smaller angle indicates better agreement with full reconstruction. This similarity was assessed for interlayer scattering between similar ($\beta_{\omega 0}$) and dissimilar ($\beta_{\omega 1}$) orbitals for both θ_R^{AA} only (red) and θ_R^{AB} only (blue) relaxation assumptions. (ω corresponds to the interlayer coupling strength.)

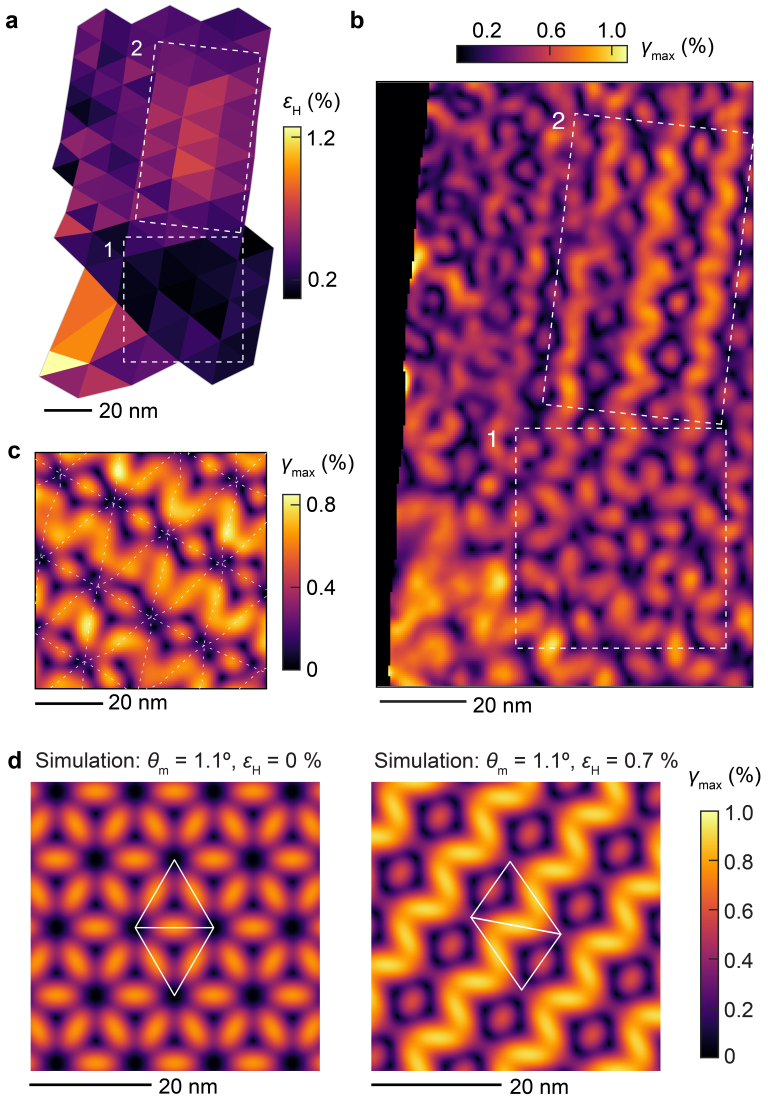

Figure 2.18: **a,** Map of the heterostrain, ε_H, determined from AA triangulation (see Methods) over the sample shown in Fig. 2.8a. Boxes 1 and 2 highlight two areas with similar θ_m ($\sim 1.1°$), but possessing a relatively large difference in ε_H. **b,** Map of γ_{max} (average per layer) over the region in **a**, showing six-fold symmetric SP strain patterns in box 1 (minimal ε_H) and striped strain features in box 2 ($\varepsilon_H \sim 0.7\%$). **c,** Map of γ_{max} (average per layer) over a homogeneously heterostrained ($\varepsilon_H \sim 0.45\%$) sample with $\theta_m = 0.63°$, showing pronounced zigzag features. The overlaid dashed lines depict the moiré pattern based on the displacement field maps. **d,** Calculations of relaxation by a finite-element method using parameters extracted from density functional theory (see Appendix, Section 12) for $theta_m = 1.1°$ without (left) and with (right) uniaxial heterostrain ($\varepsilon_H = 0.7\%$). The solid lines depict the moiré supercell.

2.10 Conclusions

Our Bragg interferometry methodology and analysis have made it possible to image moiré superlattices in MA-TBL-Gr, notwithstanding the real space colocalization of hBN multilayers. The visualization of stacking distributions at the level of individual AB/BA domains enables evaluation of the intrinsic superlattice disorder[145] in TBL-Gr. In previous studies[131], electronic effects from "long-range" variations in θ_m were considered as though, locally, each moiré superlattice represented an ideal twisted bilayer at a given θ_m, with an angle that varies in space. Accordingly, on the scale of micrometers, samples would possess patches of different electronic states, complicating transport measurements. In contrast, the "short-range" θ_m and ε_H disorder visualized here would cause fundamentally different effects[145]: the local ideal band structure is modified owing to spatial fluctuations in θ_m from one AB domain to another, and regions with the same effective θ_m could also present different electronic behavior due to disorder in ε_H[123,124]. A combination of microscale variations in θ_m and local nanoscale fluctuations in θ_m and ε_H may help explain the large variation in the observed low-temperature phases in MA-TBL-Gr.

Two-dimensional strain field mapping unveiled a rich landscape of structural mechanics. We found two reconstruction regimes in TBL-Gr involving competition between AA and AB/BA local rotations that are balanced near a moiré angle of 0.5°. The greater influence of AB counter-rotation at small angles compared with the dominance of AA rotation at 1.1° helps explain why flat bands are disrupted by reconstruction at smaller angles, whereas they persist at 1.1°. Our strain field maps and displacement-pinching model also show how mesoscale heterostrain in TBL-Gr is translated into localized, symmetry-breaking nanoscale features through the anisotropic amplification and deformation of SP regions into 1D strain structures that may be relevant to recently found nematic phases[146].

Bragg interferometry is also applicable to non-moiré heterostructures with colocalized reciprocal lattice vectors and may be performed in a manner compatible with in situ mechanical straining. Although our methodology considers only displacements and strain in the lateral plane, emerging holography techniques may provide a route towards obtaining complementary z-axis information[160,161]. The investigation of a wide range of moiré materials by this methodology will elucidate the complex interplay between intrinsic reconstruction strain, extrinsic uniaxial strain and a diverse array of physical phases, including correlated electronic states.

2.11 Experimental Details

2.11.1 Sample preparation

TBL-Gr samples were fabricated using the common tear-and-stack technique[162,163]. First, monolayer graphene (from Kish graphite, Graphene Supermarket) and ~ 5 nm thick hBN (grown by collaborators T.T. and K.W.) were mechanically exfoliated from bulk crystals onto SiO_2/Si substrates and selected using optical microscopy and atomic force microscopy. For graphene, an SiO_2 thickness of 285 nm was used and for hBN an SiO_2 thickness of 90 nm was used. A polybisphenol-A-carbonate/ polydimethylsiloxane stamp was used to pick up the hBN. The hBN was then engaged with half of a monolayer graphene crystal and the edge of the hBN was used to tear the graphene in half. The substrate was then rotated by θ_m prior to picking up the remaining half of the graphene monolayer. During this stacking process, the hBN and graphene lattices were deliberately misaligned by $> 10^\circ$ using the straight edges of the crystal layers as guides to prevent overlap of the hBN and graphene diffraction disks during 4D-STEM. Finally, the hBN/TBL-Gr stack was stamped onto a 50 nm thick Si_3N_4 TEM membrane (Norcada) with 2 μm holes for imaging.

2.11.2 Electron microscopy imaging

Electron microscopy was performed at the National Center for Electron Microscopy facility in the Molecular Foundry at Lawrence Berkeley National Laboratory. Low-magnification DF-TEM images were acquired using a Gatan UltraScan camera on a Thermo Fisher Scientific Titan-class microscope operated at 60 kV. Three frames each with an acquisition time of 5 s were summed to produce each dark-field image. These dark-field images (Fig. 2.1c) were used as references for selecting regions of interest for 4D-STEM.

4D-STEM datasets were acquired using a Gatan K3 direct detection camera located at the end of a Gatan Continuum imaging filter on a TEAM I microscope (aberration-corrected Thermo Fisher Scientific Titan 80–300) operated in energy-filtered STEM mode at 80 kV with a 10 eV energy filter centered around the zero-loss peak (to reduce background signal from inelastic scattering). In general, two sets of acquisition conditions were used, namely convergence semi-angles of 1.71 mrad (condition A) and 3 mrad (condition B), both of which allowed a sufficient signal-to-noise ratio and avoided overlap between the hBN and graphene diffraction disks. The beam current was 62–65 and 68 pA for conditions A and B, respectively. By fitting the center lobe of the STEM probes in real space using a 2D Gaussian function, we measured the full-width at half-maximum values to be 1.3 (A) and 0.8 nm (B). Diffraction patterns were collected using a step size of 0.5 nm with 100 $\times$ 100 to 300 $\times$ 300 scan positions covering an area of 50 nm $\times$ 50 nm to 150 nm $\times$ 150 nm. The K3 camera was used in full-frame electron counting mode with a binning of 4 $\times$ 4 pixels and

an energy-filtered STEM camera length of 800 mm. Each diffraction pattern had an exposure time of 10–13 ms, which is the sum of multiple counted frames.

2.11.3 Computational implementation

4D-STEM image processing and analysis were conducted in MATLAB (version $\geq$ 2016*b*, MathWorks) on a personal computer. TGV denoising was conducted according to a published algorithm[164,165]. All other code for the analysis of 4D-STEM data in this project was custom-written[166].

Chapter 3

Mapping rotational and dilational reconstruction in TMD moiré bilayers

Parts of this chapter were reproduced or adapted from: Van Winkle, M.*, Craig, I.M.*, Carr, S., Dandu, M., Craig, I.M., Bustillo, K.C., Taniguchi, Ciston, J., Ophus, C., Taniguchi, T., Watanabe, K., Raja, A., Griffin, S.M. & Bediako, D.K. Rotational and dilational reconstruction in transition metal dichalcogenide moiré bilayers. *Nat. Commun.* **14**, 2989 (2023). (*These authors contributed equally.)

Author Contributions: M.V.W. and D.K.B. conceived the study. M.V.W. designed and fabricated the samples. M.V.W., K.C.B. and J.C. acquired the 4D-STEM data. I.M.C. created the data analysis code and strain calculation framework with input from C.O. S.C. carried out DFT and relaxation simulations. M.D. performed SHG measurements. T.T. and K.W. provided the bulk hBN crystals. I.M.C. and M.V.W. processed and analyzed the data. M.V.W., I.M.C., and D.K.B. interpreted the data and wrote the manuscript. D.K.B., S.M.G., and A.R. supervised the work. All co-authors contributed to the overall scientific discussion and edited the manuscript.

3.1 Abstract

Lattice reconstruction and corresponding strain accumulation play a key role in defining the electronic structure of two-dimensional moiré superlattices, including those of transition metal dichalcogenides (TMDs). Imaging of TMD moirés has so far provided a qualitative understanding of this relaxation process in terms of interlayer stacking energy, while models of the underlying deformation mechanisms have relied on simulations. Here, we use interferometric four-dimensional scanning transmission electron

microscopy to quantitatively map the mechanical deformations through which reconstruction occurs in small-angle twisted bilayer MoS_2 and WSe_2/MoS_2 heterobilayers. We provide direct evidence that local rotations govern relaxation for twisted homobilayers, while local dilations are prominent in heterobilayers possessing a sufficiently large lattice mismatch. Encapsulation of the moiré layers in hBN further localizes and enhances these in-plane reconstruction pathways, suppressing out-of-plane corrugation. We also find that extrinsic uniaxial heterostrain, which introduces a lattice constant difference in twisted homobilayers, leads to accumulation and redistribution of reconstruction strain, demonstrating another route to modify the moiré potential.

3.2 Introduction

Moiré architectures comprised of semiconducting transition metal dichalcogenides (TMDs) are of considerable fundamental and technological interest because they exhibit distinctively tunable optoelectronic features, such as inter- and intralayer moiré excitons and trions[97–101,104,118,139,167–169], as well as relatively robust correlated electronic phases[93,95,170–174]. While the electronic band structure of a moiré superlattice is closely linked to the crystallographic misalignment between constituent layers, intrinsic lattice reconstruction also plays an underlying yet substantial role in controlling the emergent behavior in these systems[113–117,175]. Reconstruction of the superlattice and the development of intralayer shear strain subsequently lead to reconstruction of the electronic band structure, affecting features such as the depth of the moiré potential[119], the 'flatness' of low-energy bands[92,122], and the real-space localization of charge carriers[89,176,177].

Group VI (Mo- and W-based) H-phase TMDs, which are non-centrosymmetric in the monolayer limit, have two distinct reconstructed forms with unique band structures depending on whether there is a parallel (P, 3R-like, near 0°) or anti-parallel (AP, 2H-like, near 60°) orientation between layers. Scanning probe[115,117,119] and electron microscopy[114] techniques have provided a qualitative picture of reconstruction in TMD moiré homo- and heterobilayers, understood in terms of the variation in interlayer stacking energy throughout the superlattice. However, the physical mechanisms by which reconstruction occurs have thus far only been simulated. In this Chapter we use Bragg interferometry[161,175], the imaging methodology developed in Chapter 2, to directly map the intralayer mechanical deformations driving reconstruction in TMD moiré systems. We identify distinct reconstruction mechanisms for moiré homobilayers versus heterobilayers and examine their twist angle dependence, distinguishing the relative importance of local lattice rotations and dilations in both systems as well as the critical role that encapsulation layers play in affecting the balance between these in-plane deformations and out-of-plane corrugations. We also measure reconstruction-induced strain fields and demonstrate how application of an external mechanical force, e.g. heterostrain, can be leveraged to manipulate strain

distributions.

3.3 Interlayer displacement mapping

We prepared MoS_2/MoS_2 moiré homobilayers and WSe_2/MoS_2 moiré heterobilayers that were capped with thin (5–10 nm) hexagonal boron nitride (hBN). Twisted homobilayers were fabricated using the tear-and-stack method[162] to introduce a desired interlayer moiré twist angle (θ_m) (Fig. 3.1). Heterobilayers were made by stacking separate WSe_2 and MoS_2 monolayers with straight flake edges aligned. For the heterobilayers, the relative crystallographic orientation (P or AP) of stacked WSe_2 and MoS_2 monolayers cannot be pre-determined during fabrication or distinguished from optical micrographs or dark-field TEM (DF-TEM) images (Fig. 3.2a–h). Instead, the stacking orientation was assigned using polarization-resolved second harmonic generation (SHG) spectroscopy (Fig. 3.2i,j). In the case of P (AP) stacking, SHG intensity in the heterobilayer is greater than (less than) the sum of intensities from the two isolated monolayer regions[178] (see Section 9 for additional Experimental Details).

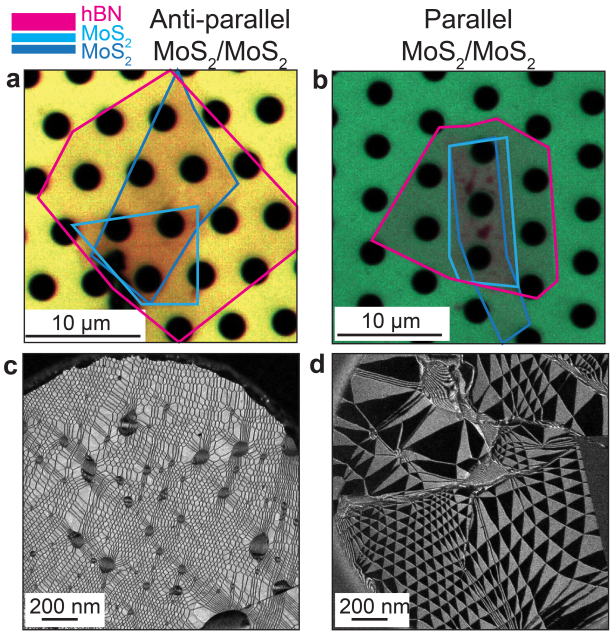

Figure 3.1: **(a,b)** Optical micrographs of example $hBN/MoS_2/MoS_2$ heterostructures on silicon nitride TEM grids. **(c,d)** Corresponding DF-TEM images, collected using the $[1\bar{2}10]$ and $[10\bar{1}0]$ TMD diffraction peaks, respectively.

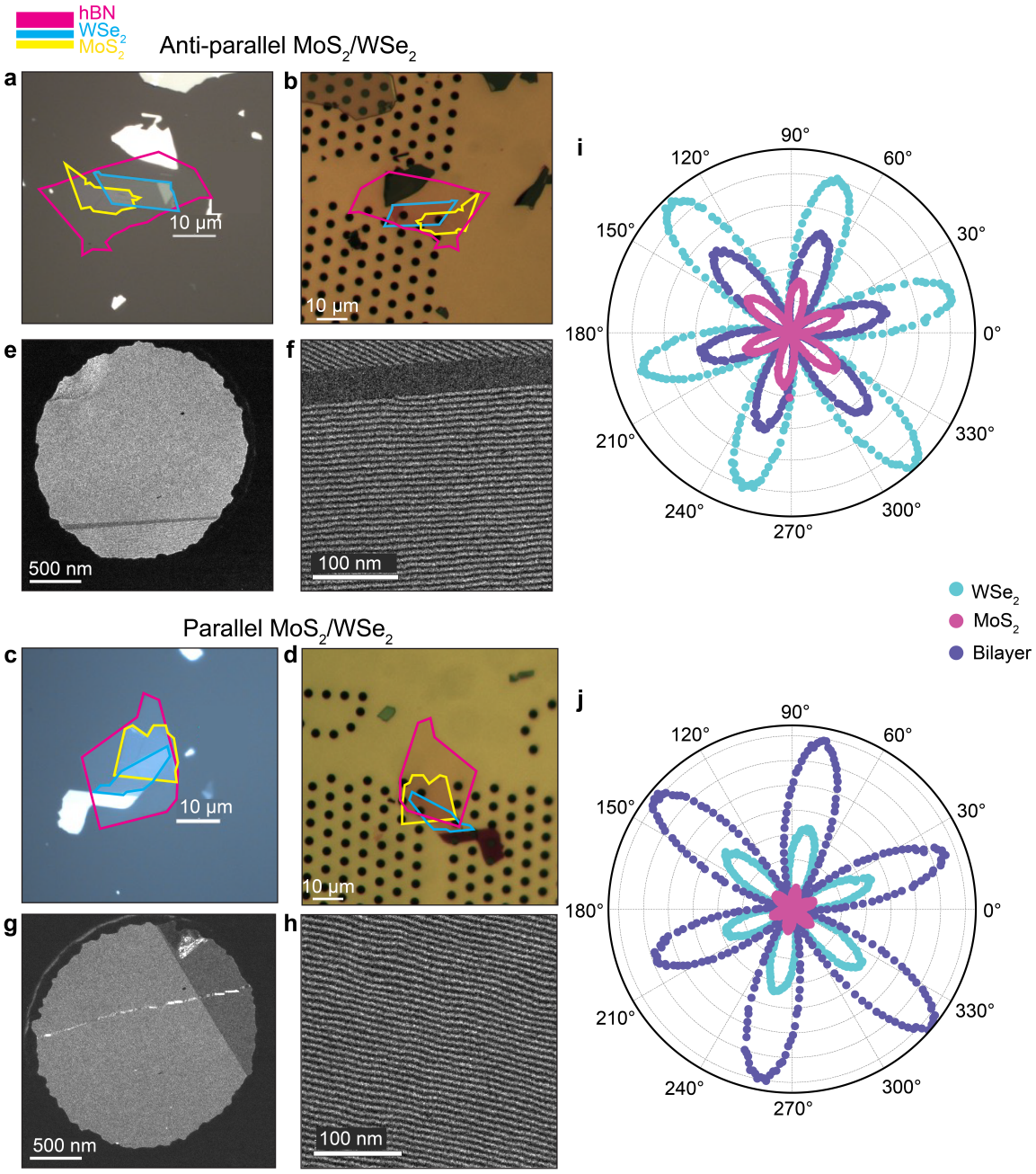

Figure 3.2: a–d, Optical micrographs of AP- and P-stacked hBN/WSe_2/MoS_2 heterostructures on PC/PDMS stamps **(a,c)** and on silicon nitride TEM grids **(b,d)**. **e–h,** Corresponding DF-TEM images and **i,j,** polarization-resolved SHG measurements. DF-TEM images were collected using the [10$\bar{1}$0] TMD diffraction peaks.

To image the moiré structures, we performed Bragg interferometry (Fig. 3.3a), based on four-dimensional scanning transmission electron microscopy (4D-STEM). As detailed in Chapter 2, the guiding principle of this imaging technique is that electron waves diffracted by the two TMD layers interfere with one another; in reciprocal space this leads to a modulation of the intensity measured in the overlapping regions of the TMD Bragg disks that depends on the local stacking sequence. Given a certain convergence angle of the incident beam, the amount of Bragg disk overlap is controlled by moiré twist angle (θ_m) for homobilayers (Fig. 3.3b) and both twist angle and lattice constant percent difference (δ) for heterobilayers (Fig. 3.3c).

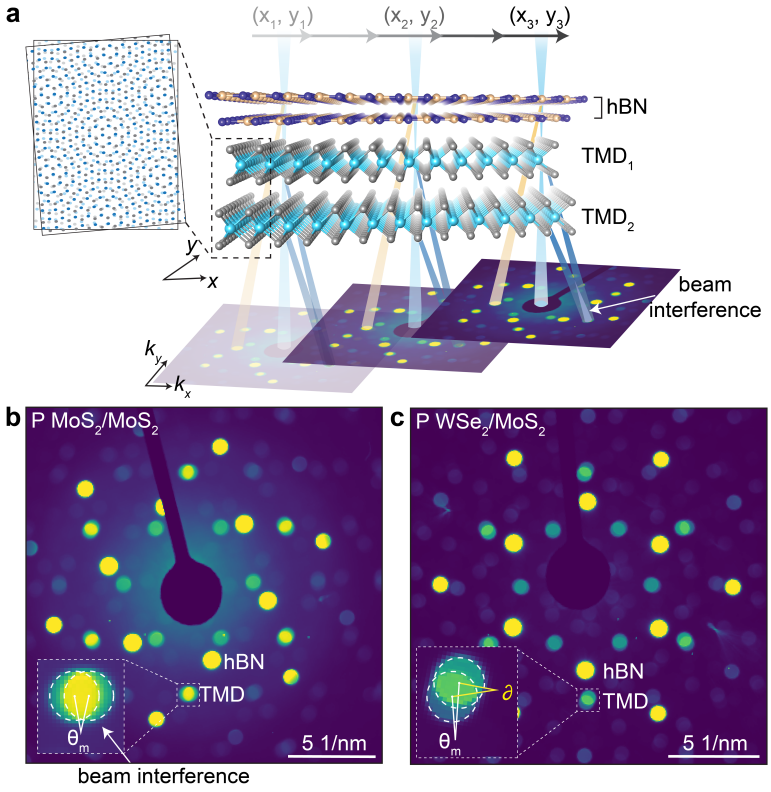

Figure 3.3: **a,** Schematic of Bragg interferometry measurement. Here (x_1, y_1), (x_2, y_2), (x_3, y_3) refer to electron beam positions. TMD_1 and TMD_2 are MoS_2 for homobilayers or MoS_2 and WSe_2 for heterobilayers. Dashed box and corresponding inset illustrate formation of a moiré superlattice between TMD_1 and TMD_2. Axis labels x, y and k_x, k_y indicate real space and reciprocal space coordinate systems, respectively. **b,c,** Average convergent beam electron diffraction patterns for a MoS_2/MoS_2 moiré homobilayer and WSe_2/MoS_2 moiré heterobilayer, respectively, with moiré twist angle θ_m and lattice constant percent difference δ. Overlapping TMD Bragg disks are highlighted in the insets.

The intensities in the regions of Bragg disk overlap can be used to determine the average interlayer atomic displacement vector at each beam position, providing structural information about the superlattice as demonstrated for twisted bilayer graphene in Chapter 2. For non-centrosymmetric systems and heterobilayers, which do not necessarily possess centrosymmetry, our methodology requires an expansion of the fitting function used for the twisted bilayer graphene case to relate I_j, the overlap intensity in the j^{th} Bragg disk pair, and $\mathbf{u} = (u_x, u_y)$, the local displacement vector that describes the interlayer offset between the TMD lattices (see the Appendix, Section 1 for a full derivation of the fitting function):

$$I_j = A_j \cos^2(\pi \mathbf{g}_j \cdot \mathbf{u}) + B_j \cos(\pi \mathbf{g}_j \cdot \mathbf{u}) \sin(\pi \mathbf{g}_j \cdot \mathbf{u}) + C_j \tag{3.1}$$

Again, although the hBN encapsulation layers are colocalized with the TMD layers in real space, the hBN Bragg disks are sufficiently offset from those of the TMD layers in reciprocal space and thus do not impede the structural analysis using Bragg interferometry. This 4D-STEM approach is therefore not restricted by buried interfaces, as in the case of scanning probe methods (which often require the sample surface to be exposed) and conventional real-space electron imaging methods (that can be obscured by encapsulating layers).

Example displacement maps for P and AP moiré bilayers are provided in Fig. 3.4a,b (see the Appendix, Section 2 for details on the displacement fitting process). For the P case, the high-symmetry stacking orders include MMXX, XM, MX, and SP (saddle point), as described in Fig. 3.4c. In comparison, the stacking orders in the AP case include XMMX, MM, XX, and SP, shown in Fig. 3.4d. It is of particular note that in Fig. 3.4a,b, each pixel color encodes quantitative information about the local displacement vector (illustrated as arrows in Fig. 3.4c,d) within the displacement zone depicted in Fig. 3.4e. We observe sharp triangular features in the displacement map for the P moiré homobilayer and a hexagonal structure for the AP orientation, similar to what has been previously reported[114,115]. The moiré pattern is much smaller for the heterobilayer cases, considering the maximum possible periodicity is $\sim$ 8 nm for $\delta_{MoS_2/WSe_2} = 3.96\%$. Notably, while the heterobilayer displacement fields appear more like that of a rigid moiré lattice (Fig. 3.4f), ostensibly suggesting that reconstruction is relatively weak compared to the twisted homobilayers, the strain mapping and geometric analyses that follow show that reconstruction remains strong even in these cases.

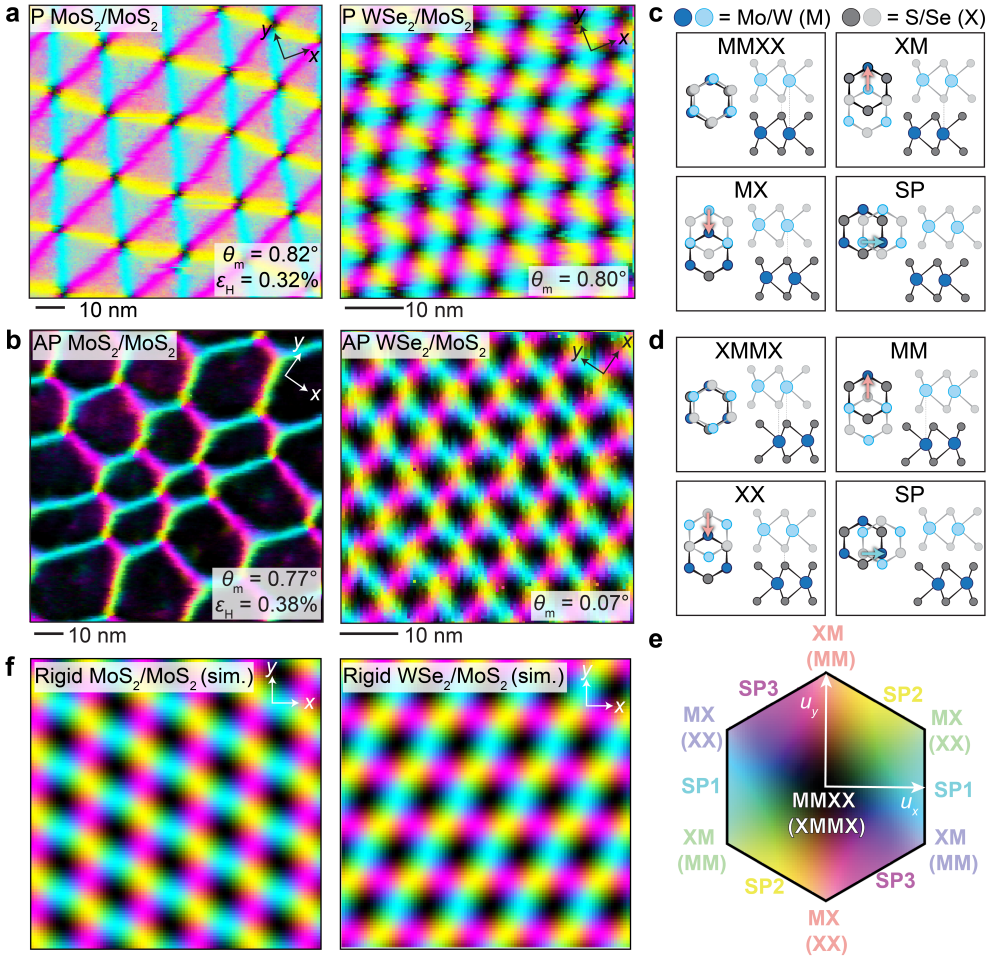

Figure 3.4: **a,b,** Representative displacement maps for moiré bilayers with parallel (P) and anti-parallel (AP) orientations, respectively. The moiré twist angle and heterostrain are labelled as θ_m and ε_H. **c,d,** High-symmetry stacking sequences and corresponding displacement vectors for P and AP H-phase TMD moiré bilayers. Saddle point stacking abbreviated as SP. Metal and chalcogen denoted as M and X, respectively. **e,** 2D displacement hexagon legend for the displacement field maps in **a** and **b**, signifying the magnitudes and directions of the local displacement vectors in pixel hues and values, respectively. Here u_x and u_y represent interlayer displacements in the x and y directions. SP_1, SP_2, and SP_3 represent the three unique saddle point stacking directions. **f,** Simulated displacement fields for a rigid twisted homobilayer (left) and rigid untwisted heterobilayer (right). The lattice vector $\mathbf{a}_1$ is oriented along the x-axis, leading to SP1 solitons oriented along the y-axis and x-axis for the twisted homobilayers and untwisted heterobilayers, respectively, as discussed in the Appendix, Section 5.

3.4 Rotational reconstruction in homobilayers

As discussed in Chapter 2, by taking the gradient of these displacement vector fields, we can calculate the intralayer 2D strain tensor at each position in the samples[155,156,175,179]. From the strain tensor, we then derive information about local intralayer fixed-body rotations and deformations in the moiré bilayer (see Appendix, Sections 4–6 and 8–9), which provides insight into the reconstruction mechanisms in these systems.

First we will consider the MoS_2 moiré homobilayers. The intralayer reconstruction rotation (θ_R), shown in Fig. 3.5a–c, indicates the difference between the pre-imposed interlayer moiré twist angle (θ_m) and the measured total fixed-body rotation (θ_T) in each TMD layer: $\theta_R = \theta_T - (\theta_m/2)$ (Equation 2.2, derived in the Appendix, Section 6). For the P orientation (Fig. 3.5a) we observe a reconstruction rotation field that is reminiscent of the triangular rotation field we observed in twisted bilayer graphene[175] (Fig. 2.7a). By plotting the average reconstruction rotation as a function of interlayer displacement (u_x, u_y) (Fig. 3.5d–f), we observe that regions with the highest calculated stacking energy (MMXX, 59.1 meV/M vs. XM/MX[114,180], see Appendix, Section 13 for calculation) have $\theta_R > 0°$, which increases the local total rotation, θ_T^{MMXX}, and consequently shrinks the MMXX stacking domain, while regions with low stacking energy (XM and MX) have $\theta_R < 0°$ and expand into commensurate triangular domains (Fig. 3.5d). For AP moiré homobilayers, a similar principle applies, but the calculated relative energies of the various high-symmetry stacking orders present changes. Here, XX regions have the highest stacking energy (58.8 meV/M vs XMMX[114,180]), thus $\theta_R > 0°$, while XMMX regions have the lowest stacking energy and $\theta_R < 0°$ (Fig. 3.5e,f). Plots like those shown in Fig. 3.5d–i were obtained by averaging the strain quantities from all pixels in the real-space maps whose displacement vectors were within the same $a_0/25$ by $a_0/25$ bins where a_0 is the average lattice constant for the two TMD layers.

To determine whether other deformation mechanisms contribute to the reconstruction process, we also calculated dilations from the measured local strain tensors. Dilation, also referred to as dilatation or an in-plane volumetric strain[155,156,179], describes the local change in volume relative to that of the rigid moiré for a given θ_m. Referring again to infinitesimal strain theory, dilation can be approximated as the sum of the normal strains[155]:

$$Dil = \frac{\Delta V}{V} = \epsilon_{xx} - \epsilon_{yy} \tag{3.2}$$

In the case of moiré bilayers the dilation effectively represents the change in the relative lattice constants of the two TMD layers (that is, a 1% dilation implies a 1% increase in the lattice constant difference, thereby shrinking the local stacking domain). Fig. 3.5g–i show the average dilation as a function of interlayer displacement. In contrast to the reconstruction rotations, we do not measure any systematic trends

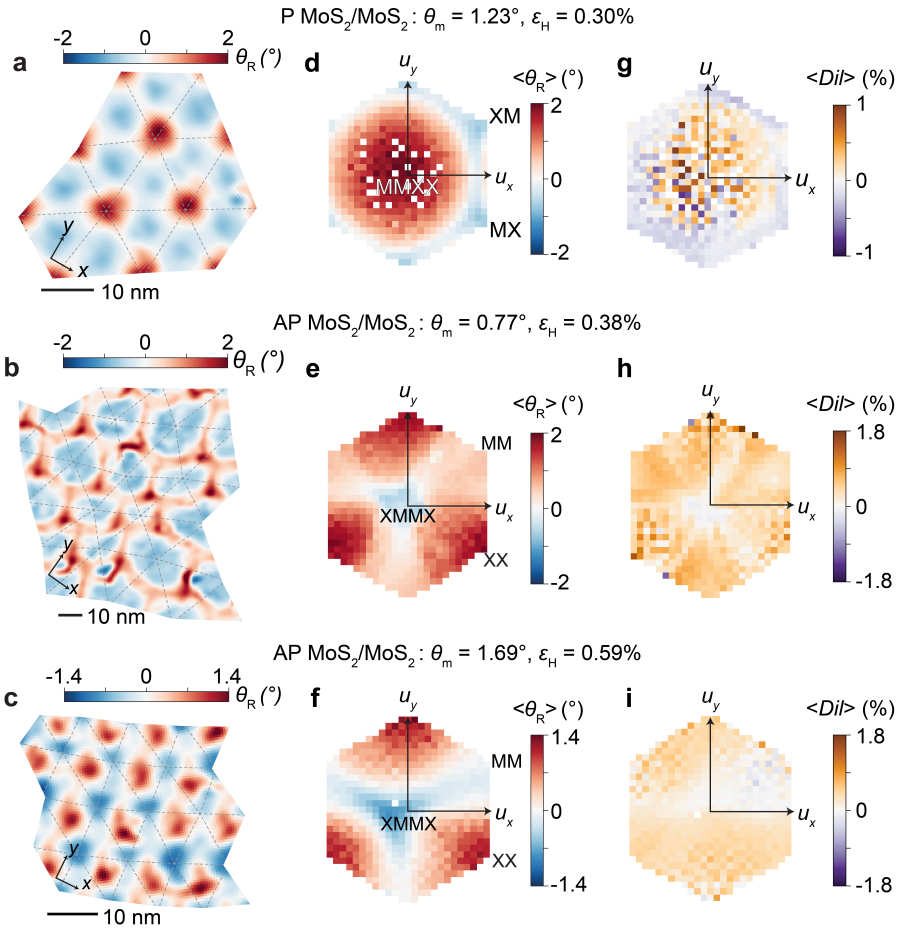

Figure 3.5: **a–c,** Maps of local reconstruction rotation (θ_R) for P-stacked MoS_2/MoS_2 with $\theta_m = 1.23°$ (**a**) and AP-stacked MoS_2/MoS_2 with $\theta_m = 0.77°$ (**b**) and 1.69° (**c**). ε_H indicates average heterostrain. **d–f,** Average reconstruction rotation ($\langle\theta_R\rangle$) and **g–i,** average dilation ($\langle Dil\rangle$) as a function of interlayer displacement (u_x, u_y). The overlaid dashed lines correspond to the moiré unit cell geometry, determined from the displacement maps.

in dilation based on the local stacking order for the moiré homobilayers (both P and AP cases). These data reveal that intralayer volumetric strains do not significantly contribute to reconstruction of the homobilayer lattices. Instead, variations in the distribution of local fixed-body rotations drive the reconstruction and are responsible for the stark morphological differences between reconstructed P and AP moiré homobilayers. This result may be intuitively rationalized considering the lattice mismatch in moiré homobilayers arises almost entirely from rotational misalignment rather than a lattice constant difference for samples measured (see Section 7 for further discussion on heterostrain considerations).

These rotation-driven lattice reconstruction mechanisms would be expected to generate intralayer strain as an inherent property of the moiré superlattice[111,112,175]. These inhomogeneous, intrinsic, intralayer strain fields are thought to be particularly important in AP moiré homobilayers, where they are implicated in the tight confinement of charge carriers in triangular quantum dot-like potential wells and subsequent formation of ultraflat electronic bands[92,176]. In the case of rotation-driven reconstruction, shear is the predominant type of strain present and has been theoretically predicted to occur at the boundaries between stacking domains[92]. To visualize and measure the reconstruction strain fields, we calculated the engineering shear strain (γ_{max}, also called principal shear) at each point in the moiré superlattice. This γ_{max} value indicates the maximum amount of intralayer shear strain present in any direction[155,156,179] (see Appendix, Section 6 for more information). Indeed, we measure a concentration of shear strain in the saddle point (SP) areas (i.e., soliton/domain walls) between regions with the same sign of θ_R (Fig. 3.6a–f). The measured shear strain fields align closely with those we obtain from simulations using a rotational reconstruction field (see Appendix, Section 13), corroborating the assertion that local rotations are the dominant type of mechanical deformation in TMD moiré homobilayers, spontaneously generating these intralayer shear strain fields. Schematics depicting the rotation-driven reconstruction model and accumulation of shear strain at domain boundaries are provided in Fig. 3.6g–i.

Figure 3.7 shows how the relative stacking areas and average θ_R vary with twist angle for each type of high-symmetry stacking order. The plotted values were obtained by assigning each real-space pixel to a stacking order according to the displacement space partitions shown in Fig. 3.8 and then averaging the strain quantity of interest for each set of pixels with the same stacking assignment. Notably, there are two regimes of reconstruction observed for the AP moiré homobilayers. While θ_R^{XMMX} is consistently $< 0°$ and $\theta_R^{XX} > 0°$ for all θ_m measured, θ_R^{MM} switches sign at a critical twist angle (θ_c) around 1.25–1.5° (Fig. 3.7a). Although MM regions are higher energy than XMMX regions for group VI TMDs, the difference is relatively small (13.8 meV/M vs. XMMX[114,180]). As a result, at larger θ_m ($> \theta_c$) we observe a slightly negative θ_R in the MM regions, allowing some local domain expansion (Fig. 3.7b). Meanwhile as θ_m decreases, MM regions instead shrink ($\theta_R > 0°$) to accommodate rapid expansion of XMMX into large hexagonal domains (Fig. 3.7a,b).

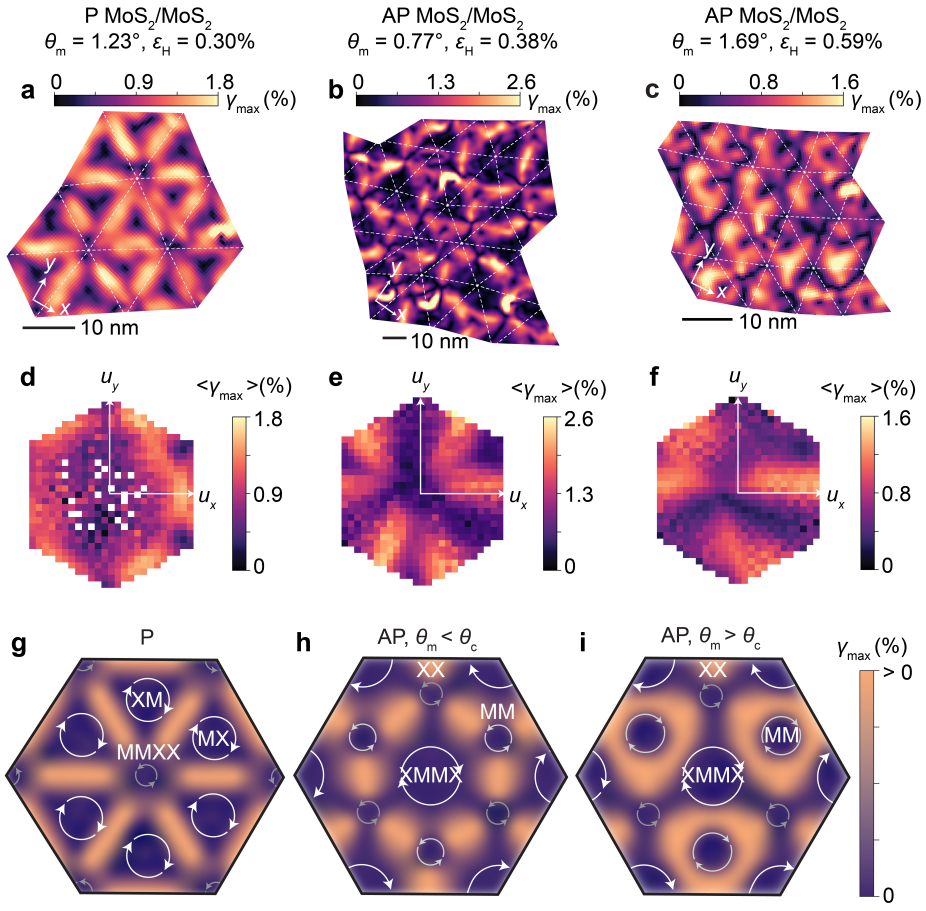

Figure 3.6: **a–c,** Maps of maximum shear strain (γ_{max}) for P-stacked MoS_2/MoS_2 with $\theta_m = 1.23°$ (**a**) and AP-stacked MoS_2/MoS_2 with $\theta_m = 0.77°$ (**b**) and 1.69° (**c**). ε_H indicates average heterostrain. The overlaid dashed lines correspond to the moiré unit cell geometry, determined from the displacement maps. **d–f,** Average γ_{max} ($\langle\gamma_{max}\rangle$ as a function of displacement. **g–i,** Rotation-driven reconstruction schematics for a P-stacked and two AP-stacked moiré homobilayer cases ($\theta_m < \theta_c$ and $\theta_m > \theta_c$, where θ_c is the critical twist angle separating two reconstruction regimes). Yellow indicates accumulation of shear strain ($\gamma_{max} > 0$) and blue indicates no shear strain. Arrows illustrate the measured direction of θ_R, with counterclockwise rotation defined as $\theta_R > 0$. Arrow sizes depict relative growth or shrinkage of local stacking domain, not drawn to scale.

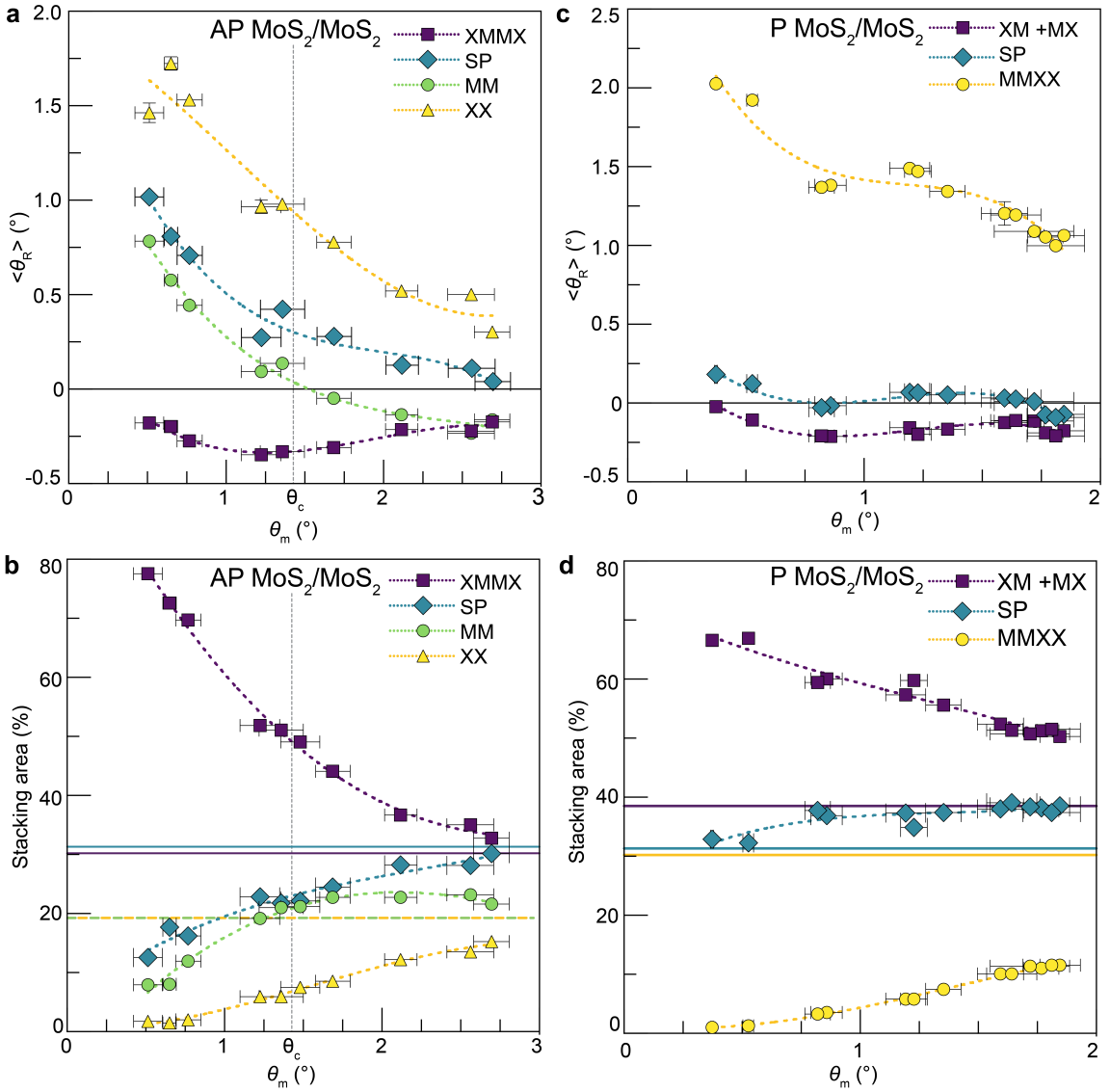

Figure 3.7: a,c) Average reconstruction rotations and (**b,d**) relative stacking areas as a function of twist angle (θ_m) for AP and P stacking orientations. Horizontal colored lines in **b,d** indicate the relative stacking areas in a rigid moiré based on the chosen partitioning of the displacement space (see **Fig. 3.8**). Horizontal error bars represent standard deviations and vertical error bars represent standard errors. Dotted trend lines are polynomial fits to the experimental data, included as visual guides.

Only one reconstruction regime was observed for P homobilayers (Fig. 3.7c,d).

Comparing how reconstruction evolves with twist angle in the P and AP moiré homobilayers, it appears that the P orientation is more strongly reconstructed overall. When $\theta_m \sim 2°$, the relative stacking area of the MMXX regions is 36% of that expected in a rigid P moiré, while the relative stacking area of the XX regions is 79% of that in a rigid AP moiré, indicating that the AP structure is nearing the rigid case by that point but the P structure is still markedly relaxed, in line with what has been theoretically computed previously[114]. These results point to the fact that, although the P and AP moiré configurations have similar ranges of interlayer stacking energies[114,180] (see Appendix Fig. A.24), fewer stacking sequences in the AP case correspond to the energy extremes. While reconstruction in a P moiré bilayer is driven by a preference for both MX and XM stacking over MMXX, reconstruction in AP moiré bilayers is driven predominantly by a preference for XMMX over XX stacking with relatively little preference for size of MM regions. This produces a stronger driving force for reconstruction in the P moiré bilayer.

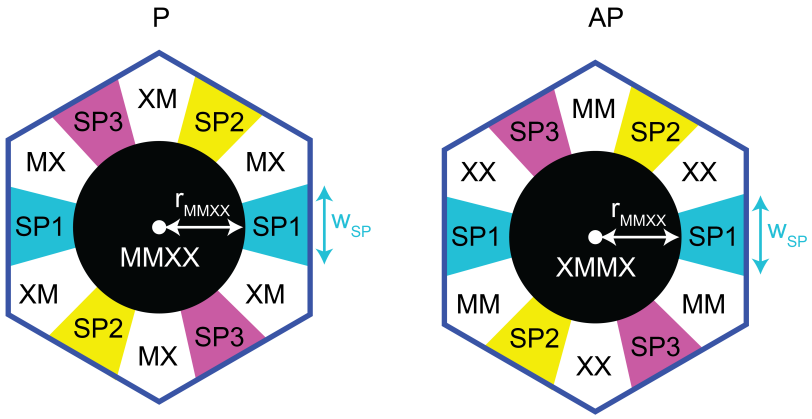

Figure 3.8: Schematic depicting classification of stacking type in a rigid moiré bilayer. Following the three-region partition used for twisted bilayer graphene (**Fig. 2.14**), displacement vectors with $|\mathbf{u}| < \frac{a_0}{2\sqrt{3}}$ were classified as MMXX (XMMX) stacking, where a_0 is the average lattice constant of the two TMD layers. The remaining displacements were classified as MX (XX), XM (MM), or SP type stacking according to their angular offset from vertical ϕ. For example, SP1 regions are defined as having a value of ϕ within $\pm\pi/12$ of 0 or π, SP2 regions as having a ϕ within $\pi/12$ of $\pi/3$ or $4\pi/3$, and so on as shown. The expected stacking area percentages for a rigid (that is, not reconstructed) moiré are then calculated geometrically as 30.2%, 38.5%, and 31.3% for XMMX (MMXX), XX+MM (XM+MX), and SP regions, respectively.

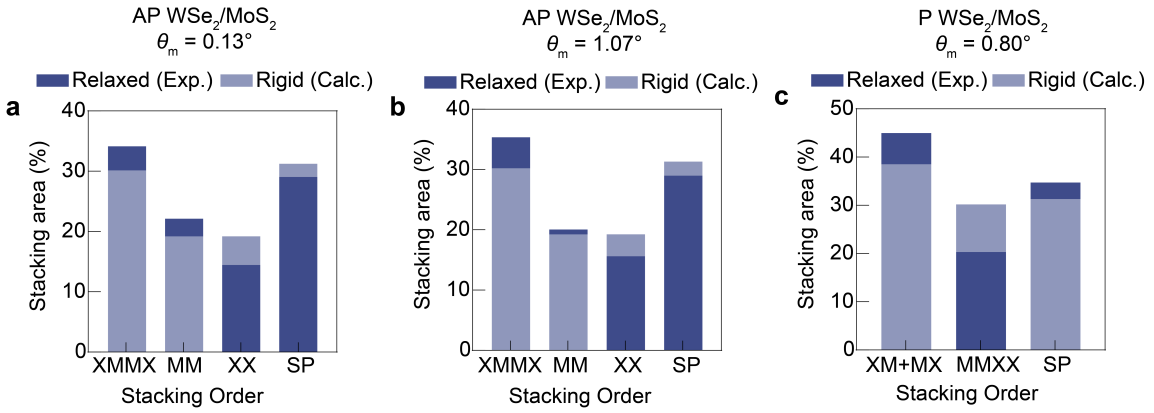

Figure 3.9: Relative stacking area percentages for **a,** AP ($\theta_m = 0.13°$), **b,** AP ($\theta_m = 1.07°$), and **c,** P ($\theta_m = 0.80°$) WSe_2/MoS_2. Light blue-gray bars indicate stacking areas calculated for the rigid (not reconstructed) moiré, and dark blue bars represent experimentally measured values.

3.5 Dilational reconstruction in heterobilayers

We next turn our attention to the moiré heterobilayers, composed of WSe_2 and MoS_2. In these systems, the lattice constant difference between the two dissimilar TMD layers, rather than (or in addition to) global interlayer rotation, generates the moiré pattern. Based on the displacement fields shown in Fig. 3.4a,b, it initially appears as though there is minimal lattice reconstruction in the heterobilayers. However, comparing the relative areas of the different stacking sequences to those expected for a rigid moiré superlattice (again calculated using the partition shown in Fig. 3.8), it becomes evident that there is an overall expansion of lower-energy XM/MX (P) and XMMX (AP) regions and contraction of higher-energy MMXX (P) and XX (AP) regions (Fig. 3.9), signifying that reconstruction has indeed occurred.

Real-space local dilation maps and corresponding average dilations as a function of displacement vector are provided for both AP (Fig. 3.10a,b and d,e) and P (Fig. 3.10c,f) heterobilayer cases. Unlike moiré homobilayers, these heterobilayers show prominent stacking order-dependent dilation patterns. Namely, there are positive dilations in the XX (AP) and MMXX (P) regions and negative dilations in XMMX (AP) and XM/MX (P) regions. There are relatively small dilations in the MM regions of the AP superlattice due to a decreased preference for the size of these domains, similar to what was observed in the AP twisted homobilayers in Fig. 3.7a,b. Altogether, these measurements show that the lattice constant mismatch decreases (increases) in domains with low (high) stacking energy to cause local volumetric expansion (contraction) of these domains, as depicted in the schematics in Fig. 3.10j.

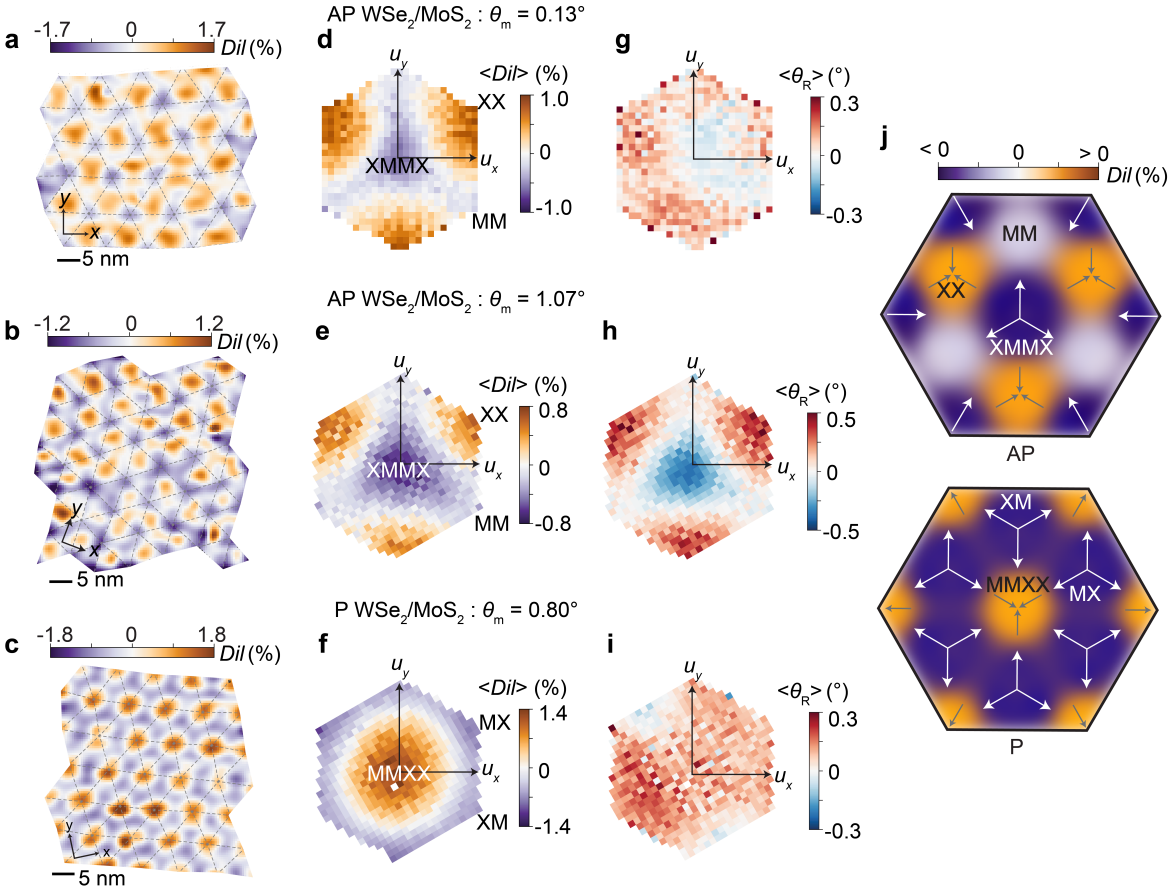

Figure 3.10: **a–c,** Maps of local dilations for the same heterobilayer samples analyzed in **Fig. 3.9**. The overlaid dashed lines correspond to the moiré unit cell geometry, determined from the displacement maps. **d–f,** Corresponding 2D plots of average dilation ($\langle Dil \rangle$) and **g–i,** average reconstruction rotation ($\langle \theta_R \rangle$) as a function of interlayer displacement (u_x, u_y). **g,** Schematics of dilation-driven reconstruction and accumulation of volumetric strain. Orange indicates a positive dilation and purple indicates a negative dilation. Arrows illustrate volumetric expansion (pointing outward) or compression (pointing inward). Arrow sizes represent relative relative growth or shrinkage of the local stacking domain, not drawn to scale.

Next we consider the effects of introducing an interlayer twist angle on heterobilayer reconstruction mechanisms. While the average local reconstruction rotations are relatively weak and independent of stacking order for the AP heterobilayer with a near zero-degree twist angle (Fig. 3.10g, $\theta_m = 0.13°$), these rotations strengthen in the AP heterobilayer with a larger interlayer twist (Fig. 3.10h, $\theta_m = 1.07°$) and their distribution resembles that of the AP twisted homobilayer (Fig. 3.5f). Thus, moiré heterobilayers can host a combination of rotational and dilational relaxation given that the imposed moiré twist angle is sufficiently large. Interestingly, we do not observe stacking-dependent rotations in the P heterobilayer with non-zero twist (Fig. 3.10i, $\theta_m = 0.80°$). This could be due to a couple of factors. First, the twist angle in the sample measured might be below the threshold for substantial contributions from rotational relaxation. A second possibility is that out-of-plane corrugations in the layers have weakened and delocalized the rotational reconstruction, as we will discuss next. Simulated dilation and rotation fields for P and AP heterobilayers are provided in the Appendix, Section 13.

3.6 Effects of encapsulation layers on reconstruction

Theoretical calculations and scanning tunneling microscopy topography measurements have suggested that heterobilayer systems can relax through out-of-plane corrugations, where there is a stacking order-dependent variation in the interlayer spacing[117,119,181]. Such corrugations have been invoked as critical to relaxation and the resulting electronic properties. However, to the best of our knowledge, there have been no experimental studies that directly compare reconstruction in encapsulated and suspended structures. To investigate this point, we prepared WSe_2/MoS_2 heterobilayers with three regions: fully encapsulated (hBN on top and bottom), partially encapsulated (hBN on top), and suspended (no hBN). Example convergent beam electron diffraction patterns from the three regions with varying extents of encapsulation are provided in Fig. 3.11a–c for an AP sample with a moiré twist angle near 0.8°. Figures 3.11d–f, g–i show the corresponding average reconstruction dilations and rotations, respectively, for these three regions in both the 0.8° sample and a similar sample with $\theta_m \sim 0.1$–$0.2°$. Corresponding real-space maps are provided in Fig. 3.12. Comparing the real-space dilation and reconstruction maps demonstrates that full encapsulation of the moiré layers dramatically increases the homogeneity of the reconstructed superlattice. Notably, in the 2D histograms (Fig. 3.11d–i), it is evident that hBN encapsulation layers affect the magnitude and extent of localization of the reconstruction rotation and dilation fields for both twist angle ranges. Specifically, the fully encapsulated regions show the strongest, most localized dilations and rotations, while these deformations are weakest and most delocalized in the fully suspended

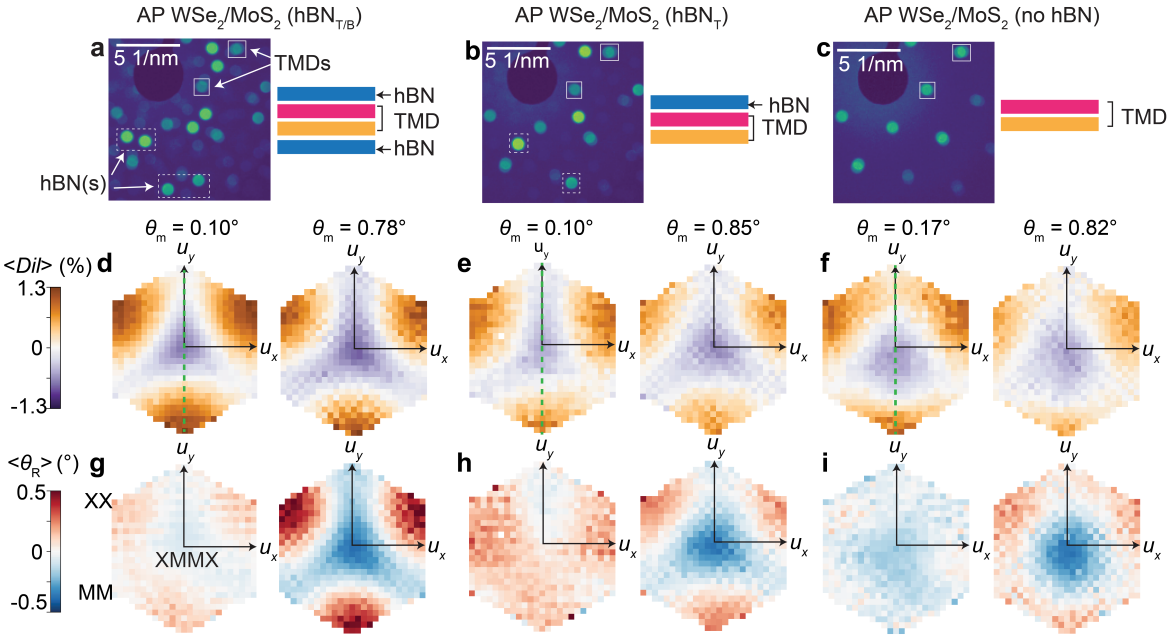

Figure 3.11: a–c, Example convergent beam electron diffraction patterns for an AP WSe_2/MoS_2 sample with three regions: fully encapsulated with hBN (**a**, $\theta_m = 0.78°$), encapsulated on one side with hBN (**b**, $\theta_m = 0.85°$), and freely suspended (**c**, $\theta_m = 0.82°$). Dashed and solid boxes highlight representative hBN and TMD diffraction disks, respectively. **d–f,** Average dilations ($\langle Dil \rangle$) as a function of interlayer displacement (u_x, u_y) for fully capped (**d**, $\theta_m = 0.10°, 0.78°$), partially capped (**e**, $\theta_m = 0.10°, 0.85°$), and suspended (**f**, $\theta_m = 0.17°, 0.82°$) AP WSe_2/MoS_2 samples. **g–i,** Corresponding 2D plots of plots of average reconstruction rotation ($\langle \theta_R \rangle$) as a function of displacement.

regions. These observations suggest that hBN encapsulation suppresses out-of-plane relaxation, in turn enhancing in-plane reconstruction pathways.

To verify the hypothesis that hBN suppresses out-of-plane corrugation, it is important to first consider the effects that such a corrugation would have on the measured in-plane projections of the displacement vectors. A pictorial representation of this scenario is shown in Fig. 3.13a and further mathematical details are provided in the Appendix, Section 14. In Fig. 3.13a, pink and blue vertical lines represent the projected positions of the atoms in layers 1 and 2, respectively, of an exemplar heterobilayer system with an interlayer lattice constant mismatch. The projected distance between an atom in layer 1 to its nearest neighbor in layer 2 reflects the measured local displacement vector. Based on this picture, it is clear that out-of-plane bending of the layers reduces both the apparent lattice constant of each layer and the magnitude of the interlayer displacement vectors in the projection. This effect is

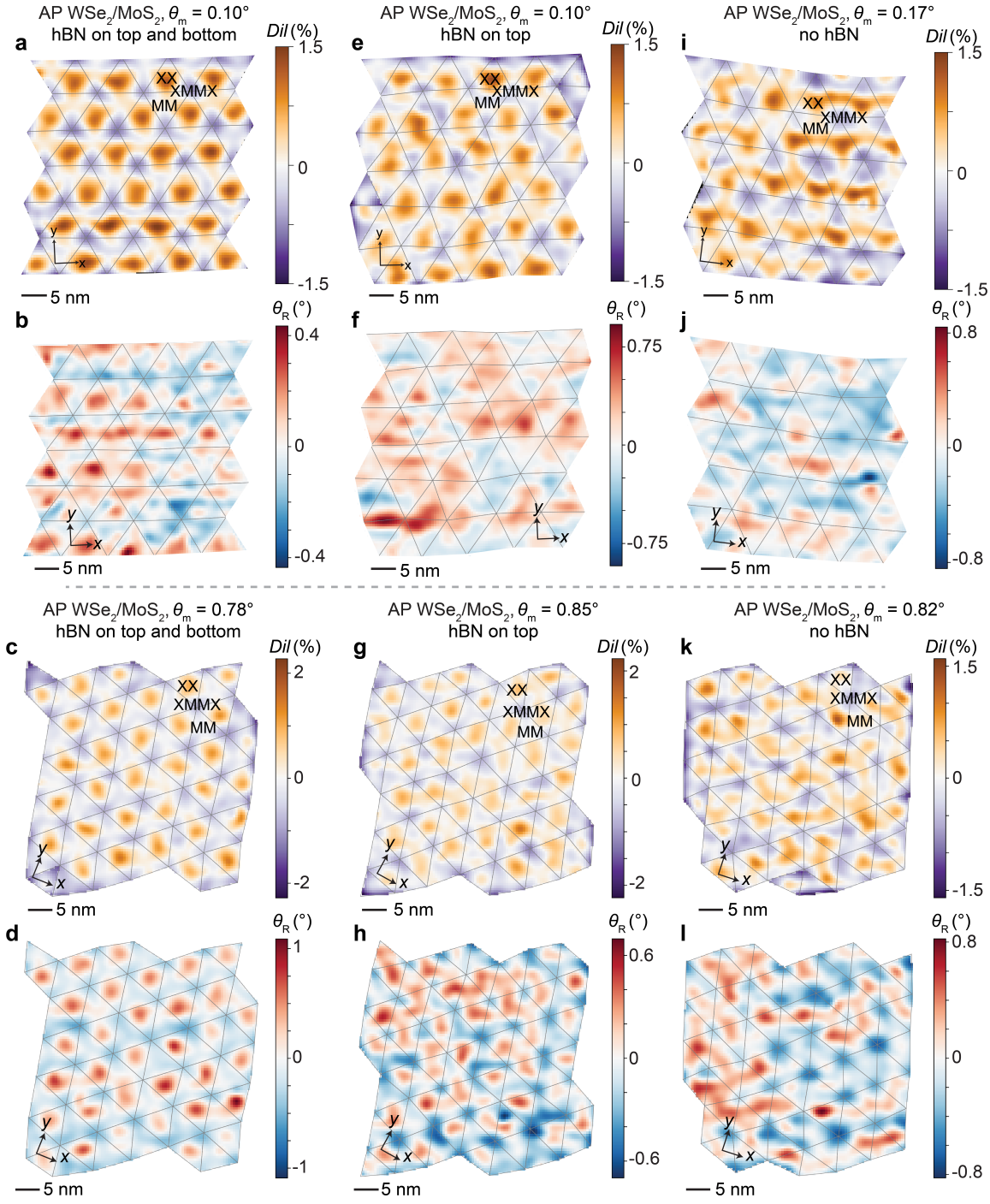

Figure 3.12: Maps of local dilations and reconstruction rotations for **a–d,** fully capped, **e–h,** partially capped, and **i–l,** suspended AP WSe_2/MoS_2 at with two sets of moiré twist angles. The overlaid solid lines correspond to the moiré unit cell geometry, determined from the displacement maps.

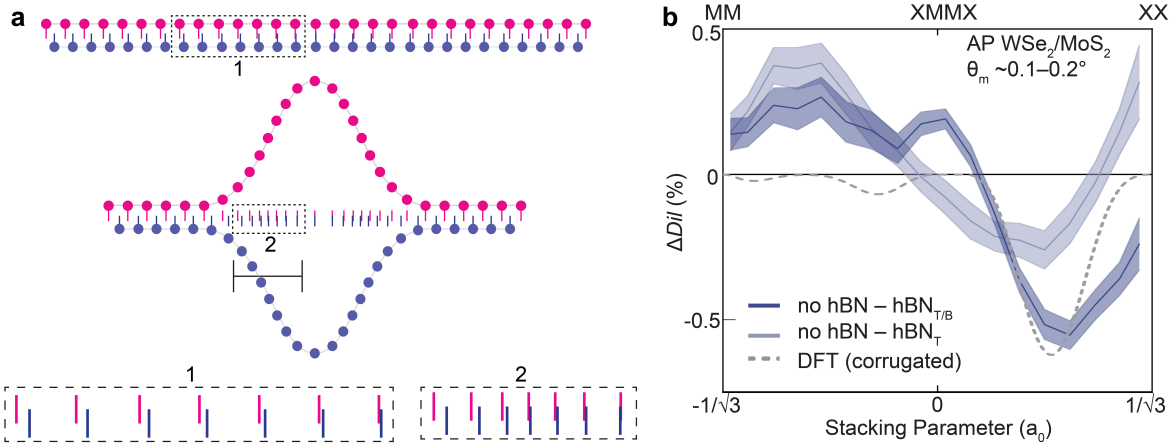

Figure 3.13: **a,** Schematic (exaggerated) depicting the effects of out-of-plane corrugation on projected interlayer displacements. Magnified pictures of select regions are provided in boxes 1 and 2. **b,** Difference in dilation (ΔDil) as a function of stacking parameter for suspended versus fully encapsulated (dark blue-gray curve) and suspended versus partially encapsulated (light blue-gray curve) structures with $\theta_m \sim 0.1$–$0.2°$. Dilation values for each case obtained by taking line cuts through the average dilation plots in **Fig. 3.11d–f**, shown as green dashed lines. Shading indicates standard error. Gray dashed line represents the theoretically calculated ΔDil comparing the corrugated versus rigid heterobilayer.

most pronounced in the boundary region between two high-symmetry stacking orders where the interlayer spacing is changing most rapidly (highlighted in boxes 1 and 2). Ultimately, this corrugation produces a perceived reduction in the interlayer lattice mismatch, analogous to a negative dilation, even in the absence of any actual changes in intralayer bond lengths. With this conceptual framework in mind, we calculate the theoretical apparent dilations as a function of stacking parameter for a corrugated AP-stacked WSe_2/MoS_2 using interlayer spacing variations determined from DFT (see Appendix, Sections 13 and 14). The results of this calculation are plotted as the gray dashed line in Fig. 3.13b.

We then quantitatively compare the dilations in the three regions of the sample with $\theta_m \sim 0.1$–$0.2°$, a twist angle range where rotational reconstruction is minimal and can effectively be ignored. To do so, we take line cuts through the average dilation plots (shown as green dashed lines in Fig. 3.11d–f) and then calculate the difference in measured dilation (ΔDil) between both the suspended and encapsulated ($no\ hBN - hBN_{T/B}$) and suspended and partially encapsulated ($no\ hBN - hBN_T$) regions as a function of stacking parameter, as shown in Fig. 3.13b. The experimental ΔDil profile for the encapsulated versus suspended case displays clear similarities to that for the theoretical corrugated structure, indicating that the suspended het-

erobilayer has undergone a combination of in-plane and out-of-plane reconstruction while the fully encapsulated structure is reconstructed almost entirely in-plane. The residual differences between the experimental and theoretical curves suggest that some out-of-plane corrugation may remain in the encapsulated structure since the thin hBN is not perfectly rigid; however, overall the corrugations have been largely suppressed by the presence of hBN on both sides. Meanwhile, the ΔDil profile for the partially encapsulated versus suspended case differs more substantially from that of the corrugated model due to further mixing of in-plane and out-of-plane reconstruction when only one side of the heterobilayer is encapsulated.

Taken together, these results show that hBN encapsulation layers markedly affect the balance between in-plane rotational and dilational reconstruction and out-of-plane corrugation. In addition, it is directly established that a considerable portion of the dilations we observe in the heterobilayer systems are from actual local lattice stretching and compressing in the constituent monolayers, rather than corrugation alone, which has until now only been theoretically predicted or assumed to occur[117–119]. The thickness of the hBN used in fabrication may also allow for some control over the extent of corrugation; thicker hBN slabs would be more rigid and should frustrate corrugations more (thus augmenting in-plane dilations and overall disorder in the sample) in comparison to thinner hBN. Such encapsulation effects may therefore be used to further tune the physics of TMD moirés. Although these encapsulation studies were only performed for the AP heterobilayer, the trends observed should be applicable to both the P heterobilayer and P/AP twisted homobilayer cases. For example, the reconstruction rotations measured for P/AP twisted bilayer MoS_2 in Fig. 3.5a–f, which were measured for partially encapsulated structures, are likely systematically smaller than those in analogous fully encapsulated structures.

3.7 Heterostrain effects

Moiré heterobilayers are prepared using two dissimilar TMD materials. However, introduction of a heterostrain, wherein one TMD layer is stretched relative to the other, also creates a lattice constant difference in moiré homobilayers, making them heterobilayer-like. This raises the question of how rotational and dilational reconstruction compete in heterostrained moiré homobilayers. To investigate these relaxation dynamics, we performed Bragg interferometry on P and AP moiré homobilayers with varying amounts of uniaxial heterostrain. Fig. 3.14a–c and 3.15a–c show the average θ_R, dilation, and γ_{max} as a function of u_x and u_y for the P and AP cases, respectively. The results show that increasing heterostrain up to typical values of $\sim 1.4\%$ does not substantially increase the prevalence of dilational reconstruction in twisted homobilayers. Instead, local rotations remain overwhelmingly dominant in governing relaxation. The effective lattice constant mismatch in a heterostrained

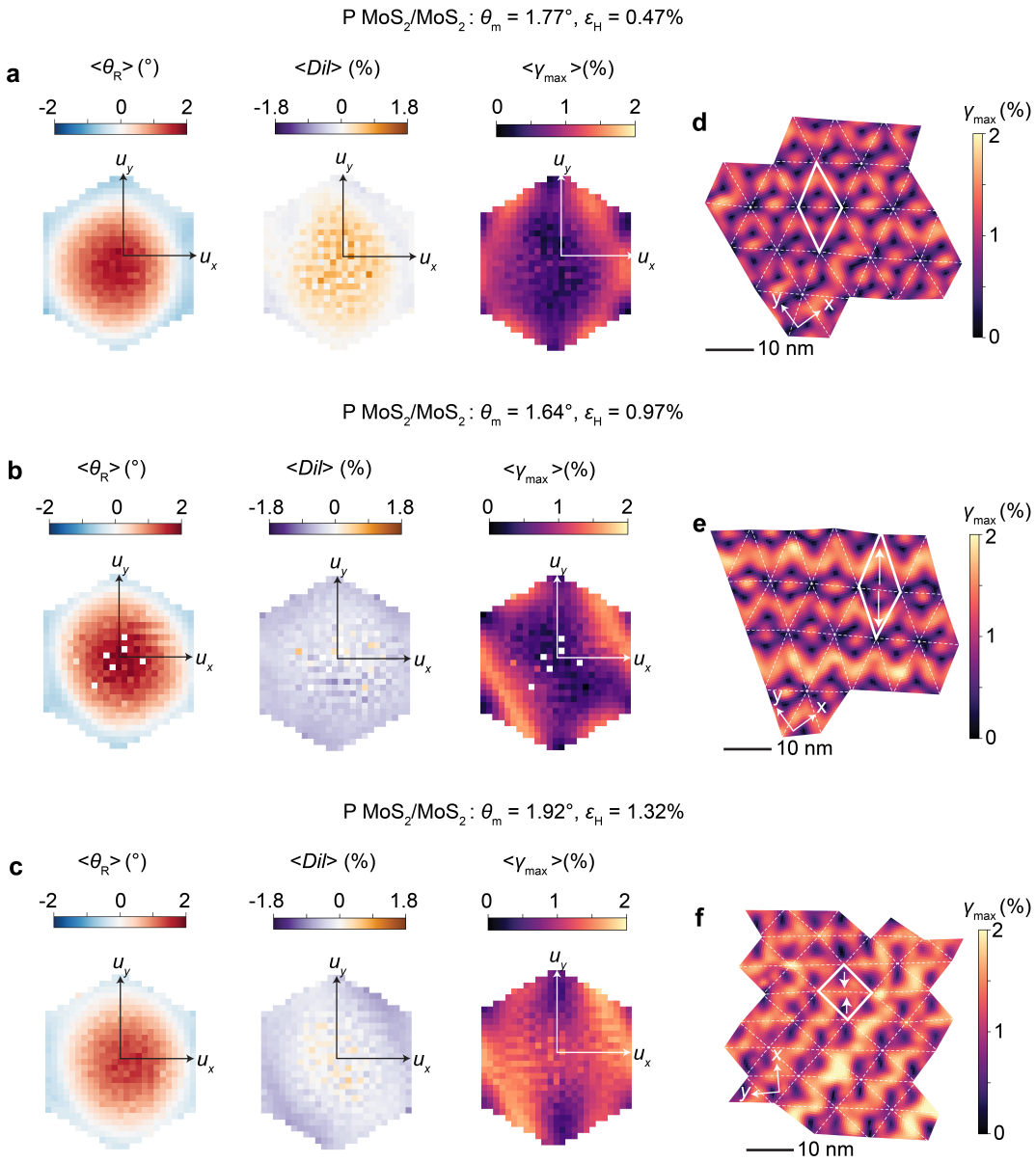

Figure 3.14: **a–c,** Average reconstruction rotation ($\langle\theta_R\rangle$), dilation ($\langle Dil\rangle$), and maximum shear strain ($\langle\gamma_{max}\rangle$) as a function of interlayer displacement (u_x, u_y) for P MoS_2/MoS_2 moiré homobilayers with varying amounts of heterostrain. **d–f,** Corresponding maps of maximum shear strain (γ_{max}). The overlaid dashed lines correspond to the moiré unit cell geometry, determined from the displacement maps. White arrows indicate moiré unit cell extension (**e**) or compression (**f**).

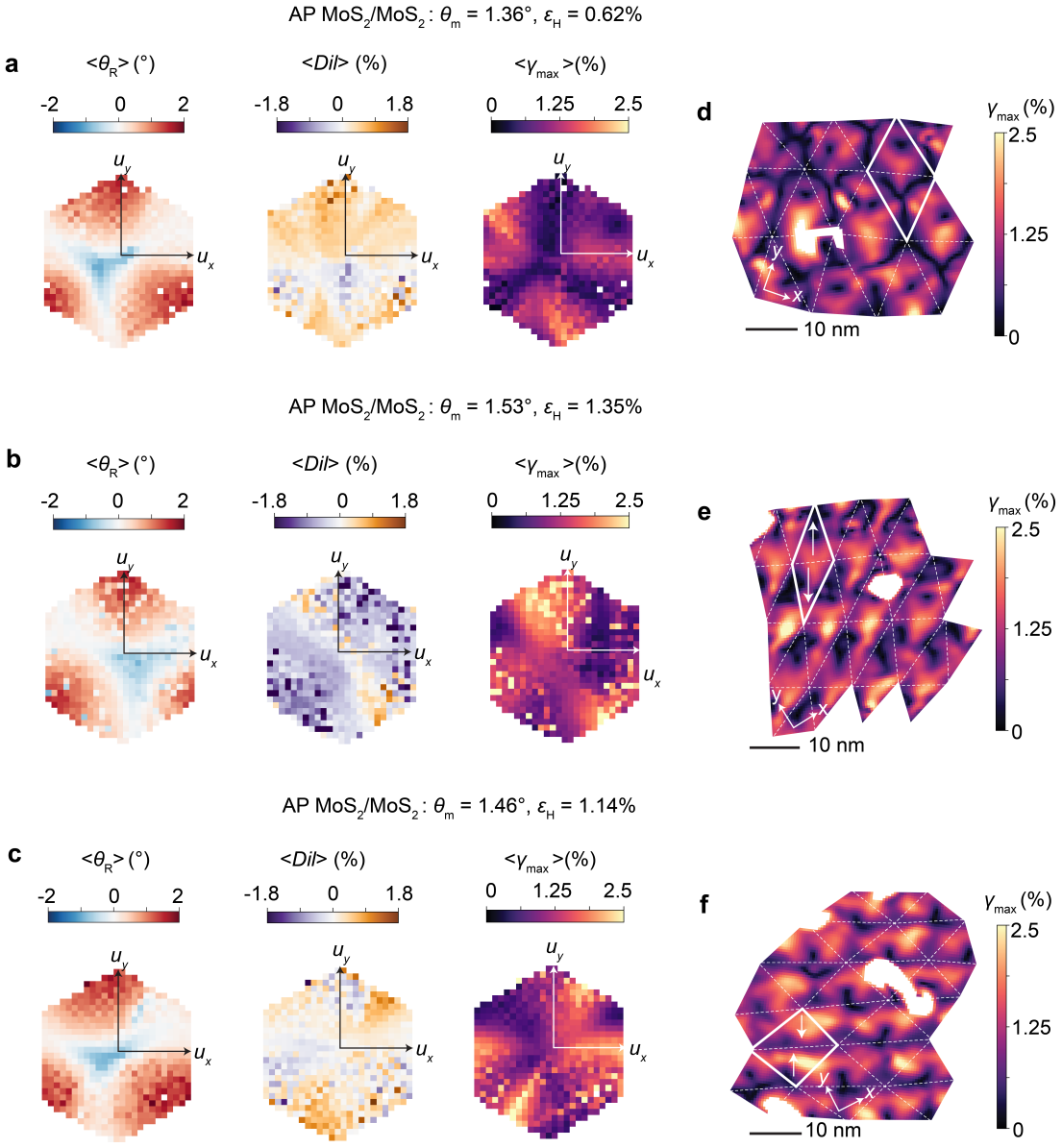

Figure 3.15: a–c, Average reconstruction rotation ($\langle\theta_R\rangle$), dilation ($\langle Dil\rangle$), and maximum shear strain ($\langle\gamma_{max}\rangle$) as a function of interlayer displacement (u_x, u_y) for AP MoS_2/MoS_2 moiré homobilayers with varying amounts of heterostrain. **d–f,** Corresponding maps of maximum shear strain (γ_{max}). The overlaid dashed lines correspond to the moiré unit cell geometry, determined from the displacement maps. White arrows indicate moiré unit cell extension (**e**) or compression (**f**). Scan regions affected by sample charging during data acquisition have been removed for clarity in **d–f**.

moiré homobilayer can be calculated using the expression:

$$\delta = (\varepsilon_H - \rho\varepsilon_H)/2 \tag{3.3}$$

where δ is the lattice mismatch, ε_H is the percent heterostrain, and ρ is the Poisson ratio (0.234 for MoS_2) (see Appendix, Section 9 for details). The effective mismatch for the samples studied is at most 0.5% (for $\varepsilon_H = 1.4\%$), nearly an order of magnitude smaller than that of the WSe_2/MoS_2 system discussed in Fig. 3.10–12. Thus, while there is a lattice constant difference present owing to heterostrain, our measurements reveal that the resulting mismatch is not large enough to induce substantial dilational reconstruction. These results suggest that similar reconstruction mechanisms may therefore be expected in moiré heterobilayers with a small lattice constant percent difference (e.g. $WSe_2/MoSe_2$, $\delta = 0.3\%$).

Instead of inducing dilational reconstruction, our strain mapping reveals that the primary effect of heterostrain is the reorganization of the intralayer shear strain fields arising from rotational reconstruction. So although heterostrain is applied uniformly, it is anisotropic in its manifestation; it is localized in the SP regions and both amplifies and distorts the existing shear strain. In addition, the primary direction of the heterostrain has significance. Fig. 3.14d–f and 3.15d–f show γ_{max} for P and AP moiré homobilayers, respectively, with the heterostrain axis stretching versus contracting the moiré unit cell. Each of these scenarios yields a distinct strain field, including stripe (Fig. 3.14e, 3.15f), square (Fig. 3.14f), and triangular patterns (Fig. 3.15e). In all cases, reconstruction rotations strongly persist and shear strain continues to concentrate in the domain walls, demonstrating that it is thermodynamically preferable to continue reducing interlayer energy by accumulating and shifting the distribution of elastic energy (see Appendix, Section 13 for simulations).

3.8 Conclusions

In summary, here we have extended the Bragg interferometry methodology for imaging non-centrosymmetric and heterobilayer systems, enabling us to directly probe intralayer mechanical deformations in TMD moiré bilayers. We demonstrate that it is variations in the symmetry of fixed-body rotation fields that are responsible for the morphological differences that have previously been observed in relaxed P and AP moiré homobilayers. The presence of an extrinsic heterostrain preserves these rotation fields and can be used to redistribute intralayer shear strain that is localized in domain boundaries, yielding a diversity of strain patterns. Since intralayer strain affects the positions of the conduction and valence band edges throughout the moiré unit cell[119] and can generate an in-plane piezopotential,[89,176] manipulating the arrangement and magnitude of reconstruction strain via extrinsic application of uniaxial heterostrain should have important implications for changing the moiré potential landscape and localization of charge carriers. For example, 1D moiré potentials have

led to linearly polarized exciton emission in uniaxially strained heterobilayers.[128] In addition, we find that when the lattice constant mismatch is further increased, periodic dilation patterns become the primary route through which reconstruction occurs, though contributions from local rotations are also present as the interlayer twist angle increases. The general twist angle and lattice mismatch-dependent reconstruction trends we observed should be widely applicable to moiré bilayers comprised of other TMDs (e.g., H-phase $MoTe_2$, WS_2, etc.) and even magnetic 2D moiré superlattices consisting of CrI_3 bilayers.[107] As a diffraction-based imaging technique, Bragg interferometry is also distinctively compatible with both freely suspended and encapsulated moiré structures. Leveraging this capability, we found that hBN capping layers suppress out-of-plane relaxation modes and subsequently promote in-plane deformations, implicating critical connections between sample design, substrate effects, and emergent properties in moiré systems. The versatility of this methodology also enables extension to more complex, multi-component vertical heterostructures, such as those containing gate electrodes (see Chapter 4). This could open avenues for direct correlative measurements, such as investigations of the relationship between lattice reconstruction and electrically controllable emergent (opto)electronic phenomena.

3.9 Experimental Details

3.9.1 Sample preparation

Moiré homobilayers were prepared using the tear-and-stack technique[162]. Briefly, monolayers of MoS_2 (HQ Graphene) and $\sim$ 5–10 nm thick hBN (grown by collaborators T.T. and K.W.) were mechanically exfoliated from bulk crystals onto SiO_2/Si substrates (285 nm SiO_2 for MoS_2 and 90 nm SiO_2 for hBN) and selected using optical microscopy and atomic force microscopy. To make each twisted heterostructure, a polybisphenol-A-carbonate/polydimethylsiloxane stamp was used to pick up the hBN first. The hBN was then engaged with part of a MoS_2 monolayer, tearing and picking up half of the monolayer. The monolayer MoS_2 half remaining on the SiO_2/Si substrate was then rotated by θ_m before being picked up. For P-stacked samples $0^\circ \leq \theta_m \leq 2^\circ$. For AP-stacked samples $57^\circ \leq \theta_m \leq 60^\circ$; however, we report θ_m as the rotation away from 60° for simplicity (e.g., $57^\circ = 3^\circ$ for AP samples). Lastly, each heterostructure was directly stamped onto a TEM grid from Norcada (200 nm silicon nitride with 2 μm holes for imaging).

Heterobilayers were prepared using a similar transfer technique, but using separate MoS_2 and $WSe2_2$ (HQ Graphene) monolayers with straight flake edges aligned to target an interlayer twist angle close to 0° (or 60°). For hBN encapsulation studies (Section 3.6), two heterobilayer samples were prepared, each of which contained three regions – one with top and bottom hBN, one with top hBN, and one with no hBN – to ensure that the twist angle was approximately constant over the three areas. In

all heterobilayer samples, the orientation (P or AP) between MoS_2 and $WSe2_2$ layers was confirmed using polarization-resolved SHG spectroscopy with an 800 nm Ti:Sa excitation source, an incident power of 1.3–2.6 mW (using a 100 x objective), and a 1° step size with an exposure time of 1 s per point.

3.9.2 Electron microscopy imaging

Electron microscopy was performed at the National Center for Electron Microscopy in the Molecular Foundry at Lawrence Berkeley National Laboratory. Low-magnification DF-TEM images were collected to identify regions of interest prior to 4D-STEM measurements. DF images were acquired using a Gatan UltraScan camera on a Thermo Fisher Scientific Titan-class microscope operated at 60 kV. Three frames with an exposure time of 5 s per frame were used to generate each image.

Four-dimensional STEM datasets were acquired using a Gatan K3 direct detection camera located at the end of a Gatan Continuum imaging filter on a TEAM I microscope (aberration-corrected Thermo Fisher Scientific Titan 80–300). The microscope was operated in energy-filtered STEM mode at 80 kV with a 10 eV energy filter centered around the zero-loss peak, an indicated convergence angle of 1.71 mrad, and a typical beam current of 40–50 pA depending on the sample. These conditions yield an effective probe size of 1.25 nm (full-width at half-maximum value). Diffraction patterns were collected using a step size of either 0.5 nm or 1 nm with 50 x 50 to 300 x 300 beam positions, covering an area ranging from 25 nm x 25 nm to 300 nm x 300 nm. The K3 camera was used in full-frame electron counting mode with a binning of 4 $\times$ 4 pixels and an energy-filtered STEM camera length of 800 mm. Each diffraction pattern had an exposure time of 13 ms, which is the sum of multiple counted frames[175].

3.9.3 Computational implementation

All processing and analyses of 4D-STEM data were performed using Python on a personal computer, using published modules for Bragg disk detection, image processing and optimization[165,182–185]. All other code was custom-written by the authors[186].

Chapter 4

Operando imaging of electric field-induced transformations in twisted trilayers

Parts of this chapter were reproduced or adapted from: Van Winkle, M., Dowlatshahi, N., Khaloo, N., Iyer, M., Craig, I.M., Dhall, R., Taniguchi, T., Watanabe, K. & Bediako, D.K. Engineering polarization switching in van der Waals multilayers. *Nat. Nanotechnol.* (2024).

Author Contributions: M.V.W. and D.K.B. conceived the study. M.V.W., N.D., and N.K. designed and fabricated the samples. M.V.W. and R.D. acquired TEM and 4D-STEM data. M.I. and M.V.W. performed multislice simulations with input from I.M.C.. I.M.C. wrote the code used for generation of color-coded virtual dark-field images. T.T. and K.W. provided the bulk hBN crystals. M.V.W. processed and analyzed the data. M.V.W. and D.K.B. wrote the manuscript with input from all co-authors.

4.1 Abstract

In conventional ferroelectric materials, polarization is an intrinsic property limited by bulk crystallographic structure and symmetry. Recently, it has been demonstrated that polar order can also be accessed using inherently non-polar van der Waals materials through layer-by-layer assembly into heterostructures, wherein interfacial interactions can generate spontaneous, switchable polarization. Here, we show that introducing interlayer rotations in multilayer vdW heterostructures modulates both the spatial ordering and switching dynamics of polar domains. The engendered tunability is unparalleled in conventional bulk ferroelectrics or polar bilayers. Using operando transmission electron microscopy, we illustrate how alterations of the relative rota-

tions of three WSe_2 layers produce structural polytypes with distinct arrangements of polar domains that exhibit either a global or localized switching response. Furthermore, the presence of uniaxial strain generates structural anisotropy that yields a range of switching behaviors, coercivities, and even tunable biased responses. The results also provide evidence of mechanical coupling between the two interfaces of the trilayer, a key consideration for the control of switching dynamics in polar multilayer structures more broadly.

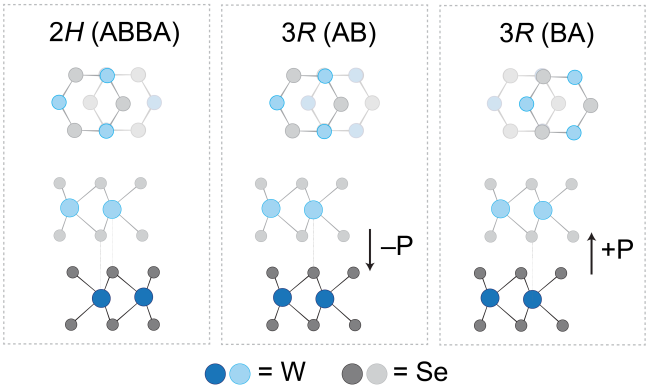

Figure 4.1: Illustrations of different stacking orders in bilayer WSe_2. The naturally occurring $2H$-type (or ABBA) stacking is non-polar due to centrosymmetry. The $3R$-type stacking has a net out-of-plane polarization, the direction of which depends on the in-plane translational offset between layers (–P for AB and +P for BA).

4.2 Introduction

Chapters 2 and 3 discussed how moiré architectures spontaneously deform through the lattice reconstruction process. In this Chapter we explore the structural transformations that take place in polar moiré materials when subjected to an external electric field. Ferroelectric (FE) materials with three-dimensional lattices have been employed in an array of applications, including nonvolatile memory, actuators, and sensors, for decades[187,188]. However, further miniaturization of electronic devices relies on the realization and manipulation of polar order in atomically thin crystals, such as two-dimensional van der Waals (vdW) materials. While many bulk, layered vdW crystals are naturally centrosymmetric and therefore non-polar, layer-by-layer assembly of individual vdW layers has been used to build non-centrosymmetric 2D heterostructures possessing an out-of-plane, interfacial polarization that can be switched via sliding of one layer (Fig. 4.1). This bottom-up approach greatly expands the number of potential 2D FE candidates and has been both predicted and experimentally demonstrated

for various common vdW materials, including hexagonal boron nitride (hBN)[189–192] and transition metal dichalcogenides (TMDs)[189,192–199].

Much of the work in the field thus far has centered on polar bilayer heterostructures[195,196,199]; however, recently it was demonstrated that interfacial polarization is cumulative in multilayer systems, enabling access to a ladder of polarization states depending on the number of layers and the translational offsets between them[192,197,198]. In this study, we use operando dark-field transmission electron microscopy (DF-TEM) to investigate how controlling the relative rotations between atomic layers in twisted trilayer tungsten diselenide (TTL-WSe_2) dictates the arrangement of polar domains in the resulting structure, offering control over a global versus local switching response. It is also observed that uniaxial strain engineers a range of switching dynamics, including moiré anti-ferroelectric, ferroelectric, and distinctively, biased responses. Further, interactions between the two interfaces of the trilayer are observed through coupling between intralayer strain and consequent switching behavior as well as pinning between commensurately stacked domain walls, providing insight into the cooperative nature of polarization switching in multilayer heterostructures and enabling electrical control over interlayer twist angle in moiré superlattices.

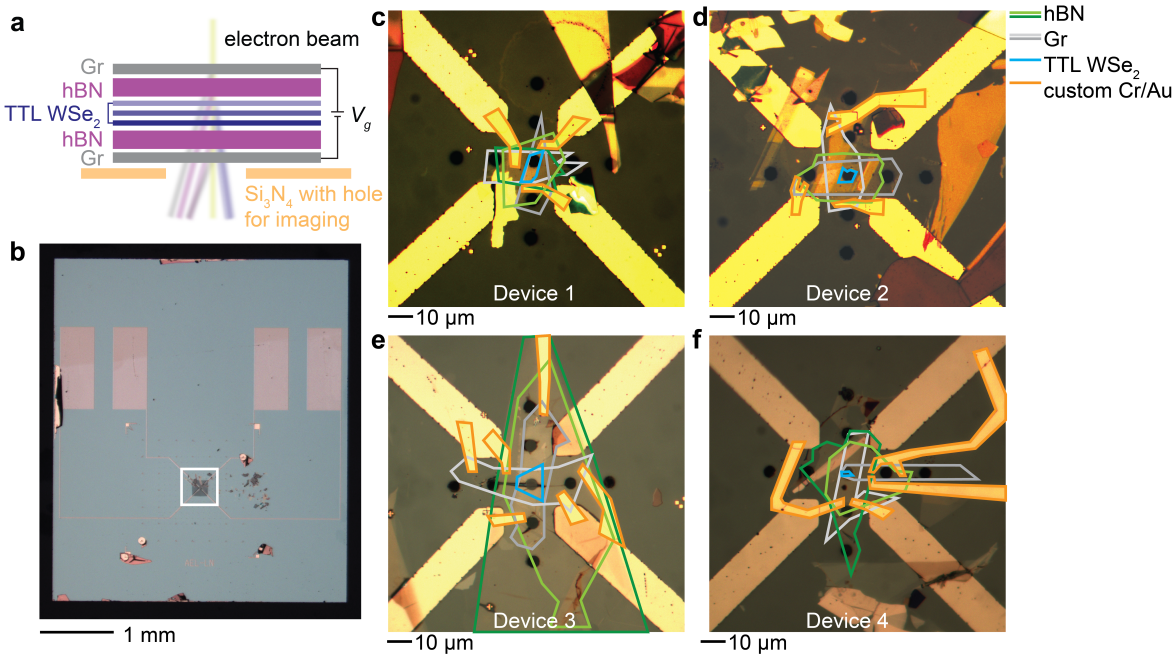

Figure 4.2: a, Schematic of TTL-WSe_2 device on a silicon nitride (Si_3N_4) membrane for operando TEM studies (cross-section view). **b,** Optical micrograph of a full Protochips electrical e-chip. Region with silicon nitride membrane and holes for electron microscopy imaging is boxed in white. **c–f,** Optical micrographs of the devices used in this work. Device components are outlined in various colors as a visual guide.

4.3 Polar domain order in TTL-WSe_2 polytypes

Samples were prepared using a dry transfer method and consist of the twisted trilayer (stacked with a parallel, or R-type, orientation between WSe_2 layers) sandwiched between thin hBN dielectric sheets (each < 15 nm thick) and few-layer graphite electrodes (Fig. 4.2). The full heterostructures are thin enough for transmission of an incident electron beam, enabling TEM imaging of the devices while simultaneously applying an out-of-plane electric field across the sample (see Section 8 for Experimental Details). Due to the presence of a rotational offset between the WSe_2 layers in the prepared heterostructures, there is a spatial variation in the crystallographic stacking order, a moiré superlattice, throughout the trilayer. Similar to the bilayer structures discussed in Chapters 2 and 3, the trilayer moiré undergoes an analogous, though arguably more complex[200], spontaneous relaxation process. After relaxation, four configurations with the lowest stacking energy comprise the majority of the moiré trilayer structure. Of these, the ABC and CBA stacking types have equal and opposite non-zero net polarization due to uncompensated charge transfer at the two stacked interfaces, while the ABA and BAB stackings have no net polarization due to mirror symmetry (Fig. 4.3).

The spatial arrangement of these polar and non-polar domains depends on the relative rotations between the WSe_2 sheets. In the A-twist-A′ (AtA′) polytype, the outer layers (layers 1 and 3) are nearly aligned ($0° < \theta_{13} < 0.1°$) while the middle layer (layer 2) is rotated further ($\theta_{12} > \theta_{13}$, Fig. 4.4a). In the twist-A-B′ (tAB′) polytype

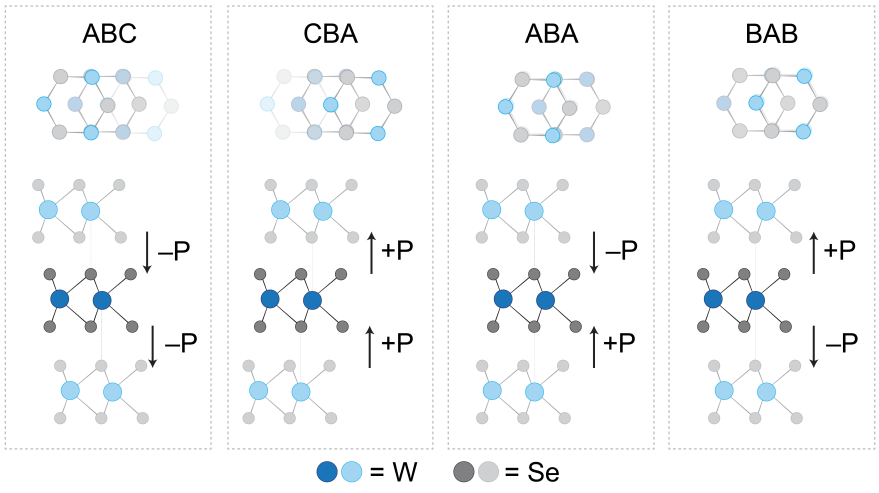

Figure 4.3: Low-energy atomic stacking configurations for parallel-stacked trilayer WSe_2, with the out-of-plane polarization direction (+P or –P) at each interface indicated by arrows. ABC and CBA configurations have equal and opposite non-zero net polarizations, while ABA and BAB configurations have no net polarization.

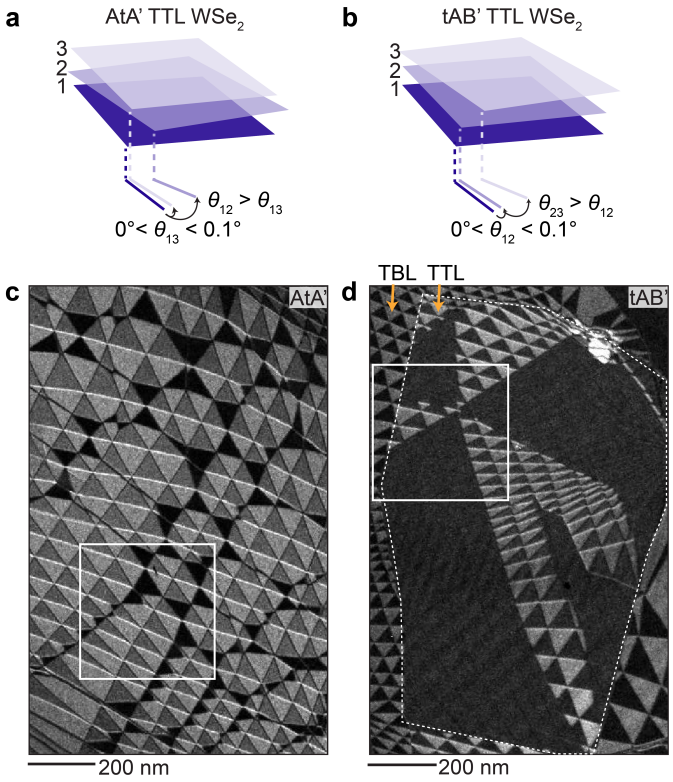

Figure 4.4: a,b, Illustrations of two main TTL polytypes, AtA′-type and tAB′-type, respectively. **c,d,** DF-TEM images of AtA′ and tAB′ WSe_2 devices, respectively, obtained using the $[10\bar{1}0]$ Bragg reflection. In the image of the tAB′-type device, twisted bilayer (TBL) and twisted trilayer (TTL) regions of the sample are marked.

the bottom and middle layers are nearly aligned ($0° < \theta_{12} < 0.1°$) while the top layer is rotated further ($\theta_{23} > \theta_{12}$, Fig. 4.4b). We image the moiré structure in these two polytypes using dark-field TEM (DF-TEM), which is a diffraction-based imaging technique that can be used to filter signal in multi-component structures[113,201], making it well-suited for the observation of buried interfaces. As shown in the DF-TEM images in Fig. 4.4c,d, the AtA′ and tAB′ polytypes produce distinct moiré patterns. In the AtA′ polytype, we see a kagome-like pattern superimposed on a triangular superlattice (Fig. 4.4c). Since $\theta_{12} > \theta_{13}$, the longer lengthscale kagome structure is attributed to the moiré between the outer layers and the shorter triangular structure to the moiré between the outer layers and middle layer. In the tAB′ polytype there are two superimposed triangular superlattices; the superlattice with the longer (shorter) periodicity comes from the bottom and middle (middle and top) layers since $\theta_{23} > \theta_{12}$ (Fig. 4.4d). The diffraction contrast observed in the DF-TEM images arises from differences in local stacking and from the presence of a global tilt of the sample away from the zone axis[202] (see Chapter 1, Section 4 for more details).

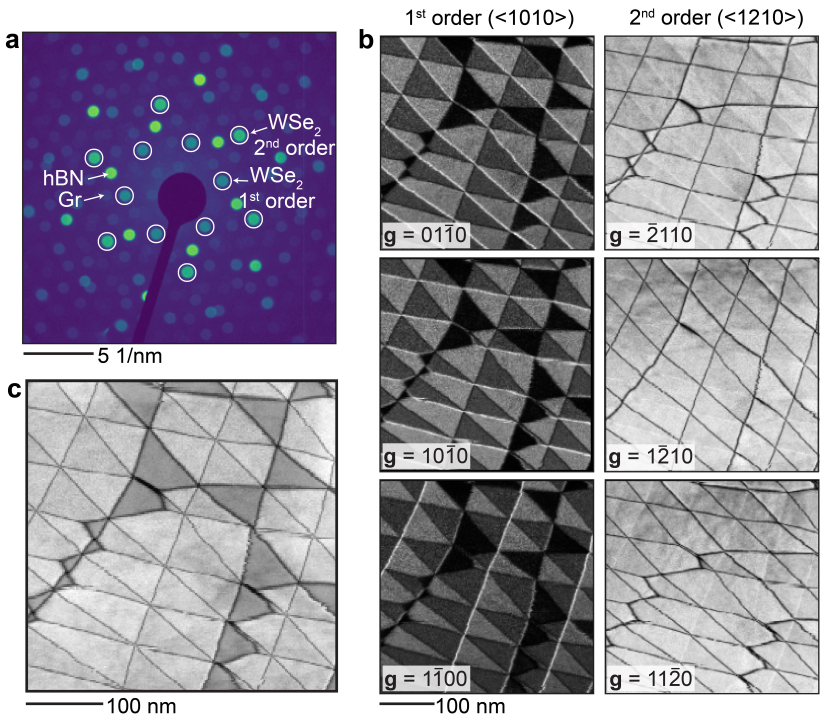

Figure 4.5: a, Average CBED pattern from a 4D-STEM data set (Device 2). Select WSe_2 Bragg disks from the first and second diffraction rings are circled in white. Other disks present include hBN, graphite, and additional WSe_2 reflections. **b,** Virtual DF images produced from a selection of first and second ring WSe_2 Bragg disks for the AtA′ sample pictured in Fig. 4.4c and **c,** corresponding composite virtual DF image.

Next we identify regions of these moiré structures that possess a net polarization using interferometric four-dimensional scanning transmission electron microscopy (4D-STEM). As detailed in Chapters 2 and 3, this imaging technique relates the intensities in interfering electron diffraction disks to the local translational offset between layers and therefore can be used to map out the stacking order throughout the moiré[161,175,200,203]. An exemplar 4D-STEM convergent beam electron diffraction (CBED) pattern for a TTL-WSe_2 device is shown in Fig. 4.5a. By integrating over the regions where the Bragg disks from the three WSe_2 layers overlap and plotting this value for each real space beam position, virtual DF images are generated, as shown in Fig. 4.5b. The pixel intensities in the virtual DF images for the first ($\langle 1010 \rangle$) and second ($\langle 1210 \rangle$) order WSe_2 Bragg disks are then normalized and summed to generate composite virtual DF images (Fig. 4.5c). Since sample tilt affects the measured Bragg disk intensities, regions used for 4D-STEM iamging are aligned onto or near ($\leq 2^\circ$ from) the [0001] zone axis prior to data acquisition (additional information on

sample tilt effects is provided in the Appendix, Section 16).

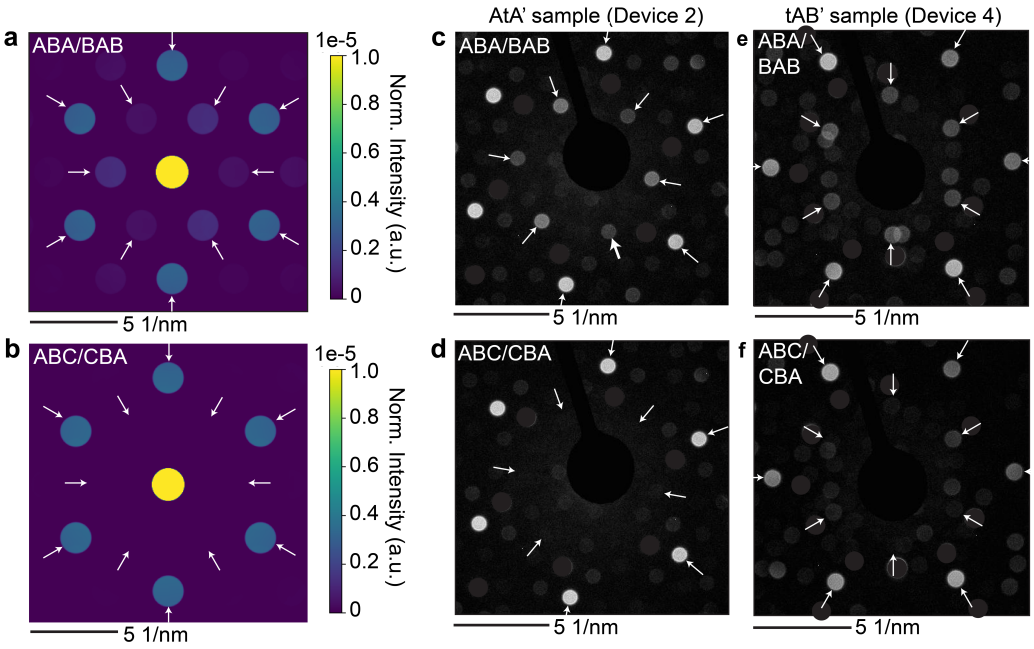

Figure 4.6: a,b, CBED patterns generated using multislice simulations for the WSe_2 ABA/BAB and CBA/ABC stacking orders, respectively. **c–f,** Corresponding experimental CBED patterns for the AtA′ and tAB′ trilayer samples shown in Fig. 4.4c,d. Bright hBN disks have been obscured for clarity. Experimental CBED patterns shown are the sum of 4 x 4 pixels in the 4D-STEM scan array, equal to an area of a 8 nm^2. White arrows mark first and second ring WSe_2 Bragg disk positions.

To assign the local stacking sequence in each region of the composite virtual DF images, we compare the experimental $\langle 10\bar{1}0 \rangle$) and $\langle 1\bar{2}10 \rangle$ diffraction intensities in each CBED pattern to computed values. First, we perform multislice simulations for various high-symmetry stacking orders (defined in Section 8, Table 4.2) in both polytypes using the published software package ABTEM[204]. A selection of simulated and experimental CBED patterns are provided in Fig. 4.6. The disk intensities in the first and second rings in the resultant theoretical diffraction patterns are then summed, normalized and translated into RGB values, and plotted on a bivariate color legend (Fig. 4.7a,b) according to the procedure and rationale applied in Ref. [200]. To summarize, the red (R), blue (B), and green (G) channels defining the color of each pixel correspond to the normalized cumulative intensities in the first ring of WSe_2 Bragg disks, second ring of WSe_2 Bragg disks, and a combination of these two values, respectively, as described by Equation Set 4.1. In these equations, the intensities from the first and second diffraction rings are weighted differently in the green channel for

the AtA′ and tAB′ cases in order to generate two distinct color schemes. Applying the same bivariate color scheme to the experimental 4D-STEM data, we produce colored virtual DF maps illustrating spatial variations in local stacking order (Fig. 4.7c,d).

$$
\begin{aligned}
R &= I_1 = I_{0\bar{1}10} + I_{01\bar{1}0} + I_{\bar{1}100} + I_{1\bar{1}00} + I_{10\bar{1}0} + I_{\bar{1}010} \\
B &= I_2 = I_{2\bar{1}\bar{1}0} + I_{\bar{2}110} + I_{1\bar{2}10} + I_{\bar{1}2\bar{1}0} + I_{\bar{1}\bar{1}20} + I_{11\bar{2}0} \\
G_{AtA'} &= 0.7 * I_1 + 0.3 * I_2 \quad , \quad G_{tAB'} = 0.3 * I_1 + 0.7 * I_2
\end{aligned}
\tag{4.1}
$$

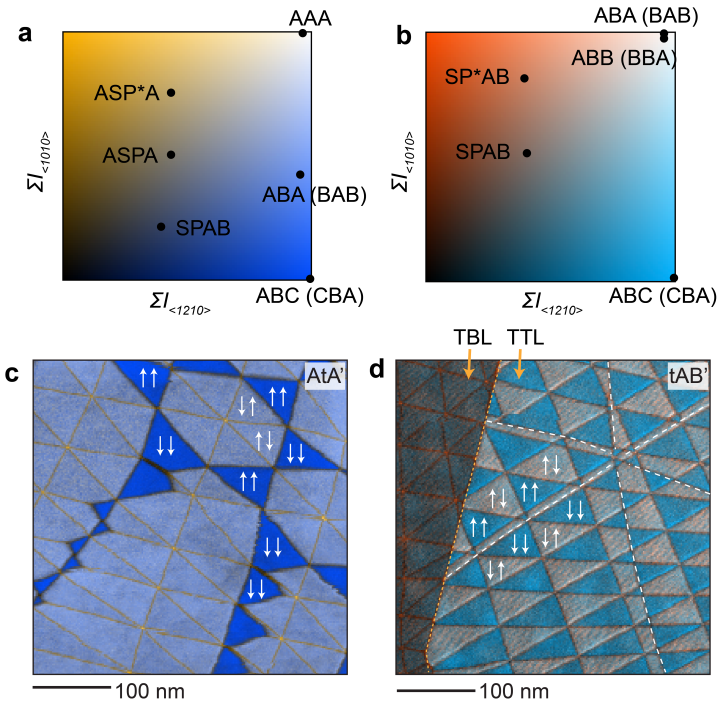

Figure 4.7: a,b, Color legends for AtA′- and tAB′-type trilayers, relating pixel color to the normalized cumulative first and second ring Bragg disk intensities ($\Sigma I_{\langle 1010 \rangle}$ and $\Sigma I_{\langle 1210 \rangle}$) obtained from the experimental CBED patterns. Plotted points indicate simulated values (normalized) for high-symmetry stacking configurations, calculated using multislice simulations. ASPA, ASP*A, SPAB, and SP*AB correspond to distinct saddle point (SP) type stacking sequences found in the boundaries between high-symmetry stacking domains. **c,d,** Corresponding 4D-STEM virtual DF images from boxed regions of the samples shown in **Fig. 4.4c,d**. Arrows indicate the local direction of polarization at the two trilayer interfaces. In **d**, the yellow dotted line marks the division between the TBL and TTL regions of the sample and the white dashed lines mark the domain walls of the large moiré. The multislice calculations pertain only to the twisted trilayer regions of the samples shown.

From this analysis, we find that in the AtA′ polytype, the ABC and CBA (that is, polar) domains are localized in the kagome-like structures, alternating in the points of each star, and on either side of elongated domain walls, the origin of which will be discussed later. Meanwhile the tAB′ polytype is divided into large sections containing either ABC or CBA stacking domains in periodic triangular arrangements. We note that interferometric 4D-STEM is purely a structural diagnostic and therefore can not be used to measure the local polarization (P) direction (i.e., net +P versus -P); however, the polarization direction in each domain can be confirmed by observing the response to an applied electric field, which is discussed next.

4.4 Polarization switching in the AtA′ polytype

The distinct arrangements of polar domains in the AtA′ and tAB′ trilayers suggest that these two polytypes will behave differently in an applied field. We first investigate the structural response in the AtA′ polytype. Fig. 4.8a shows how one of the star structures from the sample in Fig. 4.7c distorts under application of an electric bias. At zero field, the ABC (↓↓) and CBA (↑↑) regions are approximately the same size because they are energetically degenerate. As a negative (positive) bias is applied, this degeneracy is lifted and the ABC (CBA) regions grow while the CBA (ABC) regions shrink. To quantify this change, we define an order parameter, dA, which is the normalized relative area of the ABC and CBA domains, described by Equation 4.2:

$$\mathrm{d}A = \frac{A_{CBA} - A_{ABC}}{A_{CBA} + A_{ABC}} \tag{4.2}$$

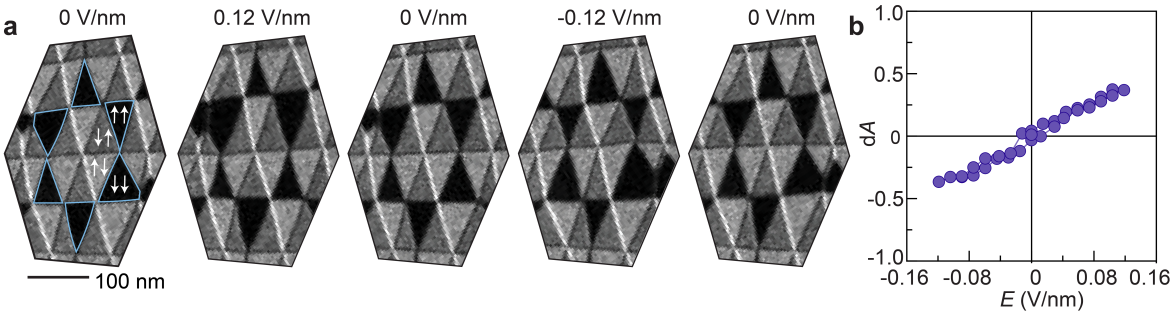

Figure 4.8: a, DF-TEM images and **b,** corresponding plot of normalized net polarization (dA) as a function of applied field (E) for an AtA′ kagome-like structure. White arrows indicate local polarization at the two trilayer interfaces. Light blue lines mark regions used for analysis.

Previous studies have demonstrated that this order parameter can be used as a proxy for net polarization.[199] The variation in dA in the star structure is plotted as a function of field (E) in Fig. 4.8b, showing an approximately linear relationship with minimal structural hysteresis or remnant net polarization. In polar twisted bilayers, this behavior has been referred to as a moiré anti-ferroelectric response (MAFE)[199] and is a direct consequence of the moiré structure, wherein the topology of the moiré domain wall network precludes complete switching of polar domains.[144,205,206] We do not observe substantial structural distortions in the surrounding non-polar regions (Fig. 4.9). While the non-polar regions encircled by polar domains do show a small increase in the size of BAB (↑↓) regions compared to ABA (↓↑) regions at negative field values, this is likely a consequence of the deformation of the surrounding polar regions. Still, the variation in dA in the non-polar domains is at least an order of magnitude smaller than in the nearby polar domains pictured in Fig. 4.8.

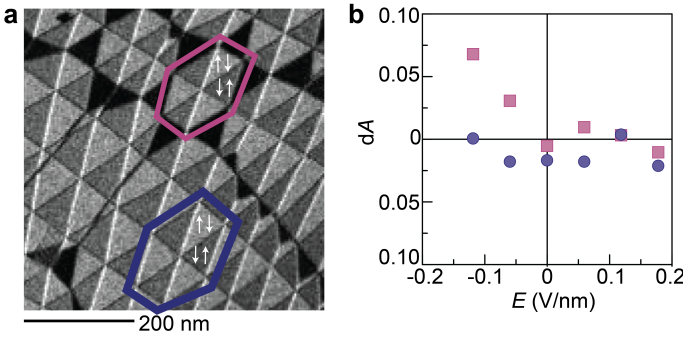

Figure 4.9: a, DF-TEM image of an AtA′ WSe_2 trilayer. Select non-polar domains surrounded by polar domains and further isolated from polar domains that were used for analysis in **b** are outlined in purple and dark blue, respectively. **b,** Corresponding plots of the relative area of BAB (↑↓) domains versus ABA (↓↑) domains (dA) as a function of field (E). Here, $\mathrm{d}A = (A_{BAB} - A_{ABA})/(A_{BAB} + A_{ABA})$.

It is also common for moiré structures to acquire heterostrain during sample fabrication, where one or more layers are uniaxially stretched relative to the adjacent layer(s)[123,130,207]. In the case of an AtA′-type TTL, introducing a unixial heterostrain between the top and bottom layers (ϵ_{13}) causes a transition from a kagome-like moiré structure to a polar domain wall (PDW) structure, as illustrated in Fig. 4.10a. To estimate the amount of heterostrain necessary to observe this transition, we consider three representative AtA′ structures, shown in Fig. 4.10b. The moiré unit cell geometry in each of these superlattices can be defined by three variables: the interlayer twist angle θ_m, the magnitude of uniaxial heterostrain ϵ, and the angle at which the heterostrain is applied θ_s. The values of these variables are uniquely determined by measuring the lengths of the three sides of each triangular moiré unit cell and inputting those side lengths in a triangulation model described in Ref. [146] and

Appendix, Section 8. Using this model, we calculate the interlayer twist angle, where $\theta_m = \theta_{13}$, and the heterostrain (ϵ_{13}) for each of the three superlattices pictured. In this case, $\theta_{13} \sim 0.1°$ for all three example structures; however, it is clear that even a relatively small increase in ϵ_{13} of around 0.1% substantially changes the moiré structure and generates extended polar domain walls. Intuitively, this makes sense since atomic scale strain is magnified in moiré systems[127], particularly when the moiré periodicity is large like in the samples studied in this work. The small non-zero value of ϵ_{13} for the un-strained system picture in Fig. 4.10b results from error in the positions of the moiré unit cell vertices, which were manually defined.

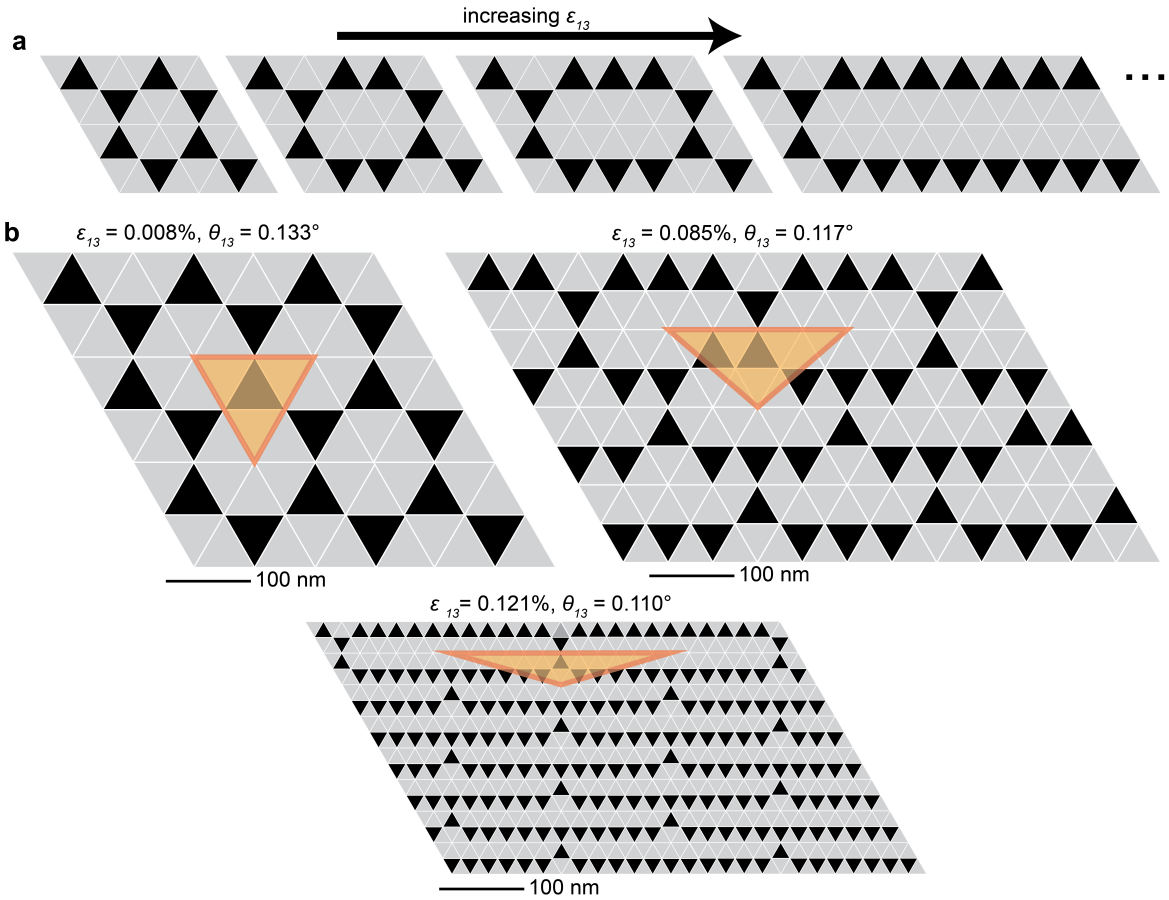

Figure 4.10: **a,** Schematic illustrating the transition from a kagome-like structure to a polar domain wall structure as heterostrain in introduced between the top and bottom layers of an AtA′ moiré superlattice. **b,** AtA′ structures with $\theta_{13} \sim 0.1°$ but a variation of roughly 0.1% heterostrain, calculated using the side lengths of the triangular moiré unit cells shown in orange. In **a** and **b**, black triangles have an ABC or CBA stacking and gray triangles have an ABA or BAB stacking.

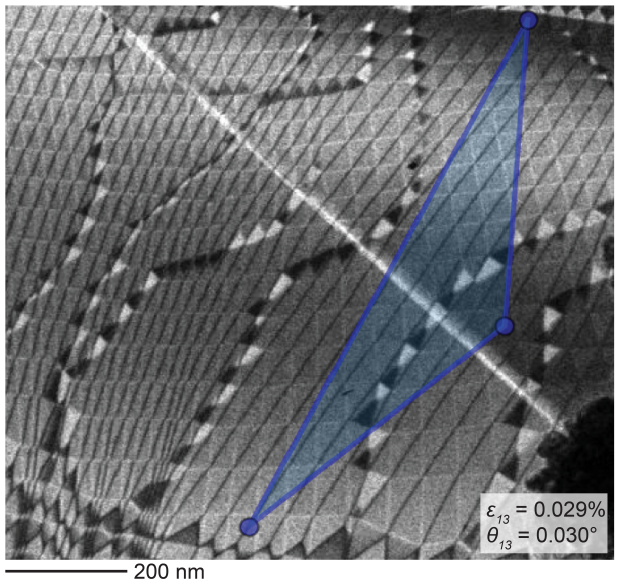

Figure 4.11: Low-magnification DF-TEM image of a slightly heterostrained (< 0.03%) AtA′ WSe_2 sample with PDWs. The moiré unit cell used for the calculation of θ_{13} and ϵ_{13} is pictured in blue. Using the triangulation model described in Chapter 2, the upper bounds for θ_{13} and ϵ_{13} are estimated to be 0.03° and 0.03%, respectively. Image produced from the $[10\bar{1}0]$ Bragg reflection.

A DF-TEM image of an AtA′-type sample with a very slight misalignnment between the outer layers ($\theta_{13} < 0.03°$) and an estimated heterostrain (ϵ_{13}) < 0.03% is shown in Fig. 4.11. Compared to the sample in Fig. 4.8a, this sample contains extended PDWs in the longer lengthscale moiré rather than a kagome-like pattern. Similar elongated domain walls have also been observed in heterostrained twisted trilayer graphene[200]. Interestingly, in this heterostrained sample we observe two groups of PDWs with different responses to an applied field. The first type displays a gradual response to the field (Fig. 4.12a,b) where the ABC (↓↓) and CBA (↑↑) domains steadily grow and shrink during biasing. However, the second type has a much sharper response where the polar domains rapidly flip between ABC and CBA stacking (Fig. 4.12c,d), similar to an untwisted polar heterostructure but on a much shorter lengthscale (10s rather than 100s of nm). Additionally, this second domain wall type has structural hysteresis and a remnant net polarization at zero field, a FE response. In the PDW shown in Fig. 4.12c,d, the coercivity is relatively small due to the small domain size; however some FE PDWs, discussed in the next section, exhibit a larger coercivity. Uniquely, the polar domains in the heterostrained twisted trilayer structures shown here are not confined by the same topology as either a twisted bilayer or a non-heterostrained twisted trilayer, enabling a true ferroelectric response in a moiré material.

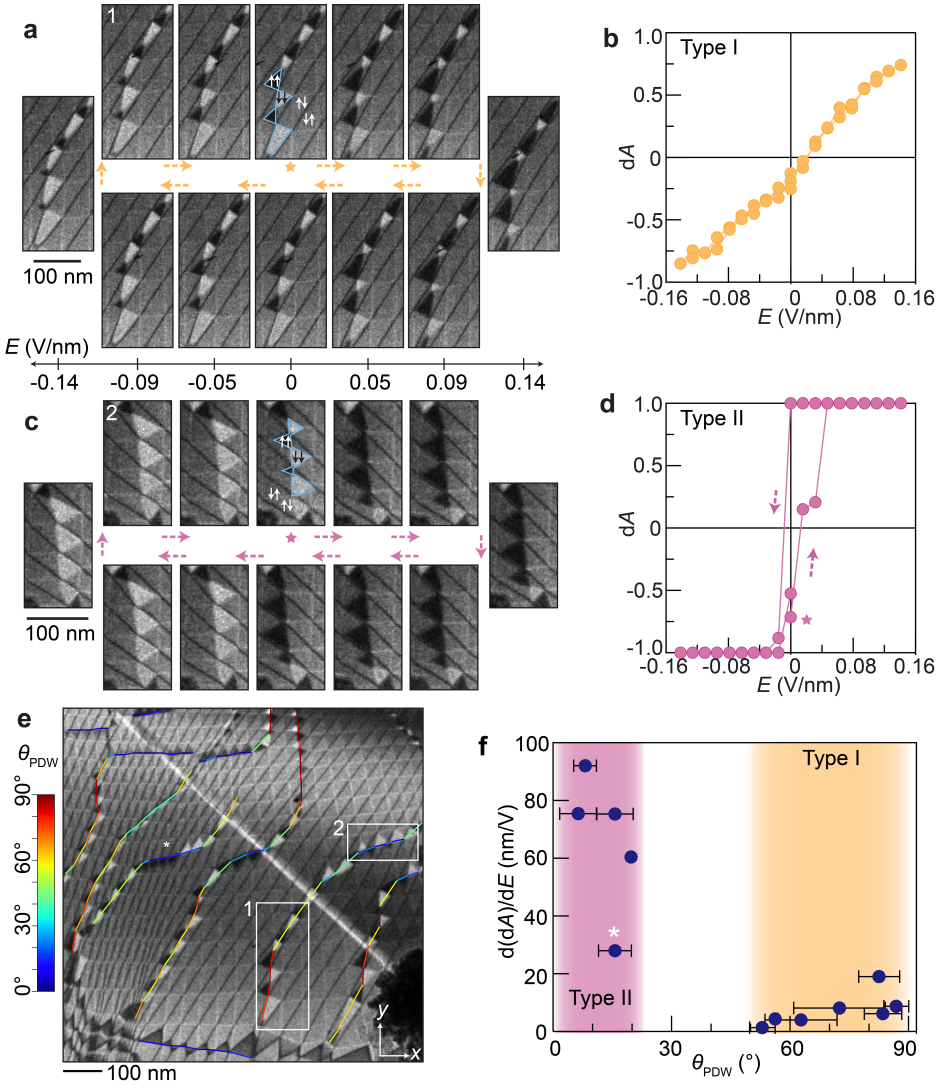

Figure 4.12: **a–d,** DF-TEM images and corresponding plots of dA versus E for two types of PDWs. Colored stars mark initial positions and dashed arrows show scan directions. **e,** Low-magnification DF-TEM image of the slightly heterostrained AtA′ sample with PDW orientations (θ_{PDW}) overlaid in color. White numbered boxes highlight regions analyzed in **a–d**. **f,** PDW polarizability (d(dA)/dE) versus average PDW orientation. Horizontal error bars indicate the s.d. of the individual domain orientations in each PDW section analyzed (see Fig. 4.13). Shading highlights two groups of PDWs, one with gradual (Type I) and one with sharp (Type II) switching. Asterisks in **e,f** mark a special PDW case exhibiting sequential switching, analyzed further in Fig. 4.18. White and black arrows in **a,c** indicate local polarization at the two trilayer interfaces. Light blue lines in **a,c** mark regions used for analysis in **b,d**, respectively. All DF-TEM images produced from the [10$\bar{1}$0] Bragg reflection.

To understand the origin of the different switching responses exhibited by these two groups of domain walls, we calculate the polarizability for various PDW segments with different orientations within the sample. Here, polarizability, the ease with which the net polarization switches, is equivalent to the slope of dA versus E (d(dA)/dE). Fig. 4.12e illustrates the orientation of the PDWs in the sample (θ_{PDW}) and Fig. 4.12f relates the polarizability of a selection of these PDWs to their average orientation. Images of all polar domain walls (PDWs) analyzed to produce Fig. 4.12f are provided in Fig. 4.13 with corresponding plots of dA versus E. The orientation of each PDW section shown in Fig. 4.13 is defined as the average angle ($0° \leq \theta_{PDW} \leq 90°$) of the constituent domain wall segments with respect to the x-axis of the image. The reported error for this measurement indicates the standard deviation. In general, the angle of each domain wall segment was measured using the relevant edge of the local polar domain (marked by the colored lines in Fig. 4.13c–n). In some cases where two polar domains share an edge (for example, Fig. 4.13e,i), the domain orientation was defined diagonally across the polar domain as an average. Polar domain areas (used for calculation of dA) were determined either 1) by applying intensity thresholds to the DF-TEM image from the $[10\bar{1}0]$ Bragg reflection (in regions with sufficient contrast between polar domains and surrounding non-polar regions) or 2) by manual tracing the outline of the polar domains on the DF-TEM image from the $[\bar{1}2\bar{1}0]$ Bragg reflection (in regions with poor contrast between polar and non-polar domains). For the sample shown in Fig. 4.13, Method 2 was used to analyze PDWs 2 and 11 and Method 1 was used to analyze all other PDWs. The linear fits used to calculate the polarizability, d(dA)/dE, of each PDW are marked as orange dotted lines in Fig. 4.13c–n. For PDWs with more than one major polarization switching event (Fig. 4.13j–n) the reported value of d(dA)/dE is an average of the fits pictured. PDWs 1–7 are classified as Type I and PDWs 8–12 are classified as Type II in Fig. 4.12f. Based on the results in Fig. 4.12f and 4.13, it is evident that, for this sample, PDWs oriented around 60-90° relative to the x-axis have a polarizability that is roughly 3-4 times lower than PDWs oriented closer to 0°.

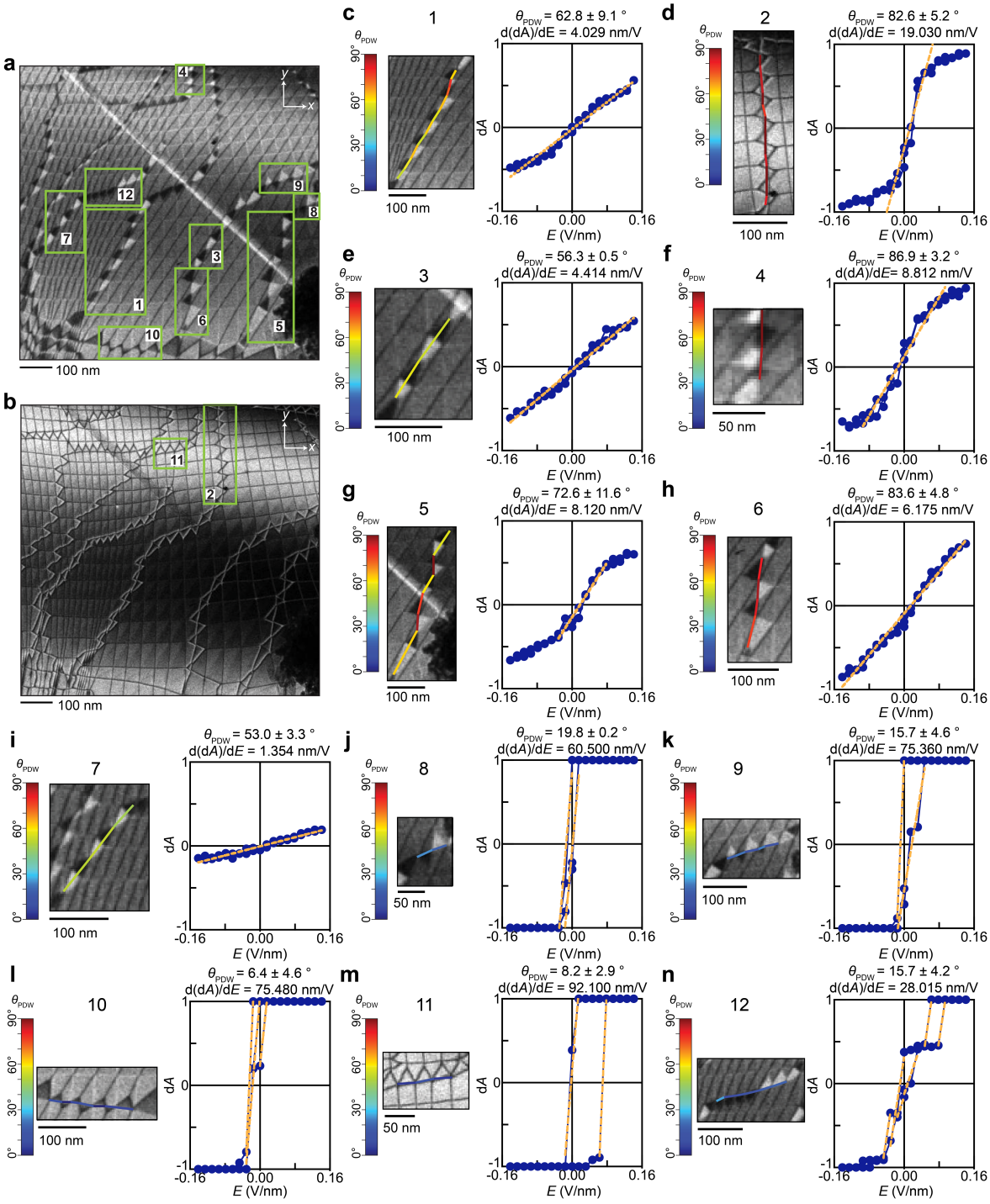
a
b
c
d
e
f
g
h
i
j
k
l
m
n
100 nm
50 nm
E (V/nm)
dA
θPDW = 62.8 ± 9.1 °
d(dA)/dE = 4.029 nm/V
θPDW = 82.6 ± 5.2 °
d(dA)/dE = 19.030 nm/V
θPDW = 56.3 ± 0.5 °
d(dA)/dE = 4.414 nm/V
θPDW = 86.9 ± 3.2 °
d(dA)/dE= 8.812 nm/V
θPDW = 72.6 ± 11.6 °
d(dA)/dE = 8.120 nm/V
θPDW = 83.6 ± 4.8 °
d(dA)/dE = 6.175 nm/V
θPDW = 53.0 ± 3.3 °
d(dA)/dE = 1.354 nm/V
θPDW = 19.8 ± 0.2 °
d(dA)/dE = 60.500 nm/V
θPDW = 15.7 ± 4.6 °
d(dA)/dE = 75.360 nm/V
θPDW = 6.4 ± 4.6 °
d(dA)/dE = 75.480 nm/V
θPDW = 8.2 ± 2.9 °
d(dA)/dE = 92.100 nm/V
θPDW = 15.7 ± 4.2 °
d(dA)/dE = 28.015 nm/V

Figure 4.13: a,b, DF-TEM images of a heterostrained AtA′ trilayer formed from the $[10\bar{1}0]$ and $[\bar{1}2\bar{1}0]$ Bragg reflections, respectively. Analyzed PDWs are numbered and boxed in green. **c–n,** Magnified images of the labeled PDWs with the orientation of each PDW segment with respect to the x-axis (θ_{PDW}) overlaid and corresponding plots of dA versus E. Reported values of θ_{PDW} indicate the average orientation of the segments in each PDW shown (error is standard deviation). d(dA)/dE is the polarizability determined from the linear fits plotted as orange dashed lines.

Knowing that domain polarizability is affected by domain anisotropy in twisted bilayers[199,208], the phenomenon we observe could be attributed to uniaxial heterostrain present in the superimposed small moiré, which is oriented on average around 72° relative to the x-axis in this sample (Fig. 4.14). This heterostrain introduces global structural anisotropy in the trilayer, as seen by the distortion of the triangular moiré unit cells, which could produce a preferential sliding axis for domain switching, analogous to an easy axis for spin reorientation in magnetic systems[209,210]. To explore this idea further, we consider how application of a uniaxial strain would affect the possible pathways for sliding between layers and subsequent polarization switching. First, when there is no strain present in the unit cells of the small moiré pattern (that is, the polar domains are symmetrical), polarization switching across the domain wall can be achieved through a set of interlayer sliding pathways that are structurally equivalent

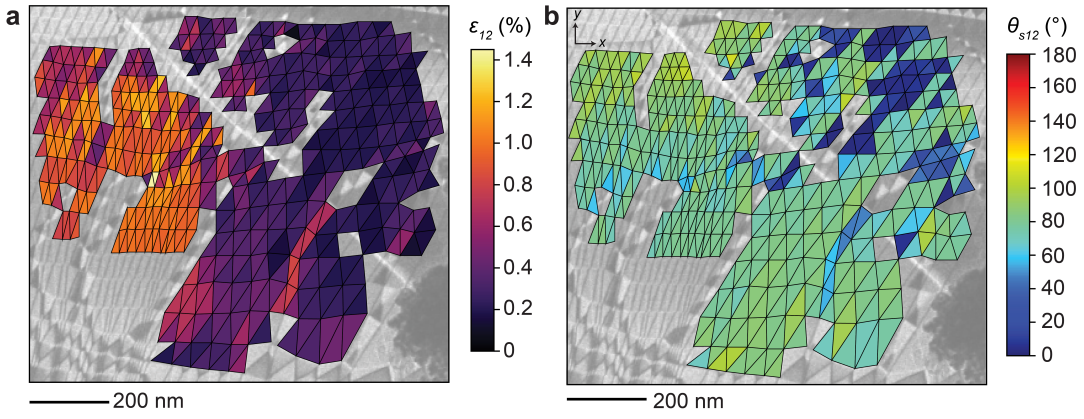

Figure 4.14: Maps of **a,** heterostrain magnitude (ϵ_{12}) and **b,** heterostrain direction (θ_{s12}) between an outer and middle layer of an AtA′ sample, indicating an average ϵ_{12} of $0.56 \pm 0.32\%$ and an average θ_{s12} of $72 \pm 24°$ relative to the x-axis. Reported errors indicate s.d..

regardless of the PDW orientation, as shown in Fig. 4.15a–d. On the other hand, when uniaxial strain is present, the polar domains, and underlying atomic lattices, become asymmetrically distorted such that four structurally inequivalent sliding pathways emerge (Fig. 4.15e–h). These four paths can be distinguished by two factors: (i) whether sliding traverses the long or short axis of the distorted atomic lattice and (ii) the orientation of the sliding axis with respect to the domain edge across which the sliding occurs. Based on published theoretical work on interlayer sliding in uniaxially strained transition metal carbides,[211] we intuitively rationalize that these structurally distinct sliding pathways in the uniaxially strained system correspond to distinct energy landscapes that could lead to the different switching responses we observe in the Type I versus Type II PDWs. While the illustrations in Fig. 4.15e–h and the strained sample used in our experiments exhibit the effects of a shear-type strain, we expect a similar rationale to be applicable for any type of symmetry-breaking uniaxial strain, including a normal strain (Fig. 4.16). Full understanding of the effects of uniaxial strain, whether shear or normal, on the interlayer sliding mechanisms and validation of the hypotheses presented here warrants future computational efforts. However, overall, it is clear that polarization switching in the AtA′ trilayer is influenced by the uniaxial strain fields in all three WSe_2 layers collectively.

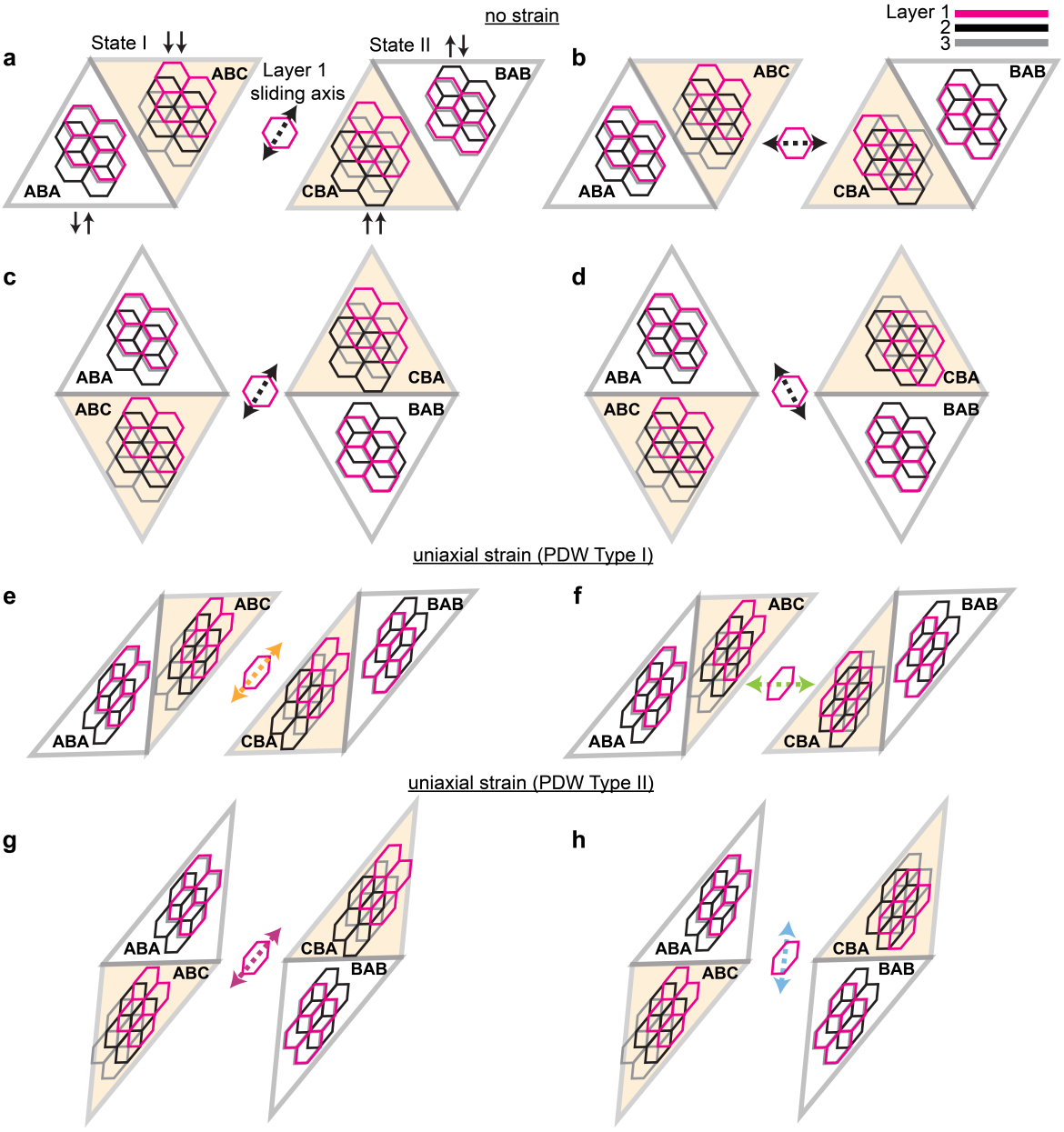

Figure 4.15: Schematics illustrating polarization switching via interlayer sliding across PDWs with **a–d,** no strain and **e–h,** uniaxial shear strain. Solid arrows in **a** indicate polarization of the two interfaces in each triangular domain. Dashed arrows in each panel indicate the axis along which layer 1 (pink) slides to switch between polarization states I and II. In **a–d**, all sliding axes (black dashed arrows) are structurally equivalent. In **e–h**, four structurally distinct sliding pathways (orange, green, purple, and blue dashed arrows) are predicted.

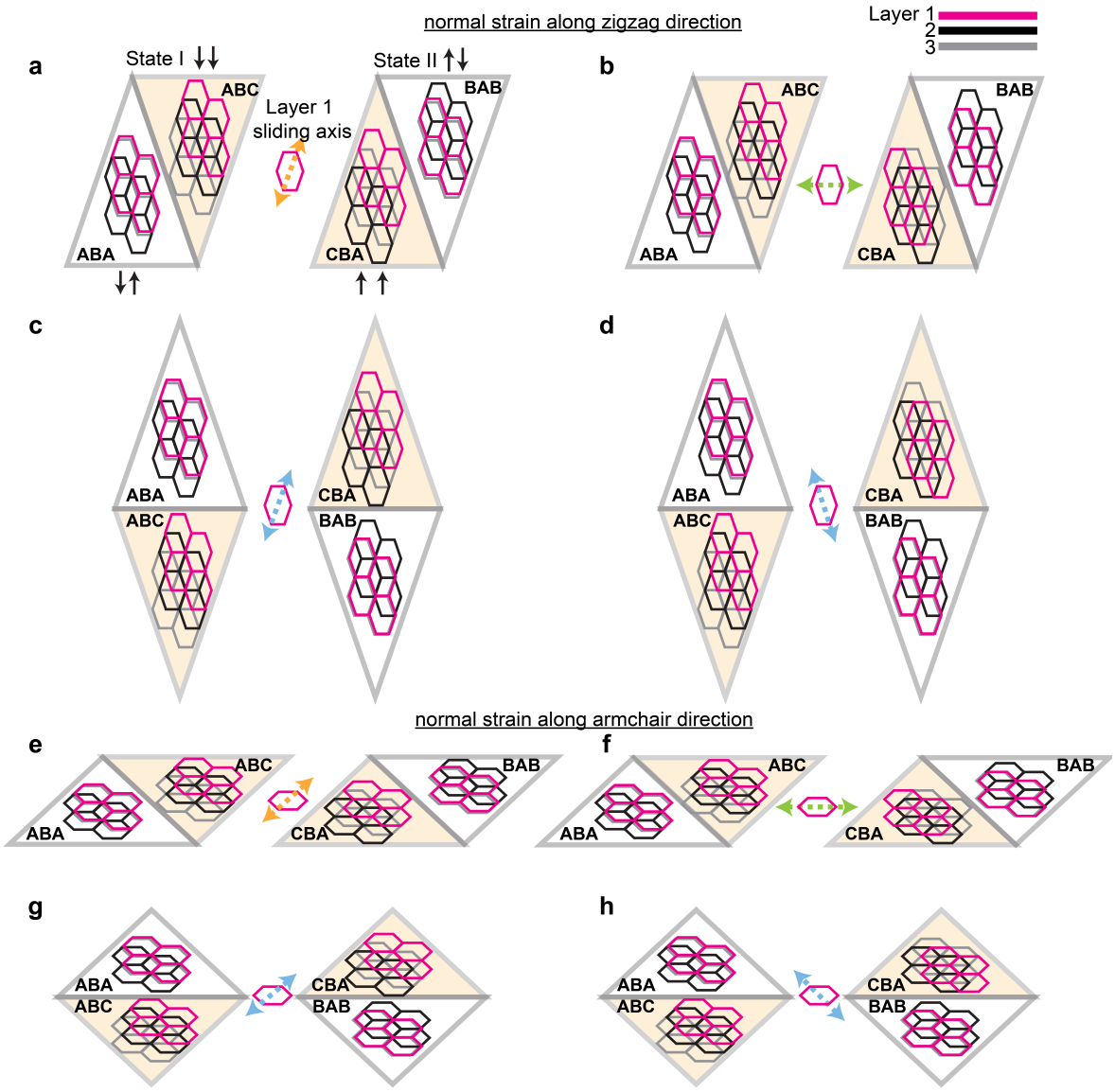

Figure 4.16: Schematics illustrating polarization switching via interlayer sliding across PDWs with normal strain applied along the **a–d,** zigzag and **e–h,** armchair directions of the hexagonal crystal lattice. Solid arrows in **a** indicate polarization of the two interfaces in each triangular domain. Dashed arrows in each panel indicate the axis along which layer 1 (pink) slides to switch between polarization states I and II. Three structurally distinct sliding pathways (orange, green, and blue dashed arrows) are predicted for each case.

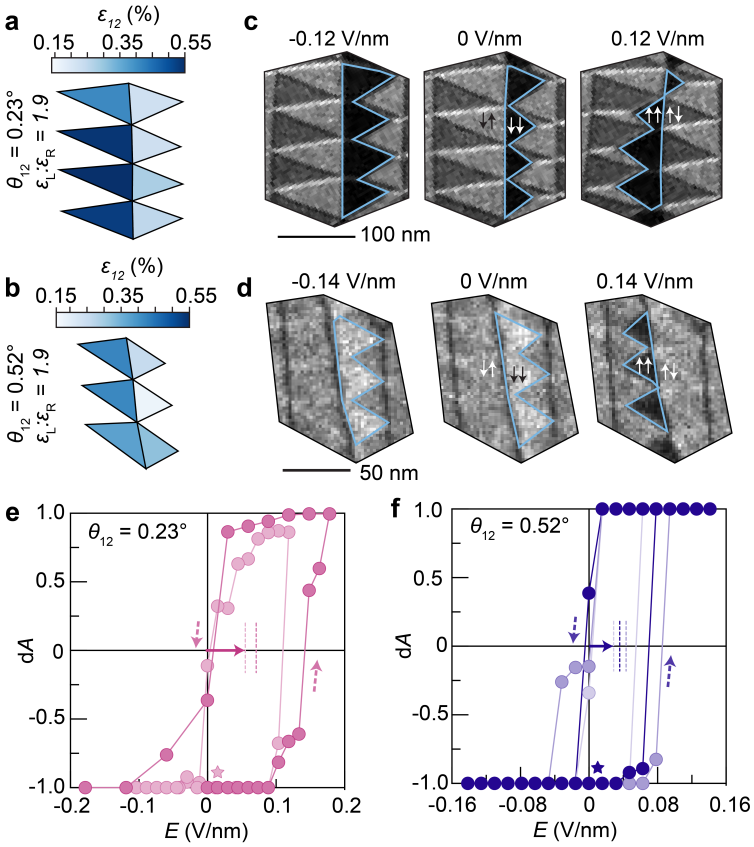

Figure 4.17: **a,b,** Maps of heterostrain in the smaller moiré (ϵ_{12}), **c,d,** DF-TEM images at different applied fields, and **e,f,** plots of normalized net polarization (dA) as a function of applied field (E) for two PDWs, one with $\theta_{12} = 0.23°$(**a,c,e**) and the other with $\theta_{12} = 0.52°$(**b,d,f**). Vertical dashed lines in **e,f** highlight shift of the center of the hysteresis loop away from 0 V/nm for each biasing cycle pictured. $\epsilon_L : \epsilon_R$ indicates the heterostrain ratio between small moiré domains on the left (L) and right (R) side of the PDW. In **c,d** white and black arrows indicate polarization at the two interfaces of select domains and light blue lines mark polar regions used for calculation of dA. DF-TEM images were produced from the $[10\bar{1}0]$ Bragg reflection.

4.5 Heterostrain control of polarization bias

Some PDWs run through a heterostrain gradient where the small moiré is considerably more distorted on one side of the domain wall than the other. For example, in the regions shown in Fig. 4.17a,b, the magnitude of heterostrain between layers 1 and 2 (ϵ_{12}) is approximately twice as large on the left side of the PDW compared to the right side ($\epsilon_L : \epsilon_R = 1.9$). In both regions, which have different interlayer twist

angles between the outer and middle layers ($\theta_{12} = 0.23°$ and $0.52°$), we observe that the polar domains localize on the less heterostrained half of the PDW at zero field (Fig. 4.17c,d). It has been demonstrated that the presence of anisotropic strain in multilayer graphene further increases the energy of the rhombohedral (ABC/CBA) stacking types relative to the Bernal (ABA/BAB) stacking[212]. Presuming that WSe_2 behaves similarly, we rationalize that the observed preferential alignment of polar domains at zero field arises from an intrinsic thermodynamic bias generated by the appreciable difference in heterostrain between the sides of the PDW. Plotting dA versus E (Fig. 4.17e,f) over two or three biasing cycles, we see that this energetic preference toward one polarization state at zero field ultimately shifts the hysteresis curve along the electric field axis. We note that the enhanced coercivity of these two PDWs compared to that shown in Fig. 4.12d likely stems from a combination of structural factors, such as domain size, local distortions of the small moiré after polarization switching, and random variations in structural pinning sites at the ends of the domain wall segments pictured[194,199]. Nevertheless, it is evident that the heterostrain gradient effectively pins the polar domains along one scan direction to produce a consistently biased FE response.

Remarkably, this asymmetry in the polarization curve can be systematically tuned down to the length scale of an individual polar domain. To demonstrate, we consider a PDW in a continuously varying heterostrain gradient. Fig. 4.18a illustrates that ϵ_{12} is smaller on the bottom side of the PDW than on the top for domains 1–4 and vice versa for domains 5–6. Based on this variation in the direction of the heterostrain gradient, at zero field polar domains 1–4 align on the bottom side of the PDW and polar domains 5–6 align on the top, as shown in Fig. 4.18b. As a field is applied, each domain responds independently in a domino-like fashion (Fig. 4.18b), where the field necessary for polarization switching is directly correlated to the magnitude and direction of the local heterostrain gradient. Specifically, increasing the magnitude of the local heterostrain gradient increases the magnitude of the field required for switching, and changing the direction of this gradient (e.g., $\epsilon_B : \epsilon_T > 1$ versus $\epsilon_B : \epsilon_T < 1$) changes the direction of the field required for switching (Fig. 4.18c). These results demonstrate that coupling strain engineering[213–215] with moiré engineering could offer a route for precise, spatially localized manipulation of interfacial polarization.

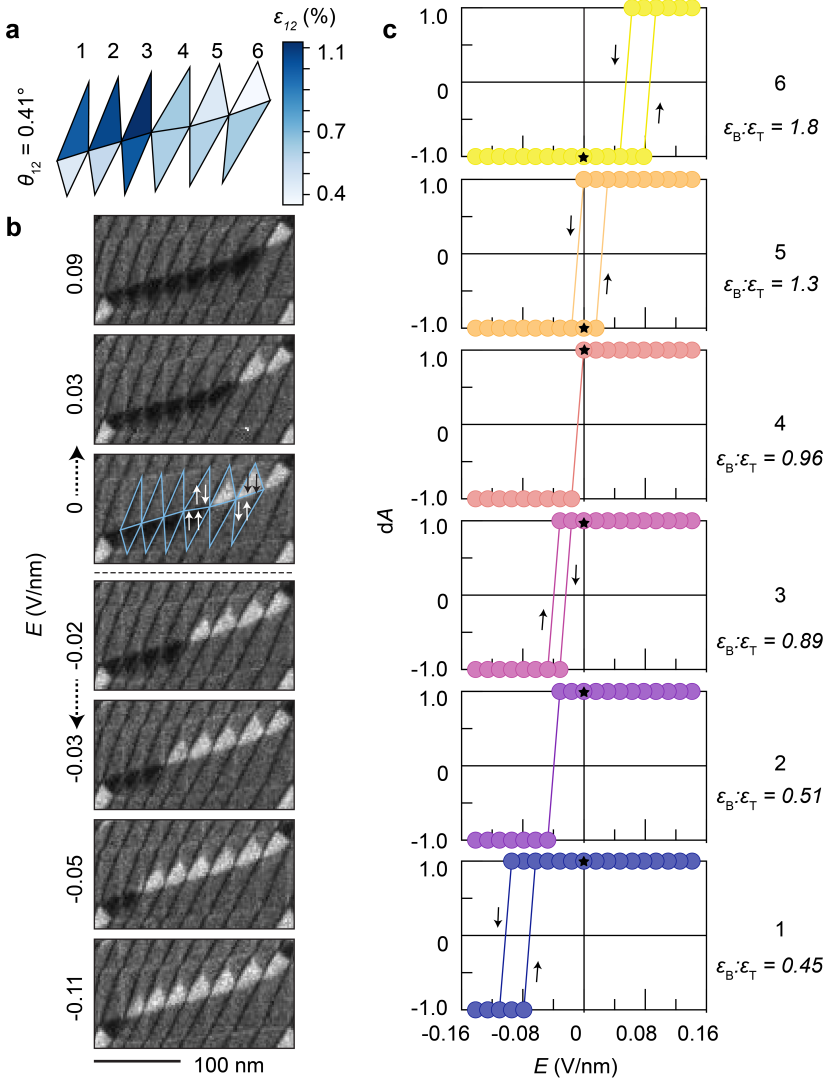

Figure 4.18: a, Map of ϵ_{12} and **b,** DF-TEM images at different applied fields for a PDW with a variation in ϵ_{12} along the length of the domain wall (average $\theta_{12} = 0.41°$). **c,** Plots of dA as a function E for each of the six polar domains pictured in **a,b**. $\epsilon_B : \epsilon_T$ indicates the heterostrain ratio between small moiré domains on the bottom (B) and (T) of the PDW. In **b** white and black arrows indicate polarization at the two interfaces of select domains. Light blue lines mark polar regions used for calculation of dA. DF-TEM images were produced from the $[10\bar{1}0]$ Bragg reflection.

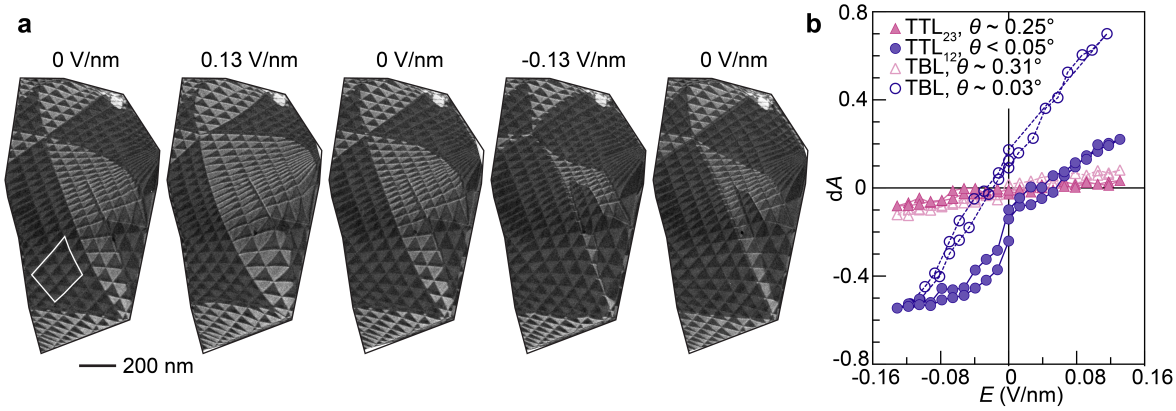

Figure 4.19: DF-TEM images for a tAB′-type WSe_2 trilayer over a series of applied fields, produced by overlaying images from the $[10\bar{1}0]$ and $[1\bar{1}00]$ Bragg reflections. **b,** Normalized relative area of light versus dark domains (dA) as a function of applied field (E), describing deformation of the large and small moiré of the twisted trilayer (TTL) shown in **a** ($\theta_{12} < 0.05°$ and $\theta_{23} = 0.25°$) compared to analagous twisted bilayer (TBL) structures ($\theta \sim 0.03°$ and $\theta = 0.31°$). The area used for analysis of the small moiré in the TTL is boxed in white in **a**. The full sample area in **a** was used for analysis of the TTL large moiré.

4.6 Polar domain switching in the tAB′ polytype

Next we discuss how the tAB′ polytype responds to an applied field. Whereas the AtA′ polytype had a highly localized polarization switching response, the tAB′ structure globally deforms under application of an electric field (Fig. 4.19a). The tAB′ polytype is quite similar structurally to a twisted bilayer considering that both the large and small moiré patterns in the tAB′ trilayer relax into triangular domains[113,175,200]. With this in mind, we analyze the field-dependent structural distortions in both moiré lengthscales of the tAB′ structure and compare them to analogous twisted WSe_2 bilayers in Fig. 4.19b. We do not observe marked differences in behavior between the smaller moiré in the trilayer ($\theta_{23} = 0.25°$) and a twisted bilayer with a similar interlayer rotation ($\theta = 0.31°$). Interestingly, the larger moiré in the trilayer ($\theta_{12} < 0.05°$), has a considerably lower polarizability than its twisted bilayer counterpart ($\theta \sim 0.03°$).

DF-TEM images of the tAB′ structure show that the domain walls of the larger moiré are roughly commensurate with the domain walls in the smaller moiré, and as a field is applied, these two sets of domain walls appear to be pinned to one another (Fig. 4.20a). At one point, around -0.01 V/nm, the domain wall of the large moiré de-pins from that of the small moiré and jumps to an adjacent domain

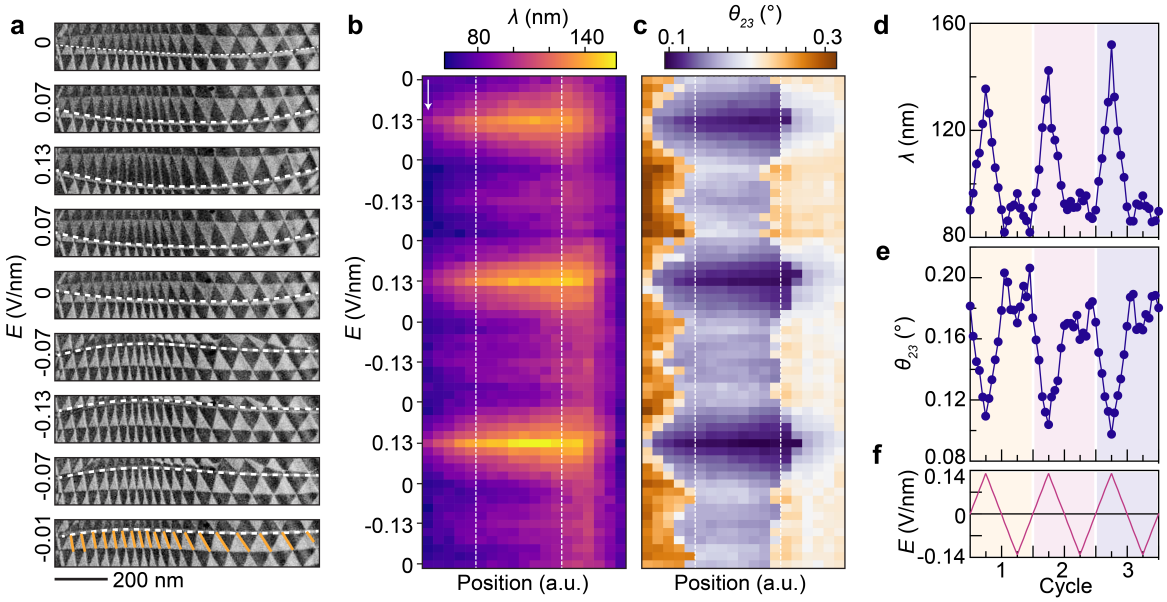

Figure 4.20: a, Magnified DF-TEM images showing pinning of a domain wall in the large TTL moiré to domain walls in the smaller moiré as a field is applied. Images produced from the $[1\bar{1}00]$ Bragg reflection. **b,c,** Plots tracking evolution of side length (λ) and local twist angle (θ_{23}) for a row of small moiré domains shown in **a** over three cycles of biasing. Side lengths used for **b** are marked with orange lines in **a**. **d,e,** Corresponding average values of λ and θ_{23}, respectively, over the course of three biasing cycles (demarcated by yellow, red, and blue shading and described by the applied field profile illustrated in **f**). Averages values plotted in d and e were calculated using the regions between the white dashed lines in **b** and **c**, respectively.

wall in the small moiré, leading to the S-shaped polarization curve in Fig. 4.19b. To quantitatively analyze this pinning effect, we track how the side lengths (λ) of the triangular domains in the small moiré (from Fig. 4.20a) evolve as a function of field along the length of one of the large moiré domain walls over three cycles of biasing. The results illustrate that the small moiré domains stretch anisotropically as the large moiré deforms in response to the field, particularly at positive field values (Fig. 4.20b). This increase in the periodicity of the small moiré could be facilitated by either a reduction in the local interlayer rotation in these domains or by a reduction in local lattice mismatch. Considering that one or more layers are sliding and stretching in response to the applied field, it is unlikely that the local lattice mismatch between layers is decreasing (we would expect the converse instead), and therefore we conclude that changes in local rotational offset between the middle and top layers (θ_{23}, Fig. 4.20c) drive the observed deformation of the small moiré domains. Fig. 4.20d,e shows how the average values of λ and θ_{23} evolve for a group of domains from the region

in Fig. 4.20a over three biasing cycles (field profile in Fig. 4.20f), showing that the small moiré length increases and the local twist angle decreases by up to a factor of two as a result of pinning between the domain walls across the two interfaces. The local change in θ_{23} is most closely related to the position of the small moiré domain along the length of the large moiré domain wall and therefore depends on the curvature of the large moiré domains in response to the field (Fig. 4.21). Importantly, these results indicate that the interfaces in polar multilayer heterostructures are not decoupled from one another and cooperative effects can influence observed switching dynamics, such as the reduction in polarizability observed in Fig. 4.19b. Notably, the results in Fig. 4.20 also demonstrate an electrical route to controlling superlattice wavelength in moiré structures.

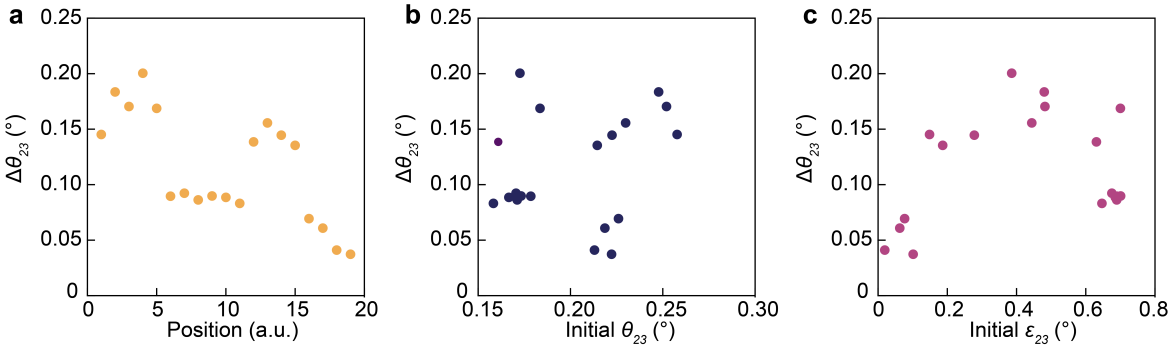

Figure 4.21: Plots describing change in local twist angle of small moiré domains pictured in Fig. 4.20a ($\Delta\theta_{23}$) as a function of **a,** position along the length of the large moiré domain wall, **b,** initial local twist angle (θ_{23}) at zero field, and **c,** initial local heterostrain (ϵ_{23}) at zero field. $\Delta\theta_{23}$ depends most closely on domain position rather than θ_{23} or ϵ_{23}.

4.7 Conclusions

Two-dimensional vdW materials have exhibited promise as FE components in emerging technologies[216,217] due to their robustness to depolarization at atomic thicknesses[218–224], their compatibility with silicon-based device schemes, and their ability to be stacked into multi-component heterostructures with sought-after functionalities, such as FE field-effect transistors (FE-FETs)[225] and multiferroic devices[226,227]. Here, using a combination of complementary diffraction-based electron microscopy techniques, we have revealed that a diverse range of polarization switching dynamics can be accessed in twisted trilayer heterostructures due to the presence of more than one moiré periodicity as well as interactions between all three layers, as summarized in

Fig. 4.22. Namely, changing relative rotations between layers and intralayer uniaxial strain fields leads to a variety of polar domain structures with different polarizabilities, coercivities, and intrinsic thermodynamic biases. This work highlights how polarization switching and structural dynamics can be engineered in polar multilayer systems, particularly as developments in 2D heterostructure fabrication and strain engineering continue to advance. For example, variations in the arrangements of polar domains in the AtA′ versus tAB′ structures as well as the highly localized, strain-tunable nature of preferential polarization states in the AtA′ polytype opens avenues for the design of structures and surfaces with deterministically patterned polarization and could have utility for neuromorphic computing. Even in untwisted polar vdW multilayers, manipulation of intralayer strain could afford control over consequent switching dynamics. In moiré multilayers comprised of semiconducting vdW materials, including WSe_2, such variability in polar order and switching responses could also lead to the emergence of exotic, electrically-tunable moiré exciton responses, beyond those that have been previously observed in bilayer heterostructures[104].

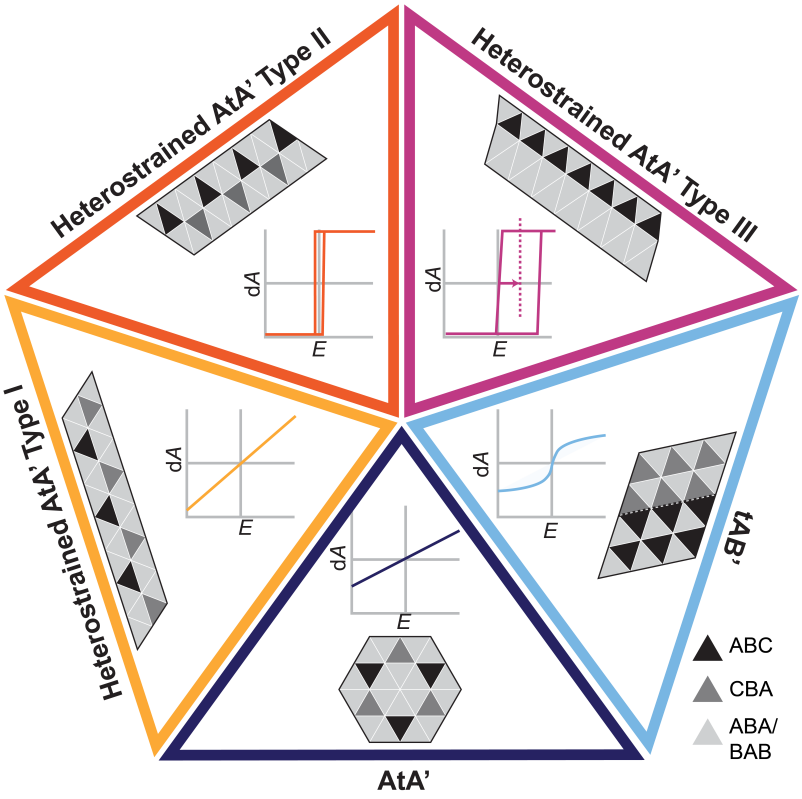

Figure 4.22: Summary of the various types of polar domain structures studied in this work and their respective switching responses.

4.8 Experimental Details

4.8.1 Sample preparation

Monolayer WSe_2 (HQ Graphene), 2–5 layer graphite (Graphene Supermarket Kish graphite) and < 15 nm-thick hBN (grown by collaborators T.T. and K.W.) were mechanically exfoliated onto SiO_2/Si substrates and selected using optical microscopy. VdW heterostructures were then fabricated using the cut-and-stack dry transfer method[162]. Briefly, a tungsten scanning tunneling microscope tip was first used to cut each WSe_2 monolayer into three pieces. A polybisphenol-A-carbonate/ polydimethylsiloxane (PC/PDMS) stamp was then used to pick up the top graphite (Gr) electrode followed by the top hBN and the first third of a pre-cut WSe_2 monolayer. The remaining WSe_2 portions were then sequentially rotated and picked up with a parallel, or R-type, orientation between WSe_2 layers to construct the desired trilayer structure, followed by pick-up of the bottom hBN and finally the bottom graphite. The final stacks were stamped onto Protochips electrical e-chips with 5 μm wide holes and Au pre-patterned electrodes in a four-point configuration and were then annealed under vacuum at 350°C to improve adhesion to the substrate. Lastly, custom electrical contacts were made from the pre-patterned electrodes to the top and bottom graphite sheets using e-beam lithography followed by reactive ion etching and thermal evaporation of Cr/Au (2 nm/100 nm).

A list of all samples used in this study is displayed in Table 4.1. The hBN thicknesses shown were measured using atomic force microscopy and the graphite thicknesses were determined by optical contrast. The WSe_2 thickness was approximated using the bulk lattice constant of 2H-WSe_2 obtained from HQ Graphene. We note that Device 2 had hBN only on the top but shows similar behavior to the other devices which have hBN on both sides of the WSe_2. Device 3 contained trilayer and bilayer WSe_2 regions, as indicated by the two values provided for the WSe_2 thickness. These thickness values were used to calculate the electric field (E) generated across the WSe_2 at a given applied voltage, V, as shown in Equation 4.1[199]. Here, d and ϵ represent the total thickness and relative permittivity, respectively, of hBN and WSe_2 in each device ($\epsilon_{hBN} = 3.76, \epsilon_{WSe_2} = 7.7$)[228]:

$$E = \frac{V}{\frac{\epsilon_{WSe_2}}{\epsilon_{hBN}} d_{hBN} + d_{WSe_2}} \tag{4.3}$$

Table 4.1: List of trilayer WSe_2 devices.

Device	**Appearance in text**	**top Gr (layers)**	**bottom Gr (layers)**	**top hBN (nm)**	**bottom hBN (nm)**	**WSe_2 (nm)**
1	TBL with $\theta = 0.03°$ in Fig. 4.19b	2	2	4.8	3.0	1.3
2	Fig. 4.4c, 4.5, 4.6(c,d), 4.7c, 4.8, 4.9, 4.17(a,c,e)	3	2	7.3	–	1.9
3	Fig. 4.11–14, 4.17(b,d,f), 4.18	5	2	4.0	10.6	1.9
4	Fig. 4.4d, 4.6(e,f), 4.7d, 4.19–21	3	4	12.4	5.6	1.9/1.3

4.8.2 Electron microscopy imaging

Electron microscopy was performed at the National Center for Electron Microscopy in the Molecular Foundry at Lawrence Berkeley National Laboratory. Dark-field TEM images were collected using a Gatan UltraScan 1000 camera on a Thermo Fisher Scientific Titan-class microscope operated at 60 kV. Three frames each with an acquisition time of 5 s were summed to produce each dark-field image. A bias voltage was applied between top and bottom graphite electrodes of each device during imaging using a Protochips Aduro double-tilt biasing holder connected to a Keithley 2650 sourcemeter. Selected area electron diffraction patterns were collected on the same microscope at 60 kV using a Gatan Orius 830 camera, summing 16 frames with an exposure time of 0.1 s each.

4D-STEM datasets were acquired using a Gatan K3 direct detection camera located at the end of a Gatan Continuum imaging filter on a TEAM I microscope (aberration-corrected Thermo Fisher Scientific Titan 80–300). The microscope was operated in energy-filtered STEM mode at 80 kV with a 10 eV energy filter centeredd around the zero-loss peak (to reduce background from inelastic scattering), an indicated convergence angle of 1.71 mrad, and a beam current of 40–50 pA. These conditions yield an effective probe size of 1.25 nm (full-width at half-maximum value). Diffraction patterns were collected using a step size of 2 nm with 200 x 200 beam positions, covering an area of 400 nm x 400 nm. The K3 camera was used in full-frame

electron counting mode with a binning of 4 × 4 pixels in each diffraction pattern and an energy-filtered STEM camera length of 800 mm. Diffraction patterns were acquired with an exposure time of 13 ms per pattern, which is the sum of multiple counted frames.[175]

4.8.3 4D-STEM Data Analysis

Analysis of 4D-STEM data was performed using the pyInterferometry[186] framework on a personal computer. This analysis incorporated published modules[165] for Bragg disk detection and integration to yield virtual dark-field images. Multislice simulations were carried out using the ABTEM[204] software package with an acceleration energy of 80 keV, convergence semi-angle cutoff of 4.0 mrad, a rolloff of 0.5, and a potential sampling of 0.2Å. The infinite projection scheme was used for all calculations. The trilayer stacking sequences used in the mutlisice simulations are defined in Table 4.2.

Table 4.2: Translational offsets between vertically stacked lattices in various trilayer stacking sequences, as defined for multislice simulations. Values are provided in Cartesian coordinates, where a_0 is the lattice constant for WSe_2 and the x- and y- axes are along the zigzag and armchair directions of the hexagonal lattice, respectively.

Stacking Order (3-2-1)	**Offset 1 ([x , y])**	**Offset 2 ([x , y])**
AAA	Layers 1 , 2 = [0 , 0]	Layers 1 , 3 = [0 , 0]
ASPA	Layers 1 , 2 = $[a_0/2$, 0]	Layers 1 , 3 = [0 , 0]
ASP*A	Layers 1 , 2 = [0 , $a_0(2\sqrt{3})^{-1}$]	Layers 1 , 3 = [0 , 0]
ABB (BAA)	Layers 1 , 2 = [0 , 0]	Layers 2 , 3 = [0 , $a_0/\sqrt{3}$]
ABA (BAB)	Layers 1 , 2 = [0 , $-a_0/\sqrt{3}$]	Layers 2 , 3 = [0 , $-a_0/\sqrt{3}$]
ABC (CBA)	Layers 1 , 2 = [0 , $a_0/\sqrt{3}$]	Layers 2 , 3 = [0 , $-a_0/\sqrt{3}$]
SPAB	Layers 1 , 2 = [0 , $a_0/\sqrt{3}$]	Layers 2 , 3 = $[a_0/2$, 0]
SP*AB	Layers 1 , 2 = [0 , $a_0/\sqrt{3}$]	Layers 2 , 3 = [0 , $a_0(2\sqrt{3})^{-1}$]

Chapter 5

Conclusions and Perspective

5.1 Summary

Bringing things full circle, one of the central aims of nanoscience, and materials science more broadly, is the controlled design of structures and their properties. A chief component in the actualization of this objective is the development of structural characterization tools that are well-suited for a particular system of interest. The nascent field of moiré engineering, or twistronics, has frequently operated as a black box thus far, where the properties of functional devices are measured and interpreted based on assumptions about their nano- to microscale structure. While these studies have generated an impressive body of literature, the fact that the emergent properties of moiré systems are so sensitive to structural perturbations that may or may not be withing user control means that substantial advancement of the field hinges on efforts toward correlative structure–property measurements within a given device. These types of experiments will also enable deeper understanding of how both structure and property can be systematically tuned through external factors, such as an applied strain or electric field.

In this vein, the portfolio of work presented in this dissertation demonstrates how diffraction-based TEM and STEM can be used to paint valuable nanoscale pictures of both spontaneous and stimulus-driven structural deformations in moiré materials that can then enhance our interpretation of their emergent properties. Chapters 2 and 3 focused on the development of a new imaging framework, Bragg interferometry, using a well-established tool, 4D-STEM, for mapping structure, strain, and disorder in moiré materials. The results revealed a two-regime model for lattice reconstruction in twisted bilayer graphene that, coupled with electronic structure calculations, explains the suppression of flat bands in reconstructed TBL-Gr with smaller twist angles $< 0.5°$ but not larger twist angles of 0.5–2°, a range that includes the largest predicted magic angle at 1.05° (Chapter 2). Distinct reconstruction mechanisms, one driven by local rotations and one by local dilations, were also uncovered when ap-

plying Bragg interferometry to twisted bilayer and heterobilayer TMD-based moirés, respectively, validating proposed theoretical models (Chapter 3). The amenability of Bragg interferometry to different heterostructure geometries enabled further measurement of how encapsulation layers affect in-plane and out-of-plane reconstruction in heterobilayers, showing that hBN encapsulation not only suppresses out-of-plane reconstruction but also increases in-plane reconstruction and overall structural order (Chapter 3). Studies on both twisted bilayer graphene and twisted bilayer MoS_2 also illustrated the interplay between intrinsic reconstruction strain fields and heterostrain, showing how heterostrain redistributes reconstruction strain. This relationship could contribute to the generation of anisotropic electronic features in twisted bilayer graphene and may guide efforts to modulate the moiré potential experienced by moiré excitons in TMD-based systems.

Chapter 4 extended the use of Bragg interferometry to the study of functional moiré-based devices for the first time, revealing twist and strain-tunable spatial arrangements of polar domains in twisted WSe_2 trilayers. Building on this insight, the fast acquisition speed, large field of view, and relatively high spatial resolution afforded by DF-TEM enabled observation of the structural responses of the twisted trilayers during application of an electric field. Simultaneous imaging of the moiré structure and approximation of net polarization unveiled a rich array of structure-dependent polarization switching dynamics, underscoring the versatility of multilayer moiré structures for use as atomically thin ferroelectric components and providing a clear example of the value of correlative measurements. Going forward, the work presented here can inspire efforts in a number of areas that are currently at the forefront of twistronics, a sampling of which are highlighted below to conclude.

5.2 Outlook

5.2.1 Ferroelectrics

While, at this time, the concept of moiré-tunable interfacial polarization switching has only been explored in vdW materials with hexagonal lattices[194,195,197,199], such as H-phase WSe_2 (Chapter 4), a growing number of vdW compounds with other symmetries can also possess a spontaneous, switchable interfacial polarization[216,229]. The T_d-phase group VI TMDs, namely T_d-WTe_2 and T_d-$MoTe_2$, are one such group of materials that could be readily studied using the methods discussed in this dissertation. Both of these compounds have a distorted octahedral structure that yields an orthorhombic rather than hexagonal atomic unit cell and are semimetals in the atomic limit rather than semiconductors, distinguishing them from the TMDs studied in Chapters 3 and 4. Uniquely, despite their metallicity, both T_d-WTe_2 and T_d-$MoTe_2$ retain an out-of-plane polarization at atomic thicknesses and behave as sliding/interfacial ferroelectrics down to the bilayer limit[222,223,230,231]. In fact, coupled

ferroelectric and superconducting transitions have even been reported in natural bilayer T_d-$MoTe_2$. In this system, the spontaneous interfacial polarization of the $MoTe_2$ generates an internal electric field that can drive a superconducting transition at low temperatures; the superconducting state can then be controllably turned on and off by switching the polarization direction with an applied electric field[231]. Very little is known about the intrinsic structures of of small-angle twisted bilayer[232] or trilayer T_d TMDs or their polarization switching dynamics; however, a combination of Bragg interferometry and DF-TEM could provide insight into how moirés built from these non-hexagonal materials reconstruct as well as how these systems switch between polarization states in comparison to the untwisted counterparts. Further, the ability to perform these structural measurements in tandem with transport measurements may reveal how moiré engineering affects the electronic phases of these materials, such as the intriguing field-driven superconductivity observed in $MoTe_2$. The T_d-phase transition metal ditellurides are also highly air sensitive[231–233] and require full encapsulation with other air stable vdW materials for typical measurements, making them great candidates for imaging with diffraction-based methods.

Recently, the idea of using interfacial twisting to control polar order has even been extended to thin films of conventional ferroelectrics materials, namely perovskite oxides. Barium titanate ($BaTiO_3$) is a well-studied perovskite oxide compound that has an intrinsic, switchable polarization at room temperature arising from displacement of the Ti^{4+} ions away from the center of the atomic unit cell[234]. Although $BaTiO_3$ is an ionic compound rather a layered vdW material, in 2024 Sánchez-Santolino et al. demonstrated that thin films of this material could be epitaxially grown and then re-stacked with a controlled interlayer twist to form moiré heterostructures[235]. Notably, using depth-sectioning atomic resolution high-angle annular dark-field (HAADF) STEM they observed that sufficiently thin layers (8–15 nm thick) could stabilize a unique polarization pattern consisting of alternating clockwise and anti-clockwise vortices and anti-vortices resulting from twist-induced, periodic intralayer shear strain gradients in the $BaTiO_3$ slabs. In particular, clockwise and anti-clockwise polarization vortices were observed in sites with minimal shear strain (AA- and AB-type sites), while antivortices were observed in soliton-type sites where there is a concentration of shear strain, suggesting a flexoelectric coupling[235]. While this work focused on moiré heterostructures with relatively large twist angles (3–50°) where lattice reconstruction is relatively weak, it would be very interesting to examine how twisted $BaTiO_3$ relaxes at smaller angles and how this enhanced reconstruction affects polar order. Intuitively, one could posit that the substantial geometric changes in stacking domain shapes and shear strain patterns that accompany strengthening reconstruction in the small-twist regime could have pronounced effects on the observed polarization texture. It is also unclear whether polarization (anti)vortices will persist, or perhaps even be stabilized further, as thickness of the twisted $BaTiO_3$ slabs is reduced to the limit of two atomic unit cells (a bilayer), and how these vortices will respond to an applied field. Bragg interferometry could again be applied to

explore these questions, particularly if coupled with ongoing efforts to use 4D-STEM for polarization mapping[236] and developments in multislice methods for mapping the structure of thicker samples[237].

5.2.2 Optoelectronic and photonic materials

As mentioned in Chapters 1 and 3, semiconducting TMD-based moirés have been very actively studied for their unique optical properties over the past several years[97,104]. During this time, the importance of being able to spatially correlate the moiré structure with local optoelectronic features has been recognized. For example, Andersen et al. used channeling modulated secondary electron imaging in a scanning electron microscope (SEM) to map the structure of reconstructed twisted bilayer WSe_2 and directly connected the spatial moiré-scale inhomogeneity to variations in excitonic features observed in photoluminescence measurements[238]. Since this method of imaging is SEM-based, it is limited in its spatial resolution compared to (S)TEM-based imaging. Bragg interferometry could be used for similar types of correlative measurements but with higher spatial resolution and with additional information about local strain, which also has important effects on emergent optoelectronic behavior. Additionally, interesting gate-tunable excitonic features have been observed in moiré bilayer systems[169]. The variety of structural responses we observed in twisted WSe_2 trilayers during polarization switching (Chapter 4) then raises questions about how different spatial organizations of polar domains and their respective switching dynamics might imbue unique excitonic behavior in moiré trilayers and multilayers upon application of an electric field, calling for future work combining microscopy and optical measurements of these structures incorporated in gated devices.

Moving to the realm of photonics, moiré engineering is also a route for designing structures with exotic polaritonic features (light–matter interactions) that have promise for applications ranging from sub-diffraction imaging[239] to molecular sensing[240]. For example, previous studies have shown that hyperbolic phonon–polaritons (light coupled to lattice vibrations) in monolayer hBN can hybridize with surface plasmon-polaritons (light coupled to collective oscillations of electrons) in graphene when the two materials are stacked together, resulting in unique hyperbolic plasmon-phonon resonances[43,241]. Some open questions include how the local polaritonic dispersion varies spatially with local atomic stacking order in these hBN/graphene superlattices and how lattice reconstruction affects both local and global polaritonic features. Correlative structural and spectroscopic measurements using Bragg interferometry and STEM electron energy loss spectroscopy (STEM-EELS)[242] could shed light on how moiré engineering can be used to tune the hybrid polaritonic phenomena in such systems.

5.2.3 Charge density wave materials

Another set of moiré materials that could be interesting to study using Bragg interferometry are those comprised of compounds that can host charge density wave (CDW) states. CDWs are spontaneous periodic lattice distortions that occur due to innate electronic instability in a material[243]. Transition from a normal state to a CDW state is accompanied by a change in material resistance and has thus been proposed as an avenue for non-volatile phase change memory[244,245]. In addition to moiré-induced band hybridization, one may also expect lattice reconstruction and intrinsic strain in moiré superlattices to play an important role in controlling CDW behavior and transition temperatures. This idea has already received some attention both experimentally and theoretically. In 2022, Zhao et al. experimentally demonstrated using scanning tunneling microscopy that small-angle parallel-stacked $1\,T$-$TiTe_2$/$1\,T$-$TiSe_2$ heterostructures exhibit a moiré-trapped CDW state with alternating domains of a 1×1 normal state and 2×2 CDW state in the $TiTe_2$ layer[246]. They attributed both the spatial segmentation of the CDW state and the persistence of this state at room temperature (compared to a transition temperature of 92 K for an isolated $TiTe_2$ monolayer) to lattice reconstruction and local intralayer strain distributions. Recent calculations on CDW behavior in twisted structures, such as twisted bilayer $NbSe_2$[247], also suggest that variations in interlayer stacking order, the presence of reconstruction strain, the presence of a P versus AP stacking between layers, and the atomic scale CDW superstructure (for example, formation of a 2×2 versus $\sqrt{3} \times \sqrt{3}$ superlattice), should all affect the tiling of CDW domains (the commensuration network) in a moiré[247,248]. Simultaneous mapping of interlayer stacking order, reconstruction strain fields, and CDW ordering (based on superlattice peaks visible in diffraction[249,250]) using variable temperature Bragg interferometry could be very useful for more detailed exploration of the effects of lattice reconstruction on the emergence of CDW phases (and vice versa) and for investigation of how the behavior observed in $1\,T$-$TiTe_2$/$1\,T$-$TiSe_2$ translates to moirés comprised of other CDW materials and with other symmetries. Operando imaging studies of the electrical tunability[244,245,249] of CDW order in moiré devices could also be very interesting and have not yet been reported; however, the development of instrumentation to simultaneously cool and apply an electrical bias to (S)TEM samples is still in its early stages, placing some practical limitations on the feasibility of this type of experiment in the immediate future.

5.2.4 Moiré magnets

Lattice reconstruction has also been invoked as a factor influencing the emergent magnetic properties of moiré structures. So far, work in this space has primarily focused on twisted heterostructures of chromium triiodide (CrI_3), a layer-by-layer anti-ferromagnet. Studies have shown that the local magnetic texture in twisted bi-

layer CrI_3 is highly sensitive to the local twist angle as well as disorder and structural deformations[251,252]. Therefore, performing both spatially-resolved magnetic measurements, such as nitrogen-vacancy scanning magnetometry[251], and detailed structural characterization, such as Bragg interferometry, on a given set of samples would be very informative for fully understanding the measured magnetic behavior. Beyond twisted bilayers, twisted double bilayers (TDBL) of CrI_3 also exhibit unusual twist angle-dependent magnetic behavior[252,253]. In 2022, Xie et al. observed that at small angles the magnetic properties of the TDBL tended toward those of natural four-layer CrI_3, and at large angles they resembled those of two isolated bilayers. Meanwhile at intermediate twist angles they measured an anomalous net magnetization in the TDBL, which the authors propose could be driven by spin frustrations in the moiré that may destabilize the typical layered anti-ferromagnetic ordering in favor of other spin textures and magnetic ground states[253]. Xie et al. suggest that further calculations that incorporate reconstruction effects are necessary to unravel the origins of the novel magnetic behavior they observed[253]. Such calculations will undoubtedly benefit from experimental measurements of the twist angle-dependent lattice reconstruction mechanics, as demonstrated in our study of twisted bilayer graphene in Chapter 2. One challenge in analyzing the reconstruction mechanisms in these structures that consist of twisted bilayer to multilayer slabs will be distinguishing the deformations at each interface. A similar problem will be encountered when imaging the twisted $BaTiO_3$ structures mentioned earlier. Addressing this broader challenge of applying Bragg interferometry to multilayer systems or relatively thick samples will require substantial modification of the data analysis framework and potentially creative heterostructure designs, but will nevertheless be quite insightful for understanding how deformations at a twisted interface propagate vertically through the rest of a material and will greatly expand the number of problems that can be interrogated with this technique in years to come.

Last but not least, work from our group and others has recently shown how intercalation of vdW materials with magnetic ions offers a versatile route for designing 2D magnetic compounds[47]. For example, Husremović et al. reported robust ferromagnetism in iron-intercalated $2H$-Tas_2 down to the bilayer limit[254]. There have been no reports to date of a moiré magnet produced by intercalation, but design of such a structure could be achievable soon with emerging synthetic schemes[254,255]. This begs the question of how filling the interstitial space between twisted layers will affect the moiré structure and reconstruction of the host lattice. One may also wonder how the intercalant ions will order on both the atomic and moiré length scales, which will impact the coupling between them and the global magnetic behavior, and how this ordering can be tailored by adjusting the intercalant identity of stoichiometry. All of these questions are ripe for multi-modal investigations bridging Bragg interferometry with techniques for mapping elemental distributions, such as STEM energy dispersive x-ray spectroscopy (STEM-EDS) or STEM-EELS, and magnetotransport measurements.

Bibliography

1. Bayda, S., Adeel, M., Tuccinardi, T., Cordani, M. & Rizzolio, F. The history of nanoscience and nanotechnology: from chemical–physical applications to nanomedicine. *Molecules* **25,** 112 (2019).
2. Feynman, R. P. There's Plenty of Room at the Bottom. *Eng. Sci.* **23,** 22–36 (1960).
3. Jariwala, D., Sangwan, V. K., Lauhon, L. J., Marks, T. J. & Hersam, M. C. Carbon nanomaterials for electronics, optoelectronics, photovoltaics, and sensing. *Chem. Soc. Rev.* **42,** 2824–2860 (2013).
4. Shirasaki, Y., Supran, G. J., Bawendi, M. G. & Bulović, V. Emergence of colloidal quantum-dot light-emitting technologies. *Nat. Photonics* **7,** 13–23 (2013).
5. Kamyshny, A. & Magdassi, S. Conductive nanomaterials for printed electronics. *Small* **10,** 3515–3535 (2014).
6. Sun, Y., Liu, N. & Cui, Y. Promises and challenges of nanomaterials for lithium-based rechargeable batteries. *Nat. Energy* **1,** 1–12 (2016).
7. Pomerantseva, E., Bonaccorso, F., Feng, X., Cui, Y. & Gogotsi, Y. Energy storage: The future enabled by nanomaterials. *Science* **366,** eaan8285 (2019).
8. Rosi, N. L. & Mirkin, C. A. Nanostructures in biodiagnostics. *Chem. Rev.* **105,** 1547–1562 (2005).
9. Ramos, A. P., Cruz, M. A., Tovani, C. B. & Ciancaglini, P. Biomedical applications of nanotechnology. *Biophys. Rev.* **9,** 79–89 (2017).
10. Müller, E. W. & Bahadur, K. Field ionization of gases at a metal surface and the resolution of the field ion microscope. *Phys. Rev.* **102,** 624 (1956).
11. Crewe, A. V., Wall, J. & Langmore, J. Visibility of single atoms. *Science* **168,** 1338–1340 (1970).
12. Binnig, G., Rohrer, H., Gerber, C. & Weibel, E. Surface studies by scanning tunneling microscopy. *Phys. Rev. Lett.* **49,** 57 (1982).
13. Bordonaro, G. J. DUV photolithography and materials. *Encyclopedia of Nanotechnology,* 1–17 (2015).

14. Wu, B. & Kumar, A. Extreme ultraviolet lithography: A review. *JVB* **25,** 1743–1761 (2007).

15. Law, M., Goldberger, J. & Yang, P. Semiconductor nanowires and nanotubes. *Annu. Rev. Mater. Res.* **34,** 83–122 (2004).

16. Wu, Z., Yang, S. & Wu, W. Shape control of inorganic nanoparticles from solution. *Nanoscale* **8,** 1237–1259 (2016).

17. Novoselov, K. S. *et al.* Electric field effect in atomically thin carbon films. *Science* **306,** 666–669 (2004).

18. Balandin, A. A. *et al.* Superior thermal conductivity of single-layer graphene. *Nano Lett.* **8,** 902–907 (2008).

19. Lee, C., Wei, X., Kysar, J. W. & Hone, J. Measurement of the elastic properties and intrinsic strength of monolayer graphene. *Science* **321,** 385–388 (2008).

20. Chhowalla, M. *et al.* The chemistry of two-dimensional layered transition metal dichalcogenide nanosheets. *Nat. Chem.* **5,** 263–275 (2013).

21. Novoselov, K. S., Mishchenko, A., Carvalho, A. & Castro Neto, A. 2D materials and van der Waals heterostructures. *Science* **353,** aac9439 (2016).

22. Saito, Y., Nojima, T. & Iwasa, Y. Highly crystalline 2D superconductors. *Nat. Rev. Mater.* **2,** 1–18 (2016).

23. Wang, H. *et al.* High-quality monolayer superconductor $NbSe_2$ grown by chemical vapour deposition. *Nat. Commun.* **8,** 394 (2017).

24. Tsen, A. W. *et al.* Structure and control of charge density waves in two-dimensional 1T-TaS_2. *Proc. Natl. Acad. Sci.* **112,** 15054–15059 (2015).

25. Chen, Y. *et al.* Raman spectra and dimensional effect on the charge density wave transition in GdTe3. *Appl. Phys. Lett.* **115** (2019).

26. Huang, B. *et al.* Layer-dependent ferromagnetism in a van der Waals crystal down to the monolayer limit. *Nature* **546,** 270–273 (2017).

27. Gong, C. *et al.* Discovery of intrinsic ferromagnetism in two-dimensional van der Waals crystals. *Nature* **546,** 265–269 (2017).

28. Dean, C. R. *et al.* Boron nitride substrates for high-quality graphene electronics. *Nat. Nanotechnol.* **5,** 722–726 (2010).

29. Radisavljevic, B., Radenovic, A., Brivio, J., Giacometti, V. & Kis, A. Single-layer MoS_2 transistors. *Nat. Nanotechnol.* **6,** 147–150 (2011).

30. Fiori, G. *et al.* Electronics based on two-dimensional materials. *Nat. Nanotechnol.* **9,** 768–779 (2014).

31. Lin, X., Yang, W., Wang, K. L. & Zhao, W. Two-dimensional spintronics for low-power electronics. *Nat. Electron.* **2,** 274–283 (2019).

32. Chen, K.-S., Balla, I., Luu, N. S. & Hersam, M. C. Emerging opportunities for two-dimensional materials in lithium-ion batteries. *ACS Energy Lett.* **2,** 2026–2034 (2017).

33. Shifa, T. A., Wang, F., Liu, Y. & He, J. Heterostructures based on 2D materials: a versatile platform for efficient catalysis. *Adv. Mater.* **31,** 1804828 (2019).

34. Yu, Y., Van Winkle, M. & Bediako, D. K. Tuning interfacial chemistry with twistronics. *Trends in Chemistry* **4,** 857–859 (2022).

35. Anichini, C. *et al.* Chemical sensing with 2D materials. *Chem. Soc. Rev.* **47,** 4860–4908 (2018).

36. Splendiani, A. *et al.* Emerging photoluminescence in monolayer MoS_2. *Nano Lett.* **10,** 1271–1275 (2010).

37. Mak, K. F., Lee, C., Hone, J., Shan, J. & Heinz, T. F. Atomically thin MoS_2: a new direct-gap semiconductor. *Phys. Rev. Lett.* **105,** 136805 (2010).

38. Tran, V., Soklaski, R., Liang, Y. & Yang, L. Layer-controlled band gap and anisotropic excitons in few-layer black phosphorus. *Phys. Rev. B* **89,** 235319 (2014).

39. Yoshida, M. *et al.* Controlling charge-density-wave states in nano-thick crystals of 1T-TaS_2. *Sci. Rep.* **4,** 7302 (2014).

40. Xi, X. *et al.* Ising pairing in superconducting $NbSe_2$ atomic layers. *Nat. Phys.* **12,** 139–143 (2016).

41. Li, X.-L. *et al.* Layer-number dependent optical properties of 2D materials and their application for thickness determination. *Adv. Func. Mater.* **27,** 1604468 (2017).

42. Koma, A., Sunouchi, K. & Miyajima, T. Fabrication of ultrathin heterostructures with van der Waals epitaxy. *J. Vac. Sci. Technol. B* **3** (1985).

43. Brar, V. W. *et al.* Hybrid surface-phonon-plasmon polariton modes in graphene/monolayer h-BN heterostructures. *Nano Lett.* **14,** 3876–3880 (2014).

44. Bediako, D. K. *et al.* Heterointerface effects in the electrointercalation of van der Waals heterostructures. *Nature* **558,** 425–429 (2018).

45. Wang, Z. *et al.* Modulating charge density wave order in a 1T-TaS_2/Black phosphorus heterostructure. *Nano Lett.* **19,** 2840–2849 (2019).

46. Zhu, X., Li, D., Liang, X. & Lu, W. D. Ionic modulation and ionic coupling effects in MoS_2 devices for neuromorphic computing. *Nat. Mater.* **18,** 141–148 (2019).

47. Xie, L. S., Husremovic, S., Gonzalez, O., Craig, I. M. & Bediako, D. K. Structure and magnetism of iron-and chromium-intercalated niobium and tantalum disulfides. *J. Am. Chem. Soc.* **144,** 9525–9542 (2022).

48. Wu, Y., Li, D., Wu, C.-L., Hwang, H. Y. & Cui, Y. Electrostatic gating and intercalation in 2D materials. *Nat. Rev. Mater.* **8,** 41–53 (2023).

49. Li, H. *et al.* Activating and optimizing MoS_2 basal planes for hydrogen evolution through the formation of strained sulphur vacancies. *Nat. Mater.* **15,** 48–53 (2016).

50. López-Polín, G. *et al.* Increasing the elastic modulus of graphene by controlled defect creation. *Nat. Phys.* **11,** 26–31 (2015).

51. Lin, Z. *et al.* Defect engineering of two-dimensional transition metal dichalcogenides. *2D Mater.* **3,** 022002 (2016).

52. Jiang, S., Li, L., Wang, Z., Mak, K. F. & Shan, J. Controlling magnetism in 2D CrI_3 by electrostatic doping. *Nat. Nanotechnol.* **13,** 549–553 (2018).

53. Velický, M. Electrolyte versus dielectric gating of two-dimensional materials. *J. Phys. Chem. C* **125,** 21803–21809 (2021).

54. Maroo, S., Yu, Y., Taniguchi, T., Watanabe, K. & Bediako, D. K. Decoupling Effects of Electrostatic Gating on Electronic Transport and Interfacial Charge-Transfer Kinetics at Few-Layer Molybdenum Disulfide. *ACS Nanosci. Au* **3,** 204–210 (2023).

55. Li, Z. *et al.* Efficient strain modulation of 2D materials via polymer encapsulation. *Nat. Commun.* **11,** 1151 (2020).

56. Dai, Z., Liu, L. & Zhang, Z. Strain engineering of 2D materials: issues and opportunities at the interface. *Adv. Mater.* **31,** 1805417 (2019).

57. Yankowitz, M. *et al.* Emergence of superlattice Dirac points in graphene on hexagonal boron nitride. *Nat. Phys.* **8,** 382–386 (2012).

58. Kuwabara, M., Clarke, D. R. & Smith, D. Anomalous superperiodicity in scanning tunneling microscope images of graphite. *Appl. Phys. Lett.* **56,** 2396–2398 (1990).

59. Rong, Z. Y. & Kuiper, P. Electronic effects in scanning tunneling microscopy: Moiré pattern on a graphite surface. *Phys. Rev. B* **48,** 17427 (1993).

60. Pong, W.-T. & Durkan, C. A review and outlook for an anomaly of scanning tunnelling microscopy (STM): superlattices on graphite. *J. Phys. D.: Appl. Phys.* **38,** R329 (2005).

61. Land, T., Michely, T., Behm, R., Hemminger, J. & Comsa, G. STM investigation of single layer graphite structures produced on Pt (111) by hydrocarbon decomposition. *Surf. Sci.* **264,** 261–270 (1992).

62. Ritter, M., Ranke, W. & Weiss, W. Growth and structure of ultrathin FeO films on Pt (111) studied by STM and LEED. *Phys. Rev. B* **57,** 7240 (1998).

63. Berger, C. *et al.* Ultrathin epitaxial graphite: 2D electron gas properties and a route toward graphene-based nanoelectronics. *J. Phys. Chem. B* **108,** 19912–19916 (2004).

64. Biedermann, L. B., Bolen, M. L., Capano, M. A., Zemlyanov, D. & Reifenberger, R. G. Insights into few-layer epitaxial graphene growth on 4H-SiC (000 1) substrates from STM studies. *Phys. Rev. B* **79,** 125411 (2009).

65. Wallace, P. R. The band theory of graphite. *Phys. Rev.* **71,** 622 (1947).

66. Neto, A. C., Guinea, F., Peres, N. M., Novoselov, K. S. & Geim, A. K. The electronic properties of graphene. *RMP* **81,** 109 (2009).

67. Novoselov, K. S. *et al.* Two-dimensional gas of massless Dirac fermions in graphene. *Nature* **438,** 197–200 (2005).

68. Dos Santos, J. L., Peres, N. & Neto, A. C. Graphene bilayer with a twist: Electronic structure. *Phys. Rev. Lett.* **99,** 256802 (2007).

69. Trambly de Laissardière, G., Mayou, D. & Magaud, L. Localization of Dirac electrons in rotated graphene bilayers. *Nano Lett.* **10,** 804–808 (2010).

70. Fang, S. & Kaxiras, E. Electronic structure theory of weakly interacting bilayers. *Phys. Rev. B* **93,** 235153 (2016).

71. Bistritzer, R. & MacDonald, A. H. Moiré bands in twisted double-layer graphene. *Proc. Natl. Acad. Sci.* **108,** 12233–12237 (2011).

72. Morell, E. S., Correa, J., Vargas, P., Pacheco, M. & Barticevic, Z. Flat bands in slightly twisted bilayer graphene: Tight-binding calculations. *Phys. Rev. B* **82,** 121407 (2010).

73. Andrei, E. Y. & MacDonald, A. H. Graphene bilayers with a twist. *Nat. Mater.* **19,** 1265–1275 (2020).

74. Kauppila, V., Aikebaier, F. & Heikkilä, T. Flat-band superconductivity in strained Dirac materials. *Phys. Rev. B* **93,** 214505 (2016).

75. Balents, L., Dean, C. R., Efetov, D. K. & Young, A. F. Superconductivity and strong correlations in moiré flat bands. *Nat. Phys.* **16,** 725–733 (2020).

76. Hunt, B. *et al.* Massive Dirac fermions and Hofstadter butterfly in a van der Waals heterostructure. *Science* **340,** 1427–1430 (2013).

77. Cao, Y. *et al.* Unconventional superconductivity in magic-angle graphene superlattices. *Nature* **556,** 43–50 (2018).

78. Codecido, E. *et al.* Correlated insulating and superconducting states in twisted bilayer graphene below the magic angle. *Sci. Adv.* **5,** eaaw9770 (2019).

79. Cao, Y. *et al.* Correlated insulator behaviour at half-filling in magic-angle graphene superlattices. *Nature* **556,** 80–84 (2018).

80. Sharpe, A. L. *et al.* Emergent ferromagnetism near three-quarters filling in twisted bilayer graphene. *Science* **365,** 605–608 (2019).

81. Chen, G. *et al.* Evidence of a gate-tunable Mott insulator in a trilayer graphene moiré superlattice. *Nat. Phys.* **15,** 237–241 (2019).

82. Park, J. M., Cao, Y., Watanabe, K., Taniguchi, T. & Jarillo-Herrero, P. Tunable strongly coupled superconductivity in magic-angle twisted trilayer graphene. *Nature* **590,** 249–255 (2021).

83. Park, J. M. *et al.* Robust superconductivity in magic-angle multilayer graphene family. *Nat. Mater.* **21,** 877–883 (2022).

84. Kim, H. *et al.* Evidence for unconventional superconductivity in twisted trilayer graphene. *Nature* **606,** 494–500 (2022).

85. Shen, C. *et al.* Correlated states in twisted double bilayer graphene. *Nat. Phys.* **16,** 520–525 (2020).

86. Yu, Y. *et al.* Tunable angle-dependent electrochemistry at twisted bilayer graphene with moiré flat bands. *Nat. Chem.* **14,** 267–273 (2022).

87. Zhang, K. *et al.* Anomalous Interfacial Electron-Transfer Kinetics in Twisted Trilayer Graphene Caused by Layer-Specific Localization. *ACS Cent. Sci.* **9,** 1119–1128 (2023).

88. Gong, C. *et al.* Band alignment of two-dimensional transition metal dichalcogenides: Application in tunnel field effect transistors. *Appl. Phys. Lett.* **103** (2013).

89. Naik, M. H. & Jain, M. Ultraflatbands and shear solitons in moiré patterns of twisted bilayer transition metal dichalcogenides. *Phys. Rev. Lett.* **121,** 266401 (2018).

90. Venkateswarlu, S., Honecker, A. & de Laissardiere, G. T. Electronic localization in twisted bilayer MoS_2 with small rotation angle. *Phys. Rev. B* **102,** 081103 (2020).

91. Zhan, Z. *et al.* Tunability of multiple ultraflat bands and effect of spin-orbit coupling in twisted bilayer transition metal dichalcogenides. *Phys. Rev. B* **102,** 241106 (2020).

92. Naik, M. H., Kundu, S., Maity, I. & Jain, M. Origin and evolution of ultraflat bands in twisted bilayer transition metal dichalcogenides: Realization of triangular quantum dots. *Phys. Rev. B* **102,** 075413 (2020).

93. Wang, L. *et al.* Correlated electronic phases in twisted bilayer transition metal dichalcogenides. *Nat. Mater.* **19,** 861–866 (2020).

94. Zhang, Z. *et al.* Flat bands in twisted bilayer transition metal dichalcogenides. *Nat. Phys.* **16,** 1093–1096 (2020).

95. Regan, E. C. *et al.* Mott and generalized Wigner crystal states in WSe_2/WS_2 moiré superlattices. *Nature* **579,** 359–363 (2020).

96. Li, T. *et al.* Continuous Mott transition in semiconductor moiré superlattices. *Nature* **597,** 350–354 (2021).

97. Mak, K. F. & Shan, J. Semiconductor moiré materials. *Nat. Nanotechnol.* **17,** 686–696 (2022).

98. Zhang, N. *et al.* Moiré intralayer excitons in a $MoSe_2/MoS_2$ heterostructure. *Nano Lett.* **18,** 7651–7657 (2018).

99. Tran, K. *et al.* Evidence for moiré excitons in van der Waals heterostructures. *Nature* **567,** 71–75 (2019).

100. Seyler, K. L. *et al.* Signatures of moiré-trapped valley excitons in $MoSe_2/WSe_2$ heterobilayers. *Nature* **567,** 66–70 (2019).

101. Alexeev, E. M. *et al.* Resonantly hybridized excitons in moiré superlattices in van der Waals heterostructures. *Nature* **567,** 81–86 (2019).

102. Lu, Z., Carr, S., Larson, D. T. & Kaxiras, E. Lithium intercalation in MoS_2 bilayers and implications for moire flat bands. *Phys. Rev. B* **102,** 125424 (2020).

103. Zhang, L. *et al.* Van der Waals heterostructure polaritons with moiré-induced nonlinearity. *Nature* **591,** 61–65 (2021).

104. Huang, D., Choi, J., Shih, C.-K. & Li, X. Excitons in semiconductor moiré superlattices. *Nat. Nanotechnol.* **17,** 227–238 (2022).

105. Zhao, S. F. *et al.* Time-reversal symmetry breaking superconductivity between twisted cuprate superconductors. *Science* **382,** 1422–1427 (2023).

106. Yu, Y. *et al.* High-temperature superconductivity in monolayer $Bi_2Sr_2CaCu_2O_{8+\delta}$. *Nature* **575,** 156–163 (2019).

107. Xu, Y. *et al.* Coexisting ferromagnetic–antiferromagnetic state in twisted bilayer CrI_3. *Nat. Nanotechnol.* **17,** 143–147 (2022).

108. Larson, D. T., Carr, S., Tritsaris, G. A. & Kaxiras, E. Effects of lithium intercalation in twisted bilayer graphene. *Phys. Rev. B* **101,** 075407 (2020).

109. Lu, W. *et al.* Implementation of high-order variational models made easy for image processing. *Math. Methods Appl. Sci.* **39,** 4208–4233 (2016).

110. Zou, Y.-C. *et al.* Ion exchange in atomically thin clays and micas. *Nat. Mater.* **20,** 1677–1682 (2021).

111. Dai, S., Xiang, Y. & Srolovitz, D. J. Twisted bilayer graphene: Moiré with a twist. *Nano Lett.* **16,** 5923–5927 (2016).

112. Zhang, K. & Tadmor, E. B. Structural and electron diffraction scaling of twisted graphene bilayers. *J. Mech. Phys. Solids* **112,** 225–238 (2018).

113. Yoo, H. *et al.* Atomic and electronic reconstruction at the van der Waals interface in twisted bilayer graphene. *Nat. Mater.* **18,** 448–453 (2019).

114. Weston, A. *et al.* Atomic reconstruction in twisted bilayers of transition metal dichalcogenides. *Nat. Nanotechnol.* **15,** 592–597 (2020).

115. Rosenberger, M. R. *et al.* Twist angle-dependent atomic reconstruction and moiré patterns in transition metal dichalcogenide heterostructures. *ACS Nano* **14,** 4550–4558 (2020).

116. Sung, S. H. *et al.* Torsional periodic lattice distortions and diffraction of twisted 2D materials. *Nat. Commun.* **13,** 7826 (2022).

117. Li, H. *et al.* Imaging moiré flat bands in three-dimensional reconstructed WSe_2/WS_2 superlattices. *Nat. Mater.* **20,** 945–950 (2021).

118. Naik, M. H. *et al.* Intralayer charge-transfer moiré excitons in van der Waals superlattices. *Nature* **609,** 52–57 (2022).

119. Shabani, S. *et al.* Deep moiré potentials in twisted transition metal dichalcogenide bilayers. *Nat. Phys.* **17,** 720–725 (2021).

120. Li, Z. *et al.* Interlayer exciton transport in $MoSe_2$/WSe_2 heterostructures. *ACS Nano* **15,** 1539–1547 (2021).

121. Ge, C. *et al.* Observation and modulation of high-temperature Moiré-locale excitons in van der Waals heterobilayers. *ACS Nano* **17,** 16115–16122 (2023).

122. Li, E. *et al.* Lattice reconstruction induced multiple ultra-flat bands in twisted bilayer WSe_2. *Nat. Commun.* **12,** 1–7 (2021).

123. Huder, L. *et al.* Electronic spectrum of twisted graphene layers under heterostrain. *Phys. Rev. Lett.* **120,** 156405 (2018).

124. Bi, Z., Yuan, N. F. & Fu, L. Designing flat bands by strain. *Phys. Rev. B* **100,** 035448 (2019).

125. Gao, X. *et al.* Heterostrain-enabled dynamically tunable moiré superlattice in twisted bilayer graphene. *Sci. Rep.* **11,** 21402 (2021).

126. Mannaı, M. & Haddad, S. Twistronics versus straintronics in twisted bilayers of graphene and transition metal dichalcogenides. *Phys. Rev. B* **103,** L201112 (2021).

127. Cosma, D. A., Wallbank, J. R., Cheianov, V. & Fal'Ko, V. I. Moiré pattern as a magnifying glass for strain and dislocations in van der Waals heterostructures. *Faraday Discuss.* **173,** 137–143 (2014).

128. Bai, Y. *et al.* Excitons in strain-induced one-dimensional moiré potentials at transition metal dichalcogenide heterojunctions. *Nat. Mater.* **19,** 1068–1073 (2020).

129. Zheng, H., Zhai, D. & Yao, W. Twist versus heterostrain control of optical properties of moiré exciton minibands. *2D Mater.* **8,** 044016 (2021).

130. Lau, C. N., Bockrath, M. W., Mak, K. F. & Zhang, F. Reproducibility in the fabrication and physics of moiré materials. *Nature* **602,** 41–50 (2022).

131. Uri, A. *et al.* Mapping the twist-angle disorder and Landau levels in magic-angle graphene. *Nature* **581,** 47–52 (2020).

132. Wang, W. *et al.* Clean assembly of van der Waals heterostructures using silicon nitride membranes. *Nat. Electron.* **6,** 981–990 (2023).

133. Kapfer, M. *et al.* Programming twist angle and strain profiles in 2D materials. *Science* **381,** 677–681 (2023).

134. McGilly, L. J. *et al.* Visualization of moiré superlattices. *Nat. Nanotechnol.* **15,** 580–584 (2020).

135. Ophus, C. Four-dimensional scanning transmission electron microscopy (4D-STEM): From scanning nanodiffraction to ptychography and beyond. *Microsc. Microanal.* **25,** 563–582 (2019).

136. Yankowitz, M., Ma, Q., Jarillo-Herrero, P. & LeRoy, B. J. van der Waals heterostructures combining graphene and hexagonal boron nitride. *Nat. Rev. Phys.* **1,** 112–125 (2019).

137. Yankowitz, M. *et al.* Tuning superconductivity in twisted bilayer graphene. *Science* **363,** 1059–1064 (2019).

138. Lu, X. *et al.* Superconductors, orbital magnets and correlated states in magic-angle bilayer graphene. *Nature* **574,** 653–657 (2019).

139. Jin, C. *et al.* Observation of moiré excitons in WSe_2/WS_2 heterostructure superlattices. *Nature* **567,** 76–80 (2019).

140. Woods, C. *et al.* Commensurate–incommensurate transition in graphene on hexagonal boron nitride. *Nat. Phys.* **10,** 451–456 (2014).

141. Van Wijk, M., Schuring, A., Katsnelson, M. & Fasolino, A. Relaxation of moiré patterns for slightly misaligned identical lattices: graphene on graphite. *2D Mater.* **2,** 034010 (2015).

142. Jain, S. K., Juričić, V. & Barkema, G. T. Structure of twisted and buckled bilayer graphene. *2D Mater.* **4,** 015018 (2016).

143. Nam, N. N. & Koshino, M. Lattice relaxation and energy band modulation in twisted bilayer graphene. *Phys. Rev. B* **96,** 075311 (2017).

144. Alden, J. S. *et al.* Strain solitons and topological defects in bilayer graphene. *Proc. Natl. Acad. Sci.* **110,** 11256–11260 (2013).

145. Wilson, J. H., Fu, Y., Sarma, S. D. & Pixley, J. Disorder in twisted bilayer graphene. *Phys. Rev. Res.* **2,** 023325 (2020).

146. Kerelsky, A. *et al.* Maximized electron interactions at the magic angle in twisted bilayer graphene. *Nature* **572,** 95–100 (2019).

147. Han, Y. *et al.* Strain mapping of two-dimensional heterostructures with subpicometer precision. *Nano Lett.* **18,** 3746–3751 (2018).

148. Yang, H. *et al. 4D STEM: High efficiency phase contrast imaging using a fast pixelated detector* in *J. Phys. Conf. Ser.* **644** (2015), 012032.

149. Jiang, Y. *et al.* Electron ptychography of 2D materials to deep sub-ångström resolution. *Nature* **559,** 343–349 (2018).

150. Yang, N. *et al.* Nanoscale characterization of crystalline and amorphous phases in silicon oxycarbide ceramics using 4D-STEM. *Mater. Charact.* **181,** 111512 (2021).

151. Panova, O. *et al.* Diffraction imaging of nanocrystalline structures in organic semiconductor molecular thin films. *Nat. Mater.* **18,** 860–865 (2019).

152. Ozdol, V. *et al.* Strain mapping at nanometer resolution using advanced nanobeam electron diffraction. *Appl. Phys. Lett.* **106** (2015).

153. Zeltmann, S. E. *et al.* Patterned probes for high precision 4D-STEM bragg measurements. *Ultramicroscopy* **209,** 112890 (2020).

154. Kulesa, A., Krzywinski, M., Blainey, P. & Altman, N. Sampling distributions and the bootstrap: the bootstrap can be used to assess uncertainty of sample estimates. *Nat. Methods* **12,** 477 (2015).

155. Kelly, P. *Solid Mechanics Lecture Notes* (University of Auckland, 2013).

156. McGinty, B. *Continuum Mechanics* `https://continuummechanics.org`. 2012.

157. Butz, B. *et al.* Dislocations in bilayer graphene. *Nature* **505,** 533–537 (2014).

158. Carr, S., Fang, S., Zhu, Z. & Kaxiras, E. Exact continuum model for low-energy electronic states of twisted bilayer graphene. *Phys. Rev. Res.* **1,** 013001 (2019).

159. Guinea, F. & Walet, N. R. Continuum models for twisted bilayer graphene: Effect of lattice deformation and hopping parameters. *Phys. Rev. B* **99,** 205134 (2019).

160. Latychevskaia, T. *et al.* Holographic reconstruction of the interlayer distance of bilayer two-dimensional crystal samples from their convergent beam electron diffraction patterns. *Ultramicroscopy* **219,** 113020 (2020).

161. Zachman, M. J. *et al.* Interferometric 4D-STEM for lattice distortion and interlayer spacing measurements of bilayer and trilayer 2D materials. *Small* **17,** 2100388 (2021).

162. Kim, K. *et al.* van der Waals heterostructures with high accuracy rotational alignment. *Nano Lett.* **16,** 1989–1995 (2016).

163. Cao, Y. *et al.* Superlattice-induced insulating states and valley-protected orbits in twisted bilayer graphene. *Phys. Rev. Lett.* **117,** 116804 (2016).

164. Duan, J. *et al.* An edge-weighted second order variational model for image decomposition. *Digit. Signal Process.* **49,** 162–181 (2016).

165. Savitzky, B. H. *et al.* py4DSTEM: A software package for four-dimensional scanning transmission electron microscopy data analysis. *Microsc. Microanal.* **27,** 712–743 (2021).

166. Kazmierczak, N. *Strain fields in twisted bilayer graphene* 2021. `https://github.com/bediakolab/StrainFieldsInTwistedBilayerGraphene`.

167. Susarla, S. *et al.* Hyperspectral imaging of exciton confinement within a moiré unit cell with a subnanometer electron probe. *Science* **378,** 1235–1239 (2022).

168. Liu, E. *et al.* Signatures of moiré trions in $WSe_2/MoSe_2$ heterobilayers. *Nature* **594,** 46–50 (2021).

169. Dandu, M. *et al.* Electrically Tunable Localized versus Delocalized Intralayer Moiré Excitons and Trions in a Twisted MoS_2 Bilayer. *ACS Nano* **16,** 8983–8992 (2022).

170. Tang, Y. *et al.* Simulation of Hubbard model physics in WSe_2/WS_2 moiré superlattices. *Nature* **579,** 353–358 (2020).

171. Xu, Y. *et al.* Correlated insulating states at fractional fillings of moiré superlattices. *Nature* **587,** 214–218 (2020).

172. Li, H. *et al.* Imaging two-dimensional generalized Wigner crystals. *Nature* **597,** 650–654 (2021).

173. Huang, X. *et al.* Correlated insulating states at fractional fillings of the WS_2/WSe_2 moiré lattice. *Nat. Phys.* **17,** 715–719 (2021).

174. Xu, Y. *et al.* A tunable bilayer Hubbard model in twisted WSe_2. *Nat. Nanotechnol.* **17,** 934–939 (2022).

175. Kazmierczak, N. P. *et al.* Strain fields in twisted bilayer graphene. *Nat. Mater.* **20,** 956–963 (2021).

176. Enaldiev, V., Zólyomi, V., Yelgel, C., Magorrian, S. & Fal'ko, V. Stacking domains and dislocation networks in marginally twisted bilayers of transition metal dichalcogenides. *Phys. Rev. Lett.* **124,** 206101 (2020).

177. Ferreira, F., Magorrian, S., Enaldiev, V., Ruiz-Tijerina, D. & Fal'ko, V. Band energy landscapes in twisted homobilayers of transition metal dichalcogenides. *Appl. Phys. Lett.* **118,** 241602 (2021).

178. Maragkakis, G. M. *et al.* Imaging the crystal orientation of 2D transition metal dichalcogenides using polarization-resolved second-harmonic generation. *Opto-Electron. Adv.* **2,** 190026–1 (2019).

179. Slaughter, W. S. in *The Linearized Theory of Elasticity* 97–155 (Birkhäuser, Boston, MA, 2002).

180. Carr, S. *et al.* Relaxation and domain formation in incommensurate two-dimensional heterostructures. *Phys. Rev. B* **98,** 224102 (2018).

181. Zhang, C. *et al.* Interlayer couplings, Moiré patterns, and 2D electronic superlattices in MoS_2/WSe_2 hetero-bilayers. *Sci. Adv.* **3,** e1601459 (2017).

182. Van der Walt, S. *et al.* scikit-image: image processing in Python. *PeerJ* **2,** e453 (2014).

183. Hedengren, J. D., Shishavan, R. A., Powell, K. M. & Edgar, T. F. Nonlinear modeling, estimation and predictive control in APMonitor. *Comput. Chem. Eng.* **70,** 133–148 (2014).

184. Beal, L., Hill, D., Martin, R. & Hedengren, J. GEKKO Optimization Suite. *Processes* **6,** 106 (2018).

185. Virtanen, P. *et al.* SciPy 1.0: fundamental algorithms for scientific computing in Python. *Nat. Methods* **17,** 261–272 (2020).

186. Craig, I. M. *pyInterferometry* 2023. `https://github.com/bediakolab/pyInterferometry`.

187. Haertling, G. H. Ferroelectric ceramics: history and technology. *J. Am. Ceram.* **82,** 797–818 (1999).

188. Mikolajick, T., Schroeder, U. & Slesazeck, S. The past, the present, and the future of ferroelectric memories. *IEEE Trans. Electron Devices* **67,** 1434–1443 (2020).

189. Li, L. & Wu, M. Binary compound bilayer and multilayer with vertical polarizations: two-dimensional ferroelectrics, multiferroics, and nanogenerators. *ACS Nano* **11,** 6382–6388 (2017).

190. Yasuda, K., Wang, X., Watanabe, K., Taniguchi, T. & Jarillo-Herrero, P. Stacking-engineered ferroelectricity in bilayer boron nitride. *Science* **372,** 1458–1462 (2021).

191. Vizner Stern, M. *et al.* Interfacial ferroelectricity by van der Waals sliding. *Science* **372,** 1462–1466 (2021).

192. Ferreira, F., Enaldiev, V. & Fal'ko, V. Scaleability of dielectric susceptibility ϵ_{zz} with the number of layers and additivity of ferroelectric polarization in van der Waals semiconductors. *Phys. Rev. B* **106,** 125408 (2022).

193. Ferreira, F., Enaldiev, V. V., Fal'ko, V. I. & Magorrian, S. J. Weak ferroelectric charge transfer in layer-asymmetric bilayers of 2D semiconductors. *Sci. Rep.* **11,** 13422 (2021).

194. Wang, X. *et al.* Interfacial ferroelectricity in rhombohedral-stacked bilayer transition metal dichalcogenides. *Nat. Nanotechnol.* **17,** 367–371 (2022).

195. Weston, A. *et al.* Interfacial ferroelectricity in marginally twisted 2D semiconductors. *Nat. Nanotechnol.* **17,** 390–395 (2022).

196. Rogée, L. *et al.* Ferroelectricity in untwisted heterobilayers of transition metal dichalcogenides. *Science* **376,** 973–978 (2022).

197. Deb, S. *et al.* Cumulative polarization in conductive interfacial ferroelectrics. *Nature* **612,** 465–469 (2022).

198. Meng, P. *et al.* Sliding induced multiple polarization states in two-dimensional ferroelectrics. *Nat. Commun.* **13,** 7696 (2022).

199. Ko, K. *et al.* Operando electron microscopy investigation of polar domain dynamics in twisted van der Waals homobilayers. *Nat. Mater.* **22,** 992–998 (2023).

200. Craig, I. M. *et al.* Local atomic stacking and symmetry in twisted graphene trilayers. *Nat. Mater.* **23,** 323–330 (2024).

201. Huang, P. Y. *et al.* Grains and grain boundaries in single-layer graphene atomic patchwork quilts. *Nature* **469,** 389–392 (2011).

202. Sung, S. H., Schnitzer, N., Brown, L., Park, J. & Hovden, R. Stacking, strain, and twist in 2D materials quantified by 3D electron diffraction. *Phys. Rev. Mater.* **3,** 064003 (2019).

203. Van Winkle, M. *et al.* Rotational and dilational reconstruction in transition metal dichalcogenide moiré bilayers. *Nat. Commun.* **14,** 2989 (2023).

204. Madsen, J. & Susi, T. The abTEM code: transmission electron microscopy from first principles. *ORE* **1,** 13015 (2021).

205. Enaldiev, V. V., Ferreira, F. & Fal'ko, V. I. A scalable network model for electrically tunable ferroelectric domain structure in twistronic bilayers of two-dimensional semiconductors. *Nano. Lett.* **22,** 1534–1540 (2022).

206. Engelke, R. *et al.* Topological Nature of dislocation networks in two-dimensional moiré materials. *Phys. Rev. B* **107,** 125413 (2023).

207. Edelberg, D., Kumar, H., Shenoy, V., Ochoa, H. & Pasupathy, A. N. Tunable strain soliton networks confine electrons in van der Waals materials. *Nat. Phys.* **16,** 1097–1102 (2020).

208. Molino, L. *et al.* Ferroelectric switching at symmetry-broken interfaces by local control of dislocation networks. *Adv. Mater.* **35,** 2207816 (2023).

209. Johnson, M., Bloemen, P., Den Broeder, F. & De Vries, J. Magnetic anisotropy in metallic multilayers. *Rep. Prog. Phys.* **59,** 1409 (1996).

210. Paes, V. Z. & Mosca, D. H. Effective elastic and magnetoelastic anisotropies for thin films with hexagonal and cubic crystal structures. *J.Magn. Magn. Mater.* **330,** 81–87 (2013).

211. Zhang, H., Fu, Z., Legut, D., Germann, T. C. & Zhang, R. Stacking stability and sliding mechanism in weakly bonded 2D transition metal carbides by van der Waals force. *RSC Adv.* **7,** 55912–55919 (2017).

212. Geisenhof, F. R. *et al.* Anisotropic strain-induced soliton movement changes stacking order and band structure of graphene multilayers: implications for charge transport. *ACS Appl. Nano Mater.* **2,** 6067–6075 (2019).

213. Lee, D. *et al.* Giant flexoelectric effect in ferroelectric epitaxial thin films. *Phys. Rev. Lett.* **107,** 057602 (2011).

214. Jeon, B. C. *et al.* Flexoelectric effect in the reversal of self-polarization and associated changes in the electronic functional properties of $BiFeO_3$ thin films. *Adv. Mater.* **25,** 5643–5649 (2013).

215. Hou, W. *et al.* Nonvolatile ferroelastic strain from flexoelectric internal bias engineering. *Phys. Rev. Appl.* **17,** 024013 (2022).

216. Wu, M. Two-dimensional van der Waals ferroelectrics: Scientific and technological opportunities. *ACS Nano* **15,** 9229–9237 (2021).

217. Wang, C., You, L., Cobden, D. & Wang, J. Towards two-dimensional van der Waals ferroelectrics. *Nat. Mater.,* 1–11 (2023).

218. Chang, K. *et al.* Discovery of robust in-plane ferroelectricity in atomic-thick SnTe. *Science* **353,** 274–278 (2016).

219. Liu, F. *et al.* Room-temperature ferroelectricity in $CuInP_2S_6$ ultrathin flakes. *Nat. Commun.* **7,** 1–6 (2016).

220. Ding, W. *et al.* Prediction of intrinsic two-dimensional ferroelectrics in In_2Se_3 and other III2-VI3 van der Waals materials. *Nat. Commun.* **8,** 14956 (2017).

221. Cui, C. *et al.* Intercorrelated in-plane and out-of-plane ferroelectricity in ultrathin two-dimensional layered semiconductor In_2Se_3. *Nano. Lett.* **18,** 1253–1258 (2018).

222. Fei, Z. *et al.* Ferroelectric switching of a two-dimensional metal. *Nature* **560,** 336–339 (2018).

223. Yuan, S. *et al.* Room-temperature ferroelectricity in $MoTe_2$ down to the atomic monolayer limit. *Nat. Commun.* **10,** 1775 (2019).

224. Higashitarumizu, N. *et al.* Purely in-plane ferroelectricity in monolayer SnS at room temperature. *Nat. Commun.* **11,** 2428 (2020).

225. Huang, W. *et al.* Gate-coupling-enabled robust hysteresis for nonvolatile memory and programmable rectifier in van der Waals ferroelectric heterojunctions. *Adv. Mater.* **32,** 1908040 (2020).

226. Gong, C., Kim, E. M., Wang, Y., Lee, G. & Zhang, X. Multiferroicity in atomic van der Waals heterostructures. *Nat. Commun.* **10,** 2657 (2019).

227. Dou, K., Du, W., Dai, Y., Huang, B. & Ma, Y. Two-dimensional magnetoelectric multiferroics in a $MnSTe/In_2Se_3$ heterobilayer with ferroelectrically controllable skyrmions. *Phys. Rev. B* **105,** 205427 (2022).

228. Laturia, A., Van de Put, M. L. & Vandenberghe, W. G. Dielectric properties of hexagonal boron nitride and transition metal dichalcogenides: from monolayer to bulk. *npj 2D Mater. Appl.* **2,** 6 (2018).

229. Wu, M. & Li, J. Sliding ferroelectricity in 2D van der Waals materials: Related physics and future opportunities. *Proc. Natl. Acad. Sci.* **118,** e2115703118 (2021).

230. De la Barrera, S. C. *et al.* Direct measurement of ferroelectric polarization in a tunable semimetal. *Nature Commun.* **12,** 5298 (2021).

231. Jindal, A. *et al.* Coupled ferroelectricity and superconductivity in bilayer T_d-$MoTe_2$. *Nature* **613,** 48–52 (2023).

232. Yuan, F. *et al.* Atomic resolution imaging of highly air-sensitive monolayer and twisted-bilayer WTe_2. *Nano Lett.* **23,** 6868–6874 (2023).

233. Ye, F. *et al.* Environmental instability and degradation of single-and few-layer WTe_2 nanosheets in ambient conditions. *Small* **12,** 5802–5808 (2016).

234. Megaw, H. D. Origin of ferroelectricity in barium titanate and other perovskite-type crystals. *Acta Crystallogr.* **5,** 739–749 (1952).

235. Sánchez-Santolino, G. *et al.* A 2D ferroelectric vortex pattern in twisted $BaTiO_3$ freestanding layers. *Nature* **626,** 529–534 (2024).

236. Shao, Y.-T. *et al.* Emergent chirality in a polar meron to skyrmion phase transition. *Nat. Commun.* **14,** 1355 (2023).

237. Chen, Z. *et al.* Electron ptychography achieves atomic-resolution limits set by lattice vibrations. *Science* **372,** 826–831 (2021).

238. Andersen, T. I. *et al.* Excitons in a reconstructed moiré potential in twisted WSe_2 /WSe_2 homobilayers. *Nat. Mater.* **20,** 480–487 (2021).

239. Dai, S. *et al.* Subdiffractional focusing and guiding of polaritonic rays in a natural hyperbolic material. *Nat. Commun.* **6,** 6963 (2015).

240. Rodrigo, D. *et al.* Mid-infrared plasmonic biosensing with graphene. *Science* **349,** 165–168 (2015).

241. Dai, S. *et al.* Graphene on hexagonal boron nitride as a tunable hyperbolic metamaterial. *Nat. Nanotechnol.* **10,** 682–686 (2015).

242. Konečná, A., Li, J., Edgar, J. H., García de Abajo, F. J. & Hachtel, J. A. Revealing nanoscale confinement effects on hyperbolic phonon polaritons with an electron beam. *Small* **17,** 2103404 (2021).

243. Zhu, X., Cao, Y., Zhang, J., Plummer, E. & Guo, J. Classification of charge density waves based on their nature. *Proc. Natl. Acad. Sci.* **112,** 2367–2371 (2015).

244. Yoshida, M., Suzuki, R., Zhang, Y., Nakano, M. & Iwasa, Y. Memristive phase switching in two-dimensional 1T-TaS_2 crystals. *Sci. Adv.* **1,** e1500606 (2015).

245. Vaskivskyi, I. *et al.* Fast electronic resistance switching involving hidden charge density wave states. *Nat. Commun.* **7,** 11442 (2016).

246. Zhao, W.-M. *et al.* Moiré enhanced charge density wave state in twisted 1T-$TiTe_2$/ 1T-$TiSe_2$ heterostructures. *Nat. Mater.* **21,** 284–289 (2022).

247. McHugh, J. G., Enaldiev, V. V. & Fal'ko, V. I. Moiré superstructures in marginally twisted $NbSe_2$ bilayers. *Phys. Rev. B* **108,** 224111 (2023).

248. Goodwin, Z. A. & Fal'ko, V. I. Moiré modulation of charge density waves. *J. Condens. Matter Phys.* **34,** 494001 (2022).

249. Zong, A. *et al.* Ultrafast manipulation of mirror domain walls in a charge density wave. *Sci. Adv.* **4,** eaau5501 (2018).

250. Husremović, S. *et al.* Encoding multistate charge order and chirality in endotaxial heterostructures. *Nat. Commun.* **14,** 6031 (2023).

251. Song, T. *et al.* Direct visualization of magnetic domains and moiré magnetism in twisted 2D magnets. *Science* **374,** 1140–1144 (2021).

252. Cheng, G. *et al.* Electrically tunable moiré magnetism in twisted double bilayers of chromium triiodide. *Nat. Electron.* **6,** 434–442 (2023).

253. Xie, H. *et al.* Twist engineering of the two-dimensional magnetism in double bilayer chromium triiodide homostructures. *Nat. Phys.* **18,** 30–36 (2022).

254. Husremović, S. *et al.* Hard ferromagnetism down to the thinnest limit of iron-intercalated tantalum disulfide. *J. Am. Chem. Soc.* **144,** 12167–12176 (2022).

255. Jia, Y. *et al.* Surface-confined two-dimensional mass transport and crystal growth on monolayer materials. *Nat. Synth.* **3,** 386–393 (2024).

256. Vulović, M., Voortman, L. M., van Vliet, L. J. & Rieger, B. When to use the projection assumption and the weak-phase object approximation in phase contrast cryo-EM. *Ultramicroscopy* **136,** 61–66 (2014).

257. Latychevskaia, T. *et al.* Convergent beam electron holography for analysis of van der Waals heterostructures. *Proc. Natl. Acad. Sci.* **115,** 7473–7478 (2018).

258. Metcalf, T. R. Resolving the 180-degree ambiguity in vector magnetic field measurements: The 'minimum'energy solution. *Sol. Phys.* **155,** 235–242 (1994).

259. Boresi, A. P. & Schmidt, R. J. *Advanced mechanics of materials* (John Wiley & Sons, 2002).

260. Cao, G. Atomistic studies of mechanical properties of graphene. *Polymers* **6,** 2404–2432 (2014).

261. Falin, A. *et al.* Mechanical properties of atomically thin tungsten dichalcogenides: WS_2, WSe_2, and WTe_2. *ACS Nano* **15,** 2600–2610 (2021).

262. Zeng, F., Zhang, W.-B. & Tang, B.-Y. Electronic structures and elastic properties of monolayer and bilayer transition metal dichalcogenides MX_2 (M= Mo, W; X= O, S, Se, Te): a comparative first-principles study. *Chin. Phys. B* **24,** 097103 (2015).

263. Ophus, C., Ciston, J. & Nelson, C. T. Correcting nonlinear drift distortion of scanning probe and scanning transmission electron microscopies from image pairs with orthogonal scan directions. *Ultramicroscopy* **162,** 1–9 (2016).

264. Massatt, D., Carr, S., Luskin, M. & Ortner, C. Incommensurate heterostructures in momentum space. *MMS* **16,** 429–451 (2018).

265. Zhou, S., Han, J., Dai, S., Sun, J. & Srolovitz, D. J. van der Waals bilayer energetics: Generalized stacking-fault energy of graphene, boron nitride, and graphene/boron nitride bilayers. *Phys. Rev. B* **92,** 155438 (2015).

266. Kresse, G. & Furthmüller, J. Efficient iterative schemes for ab initio total-energy calculations using a plane-wave basis set. *Phys. Rev. B* **54,** 11169–11186 (1996).

267. Peng, H., Yang, Z.-H., Perdew, J. P. & Sun, J. Versatile van der Waals Density Functional Based on a Meta-Generalized Gradient Approximation. *Phys. Rev. X* **6,** 041005 (2016).

268. Kresse, G. & Joubert, D. From ultrasoft pseudopotentials to the projector augmented-wave method. *Phys. Rev. B* **59,** 1758–1775 (1999).

269. Mogensen, P. K. & Riseth, A. N. Optim: A mathematical optimization package for Julia. *JOSS* **3,** 615 (2018).

Appendix A

Supplementary Information

A.1 Derivation of the Bragg interferometry fitting function

In order to arrive at our expression for modulation of the Bragg disk overlap intensity as a function of interlayer displacement, we first assume that we have a generic bilayer structure in which each of the two layers is represented by a projected electrostatic potential $V_1(\mathbf{r})$ and $V_2(\mathbf{r})$. We denote the interlayer displacement between the atomic coordinates of the two layers in the xy plane as $\mathbf{u} = (u_x, u_y)$ and assume the gap between the layers is negligible such that the outgoing electron beam wavefunction is well-described by a phase shift due to the total electrostatic potential $V_1(\mathbf{r}) + V_2(\mathbf{r})$ (*i.e.* we are assuming that diffraction takes place within a single plane). Accounting for the offset between layers, the total projected potential is then given by the sum $V_1(\mathbf{r} - \mathbf{u}/2) + V_2(\mathbf{r} + \mathbf{u}/2)$. This convention is consistent with our choice to work in the coordinate system defined by the average of the two monolayer lattices. Since the bilayer thickness ($<$ 1–2 nm) is much smaller than the depth of field of the electron probe ($>$ 100 nm for an 80 keV probe with 1.71–3.00 mrad convergence semi-angle) and the incident electron wave function $\psi_0(\mathbf{r})$ will only be weakly scattered by the two layers comprising the moiré, we may express the scattered electron probe wavefunction $\psi(\mathbf{r})$ to a very good approximation using the weak phase object approximation[256]:

$$\begin{aligned}\psi(\mathbf{r}) &= e^{i\sigma V_1(\mathbf{r}-\mathbf{u}/2)+i\sigma V_2(\mathbf{r}+\mathbf{u}/2)}\psi_{illum}(\mathbf{r}) \\ &\approx (1 + i\sigma V_1(\mathbf{r} - \mathbf{u}/2) + i\sigma V_2(\mathbf{r} + \mathbf{u}/2))\psi_0(\mathbf{r})\end{aligned} \tag{A.1}$$

where σ is the relativistic interaction parameter. We also assume a fully focused probe such that the contrast transfer function (and thus the more complex interference fringes encountered in holographic approaches[161,257]) does not appear.

The Fourier space intensity (*i.e.* the measured intensity in the region of Bragg disk overlap) $I(\mathbf{k})$ is then given by the following, in which $\circledast$ denotes convolution.

$$I(\mathbf{k}) = |\psi(\mathbf{k})|^2 = |(\delta(\mathbf{k}) + i\sigma \sum_{\mathbf{g}} \delta(\mathbf{k}-\mathbf{g})(V_1(\mathbf{g})e^{i\pi\mathbf{g}\cdot\mathbf{u}} + V_2(\mathbf{g})e^{-i\pi\mathbf{g}\cdot\mathbf{u}})) \circledast \psi_0(\mathbf{r})|^2 \tag{A.2}$$

Assuming that the convergence semi-angle is chosen to ensure that Bragg disks within a single layer do not overlap, we arrive at the following expression.

$$I(\mathbf{k}) = |\psi_0(\mathbf{k})|^2 + \sigma^2 \sum_{\mathbf{g}} |\psi_0(\mathbf{k}-\mathbf{g})|^2(|V_1(\mathbf{g})|^2 + |V_2(\mathbf{g})|^2 + 2Re(V_1(\mathbf{g})V_2^*(\mathbf{g})e^{2i\pi\mathbf{g}\cdot\mathbf{u}})) \tag{A.3}$$

This is equivalent to the following, in which we defined $A(\mathbf{g}) = 4\,\mathrm{Re}(V_1(\mathbf{g})V_2^*(\mathbf{g}))$, $B(\mathbf{g}) = 4\,\mathrm{Im}(V_1(\mathbf{g})V_2^*(\mathbf{g}))$, and $C(\mathbf{g}) = (|V_1(\mathbf{g})|^2 + |V_2(\mathbf{g})|^2 - 2\,\mathrm{Re}(V_1(\mathbf{g})V_2^*(\mathbf{g})))$.

$$\begin{aligned} I(\mathbf{k}) = |\psi_0(\mathbf{k})|^2 + \sigma^2 \sum_{\mathbf{g}} |\psi_0(\mathbf{k}-\mathbf{g})|^2 (A(\mathbf{g})\cos^2(\pi\mathbf{g}\cdot\mathbf{u}) \\ + B(\mathbf{g})\cos(\pi\mathbf{g}\cdot\mathbf{u})\sin(\pi\mathbf{g}\cdot\mathbf{u}) + C(\mathbf{g})) \end{aligned} \tag{A.4}$$

At each real space coordinate $\mathbf{r}$, we therefore have the following relationship between the projected displacement vector $\mathbf{u}$ and the modulation in intensity I_j for a set of selected Bragg disks at positions $\mathbf{g}_j$, where $A_j = A(\mathbf{g}_j)$, $B_j = B(\mathbf{g}_j)$, and $C_j = C(\mathbf{g}_j)$ are the coefficients that we treat as fitting parameters which may in general be different for each region of overlap.

$$I_j = A_j \cos^2(\pi\mathbf{g}_j\cdot\mathbf{u}) + B_j \cos(\pi\mathbf{g}_j\cdot\mathbf{u})\sin(\pi\mathbf{g}_j\cdot\mathbf{u}) + C_j \tag{A.5}$$

Equation A.5 is a general expression that is compatible with bilayer structures including those that lack inversion symmetry and heterobilayers, as described in Chapter 3. However, we note that when the projected real space potentials are symmetric with respect to inversion (in the plane perpendicular to the electron beam), it is straightforward to show that the Fourier space potentials are necessarily purely real. As a consequence, $B_j = 0$ in materials whose in-plane projections preserve inversion symmetry. Further, C_j vanishes in homobilayer structures when $V_1 = V_2$. Therefore, for inversion symmetric homobilayers such as twisted bilayer graphene (see Chapter 2), Equation A.5 can be simplified to the following:

$$I_j = A_j \cos^2(\pi\mathbf{g}_j\cdot\mathbf{u}) \tag{A.6}$$

A.2 Displacement fitting procedures

A.2.1 Displacement fitting for twisted bilayer graphene

Here we outline the procedure used in Chapter 2 to assign each region of the TBL-Gr samples to a particular interlayer stacking order. First the unwanted background scattering is removed by fitting the averaged diffraction pattern to a Lorentzian function after masking off all Bragg disks and the beamstop. The residuals of the background fit are then interpolated radially through the Bragg disks from the center of the CBED pattern, and both the fit and the interpolated residuals are subtracted from each CBED pattern. This correction removes unwanted scattering contributions from the CBED intensities. Next, the overlap regions between each pair of TBL-Gr Bragg disks are manually defined, and all pixel intensity values in each region are summed. Because we use all first order TBL-Gr Bragg reflections in the fitting procedure, this converts each CBED pattern into a twelve-component vector characterizing the local interferometry pattern. Shifts in the Bragg disk positions contribute no information in this method. Therefore, the manually defined summation region may be centerd on the reciprocal lattice vector from either graphene layer, as long as the summation region lies entirely within the Bragg disk overlap region. In general, we place the summation region on the centre of the CBED overlap region, corresponding to the average of the reciprocal lattice vectors from each layer. This procedure allows visualization of the virtual dark-field images from each TBL-Gr reflection pair. Note that this technique is superior to sequentially acquiring twelve separate conventional DF images for each reflection, as it eliminates systematic/correlated errors due to sample drift in-between acquisitions, does not incidentally incorporate signals from adjacent hBN diffraction disks owing to the typical sizes of selected area diffraction apertures, and enables measurement of a wide range of twist angles without changing microscope parameters.

The twelve "virtual" DF datasets are then converted into a single displacement map by nonlinear regression (Fig. A.1) using Equation 2.1 (A.6), where the I_j values for each of the twelve reflections ($j \in \langle 1100 \rangle, \langle 2110 \rangle$) are the response variables and the two-component displacement vector $\mathbf{u}$ is the predictor variable. We confine $\mathbf{u}$ to the half-hexagon fitting region shown in Fig. 2.4b so that each $\mathbf{u}$ predicts a unique interferometry pattern. This region contains all possible shortest vectors from a lattice site in graphene layer 1 to graphene layer 2 or vice-versa, modulo inversion through the origin. This 180° phase ambiguity implies that AB and BA regions give identical interferometry patterns for on-zone-axis experiments (see Chapter 1, Section 4 for a discussion on sample tilt effects). Subject to these constraints, the nonlinear regression finds the unique $\mathbf{u}$ that best predicts the intensity values for each pixel.

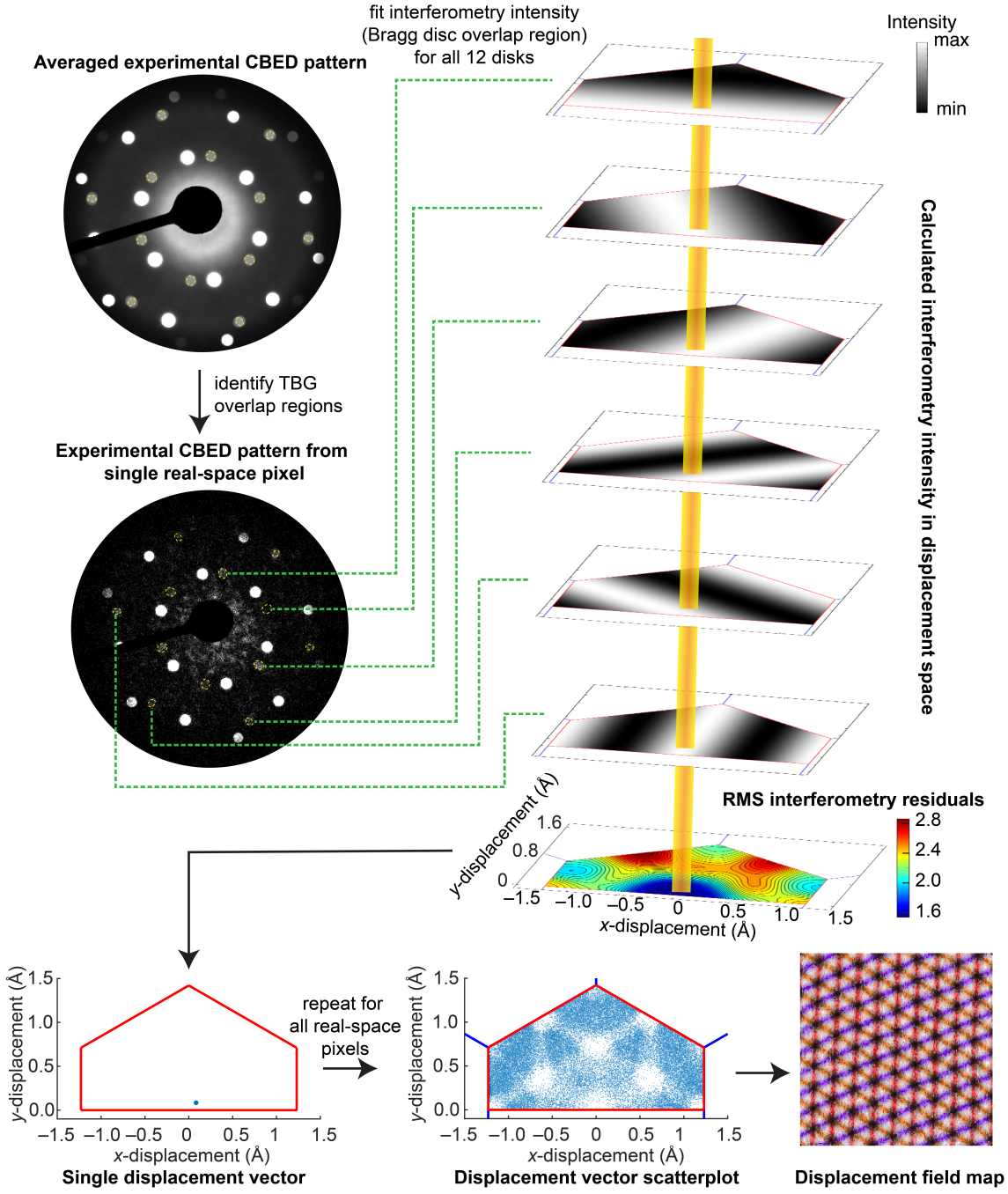

Figure A.1: Schematic of the fitting process showing how the TBL-Gr interferometry intensity in one CBED pattern is fit to extract a single displacement vector (shown here for an AA site). In the final steps, the entire 4D data set is assembled into a displacement field map for a region with $\theta_m = 1.23°$.

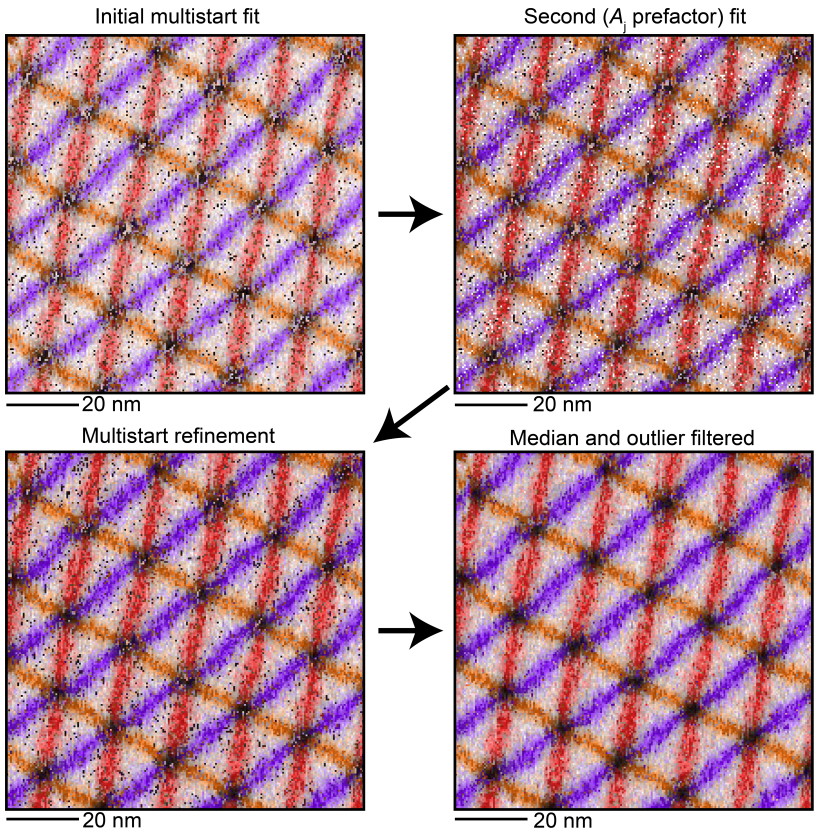

Figure A.2: Sequence of fitting, refinement, and filtering used to reconstruct a displacement field map a TBL-Gr sample with $\theta_m = 0.63°$.

To account for the unknown prefactor coefficients A_j, a three-step fitting process is followed to obtain the optimized A_j values (Fig. A.2). First, the A_j values are estimated by manually defining an AB/BA-stacked region and averaging all virtual dark-field intensities within for each disk. Equation 2.1 predicts that the AB/BA stacking order gives $\langle 1100 \rangle$ overlap regions of $0.25A_j$ and $\langle 2110 \rangle$ overlap regions of simply A_j (see relative intensities in Fig. 2.3c). This is only an initial estimate, chosen because AB/BA regions are the most readily spotted from superimposition of the virtual dark-field images. In the first regression, the A_j calculated this way are held constant while the $\mathbf{u}$ is optimized separately for each pixel. Multiple local minima can arise on the optimization surface because of the trigonometric fitting function; therefore, twelve gradient-based optimization runs are initiated from different locations in the fitting region to ensure global convergence for each pixel (referred to as a multistart process). The initial estimate of the displacement map obtained this way is typically already quite good (Fig. A.2). In the second fit, the A_j are allowed to optimize simultaneously with all $\mathbf{u}$ for each pixel, using the displacement map obtained in the first fit as a starting guess. Owing to the large scale of this

regression, the multistart optimization strategy employed in the first fit cannot be used. Finally, the first pixel-by-pixel fit is performed again, but this time using the optimized values of the A_j prefactors from the second fit. The displacement vectors from this third fit are lightly filtered to remove outliers on the basis of amplitude, via deviations from the median value in a 5×5 moving pixel window. Where possible, replacements are made from alternate displacement vector convergence locations (i.e. local minima) arising from the multistart displacement fit. Where no good multistart candidates exist, outlier displacement values are replaced by the median value in the moving window. The proportion of displacement vectors modified by outlier filtering is typically fewer than 5% for any given dataset. We use the results of the filtered third fit as the displacement map for each dataset in Chapter 2.

A.2.2 Displacement fitting for TMD moiré bilayers

The local in-plane interlayer displacement vectors $\mathbf{u}$ for the TMD moiré bilayers (Chapter 3) were extracted from the 4D-STEM datasets following a procedure generalized from that used for TBL-Gr. To start, the average diffuse scattering was fit to a Lorentzian profile and removed for each CBED pattern (associated with an individual real space pixel). Similar to the TBL-Gr analysis, the overlap regions in the twelve first-order TMD Bragg disks were then used to obtain the optimal interlayer displacements $\mathbf{u}$ and coefficients A_j, B_j, C_j via a least squares fitting procedure with Eq. 3.1 as the fitting function. In this process, it was assumed that the coefficients remained constant over the sample field of view, resulting in 36 total coefficient variables and $n_x n_y$ displacement variables for a n_x by n_y scan.

To summarize the fitting process, first we normalized I_j, assumed $A_j = 1, B_j = 0, C_j = 0$, and determined the optimal displacement vector independently at each pixel using a quasi-Newton non-linear least squares optimization (specifically the trust region reflective algorithm as implemented in scipy)[185]. We used a uniform grid of 9 initial guesses (i.e., a multistart procedure) for $\mathbf{u}$ to decrease the chance of obtaining local minima. The values of $\mathbf{u}$ were constrained to reside within a single unit cell such that $\mathbf{u} = c_1\mathbf{a}_1 + c_2\mathbf{a}_2$ with $|c_1| \leq 1/2, |c_2| \leq 1/2$, where $\mathbf{a}_1, \mathbf{a}_2$ are the average of the monolayer real space lattice vectors rotated into a convenient basis (see Appendix, Section 5 for notes on rotation calibration). We subsequently determined the optimal coefficients A_j, B_j, C_j given this $\mathbf{u}$ independently for each of the twelve Bragg disk intensities I_j using linear least squares. These two steps were then repeated, where subsequent iterations used the previous iteration $\mathbf{u}$ in the pixel of interest and all four directly adjacent pixels as starting conditions instead of the uniform grid. Fitting the displacements and coefficients in tandem, rather than simultaneously as done for our study of TBL-Gr, allowed us to both parallelize the procedure and to use a linear optimization for the coefficients, improving efficiency. We found that the $\mathbf{u}$ values converged within 5 iterations of this procedure. To avoid over-fitting and for computational speed, we also found it effective to first bin the displacement field

(using an L_2 norm and a bin width of 2) and perform the aforementioned procedure to obtain the coefficients and $\mathbf{u}_{bin}$. The raw $\mathbf{u}$ were then fit using $\mathbf{u}_{bin}$ as starting conditions and the coefficients deemed optimal for the binned data, which were held fixed. The final $\mathbf{u}$ were converted from dimensionless units assuming lattice constants a_0 of 0.315 and 0.328 nm for MoS_2 and WSe_2 (values from HQ Graphene) respectively as the data acquisition was not set up to ensure an unbiased estimate of these values. An overview of the optimized fitting procedure is shown in Fig. A.3.

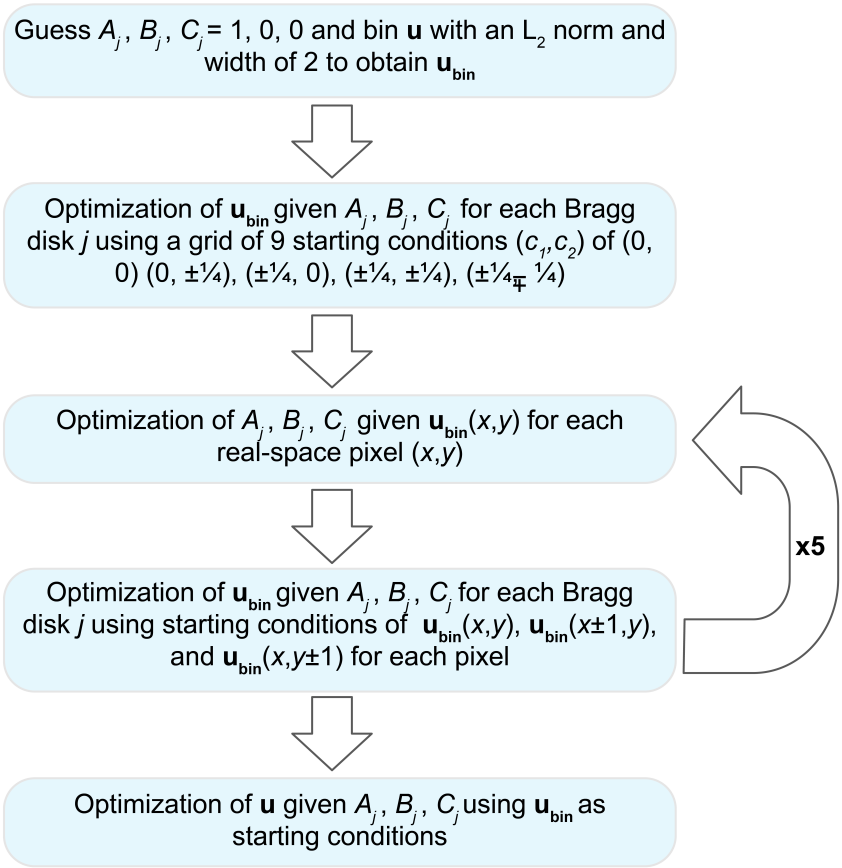

Figure A.3: General computational workflow for the displacement fitting procedure used in Chapter 3.

A.3 Evaluation of fitting bias

Displacement histograms obtained through Bragg interferometry frequently show geometric patterns, in which some displacement values cluster together and some displacement values are avoided, as seen in Fig. 2.4a, bottom left. To investigate the origins of this, we performed a simulation mimicking the effects of a finite probe radius (Fig. A.4). The displacement half-hexagon fitting region was populated with a grid of points representing true probe positions. For each point, the interferometry patterns for all displacements within a 0.2 Å radius were calculated according to Equation 2.1 and averaged. The averaged pattern was then re-fit to a displacement vector using Equation 1. The discrepancy between the original probe position in displacement space and the final fitted displacement estimates the bias introduced from a finite probe width. Note that this a simplified model, not accounting for the radial intensity profile of the probe or the effects of reconstruction, which will produce a non-uniform density of points in displacement space. Fig. A.4 shows that probe averaging induces bias matching the clustering pattern in the displacement histogram shown in Fig. 2.4a (bottom left). The "avoided regions" with large biasing correspond to high symmetry interferometry patterns. For example, Equation 2.1 predicts an SP pattern will have 8 of 12 disks with zero intensity. Many of these disks will be nonzero for intermediate stacking orders surrounding pure SP stacking. Probe averaging thereby obtains an interferometry pattern that does not quite look like pure SP stacking, leading to the bias. Despite these effects, the design of the data analysis procedure renders the strain maps robust against biasing artifacts. When the displacement histogram is unwrapped for strain mapping (see Appendix, Section 4), the avoided regions manifest themselves as losses in continuity at the boundaries between moiré unit cells. Application of a total generalized variation (TGV) filter removes these discontinuities, essentially eliminating the bias through interpolation. The strain filter parameters thus set the systematic uncertainty on the calculated strain values, as discussed in Section A.6.

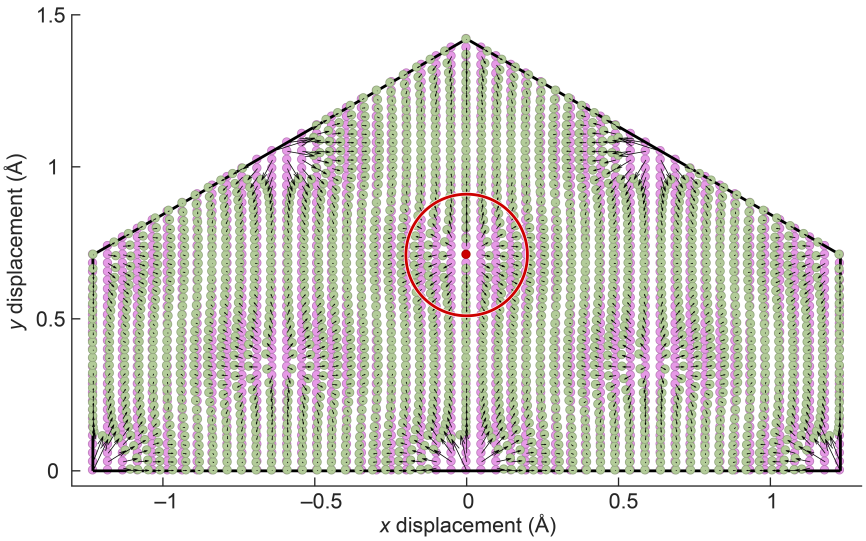

Figure A.4: Simulation of bias induced by the finite probe width. Purple markers represent beam positions in displacement space. Predicted interferometry patterns are averaged in a 0.2 Å radius circle around each point; the averaging radius is shown with a red circle for one probe position as an example. Fitted displacement values are shown with green markers, with a black arrow connecting the fitted displacement values to the true probe position.

A.4 Displacement field unwrapping

A.4.1 Unwrapping procedure for twisted bilayer graphene

The displacement fitting procedure produces vectors contained entirely within the half-hexagon fitting region, which displays discontinuities at the edges. Before differentiation can occur, the displacement data must therefore be unwrapped to both eliminate the 180° ambiguity[258] and also establish a continuous vector field between adjacent moiré domains. This multidimensional vector field unwrapping problem presents a problem for standard algorithms, which typically can handle either 180° ambiguity or multidimensional unwrapping, but not both. To overcome this problem, we developed a geometry-based approach. The AA, AB and SP regions were algorithmically detected from their characteristic displacement vectors, and the stacking order change from crossing each SP region was stored. An initial reference displacement was assigned to a starting AB domain centroid, and then a reference displacement vector was assigned to each neighbouring AB centroid by finding the vectors that satisfy the SP stacking order change criteria. Each AB centroid was assigned recursively. Next, each individual real space pixel was assigned to an AB centroid through geometry domain registration, so that each pixel had a reference vector indicating the approximate region where its unwrapped displacement vector should fall. The precise vector was obtained by choosing the new displacement vector that (1) produced an equivalent interferometry pattern to that of the original displacement vector in the half-hexagon fitting region and (2) was as close as possible to the reference vector. The unwrapped displacement field was then refined by a 3×3 moving window that interchanges displacement vectors to maximize local continuity. After applying the moving window ten times, the remaining discontinuities at the AA and SP boundaries were eliminated. Note that the displacement unwrapping process did not change the model fit to the virtual dark-field images because each unwrapped displacement vector predicts the same interferometry pattern as the original vector. The unwrapping process converted a single half-hexagon fitting region into a series of continuously connected fitting regions amenable to differentiation, as shown in Fig. A.5. The unwrapped displacement field was denoised (Fig. A.6) by total generalized variation (TGV)[109,164] and differentiated to produce the strain maps. We note that the calculated strain and rotation values can change by around ±10%, depending on the exact TGV filter settings used, implying some systematic uncertainty in the exact magnitude of the reconstruction strain. However, filter settings were kept consistent so that the twist angle trends were not impacted and the good agreement between finite-element method simulations and experiment provided support for the filter settings used.

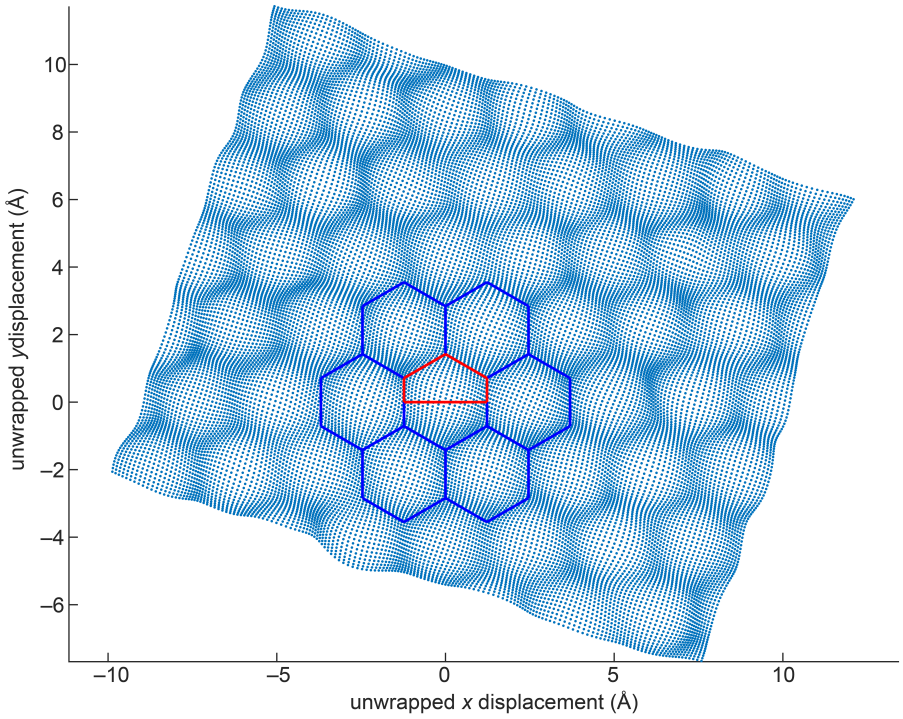

Figure A.5: Displacement unwrapping and TGV filtering of the displacement field converts the displacement half-hexagon into a continuous vector field between adjacent moiré domains that is amenable to differentiation.

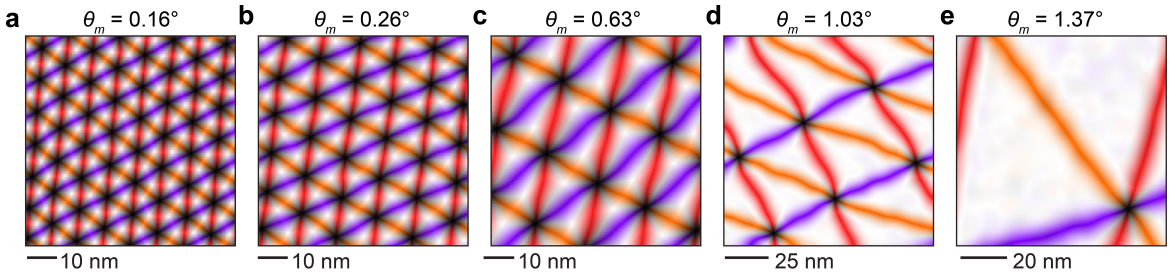

Figure A.6: Unwrapped and TGV denoised displacement maps for the datasets shown in Fig. 2.4c. A border of ≤ 30 nm is lost in the unwrapping–denoising process compared to the original displacement maps.

A.4.2 Unwrapping procedure for TMD moiré bilayers

The displacement unwrapping procedure was modified for our study of TMD moiré bilayers. To summarize, the new procedure amounts to finding the optimal (n,m,s) at each pixel location given $\mathbf{u}_{fit}$ such that the Euclidean distance of $\mathbf{u}_{unwrap}$ from its neighbors is minimized. This yields a continuously varying $\mathbf{u}_{unwrap}$ amenable to differentiation. While it is in principle possible to circumvent such a procedure through accounting for the degeneracy of $\mathbf{u}$ in the differentiation process, we found approaches along these lines less robust to noise due to the decreased ability to smooth the data prior to differentiation.

$$\mathbf{u}_{unwrap} = s\mathbf{u}_{fit} + n\mathbf{a}_1 + m\mathbf{a}_2 \qquad n, m \in Z, s = \pm 1 \tag{A.7}$$

Instead, we chose to first partition the data into zones expected to have the same offsets n and m. For most of the data sets we used the Watershed segmentation algorithm[182] on $|\mathbf{u}|$, which proved effective in unwrapping displacement fields with decently large regions of $\mathbf{u} \approx 0$ stacking separated by thin boundaries (all but the parallel stacked homobilayers). For the parallel stacked homobilayers, which contained small $\mathbf{u} \approx 0$ stacking regions, a Voronoi partition[185] instead proved more robust to noise. After segmentation, the zone offsets (n,m) of each region were determined based on the region's connectivity, as shown in Fig. A.7. For instance, in our convention, regions connected by SP1(SP2) soliton walls have the same $m(n)$ offset and a $n(m)$ offsets differing by ± 1, allowing us to successively assign all zones with a breadth first search (starting from the region closest to the center of the data). Large sample deformations will result in the breakdown of this simple algorithm, although we did not find more elaborate approaches necessary for this study. The s of each pixel was then chosen to maximize the local curl in data sets for which $B_j \approx 0$ introduced a sign ambiguity.

Given these estimates for the displacement orientation and lattice vector offsets, we then used an integer program to optimize the parameters along the zone boundaries. The optimization of (n,m,s) along the zone boundaries was accomplished using the following procedure, which proved sufficient for obtaining smoothly varying displacement fields in this work. Before using a more costly integer program, we first chose the (n,m,s) offsets that gave a $\mathbf{u}_{unwrap}$ closest to the region local mean $\mathbf{u}$ within a 2 x 2 pixel moving window propagated outwards from the center of the data. Both previously assigned pixels and those assigned with confidence in the geometric partition (within 1% of the maximum distance from a region center) were held constant. Each 2 x 2 region after the initial solve was chosen to contain at least one previously assigned pixel. Following this, we identified contours in the data associated with $\mathbf{u}_{unwrap}$ discontinuities where adjacent pixels had a $\mathbf{u}_{unwrap}$ difference larger than what could be obtained by choosing locally optimal (n,m,s). These contours were then used to form a convex mask associated with large regions that had been optimized to a different global offset. For all convex regions of 5 or more pixels, we then

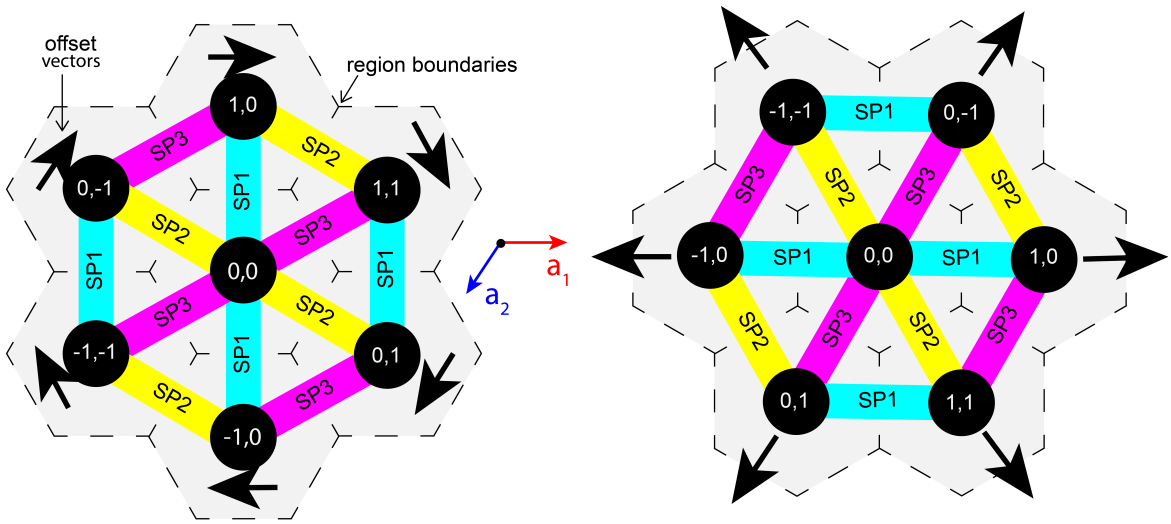

Figure A.7: Region offsets determined geometrically for a twisted homobilayer structure (left) and untwisted heterobilayer structure (right). The integer offsets (n, m) of each zone are shown in the black centers of each hexagonal region, and the corresponding offset vectors $n\mathbf{a}_1 + m\mathbf{a}_2$ are depicted as black arrows. In practice, the heterobilayer displacement fields were first rotated (changing only the lattice vector convention) so that they could be processed similarly to the twisted displacement fields and then rotated back to obtain the diverging displacement field expected for a heterobilayer.

used an integer program to successively re-assign the optimal (n,m,s) offsets within these regions, working inwards from their boundaries using a moving 2 x 2 window. This entire process was iterated until the total number of pixels in the convex regions stopped improving. We then used the same integer program to optimize the offsets in a 3 x 3 moving window for areas where the identified discontinuity regions were 5 pixels or fewer. Throughout, the integer program searched for n and m within ± 2 of the offsets determined from the geometric partitioning. The objective minimized was the sum of all L_2 norms between neighboring pixels, equally weighting both the fixed and variable cells within the region of interest. In practice we optimized s for all datasets (implemented as $s' = 2s - 1$ for convenience in constraints), as we found the sign of $\mathbf{u}$ was more susceptible to experimental noise than its magnitude. The resulting quadratic integer program was solved using APOPT interfaced by GEKKO.[183,184] The optimized unwrapping procedure is summarized in Fig. A.8. The unwrapped displacement fields $\mathbf{u}$ were then smoothed with a Gaussian filter ($\sigma = 2$ pixels per a_0 where a_0 is the average lattice constant for the two layers) and differentiated numerically using a centered 3-pt finite difference stencil to obtain the strain maps shown in Chapter 3. We note that the Gaussian smoothing, finite difference stencil, and finite

width of the electron beam (see Appendix, Section 3) may soften the observed strain and stacking features but do not affect the overall trends or conclusions drawn.

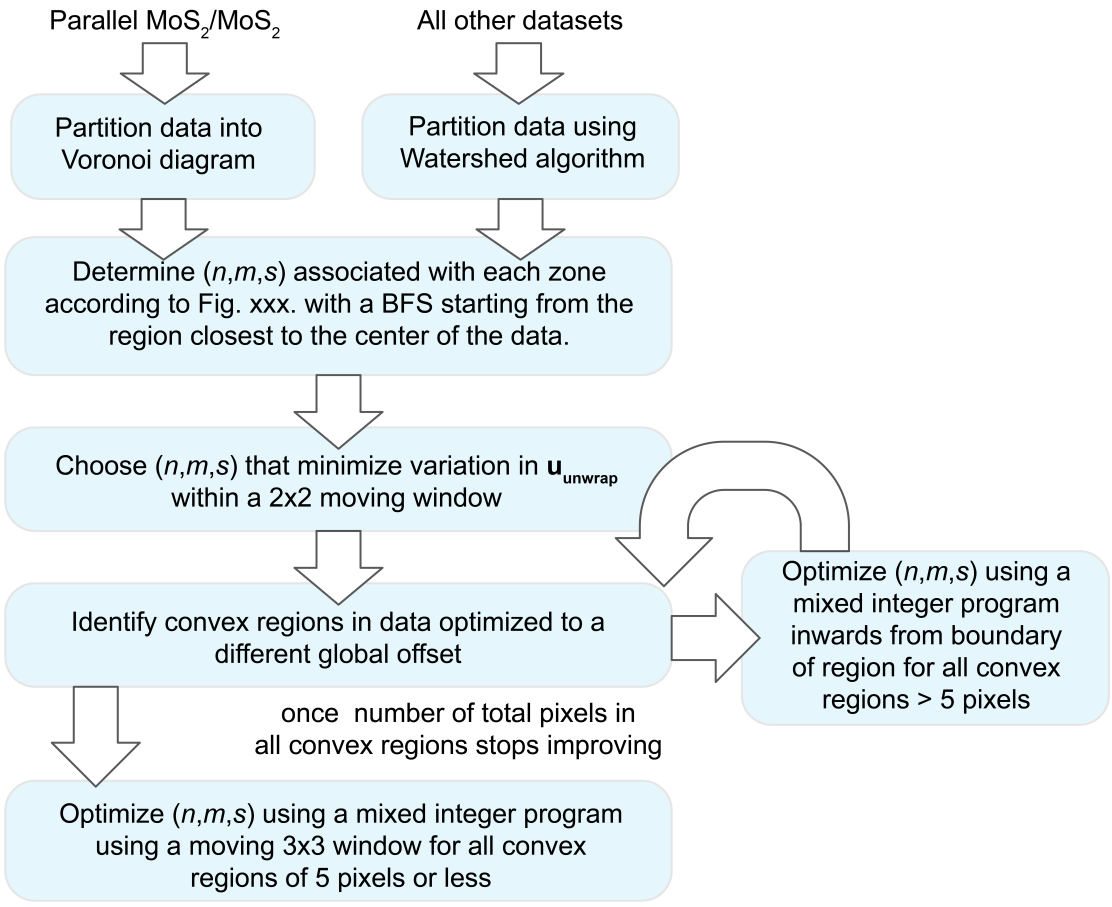

Figure A.8: General computational workflow for displacement field unwrapping, used in Chapter 3.

A.5 Rotational calibration

Prior to obtaining the strain tensor via differentiation of the displacement field, we also need to account for the rotational offset between the displacement vector coordinate system and the 4D-STEM scan axes. This rotational offset is controlled by two factors. The first is a rotation between the diffraction pattern and the scan direction inherent to the instrument. For our study of TBL-Gr, we calibrated this rotational offset by obtaining defocused images of gold nanoparticles[165], determining that the diffraction pattern is rotated 199° (or, equivalently, 19°) clockwise from the STEM image. We

performed the same calibration for the study of the TMD systems, measuring a rotation of 191° (or equivalently 11°) from comparison of a STEM image of a straight edge in one of the samples and the corresponding unscattered beam in the diffraction pattern using a defocused STEM probe. The variation in these two measurements could be a result of re-mounting of the camera sensor in the microscope in the time between the two studies. The second rotational offset is one of convenience that arises because we rotated the y-axis to align with the $1\bar{1}00$ overlap region (corresponding to orienting the x-axis along the average of the two layers' real space lattice vectors) in order to simplify the mathematics for the fitting and unwrapping procedures.

After accounting for these two factors, samples with moiré patterns controlled only by interlayer twist should have a y-axis oriented along SP1 soliton walls, samples with moiré patterns controlled only by lattice mismatch or heterostrain should have an x-axis oriented along the SP1 solitons, and moirés formed from a combination should have soliton orientations somewhere in between, as depicted in Fig. A.9. To justify this claim mathematically, we first define $\mathbf{a}_1$ and $\mathbf{a}_2$ as the average of the monolayer real space lattice vectors (defined as $\mathbf{b}_1$, $\mathbf{b}_2$ for layer 1 and $\mathbf{c}_1$, $\mathbf{c}_2$ for layer 2) with $\mathbf{a}_1$ oriented along the x-axis (Fig. A.9a). For a generic heterostructure, with an interlayer twist of θ and a lattice mismatch of $\delta = 1 - a_S/a_L$ (where a_S and a_L are the smaller and larger lattice constants of the two layers, respectively), we define k vectors $\mathbf{k}_1$, $\mathbf{k}_2$ in the first Brillouin zones for the two layers, as shown in Equation A.8. These k vectors are rotated with respect to each other due to the interlayer twist in real space and the vector associated with the larger lattice is scaled by $1/(1+\delta)$ due to the lattice mismatch in real space.

$$\begin{aligned} \mathbf{k_1} &= \frac{2\pi}{a(1+\delta)}\left(cos\left(\frac{\theta}{2}\right), -sin\left(\frac{\theta}{2}\right)\right) \\ \mathbf{k_2} &= \frac{2\pi}{a}\left(cos\left(\frac{\theta}{2}\right), sin\left(\frac{\theta}{2}\right)\right) \end{aligned} \tag{A.8}$$

We also define $\mathbf{k}_m$ as a k vector in the moiré Brillouin zone. The size and orientation of $\mathbf{k}_m$ can be determined from the difference between $\mathbf{k}_1$ and $\mathbf{k}_2$ (Fig. A.9b–d):

$$\begin{aligned} \mathbf{k_m} &= \mathbf{k_1} - \mathbf{k_2} \\ \mathbf{k_m} &= \frac{2\pi}{a}\left(cos\left(\frac{\theta}{2}\right)\left(\frac{1}{1+\delta} - 1\right), sin\left(\frac{\theta}{2}\right)\left(-\frac{1}{1+\delta} - 1\right)\right) \end{aligned} \tag{A.9}$$

Using a geometric analysis to compute the angle φ between the x-axis and $\mathbf{k}_m$ yields the following expression:

$$\varphi = \tan^{-1}\left(-\frac{(\delta+1)^{-1}+1}{(\delta+1)^{-1}-1}\tan\left(\frac{\theta}{2}\right)\right) \tag{A.10}$$

In Equation A.10, φ corresponds to the target orientation of the SP1 soliton walls for self-consistency in our chosen coordinate system. From this expression it is evident that $\varphi = 90°$ (SP1 oriented along y-axis) for $\theta_m > 0°$ and $\delta = 0$, $\varphi = 0°$ (SP1 oriented along x-axis) for $\theta_m = 0°$ and $\delta > 0$, and $0° < \varphi < 90°$ (SP1 oriented between the x- and y-axes) for $\theta_m > 0°$ and $\delta > 0$.

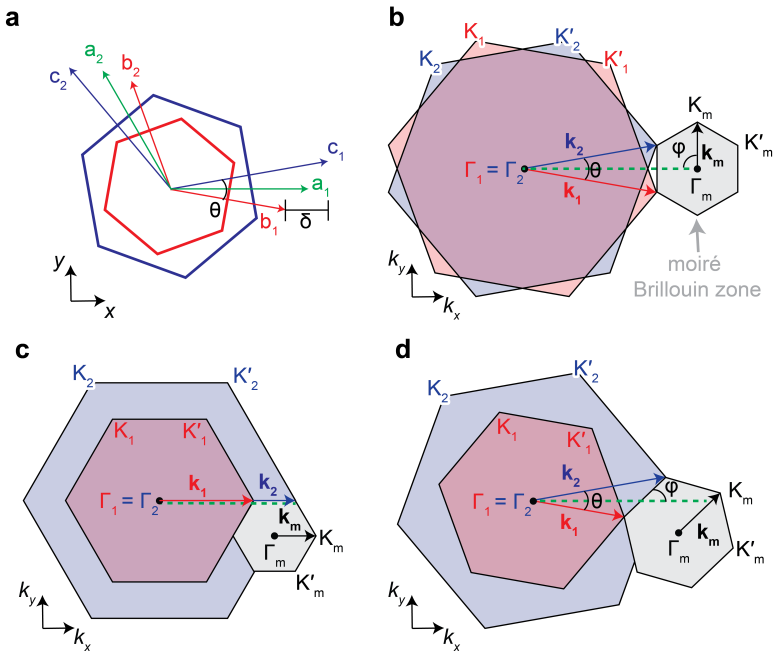

Figure A.9: a, Real space orientation of two atomic layers with an abitrary twist angle (θ) and lattice mismatch (δ). Vectors $\mathbf{a_1}$, $\mathbf{a_2}$ are defined as the average of the real space vectors from the two layers ($\mathbf{b_1}$, $\mathbf{b_2}$ for layer 1 and $\mathbf{c_1}$, $\mathbf{c_2}$ for layer 2). The x-axis is parallel to $\mathbf{a_1}$. **b–d,** Reciprocal space orientation of moiré Brillouin zone for a moiré homobilayer (**b**) , a lattice constant mismatch-driven moiré (**c**) , and a moiré superlattice resulting from both twist and lattice constant mismatch (**d**). k vectors are shown in the first Brillouin zone for each atomic lattice (shown in red in blue for layers 1 and 2, respectively) and for the moiré supercell (depicted in black/gray).

A.6 Strain mapping

After unwrapping and performing rotational calibration, the displacement fields were differentiated according to infinitesimal strain theory[155,156,259] to obtain the strain fields presented in Chapters 2 and 3. Here we provide an overview of this process. We first draw a distinction between the interlayer displacement field $\mathbf{u}_{inter}(x, y)$ as opposed to the single-layer or intralayer displacement field $\mathbf{u}_{intra}(x, y)$. The experimentally measurable quantity is $\mathbf{u}_{inter}(x, y)$, which determines the lattice plane offset giving rise to the interferometry signal. However, to obtain strain quantities that relate to the deformation experienced by a single atomic layer, it is useful to consider a reference state in which both layers have AA-type commensurate stacking, reaching their final positions by some equal-and-opposite combination of rotation and deformation. Because rotations are $\leq 2^\circ$, the small-angle approximation implies that $\mathbf{u}_{intra}(x, y) = \mathbf{u}_{inter}(x, y)/2$. In its present form, Bragg interferometry analysis is unable to independently resolve strain fields in the top and bottom layers of the moiré. As such, $\mathbf{u}_{intra}(x, y)$ is the best quantity to use to determine the average deformation of a single atomic layer. In homobilayers, the assumption that the deformations are equally partitioned between the two layers is enforced by symmetry. While this may not in principle hold true for all heterobilayers, simulations suggest that the relaxation magnitudes in MoS_2 and WSe_2 (studied in Chapter 3) differ by only 13% (See Appendix, Section 13) .

A vector-valued displacement field, $\mathbf{u}(x, y)$, has four associated derivatives arising from the gradients of the scalar-value x and y displacements. The elements of the strain tensor can then be calculated from the displacement field derivatives as follows:

$$\epsilon_{xx} = \frac{\partial u_{intra,x}}{\partial x} = \frac{1}{2}\left(\frac{\partial u_{inter,x}}{\partial x}\right) \tag{A.11}$$

$$s_{xy} = \frac{\partial u_{intra,x}}{\partial y} = \frac{1}{2}\left(\frac{\partial u_{inter,x}}{\partial y} + \theta_m\right) \tag{A.12}$$

$$s_{yx} = \frac{\partial u_{intra,y}}{\partial x} = \frac{1}{2}\left(\frac{\partial u_{inter,y}}{\partial x} - \theta_m\right) \tag{A.13}$$

$$\epsilon_{yy} = \frac{\partial u_{intra,y}}{\partial y} = \frac{1}{2}\left(\frac{\partial u_{inter,y}}{\partial y}\right) \tag{A.14}$$

$$\epsilon_{xy} = \frac{1}{2}(s_{xy} + s_{yx}) \tag{A.15}$$

The strain tensor is formally composed of the normal strains ϵ_{xx} and ϵ_{yy} for the diagonal elements along with the tensorial pure shear strain ϵ_{xy} on the off-diagonal

elements. The difference between the normal strains represents volumetric strain, or dilation:

$$Dil = \frac{\Delta V}{V} = \epsilon_{xx} - \epsilon_{yy} \tag{A.16}$$

The terms s_{xy} and s_{yx} are referred to as simple shear strains[155]. These terms contain information about both strain and fixed body rotation. To analyze the simple shear quantities arising from reconstruction, we first removed the moiré rotation, θ_m, so that only reconstruction rotation would be included. The rotation θ_m was estimated from the moiré superlattice geometry through triangulation (see Appendix, Section 8 for details). This procedure has no effect on the strain tensor itself, as the θ_m terms cancel out in the sum for calculating ϵ_{xy} (Equation 2.15). Note that ϵ_{xy} is the correct term to use for the strain tensor to perform correct tensor rotations, but is not directly comparable in magnitude to the normal strains ϵ_{xx} and ϵ_{yy}. It is therefore useful to define the 'engineering' pure shear strain as follows[155,156,259]:

$$\gamma_{xy} = s_{xy} = s_{yx} = 2\epsilon_{xy} \tag{A.17}$$

The quantity γ_{xy} exerts the same magnitude of deformation per unit strain as ϵ_{xx} and ϵ_{yy}.

The quantities ϵ_{xx}, ϵ_{yy}, s_{xy}. s_{yx}, and ϵ_{xy} (and therefore γ_{xy}) are each dependent on the coordinate axes chosen to visualize the strain tensor (Fig. A.10–12). This makes it challenging to compare strains between different SP regions in one image. To overcome this, it is useful to employ the principal strain equations[156]:

$$\varepsilon_{max} = \frac{\epsilon_{xx} + \epsilon_{yy}}{2} + \sqrt{\left(\frac{\epsilon_{xx} - \epsilon_{yy}}{2}\right)^2 + (\epsilon_{xy})^2} \tag{A.18}$$

$$\varepsilon_{min} = \frac{\epsilon_{xx} + \epsilon_{yy}}{2} - \sqrt{\left(\frac{\epsilon_{xx} - \epsilon_{yy}}{2}\right)^2 + (\epsilon_{xy})^2} \tag{A.19}$$

These equations correspond to local rotations of the tensor coordinate system to express the strain at each pixel entirely in terms of normal strain. The tensor rotation angle is known as the principal angle, θ_P[156]:

$$tan(2\theta_P) = \frac{2\epsilon_{xy}}{\epsilon_{xx} - \epsilon_{yy}} \tag{A.20}$$

The principal angle describes the orientation of the rotated x-axis (that is, the orientation of ε_{max}) relative to the starting coordinate system of the tensor. By convention, we chose the direction perpendicular to the SP1 regions as the x-axis starting coordinate system. The direction of maximum shear is located 45° counter-clockwise from θ_P. Thus, for an SP region undergoing shear strain due to rotations in

surrounding stacking regions, θ_P should be offset by 45° from the direction of the SP region. For TBL-Gr, we found this indeed to be the case, confirming that the strain in SP regions is predominantly characterized by shearing (Fig. 2.10).

The maximum shear strain (also known as the principal shear strain), γ_{max}, occurs at a 45° angle from the ε_{max} coordinate axis at each pixel, and is given by the difference in principal strains[156]:

$$\gamma_{max} = \varepsilon_{max} - \varepsilon_{min} \tag{A.21}$$

Because the intralayer strain in the atomic layers arises almost entirely from shearing processes, γ_{max} is a natural quantity to summarize the strain mechanics of a sample in one image. As noted in Chapter 2, Section 6, γ_{max} does not require definition of a local tensor coordinate system, unlike the elements of the strain tensor defined in Equations 2.11–15.

In the evaluation of the magnitude of simple strains s_{xy} and s_{yx} as a function of θ_m in Fig. 2.12a, for each displacement field map at a particular θ_m, the axes of the simple shear strains were rotated three times for maximum compatibility with each of the three SPs, and then the s_{xy} and s_{yx} values from these three tensor rotations were averaged to plot the result as a function of θ_m.

All equations described thus far consider the average intralayer strain experienced when a single layer of graphene deforms due to reconstruction. When analyzing rotation, however, it is more natural to consider the effect of both layers simultaneously to obtain the relative rotational misalignment. The relationship between simple shear and interlayer reconstruction rotation, θ_R, is therefore given by the following expression:

$$\theta_R = s_{yx} - s_{xy} \tag{A.22}$$

The fixed-body rotation equation normally has a factor of one-half; however, here, we multiplied by two to emphasize that we have gone from intralayer quantities s_{xy} and s_{yx} to the interlayer quantity θ_R. The total rotation, including the moiré rotation, can be expressed directly in terms of the interlayer displacement field:

$$\theta_T = \frac{1}{2}\left(\frac{\partial u_{inter,y}}{\partial x} - \frac{\partial u_{inter,x}}{\partial y}\right) \tag{A.23}$$

We employed this expression when the moiré angle changed rapidly over the field of view, such as near a tear or defect in the sample (Fig. 2.8). The moiré angle and the reconstruction angle are related as follows:

$$\theta_T = \theta_m + \theta_R \tag{A.24}$$

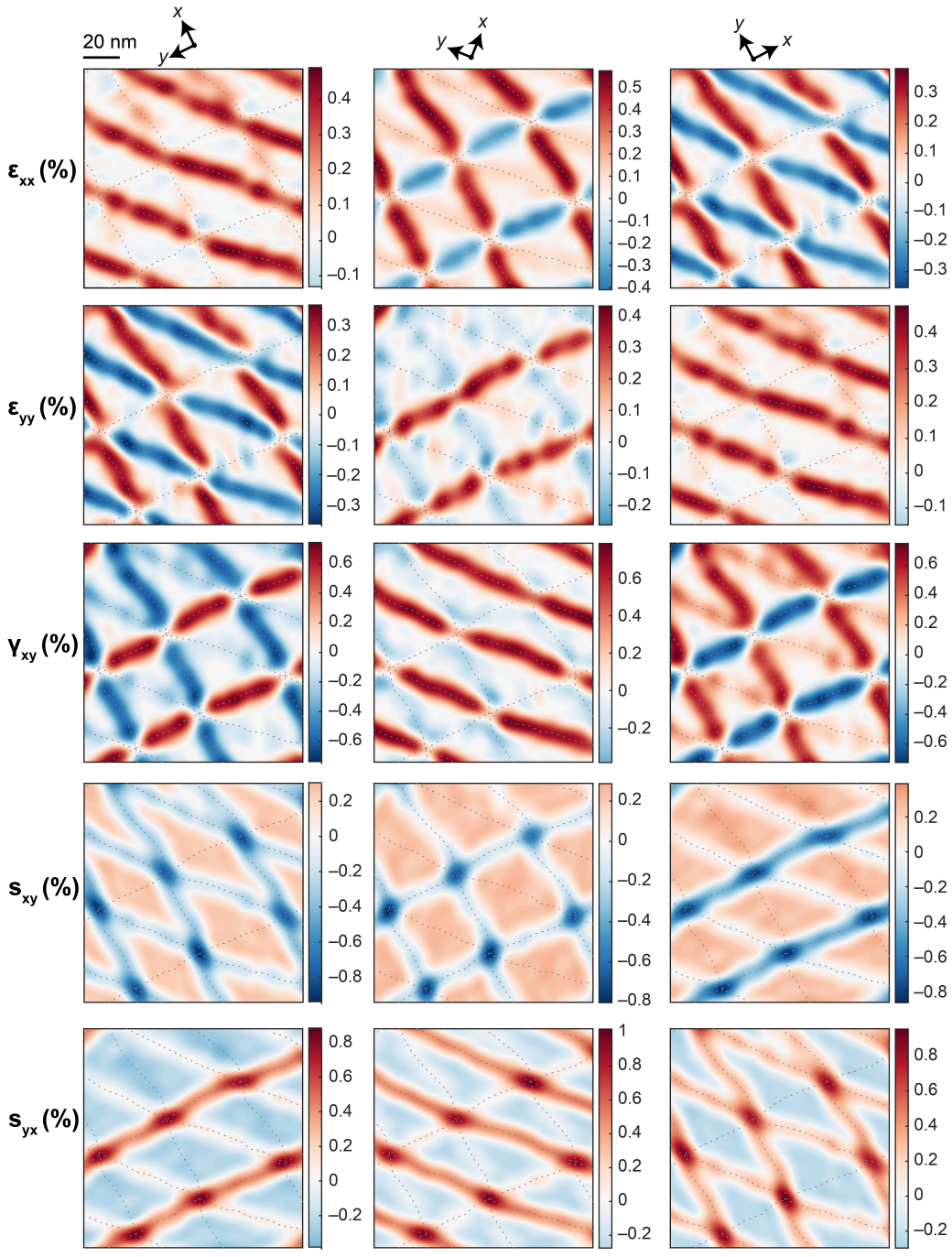

Figure A.10: Maps of normal strains, ϵ_{xx} andϵ_{yy}, engineering pure shear strain, γ_{xy}, and simple shear strains, s_{xy} and s_{yx}, produced with tensor rotations wherein the x-axis is successively aligned perpendicular to the three SP directions. These maps arise from the same dataset with $\theta_m = 0.26°$ shown in Fig. 2.4c and 2.7.

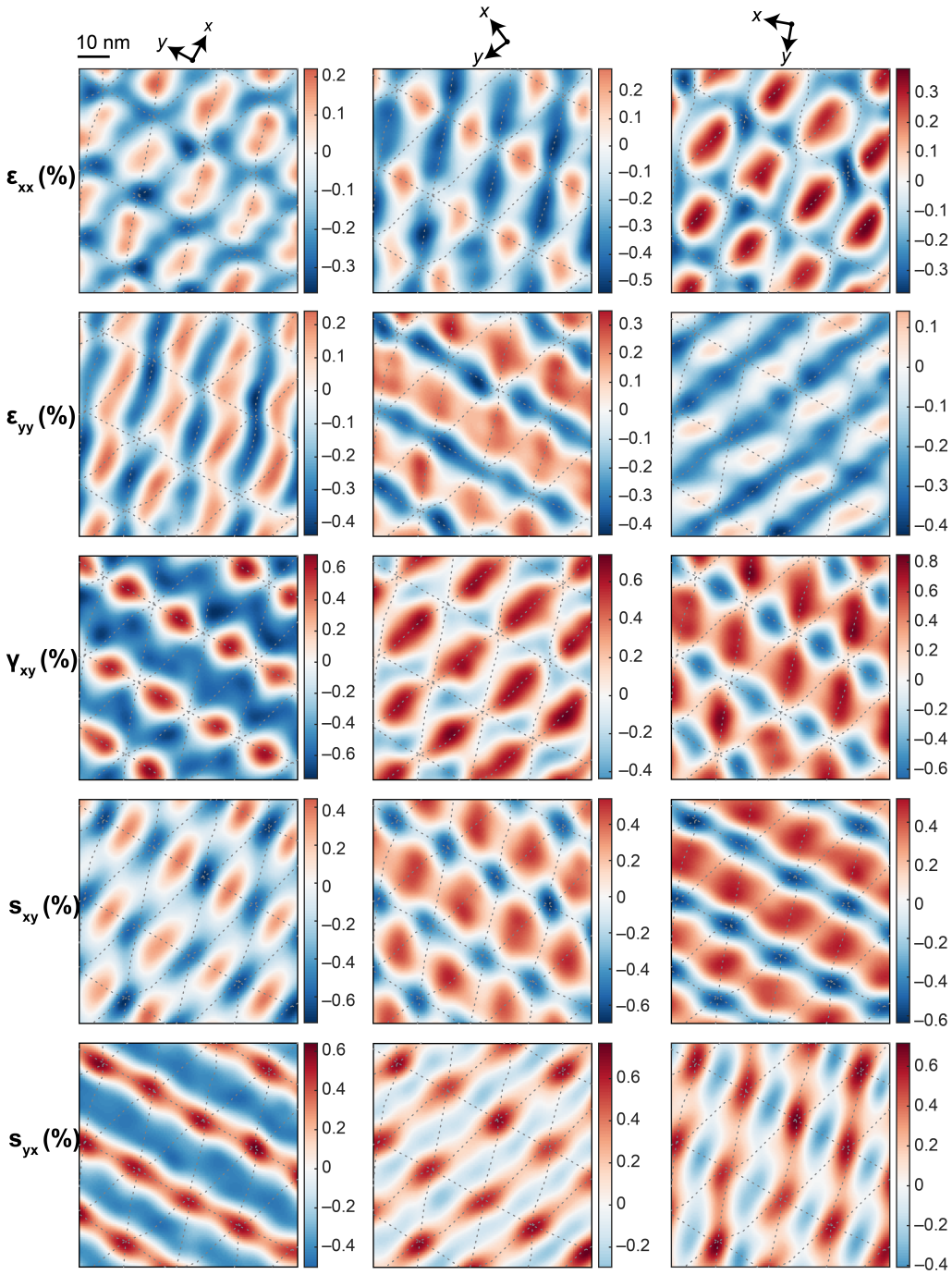

Figure A.11: Maps of normal strains, ϵ_{xx} andϵ_{yy}, engineering pure shear strain, γ_{xy}, and simple shear strains, s_{xy} and s_{yx}, produced with tensor rotations wherein the x-axis is successively aligned perpendicular to the three SP directions. These maps arise from the same dataset with $\theta_m = 0.63°$ shown in Fig. 2.4c and 2.7.

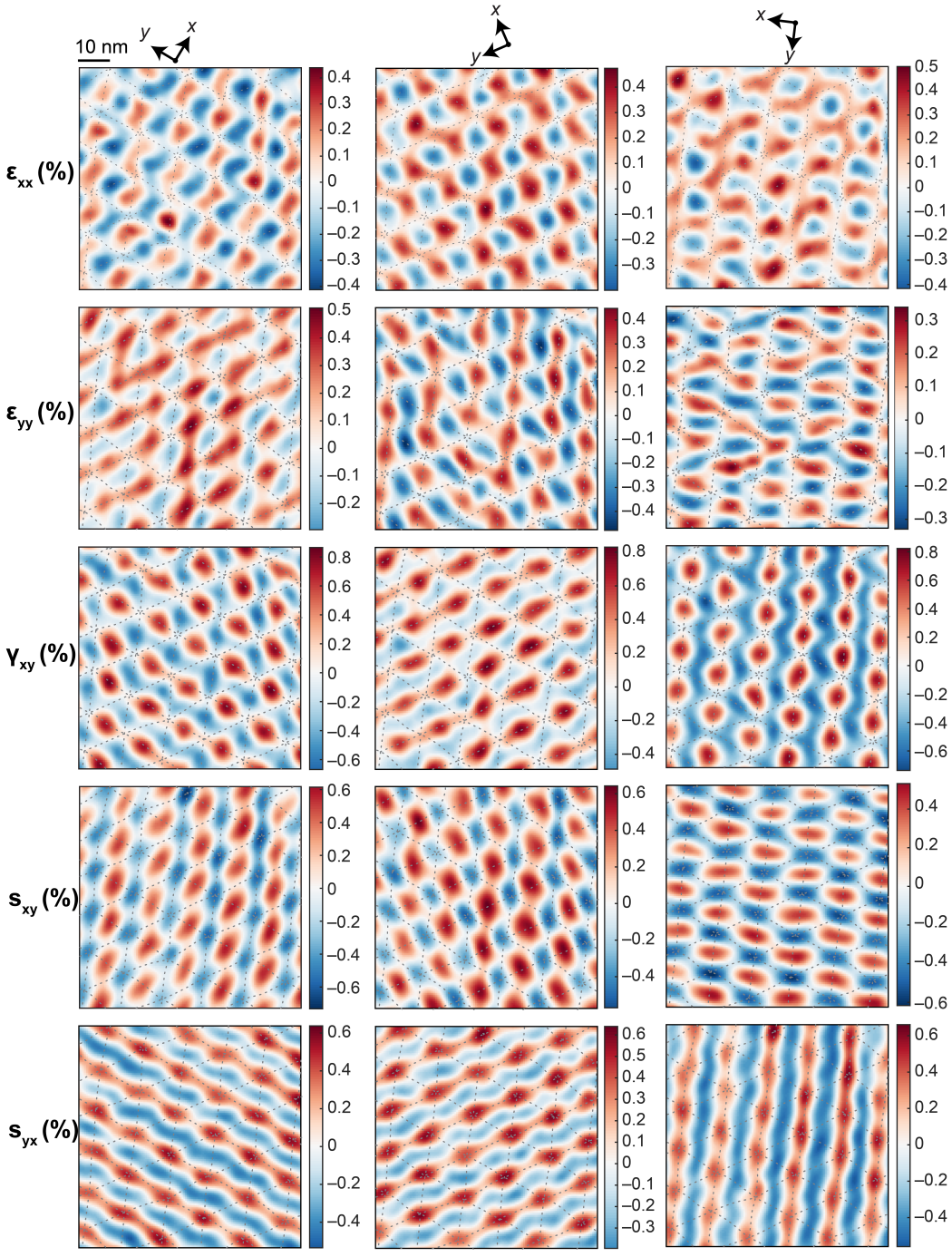

Figure A.12: Maps of normal strains, ϵ_{xx} andϵ_{yy}, engineering pure shear strain, γ_{xy}, and simple shear strains, s_{xy} and s_{yx}, produced with tensor rotations wherein the x-axis is successively aligned perpendicular to the three SP directions. These maps arise from the same dataset with $\theta_m = 1.03°$ shown in Fig. 2.4c and 2.7.

A.7 Simple shear decomposition

Simple shear strain from local stacking domain rotations constitutes the dominant strain mechanic in twisted bilayer reconstruction, incorporating both pure strain and fixed-body rotation as discussed previously. Although the maximum shear strain, γ_{max}, is commonly used to isotropically visualize the strain component, we sought a similar metric for visualization of both the strain and rotation effects found in simple shear. We constructed a simple shear decomposition to show the magnitude and direction of simple shear, by analogy to the principal strains technique for normal strain. In principal strain, the coordinate system is rotated to diagonalize the strain tensor, thereby completely eliminating shear strain[156]:

$$\begin{bmatrix} \varepsilon_{max} & 0 \\ 0 & \varepsilon_{min} \end{bmatrix} = \begin{bmatrix} cos(\theta_P) & sin(\theta_P) \\ -sin(\theta_P) & cos(\theta_P) \end{bmatrix} \begin{bmatrix} \epsilon_{xx} & \epsilon_{xy} \\ \epsilon_{xy} & \epsilon_{yy} \end{bmatrix} \begin{bmatrix} cos(\theta_P) & -sin(\theta_P) \\ sin(\theta_P) & cos(\theta_P) \end{bmatrix} \tag{A.25}$$

Here, θ_P is the principal angle, defining the rotated coordinate system. Analogously, we could seek to 'off-diagonalize' the 'strain–rotation' tensor to obtain a simple shear strain description:

$$\begin{bmatrix} 0 & s_1' \\ s_2' & 0 \end{bmatrix} = \begin{bmatrix} cos(\theta_s) & sin(\theta_s) \\ -sin(\theta_s) & cos(\theta_s) \end{bmatrix} \begin{bmatrix} \frac{\partial u_{intra,x}}{\partial x} & \frac{\partial u_{intra,x}}{\partial y} \\ \frac{\partial u_{intra,y}}{\partial x} & \frac{\partial u_{intra,y}}{\partial y} \end{bmatrix} \begin{bmatrix} cos(\theta_s) & -sin(\theta_s) \\ sin(\theta_s) & cos(\theta_s) \end{bmatrix} \tag{A.26}$$

This equation has one free variable (θ_s, the simple shear angle), but two variables on the diagonal to eliminate (denoted ϵ_{xx}' and ϵ_{yy}'). Thus, the equation will in general not have an exact solution, but we could solve for θ_s in the least-squares sense to minimize $\epsilon_{xx}'^2 + \epsilon_{yy}'^2$. By performing this least-squares regression for each pixel, we obtained the best possible simple shear representation of the strain field, which we refer to as the simple shear decomposition. Thus, θ_s obtained in this way has a 90° phase ambiguity, which can make visualization challenging. To obtain components of a continuous simple shear vector field, we examined the rotated tensor value, s_2', for both θ_s and $\theta_s + 90°$, and chose the simple shear angle that maximizes the signed value of s_2'. When plotted as a vector field quiver plot with two-headed arrows, the components s_1' and s_2' take on the natural interpretation of simple shear strain. For the case of TBL-Gr in Chapter 2, this simple shear strain is produced by AA and AB/BA reconstruction rotation (Fig. 2.16a,b).

A.8 Twist angle, lattice mismatch, and heterostrain calculations

Uniaxial heterostrain, local twist angle, and local lattice constant mismatch can be measured through their effects on the moiré pattern. For instance when one of two layers has been twisted by θ_m and subjected to a uniaxial heterostrain ε_H along the direction θ_s from the x-axis, the set of three experimentally accessible real space moire wavelengths λ_i can be expressed in terms of θ_m, θ_s, ε_H, the unstrained monolayer reciprocal lattice vectors $\mathbf{k}_i$, and the Poisson ratio ρ as follows[146]:

$$\lambda_i = \frac{4\pi}{\sqrt{3}} \left| \begin{bmatrix} \cos(\theta_m - \theta_s) & -\sin(\theta_m - \theta_s)) \\ \sin(\theta_m - \theta_s) & \cos(\theta_m - \theta_s) \end{bmatrix} \begin{bmatrix} \frac{1}{1+\varepsilon_H} & 0 \\ 0 & \frac{1}{1-\rho\varepsilon_H} \end{bmatrix} \begin{bmatrix} \cos(\theta_s) & -\sin(\theta_s) \\ \sin(\theta_s) & \cos(\theta_s) \end{bmatrix} \mathbf{k}_i - \mathbf{k}_i \right|^{-1} \tag{A.27}$$

We used a ρ of 0.16 for graphene[260] in Chapter 2 and 0.19[261] for WSe_2 in Chapter 4. In Chapter 3, we used a ρ of 0.23 and 0.25 for P and AP MoS_2 respectively[262]. These values assume the elastic response of each material is roughly equivalent to that of the most energetically favorable stacking order. While this choice neglects the variation in stacking order throughout the moiré, we found that using alternative estimates of ρ has a minor effect on the obtained θ_m and ε_H values.

For homobilayers, we obtained the local twist angle and heterostrain by triangulating using the centers of the AA (for TBL-Gr), MMXX (for P TMDs), or XMMX (for AP TMDs) regions and fitting the resultant moiré wavelengths λ_i to Equation A.27 using with nonlinear least squares. A similar approach was used for the twisted trilayers, as shown in Fig. 4.10, 4.11 and 4.14. However, heterobilayer systems have an added complication, where the difference in material responses of the two layers results in an under-determined set of equations. This prohibits us from relating any asymmetry in the three moiré wavelengths to a well-defined heterostrain for these systems. Further, the average real space moiré wavelength λ in heterobilayer samples is set by both the twist angle and local lattice constant mismatch[57] $\delta = 1 - a_S/a_L$ (see Equation A.28), both of which can vary throughout a given sample. Again, here a_S and a_L are the smaller and larger lattice constants, respectively:

$$\lambda = \frac{(1-\delta)a_L}{\sqrt{\delta^2 + 2(1-\delta)(1-\cos(\theta_m))}} \tag{A.28}$$

In response to this, we calculated the local lattice constant mismatch of the heterobilayer samples by assuming a constant twist angle for a given dataset, which was obtained from the average CBED pattern for each dataset. To control for heterostrain effects and twist angle heterogeneity, we then narrowed our analysis to heterobilayers samples displaying both minimal asymmetry in the three moiré wavelengths and minimal λ variation.

A.9 Rigid moiré subtraction

For our study of TBL-Gr in Chapter 2, we calculated the reconstruction rotation (θ_R) and simple shear strains by subtracting the average moiré twist angle obtained from triangulation (described in Appendix, Section 8) from the total fixed-body rotation (Equations 2.2 and A.24). For our study of TMD moiré bilayers in Chapter 3, we updated this procedure to also account for lattice mismatch and uniaxial heterostrain. In order to assess the local rotation and dilation due to reconstruction in these samples, we subtracted off the rotation and dilation expected from a rigid moiré with the same interlayer twist angle, lattice constant mismatch, and/or heterostrain (again obtained from the model described in Appendix, Section 8). Assuming an interlayer twist of θ_m and a heterostrain of ε_H in the direction θ_s from the x-axis, we can relate the atomic positions of the two layers $\mathbf{r}_{ij}^{top}$ and $\mathbf{r}_{ij}^{bottom}$ as follows, where ρ is the material's Poisson ratio (see Appendix, Section 8 for values used):

$$\mathbf{r}_{ij}^{top} = \begin{bmatrix} \cos(\theta_m - \theta_s) & -\sin(\theta_m - \theta_s) \\ \sin(\theta_m - \theta_s) & \cos(\theta_m - \theta_s) \end{bmatrix} \begin{bmatrix} 1+\varepsilon_H & 0 \\ 0 & 1-\rho\varepsilon_H \end{bmatrix} \begin{bmatrix} \cos(\theta_s) & -\sin(\theta_s) \\ \sin(\theta_s) & \cos(\theta_s) \end{bmatrix} \mathbf{r}_{ij}^{bottom}$$

The interlayer displacement of the top layer $\mathbf{u}^{top}$ associated with each atom in the rigid moiré is therefore given by $\mathbf{u}_{ij}^{top} = (\mathbf{r}_{ij}^{top} - \mathbf{r}_{ij}^{bottom})/2$ at each pixel location defined in reference to the bottom layer $\mathbf{r}_{ij}^{bottom} = a_0(x_i, y_j)$ where a_0^{bottom} is the lattice constant of the bottom layer. Example calculated rigid displacement maps are shown in Fig. 3.4f. Computing the local total rotation and dilation from this displacement field, in accordance with the strain mapping procedure outlined in Appendix, Section 6, results in (to first order in θ_m) a θ_T^{top} of $(2 + \varepsilon_H - \rho\varepsilon_H)\theta_m/2$ and a dilation of $(\varepsilon_H - \rho\varepsilon_H)/2$, both irrespective of θ_s and given in units of a_0^{bottom}.

Similarly, a twisted heterobilayer with an interlayer twist of θ_m and a lattice constant mismatch of δ results in the following displacements.

$$\mathbf{r}_{ij}^{top} = \begin{bmatrix} \cos(\theta_m) & -\sin(\theta_m) \\ \sin(\theta_m) & \cos(\theta_m) \end{bmatrix} \begin{bmatrix} 1+\delta & 0 \\ 0 & 1+\delta \end{bmatrix} \mathbf{r}_{ij}^{bottom}$$

This is the same expression as the heterostrained homobilayer with $\rho = -1$, $\varepsilon_H = \delta$, and $\theta_s = 0$ such that the interlayer dilation $\nabla \cdot \mathbf{u}^{top} = \delta$ and total intralayer rotation $\theta_T^{top} = (1+\delta)\theta_m/2$. We therefore see that, in terms of local rotations and dilations, heterostrained samples act like heterobilayers with an effective lattice constant mismatch of $(\varepsilon_H - \rho\varepsilon_H)/2$. For the strain maps presented in Chapter 3, these rigid values were subtracted from the obtained local rotations and dilations to obtain the reported interlayer reconstruction rotation and dilation. We note that this analysis (and that of the twist angle and lattice mismatch extraction) is carried out using one of the two layers as a reference configuration rather than their average. This slightly modifies the obtained rigid values (by less than 1%) with negligible impact on the resulting analysis.

A.10 Uncertainty in strain measurements

In order to estimate the percent uncertainty and detection limit of the reported strain calculations, we calculated the residuals between the raw disk intensities $I_{raw}(g_j)$ and the predicted $I_{fit}(g_j)$ following the displacement fitting procedure described in Appendix, Section 2. The mean and standard deviations of the residuals in the normalized intensities were on the order of -0.05 and 0.15 respectively, representing systematic bias and root mean squared error (RMSE) respectively. We note that this RMSE uncertainty in the intensities will reflect a larger displacement uncertainty in the $\mathbf{u} \approx 0$ domains in which the dependence of u on intensity is steeper. The small negative systematic bias in the intensity residuals is larger for samples with more background noise and reflects the fact that the high frequency noise not captured by the fitting function increases the average normalized intensity of the raw data. We believe the error from the fit procedure originates primarily from 1) experimental noise (carbon contamination, sample defects, and variation in tilt) causing a deviation from the expected intensity variation, 2) the validity of the approximations used in the fitting function derivation, and 3) the optimization procedure. We note that some of these effects may not be reflected in the obtained residuals and instead result in a good fit to a biased displacement value, which is difficult to quantify. Through collecting and averaging over strain values obtained at many different pixel locations, we are able to obtain a significantly lower standard error than through propagating the intensity uncertainties within a single pixel. The standard error measured is on the order of 0.1% dilation and a 0.1° rotation as seen in the presented strain values obtained across samples, which is associated with dilation and rotation detection limits roughly three times as large.

A.11 Distinguishing heterostrain from sample drift

A distorted moiré image alone is insufficient evidence to conclude the presence and magnitude of heterostrain, as sample drift could induce similar distortions. To estimate the amount of sample drift present, we collected replicate images at different STEM scan angles of two twist-angle-homogeneous regions that exhibited heterostrain in the DF-TEM images (Fig. A.13). Because sample drift is typically determined by the orientation of the sample holder and not the STEM scan direction, the distortions produced by two subsequent scans should be different for different scan directions relative to the true moiré geometry[263]. We computed the average angles between different SP regions to quantify the change in unit cell distortion. For both pairs of images, the change in angle with STEM scan direction was no greater than 2°, whereas the difference between the smallest and largest SP region angles was greater than 20° (Fig. A.13 and Table A.1). Furthermore, the 1D shear strain features discussed in

Chapter 2 (Fig. 2.18b,c) rotated consistently with the STEM scan direction (Fig. A.13). We conclude, therefore, that the moiré superlattice distortions seen in our images can be reliably attributed to heterostrain. This conclusion is further corroborated by (1) conventional DF-TEM images of the 4D-STEM scan areas (Fig. 2.1c), which also revealed these same distortions, and (2) the strong variations observed within individual scans, particularly near a tear in one graphene layer (Fig. 2.8 and Fig. 2.18b).

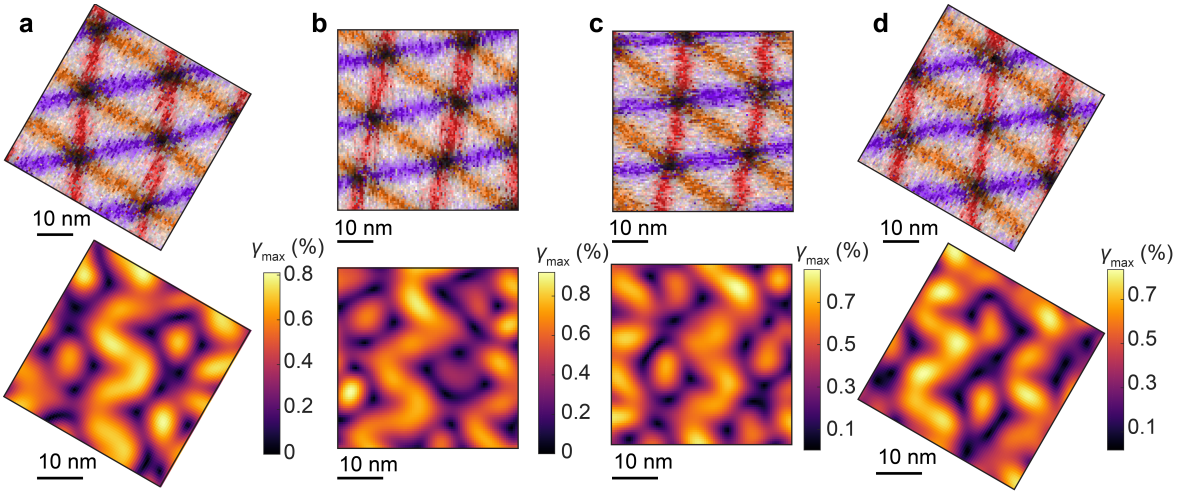

Figure A.13: Displacement field (top) and maximum shear strain (bottom) maps. Replicate pairs of images at different STEM scan directions in twist angle homogeneous regions with $\theta_m = 0.64°$ (**a,b**) and $\theta_m = 0.65°$ (**c,d**). STEM scan directions are 210° (**a**), 180° (**b**), 270° (**c**), and 210° (**d**). These regions are in close proximity (within ≈50 nm of each other) and exhibit heterostrain in DF-TEM images (region 3 of Fig. 2.1c). These maps have been counterrotated by the scan direction. Since the displacement field and strain amps are aligned in both sets of images (**a** aligns with **b** and **c** aligns with **d**), we conclude that drift is negligible and cannot be responsible for the observed heterostrain. Analysis of SP intersection angles (Table A.1) and the DF-TEM images provides additional corroboration.

Table A.1: Effect of STEM scan direction on observed moiré distortions. Reported values indicate the average measured angle between the listed SP types.

	270° Scan ($\theta_m = 0.65°$)	**210° Scan** ($\theta_m = 0.65°$)	**210° Scan** ($\theta_m = 0.64°$)	**180° Scan** ($\theta_m = 0.64°$)
Purple–Red	71.8°	73.5°	68.5°	67.6°
Red–Orange	61.9°	60.2°	66.1°	68.2°
Orange–Purple	46.3°	46.3°	45.4°	44.2°

A.12 Relaxation simulations for twisted bilayer graphene

A.12.1 Reconstruction model

To enable band structure calculations considering the effects of AA and AB reconstruction separately, a simple parameterized model was developed. AA reconstruction was modelled by a 2D Gaussian rotation field centred on each AA region. AB reconstruction was modelled by including a constant rotation field within each triangular AB domain. The AB domain edges were drawn at a buffer distance b_{AB} from the lines connecting two AA regions, and the edges were then smoothed by a Gaussian filter. Consequently, the AB reconstruction rotation is constant within the centre of the AB domain and tapers off near the edges, matching our experimental observations. The reconstruction parameters used for the band structure calculations are given in Table A.2. Note that the maximum applied rotation angle in the individual AA and AB domains (α_{AA} and α_{AB}) are not mathematically the same as the fixed-body rotation of the sample in the AA and AB regions (θ_R^{AA} and θ_R^{AB}), owing to the overlap between rotation fields centred on multiple AA and AB domains within this model. Reconstruction parameters were chosen to give a good match to the sample geometry and θ_R^{AA}, θ_R^{AB} values within the constraints of the model.

A.12.2 Band structures of relaxed TBL-Gr from a continuum model

For evaluation of the interlayer electronic tunnelling functions, we use a tight-binding model extracted from DFT calculations[70]. We follow an electronic continuum model prescription[264], updated to allow for atomic relaxations. The relaxations are included by evaluating the Fourier transform of the interlayer tight-binding coupling at the relaxed configurations, $\tilde{t}(b+\mathbf{u}(b))$, instead of the bare configurations, $\tilde{t}(b)$ (see below).

Table A.2: Parameters used in the simplified TBL-Gr reconstruction model. Here α_{AA} and α_{AB} give the applied rotation field centered on each individual AA or AB domain, σ_{AA} and σ_{AB} give the Gaussian standard deviations for AA rotation decay and the AB smoothing kernel, and b_{AB} gives the buffer distance for defining the AB rotation field area.

$\theta_{\mathbf{m}}(^\circ)$	$\alpha_{\mathbf{AA}}(^\circ)$	$\alpha_{\mathbf{AB}}(^\circ)$	$\sigma_{\mathbf{AA}}$ (Å)	$\sigma_{\mathbf{AB}}$ (Å)	$\mathbf{b_{AB}}$ (Å)
1.15	0.65	-0.20	45	15	10
0.50	0.65	-0.35	50	25	15
0.30	0.85	-0.30	50	25	15

The continuum model for the band structure of TBL-Gr[71] can be extended to include arbitrary relaxations[158,159]. The central idea is to extract the effective interlayer scattering terms between momenta q_i and q_j, usually notated as T_{ij}, by Fourier transforming the interlayer orbital-to-orbital couplings, $t(b)$, where b is the configuration (relative distance between the pairs of carbon atoms) and quickly falls to zero within 5 Å. Generally, the T matrices take the form:

$$T_{ij} = \begin{pmatrix} \omega_0 e^{i\phi_{ij}^{11}} & \omega_1 e^{i\phi_{ij}^{12}} \\ \omega_1 e^{i\phi_{ij}^{21}} & \omega_0 e^{i\phi_{ij}^{22}} \end{pmatrix} \tag{A.29}$$

Here, the phases ϕ_{ij}^{mn} depend on the position of the orbitals and the choice of origin, and the $\omega_0 \equiv \omega_{AA}$ and $\omega_1 \equiv \omega_{AB}$ correspond to the effective interlayer coupling strength between similar and dissimilar orbitals of opposite layers, respectively. Relaxations, defined by a vector field u for interlayer relaxation, modify the relative displacement of each pair of atoms, and so we need to consider the transform of the object $t(b + u(b))$. For simplicity, we ignore out-of-plane corrugations of the two lattices, and consider only local rotations around AA and AB stacking sites as discussed in the Reconstruction Model section (Section A.9). We also ignore in-plane corrections to the Hamiltonian caused by modifications to the (intralayer) couplings of monolayer graphene under shearing strain. These corrections require in-plane momentum scattering based on the Fourier coefficients of the relaxation pattern and, for the assumptions of Gaussian rotations, do not take simple analytic forms.

Fig. 2.17a–c shows the band structures under various relaxation assumptions. The effective interlayer coupling terms $(\omega_{AA}, \omega_{AB})$ are provided in Table A.3. Note that this model has not been explicitly symmetrized, and so some erroneous gaps of order 2 meV are present due to symmetry-breaking errors introduced during numerical interpolation of the interlayer tunneling. These errors are most noticeable for the 0.35° band structure (Fig. 2.17a). The rigid lattice has no moiré superlattice gaps, but including either the AA or AB relaxation assumption for $\theta_m = 1.15^\circ$ opens up gaps above and below the flat-band manifold (Fig. 2.17c). In general, inclusion of

either assumption reduces ω_{AA} and increases ω_{AB}. At smaller angles, the AB rotation plays a larger role than the AA rotation, while near the magic angle the opposite is true.

Table A.3: Calculated interlayer coupling terms (in meV) for TBL-Gr at three values of θ_m under four relaxation assumptions: no reconstruction, AA rotation alone, AB rotation alone, and full reconstruction (AA and AB rotations).

	No reconstruction		AA rotation only		AB rotation only		Both rotations	
$\theta_m(^\circ)$	ω_{AA}	ω_{AB}	ω_{AA}	ω_{AB}	ω_{AA}	ω_{AB}	ω_{AA}	ω_{AB}
0.35	88	88	73	93	45	95	27	95
0.50	88	88	67	95	63	95	39	97
1.15	88	88	78	92	84	90	74	94

A.12.3 Computation of interlayer tunneling functions

The values given in Table A.3 and for $(\omega_{AA}, \omega_{AB})$ are only approximate measures of the effective interlayer electronic tunneling. For a momentum basis centered at $K_0 = K_1$, the K-point of Layer 1's (bottom layer) Brillouin zone, there are three highest order scatterings to Layer 2, given by the three smallest values of $K_0 + G_2$, where G_2 is any reciprocal lattice vector of Layer 2. These couplings are given by $\tilde{t}(K_0 + G_2)$, and this is often the value taken to estimate ω_{AA} and ω_{AB}. The general form of the tunneling is given by $\tilde{t}(K_0+G_1+G_2)$, where G_1 is any reciprocal lattice of Layer 1. As long as $G_1+G_2 \approx 0$, the coupling stays near K_0, but is now sampled in a regular grid of the moiré reciprocal lattice. For rigid lattices, $\tilde{t}$ is smooth and non-zero in the vicinity of K_0, and so the approximation $\tilde{t}(K_0+G_1+G_2) \approx \tilde{t}(K_0) \equiv \omega_{AA} = \omega_{AB}$ is a fairly good choice[71]. However, for relaxed lattices, this assumption is not always well justified[158,159]. The variation in $\tilde{t}(k)$ can become quite severe near K_0, and can even be sampled right on a nodal point of the Fourier transform, as in the case of the fully relaxed AA coupling at $\theta_m = 0.5^\circ$, shown in Fig. 2.17b. For this reason, analysis of the effective ω strengths at the magic-angle does not always generalize easily to relaxed TBL-Gr at smaller angles. The interlayer tunneling functions for orbitals of similar type (i.e., A-to-A and B-to-B) for three different twist angles are displayed in Fig. A.17, A.19, and A.21 respectively. The interlayer tunneling functions for orbitals of dissimilar type (i.e., A-to-B and B-to-A) are displayed in Fig. A.18, A.20, and A.22.

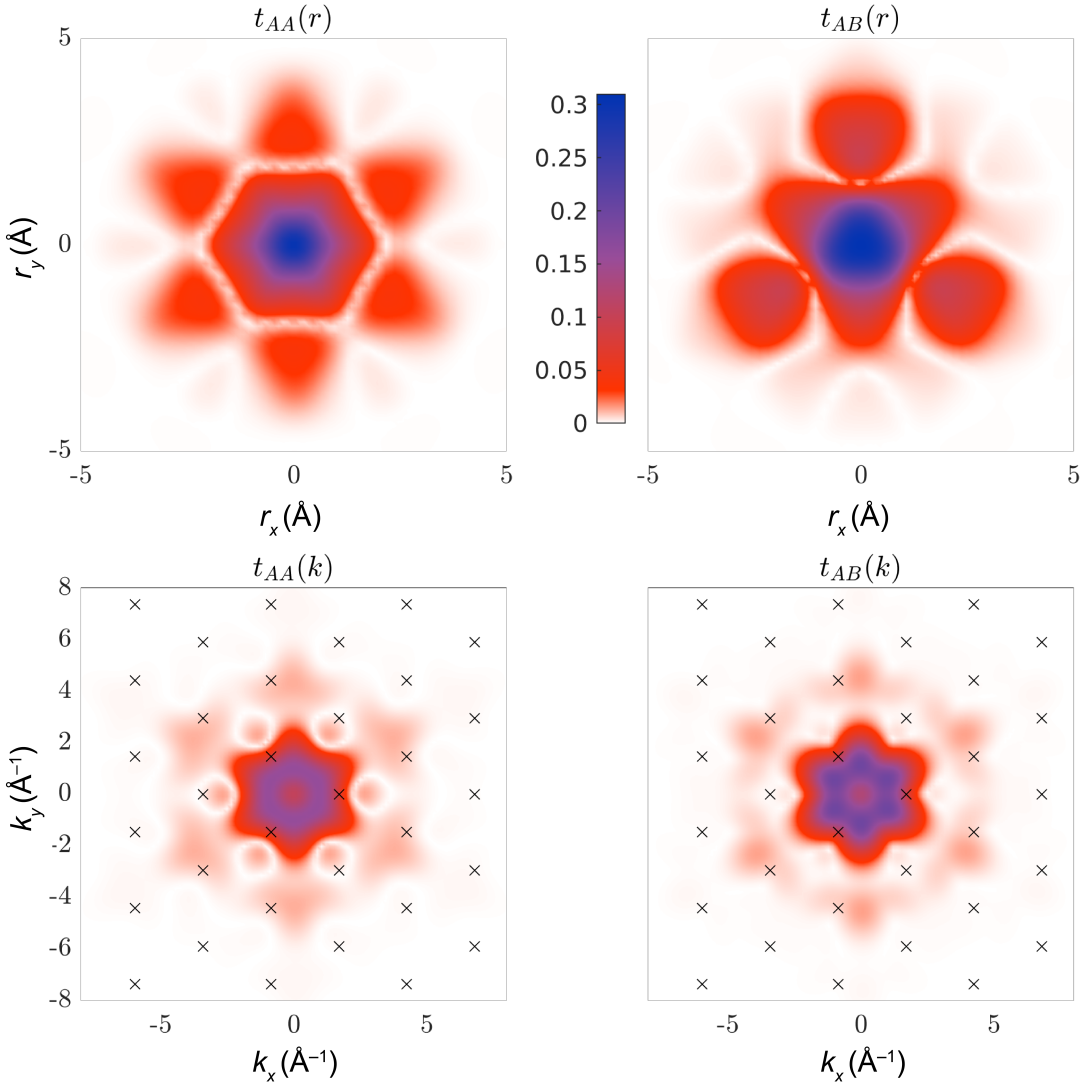

Figure A.14: Absolute values of the interlayer coupling for the fully relaxed TBL-Gr model at $\theta_m = 1.15°$ (i.e., both AA and AB centred rotations included). Top panels present the real space interlayer coupling after full relaxation, while bottom panels display their Fourier transform. The black "×" marks indicate the relevant scattering momenta, $K_0 + G$, where K_0 is the momentum corresponding to the valley we are expanding around and G is the reciprocal lattice of untwisted graphene. Left panels show couplings between similar orbitals (A–A, or ω_o), while right panels show couplings between dissimilar orbitals (A–B, or ω_1).

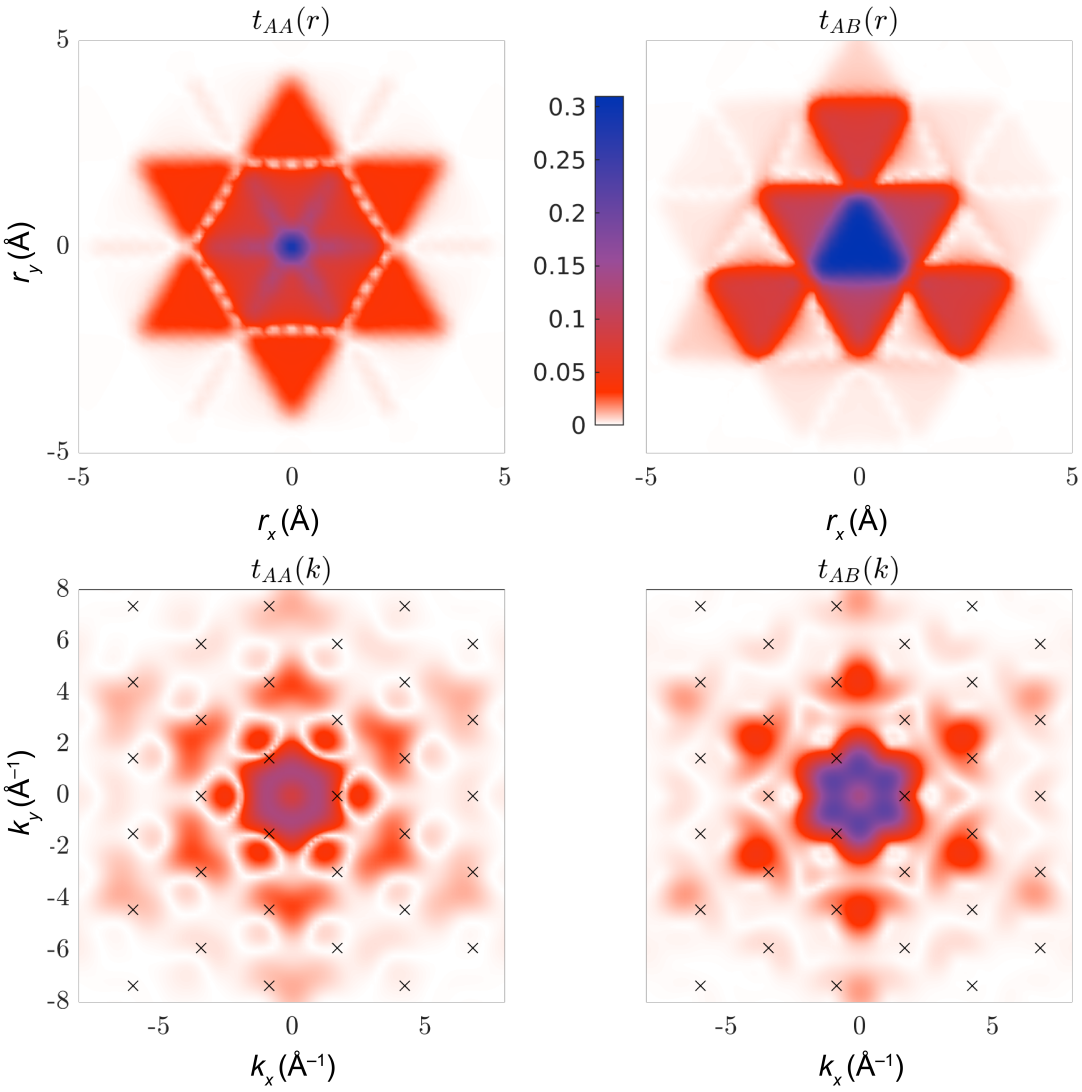

Figure A.15: Absolute values of the interlayer coupling for the fully relaxed TBL-Gr model at $\theta_m = 0.5°$ (i.e., both AA and AB centred rotations included). Top panels present the real space interlayer coupling after full relaxation, while bottom panels display their Fourier transform. The black "×" marks indicate the relevant scattering momenta, $K_0 + G$, where K_0 is the momentum corresponding to the valley we are expanding around and G is the reciprocal lattice of untwisted graphene. Left panels show couplings between similar orbitals (A–A, or ω_o), while right panels show couplings between dissimilar orbitals (A–B, or ω_1).

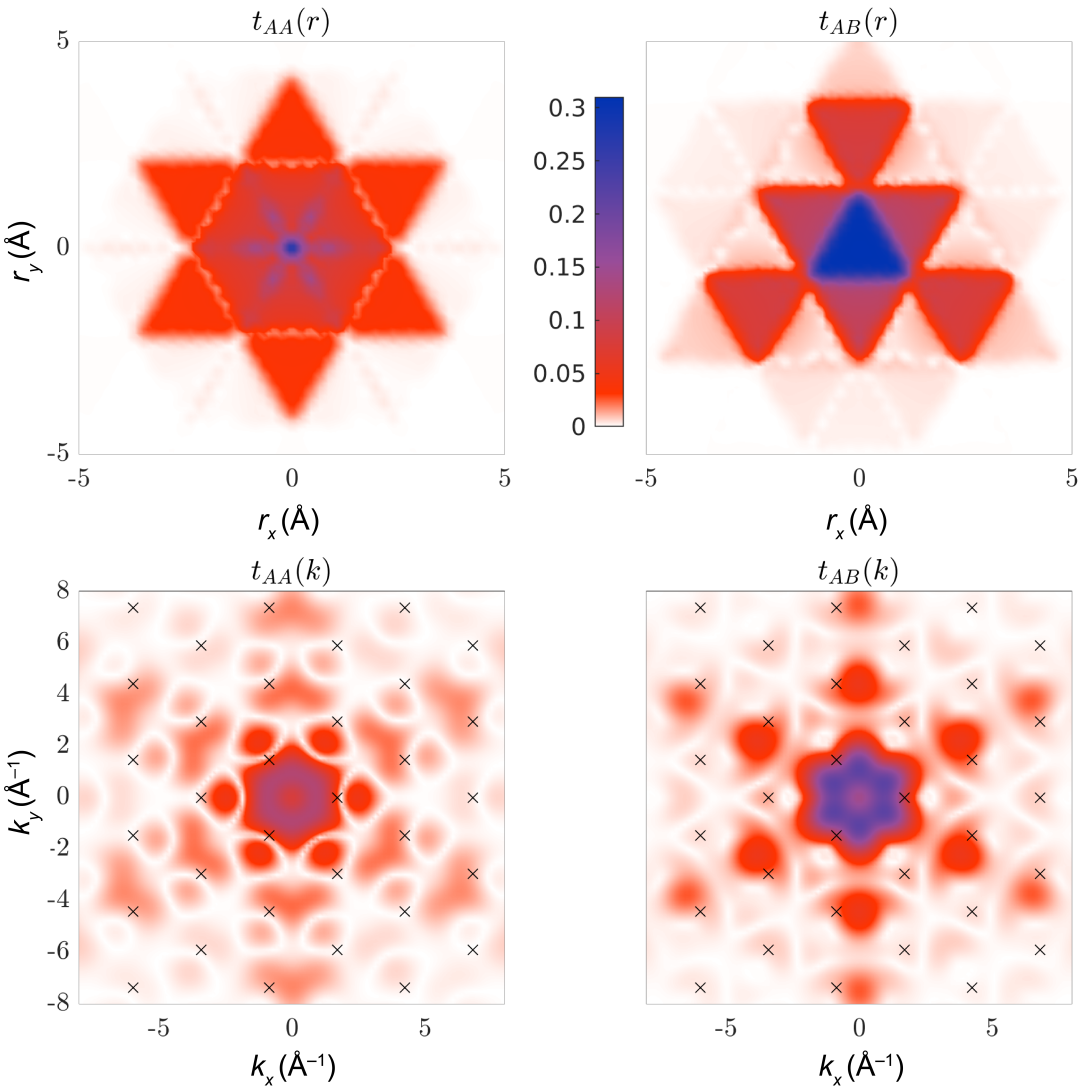

Figure A.16: Absolute values of the interlayer coupling for the fully relaxed TBL-Gr model at $\theta_m = 0.35°$ (i.e., both AA and AB centred rotations included). Top panels present the real space interlayer coupling after full relaxation, while bottom panels display their Fourier transform. The black "×" marks indicate the relevant scattering momenta, $K_0 + G$, where K_0 is the momentum corresponding to the valley we are expanding around and G is the reciprocal lattice of untwisted graphene. Left panels show couplings between similar orbitals (A–A, or ω_o), while right panels show couplings between dissimilar orbitals (A–B, or ω_1).

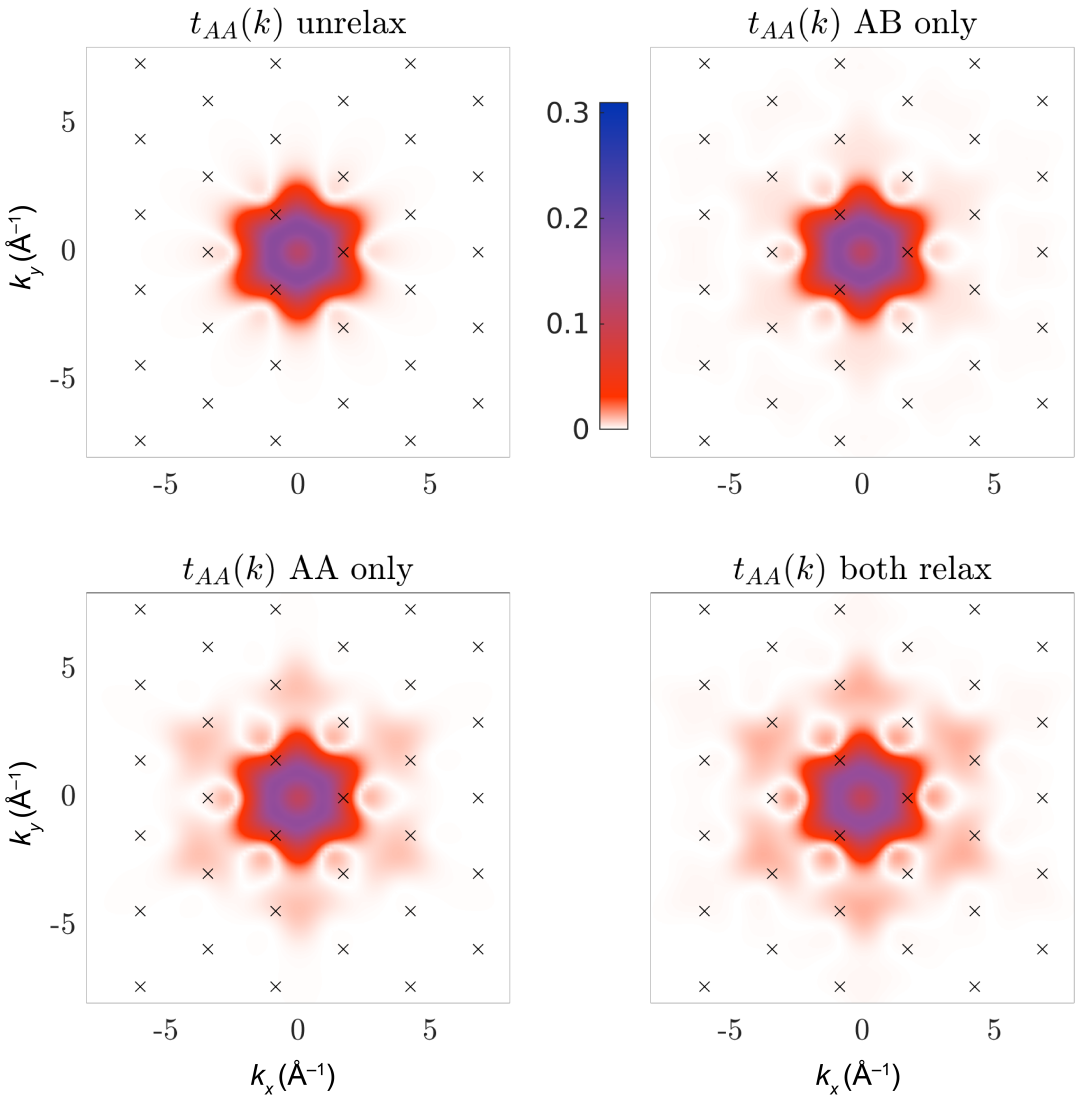

Figure A.17: Absolute value of interlayer A-to-A and B-to-B (ω_0) scattering between the layers (in momentum space) for TBL-Gr at $\theta_m = 1.15°$ for all four possible relaxation assumptions. The black "×" marks indicate the momenta which all relevant scatterings are near, $K_0 + G$.

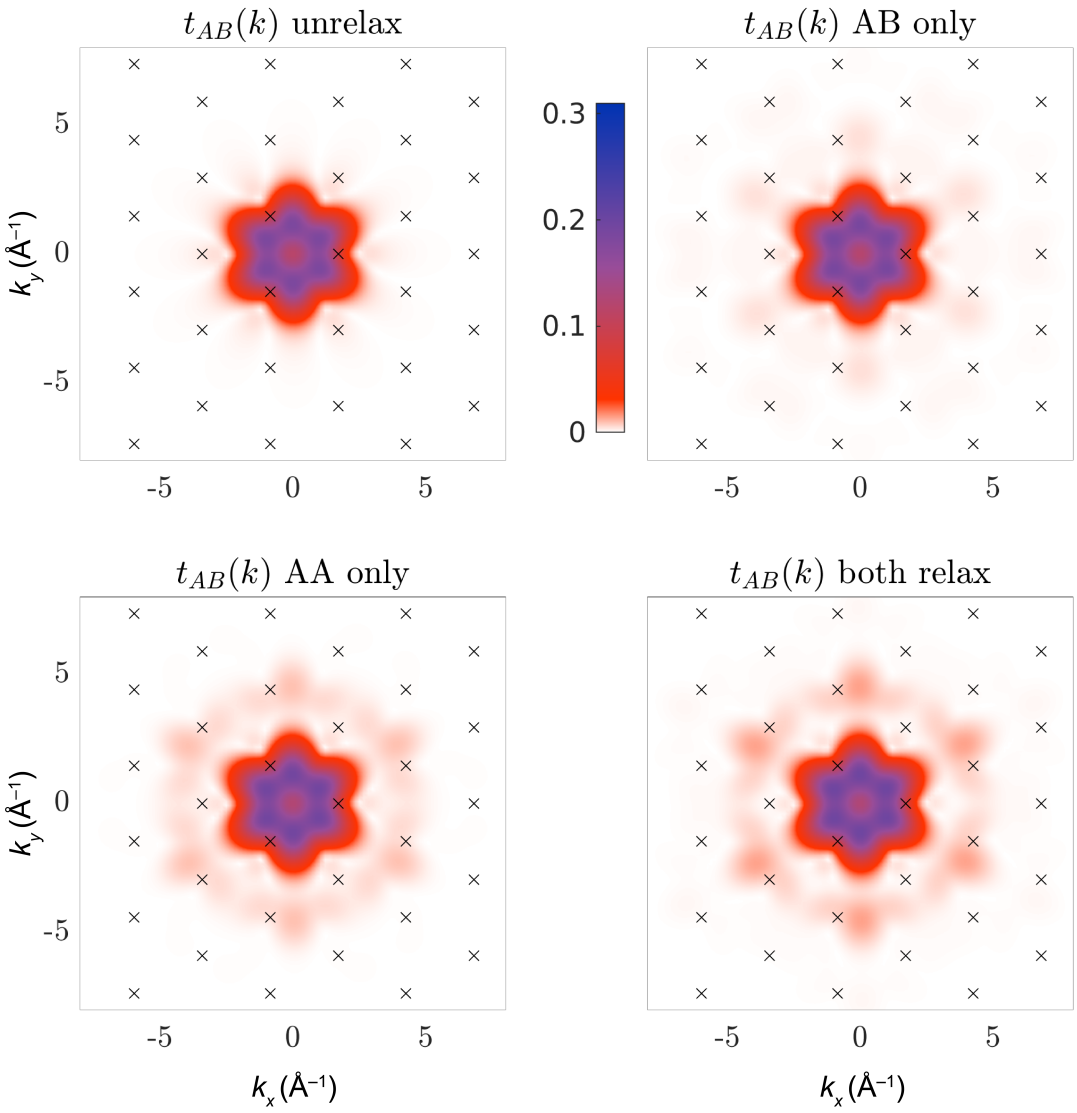

Figure A.18: Absolute value of interlayer A-to-B and B-to-A (ω_1) scattering between the layers (in momentum space) for TBL-Gr at $\theta_m = 1.15°$ for all four possible relaxation assumptions. The black "×" marks indicate the momenta which all relevant scatterings are near, $K_0 + G$.

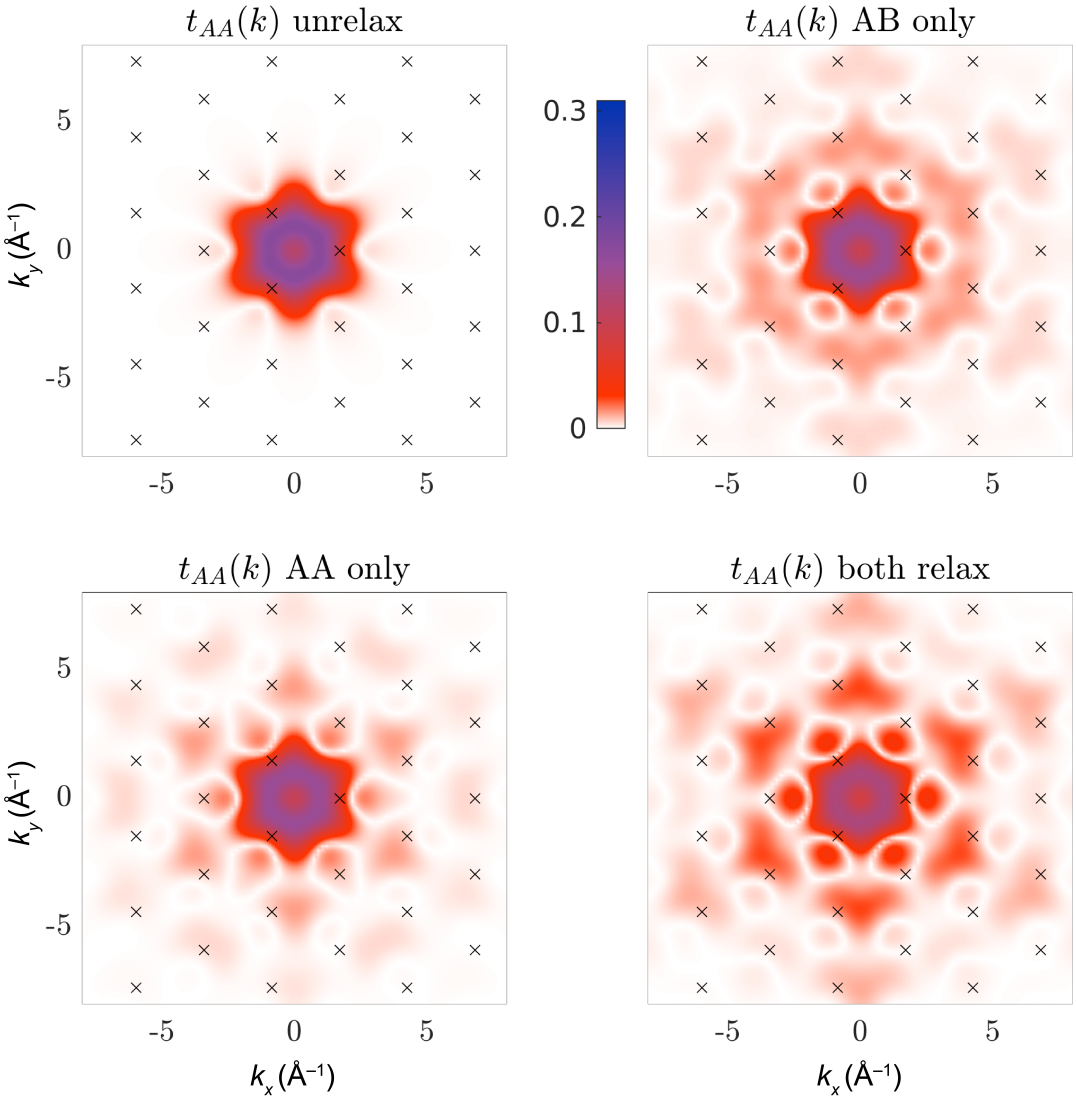

Figure A.19: Absolute value of interlayer A-to-A and B-to-B (ω_0) scattering between the layers (in momentum space) for TBL-Gr at $\theta_m = 0.5°$ for all four possible relaxation assumptions. The black "×" marks indicate the momenta which all relevant scatterings are near, $K_0 + G$.

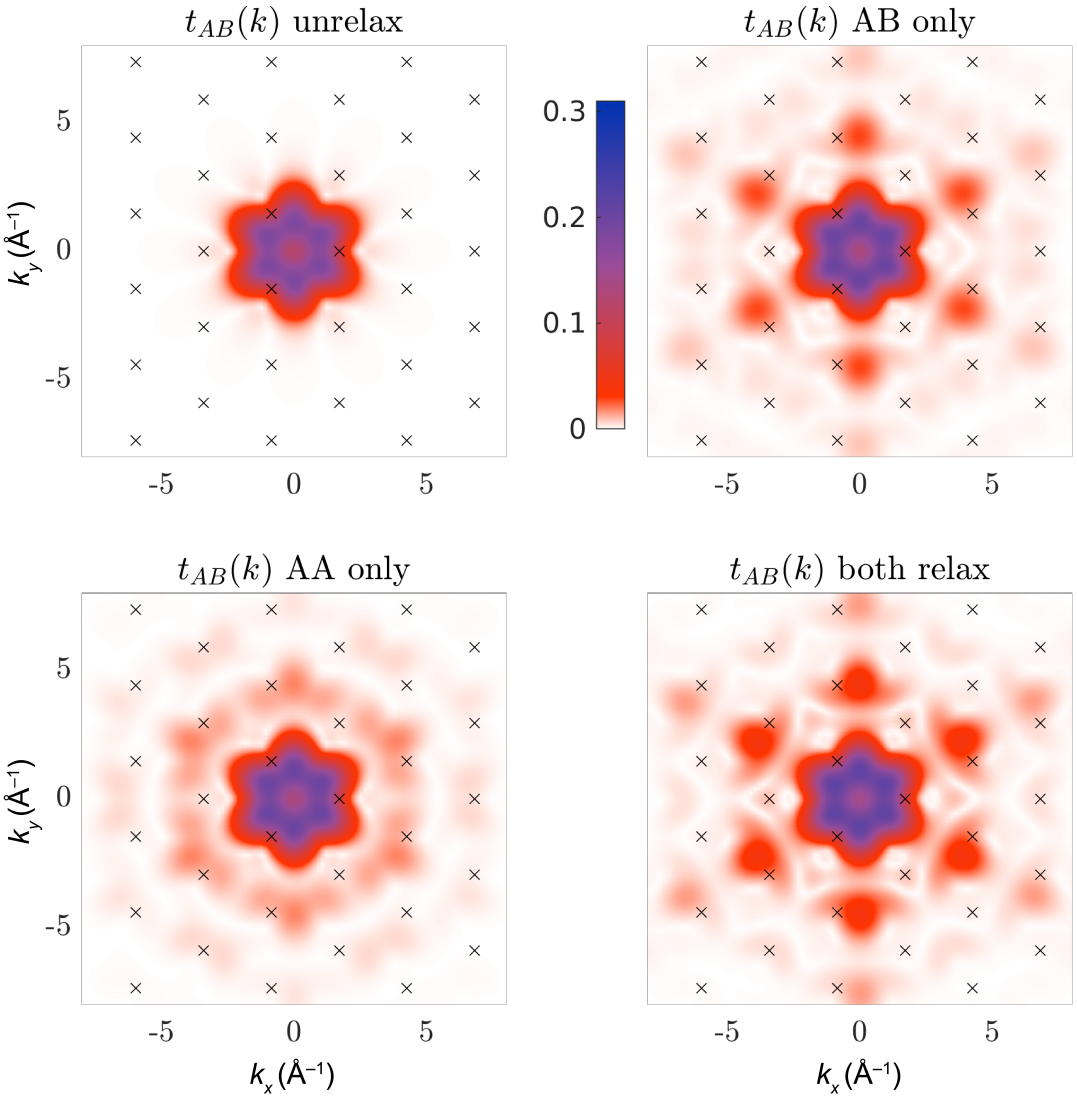

Figure A.20: Absolute value of interlayer A-to-B and B-to-A (ω_1) scattering between the layers (in momentum space) for TBL-Gr at $\theta_m = 0.5°$ for all four possible relaxation assumptions. The black "×" marks indicate the momenta which all relevant scatterings are near, $K_0 + G$.

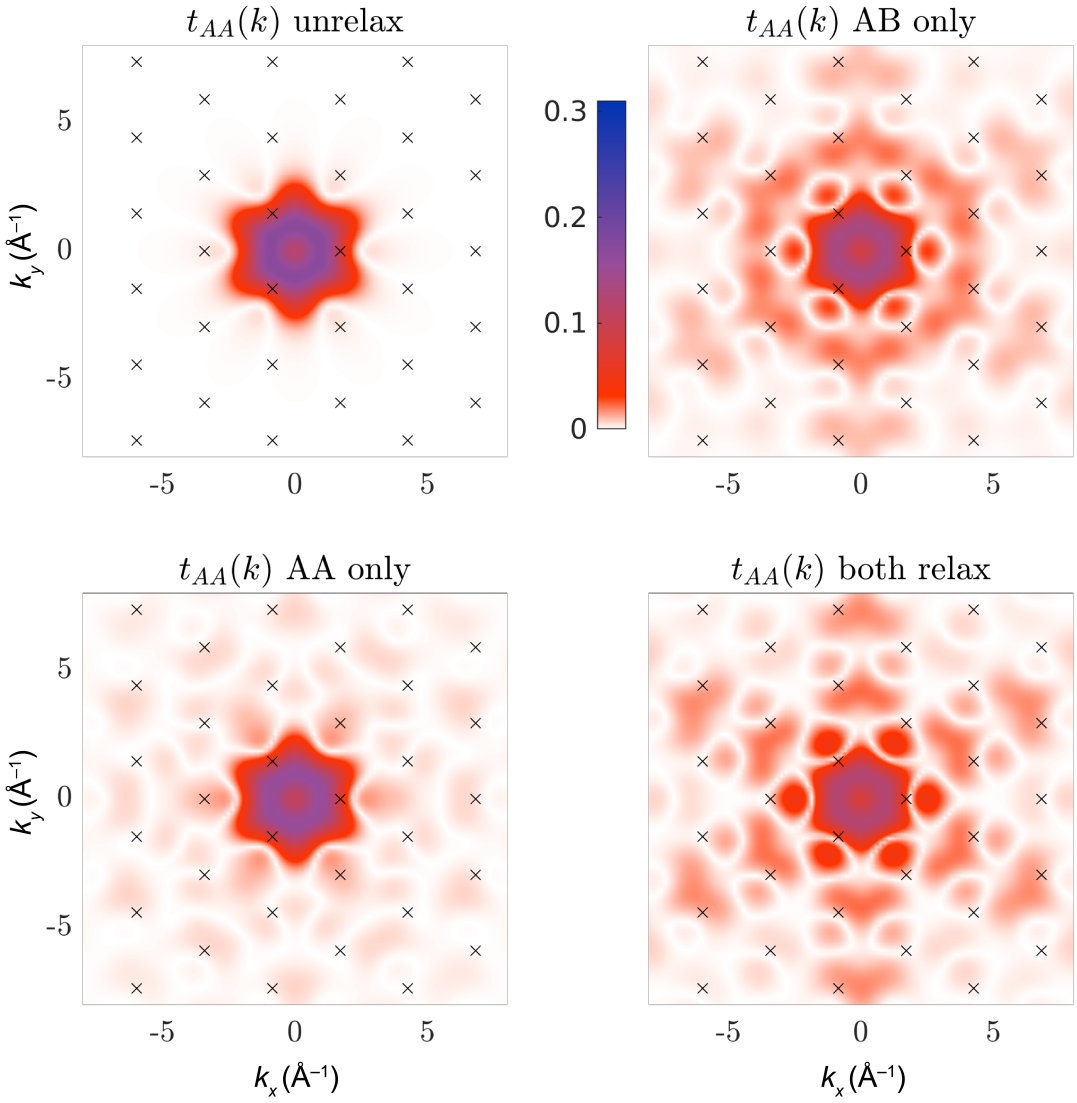

Figure A.21: Absolute value of interlayer A-to-A and B-to-B (ω_0) scattering between the layers (in momentum space) for TBL-Gr at $\theta_m = 0.35°$ for all four possible relaxation assumptions. The black "×" marks indicate the momenta which all relevant scatterings are near, $K_0 + G$.

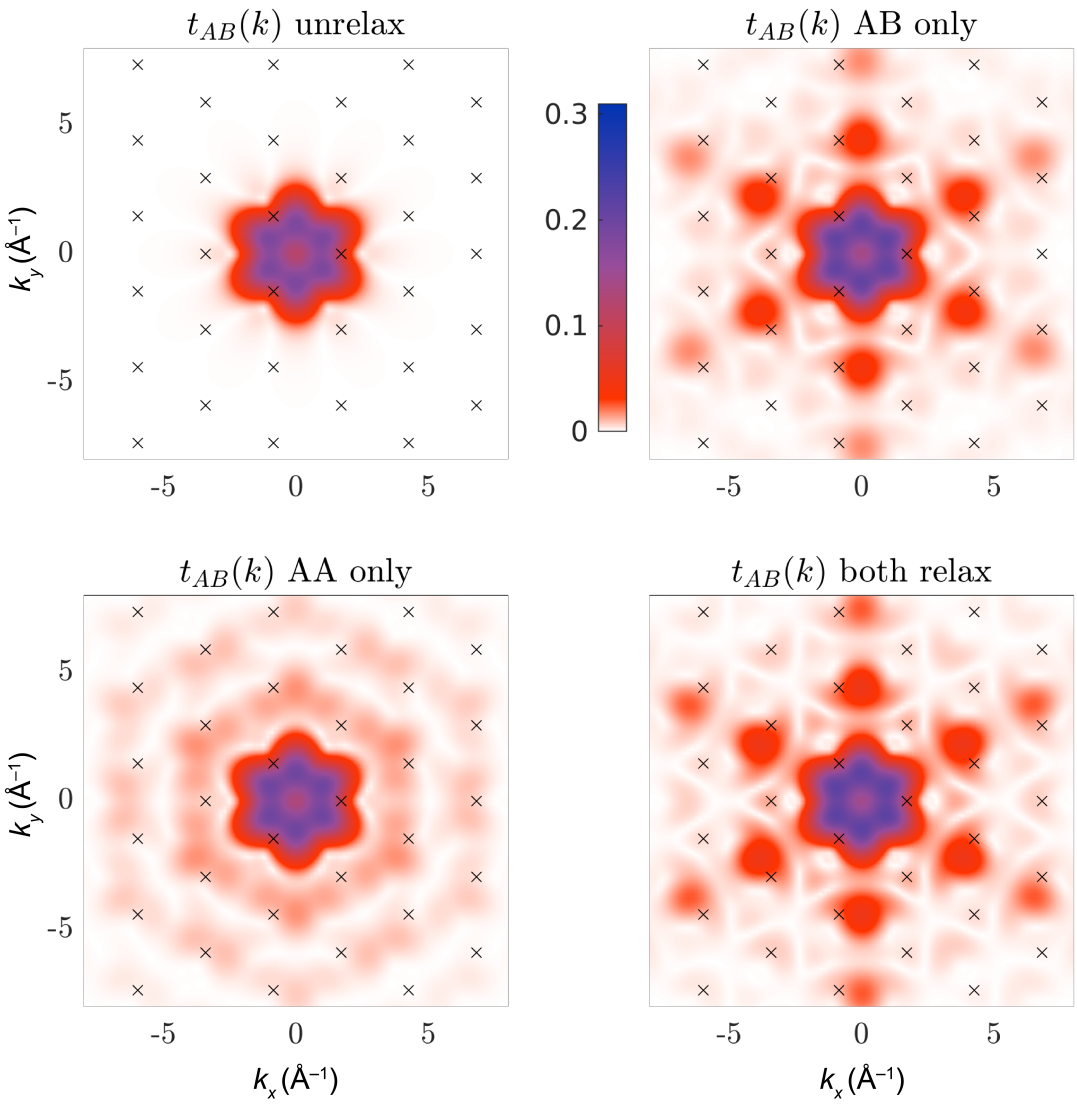

Figure A.22: Absolute value of interlayer A-to-B and B-to-A (ω_1) scattering between the layers (in momentum space) for TBL-Gr at $\theta_m = 0.35°$ for all four possible relaxation assumptions. The black "×" marks indicate the momenta which all relevant scatterings are near, $K_0 + G$.

A.12.4 Definition of β_{ω_0} and β_{ω_1}

In Fig. 2.17d, we presented variables β_{ω_0} and β_{ω_1} as the value of a relative "angle" between interlayer couplings ($\tilde{t}(\vec{k})$) for θ_{AA} and θ_{AB} rotations only versus the fully relaxed interlayer coupling. This is defined by introducing a generalized inner-product between two different complex interlayer tunneling functionals, $f(\vec{k})$ and $g(\vec{k})$:

$$\langle f, g\rangle = \int d\vec{k} f^*(\vec{k}) g(\vec{k}). \tag{A.30}$$

The relative angle between two interlayer tunneling functionals is then given by:

$$\beta_{fg} = \cos^{-1}\left(\frac{\mathrm{Re}\left(\langle f, g\rangle\right)}{\sqrt{\langle f, f\rangle\langle g, g\rangle}}\right). \tag{A.31}$$

We define $\beta_{\omega_0} \equiv \beta_{\tilde{t}^{\mu}_{AA}\tilde{t}^{\mathrm{f}}_{AA}}$ and $\beta_{\omega_1} \equiv \beta_{\tilde{t}^{\mu}_{AB}\tilde{t}^{\mathrm{f}}_{AB}}$, with $\tilde{t}^{\mu}_{ij}$ the interlayer coupling between orbitals i and j relaxation indexed by μ for θ_{AA} or θ_{AB} rotation only, and $\tilde{t}^{f}_{ij}$ the coupling for the full relaxation model with both rotations.

A.12.5 Finite element relaxation of TBL-Gr

The finite-element relaxation method uses a generalized stacking fault energy (GSFE) and elastic moduli for bilayer graphene, both of which are extracted from previous Density Functional Theory (DFT) calculations[180,265]. The elastic relaxation model consists of an elastic energy term, capturing the strain energy of each layer, and a GSFE term, capturing the variations in interlayer binding energy (see below). To allow for the evaluation of the relaxation for real space superlattices with heterostrain, we impose an initial spatially-dependent interlayer displacement $\mathbf{b}_0(r)$ that includes both rotation and shear. The total energy is then minimized by optimizing the interlayer relaxation field $\vec{u}(r)$. The initial constant shear in $\mathbf{b}_0$ is added to the gradients of $\mathbf{u}$ in the evaluation of the elastic energy. This allows for the optimization of the periodic function $\mathbf{u}$, instead of having to explicitly encode the twisted boundary conditions of the moiré superlattice.

The planar relaxation of twisted 2D bilayers can be well captured by finite-element approaches with parameters extracted from DFT[180,265]. The relative displacement between the layers is given by a spatially-varying interlayer displacement, which will be a sum of an initial displacement $b_0(r)$ and a relaxation field $u(r)$. The moiré supercell is defined by a pair of lattice vectors, which are columns of the 2×2 matrix:

$$A_{\mathrm{sc}} = \begin{pmatrix} m\sin(\beta/2) & -n\sin(\beta/2) \\ m\cos(\beta/2) & n\cos(\beta/2) \end{pmatrix} \tag{A.32}$$

where β is the interior angle of the moiré supercell and m, n are the side lengths of the cell ($\beta = 60^\circ$ and $m = n$ in the absence of heterostrain). The initial displacement

between the layers is given by the vector field:

$$b_0(r) = A_{\text{uc}} A_{\text{sc}}^{-1} r \tag{A.33}$$

where A_{uc} is the 2×2 matrix representing the unit cell of monolayer graphene:

$$A_{\text{uc}} = l/2 \begin{pmatrix} 3 & 3 \\ -\sqrt{3} & \sqrt{3} \end{pmatrix} \tag{A.34}$$

where $l = 1.42$ Å, the nearest-neighbor bonding distance of graphene. The relative orientations of A_{sc} and A_{uc} ensure that the initial configuration is uniformly distributed over the supercell, and the shape of the supercell (e.g. the side lengths and angle β) determines the initial twist angle and heterostrain for the simulation. It also allows us to introduce a relaxation field that is periodic with respect to the moiré supercell as the twisted boundary condition is entirely captured by b_0, allowing for the derivatives of the relaxation field to be evaluated via its Fourier components, instead of finite-element derivative stencils.

We assume the two layers share the displacement equally, e.g. $u_1(r) = -u_2(r) = u(r)/2$. The elastic ("kinetic") energy, related to in-plane deformation of a single layer, is given by:

$$E_{\text{intra}}(u) = \frac{1}{2} \int K \left(\frac{\partial u_x}{\partial x} + \frac{\partial u_y}{\partial y} \right)^2 + G \left[\left(\frac{\partial u_x}{\partial x} - \frac{\partial u_y}{\partial y} \right)^2 + \left(\frac{\partial u_x}{\partial y} + \frac{\partial u_y}{\partial x} \right)^2 \right] dr \tag{A.35}$$

with $[K, G] = [69.518, 47.352]$ eV per unit cell area of graphene[180].

To define the interlayer binding energy between the graphene layers, we employ a generalized stacking fault energy function ($V_{\text{GSFE}}(b)$) which represents the relative energy of each stacking configuration, as extracted from DFT calculations[265]. To respect the symmetries of graphene, we expand V_{GSFE} in terms of its three lowest even Fourier components[180]:

$$\begin{aligned} V_{\text{GSFE}}(b) = c_0 &+ c_1(\cos v + \cos w + \cos(v+w)) \\ &+ c_2(\cos(v+2w) + \cos(v-w) + \cos(2v+w)) \\ &+ c_3(\cos(2v) + \cos(2w) + \cos(2v+2w)) \end{aligned} \tag{A.36}$$

where

$$\begin{pmatrix} v \\ w \end{pmatrix} = 2\pi A_{\text{uc}}^{-1} \begin{pmatrix} b_x \\ b_y \end{pmatrix} \tag{A.37}$$

and $[c_0, c_1, c_2, c_3] = [6.832, 4.064, -0.374, -0.095]$ meV per unit cell area[265]. The total interlayer ("potential") energy is then given by:

$$E_{\text{inter}}(b) = \int V_{\text{GSFE}}(b(r))dr \tag{A.38}$$

To find the relaxed geometry, we initialize the relaxation field $u(r) = 0$, and then minimize

$$E = 2E_{\text{intra}}((b_0 + u)/2) + E_{\text{inter}}(b_0 + u). \tag{A.39}$$

Here we have used the assumption that the two layers have identical relaxations, and thus identical strain energy. During entry to E_{intra}, the gradients of u are evaluated in the Fourier basis and then added to the gradients of b_0 (which are constant throughout the supercell). After optimizing u, the interlayer displacement is given by $u_{\text{inter}} = b_0 + u$, and the effective strain (γ_{max}) is easily extracted.

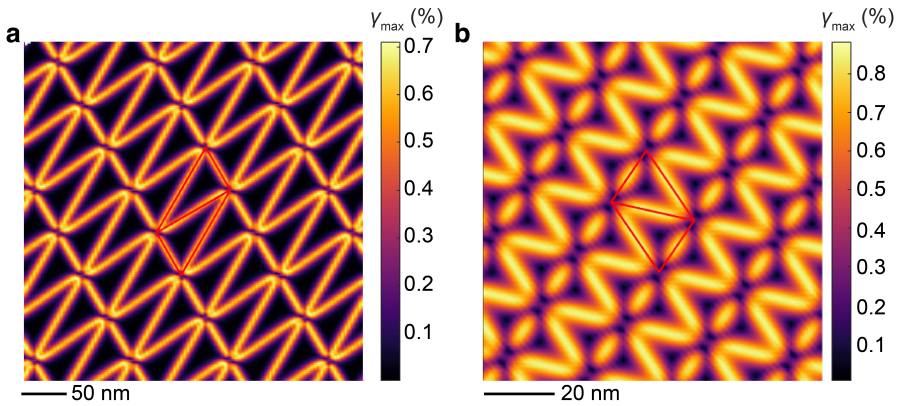

Figure A.23: Finite-element-relaxed maximum shear strain (γ_{max}) maps for **a,** $\theta_m = 0.14°$, $\varepsilon_H = 0.31\%$ and **b,** $\theta_m = 0.63°$, $\varepsilon_H = 0.45\%$.

A.13 Relaxation simulations for TMD moiré bilayers

A.13.1 Density functional theory

In order to model the atomic relaxation vector fields **u** of the moiré bilayers via a continuum elasticity model, three pieces of information are necessary. These are the crystal lattice parameter a, the bulk and shear strain moduli K and G, and the stacking-dependent interfacial energy between pairs of layers which is called the generalized stacking fault energy (GSFE) given by $V_{GSFE}(\mathbf{u})$. For all layers' strain moduli, and the V_{GSFE} of MoS_2, we use previously computed values from DFT[119,180].

For the modeling of the MoS_2/WSe_2 heterointerface, new DFT calculations were needed. We used the Vienna ab initio Simulation package (VASP)[266], and performed

slab calculations of the monolayer and heterolayer with a vertical (c) axis of 30 Å to prevent interaction between periodic images. The electronic structure was optimized on a Γ-centered k-grid of size $21 \times 21 \times 1$, the energy cutoff was set to 500 eV, and the energy smearing was set to 50 meV. The meta-GGA functional SCAN+rVV10[267] was used alongside the PAW-PBE pseudo potentials for all atoms[268]. To obtain the V_{GSFE}, the stacking configurations between the two layers were sampled over a 9×9 grid of the unit-cell. Each of these 36 heterolayer calculations fixed the in-plane location of all atoms, but allowed the vertical positions to relax via a conjugate gradient algorithm. The five lowest harmonic modes of the V_{GSFE} were then extracted, following the formula

$$\begin{aligned} V_{GSFE}(v,w) = & \\ & c_0 + c_1(\cos v + \cos w + \cos(v+w)) \\ & \quad + c_2(\cos(v+2w) + \cos(v-w) + \cos(2v+w)) \\ & \quad + c_3(\cos(2v) + \cos(2w) + \cos(2v+2w)) \\ & \quad + c_4(\sin v + \sin w - \sin(v+w)) \\ & \quad + c_5(\sin(2v+w2) - \sin(2v) - \sin(2w)) \end{aligned} \tag{A.40}$$

which uses normalized stacking-parameters (v, w) which are given by the transformation

$$\begin{pmatrix} v \\ w \end{pmatrix} = 2\pi A_1^{-1} \begin{pmatrix} b_x \\ b_y \end{pmatrix} \tag{A.41}$$

for $\mathbf{b} = (b_x, b_y)$ the stacking configuration of the top layer and A_1 the matrix composed of the lattice vectors of the bottom layer. For both the P (e.g. near 0° alignment) and AP (e.g. near 60° alignment) of the MoS_2/WSe_2 V_{GSFE}, $\mathbf{b} = 0$ was defined as the highest energy stacking point. For the P configuration, $\mathbf{b} = 0$ corresponds to where both the metals and chalcogenides are vertically aligned. The lowest energy stacking (which occurs when $v = w = 2\pi/3$) corresponds to where the S and W atoms are vertically aligned. For the AP configuration, $\mathbf{b} = 0$ corresponds to where the S and Se atoms are vertically aligned. The lowest energy stacking (which occurs when $v = w = 4\pi/3$) corresponds to where the Mo and Se atoms (also, W and S atoms) are vertically aligned. The coefficients for the V_{GSFE} are given in Table A.5 and those which generate the configuration-dependent equilibrium interlayer distance are given in Table A.6.

Table A.4: Monolayer parameters extracted from DFT[119,180]. The lattice parameter a is given in units of AA, and the shear moduli K and G are given in units of eV.

Material	a	K	G
MoS_2	3.17	49.866	31.548
WSe_2	3.28	43.113	30.770

Table A.5: Coefficients for V_{GSFE} (Eq. A.40) for the four interfaces modeled in this work. All values are given in units of meV per unit-cell of MoS_2.

Interface	c_0	c_1	c_2	c_3	c_4	c_5
P-MoS_2/MoS_2	27.332	14.020	-2.542	-0.884	0.000	0.000
AP-MoS_2/MoS_2	30.423	12.322	-2.077	-0.783	2.397	0.259
P-MoS_2/WSe_2	32.967	13.888	-3.281	-0.748	-1.139	-0.175
AP-MoS_2/WSe_2	37.233	12.317	-2.691	-0.234	3.535	0.712

Table A.6: Coefficients for the configuration-dependence of the interlayer distance between metal atoms (using same form as Eq. A.40) for the two heterointerfaces, in units of Å.

Interface	c_0	c_1	c_2	c_3	c_4	c_5
P-MoS_2/WSe_2	6.561	0.133	0.001	-0.012	-0.001	-0.002
AP-MoS_2/WSe_2	6.558	0.115	-0.002	-0.019	-0.011	-0.013

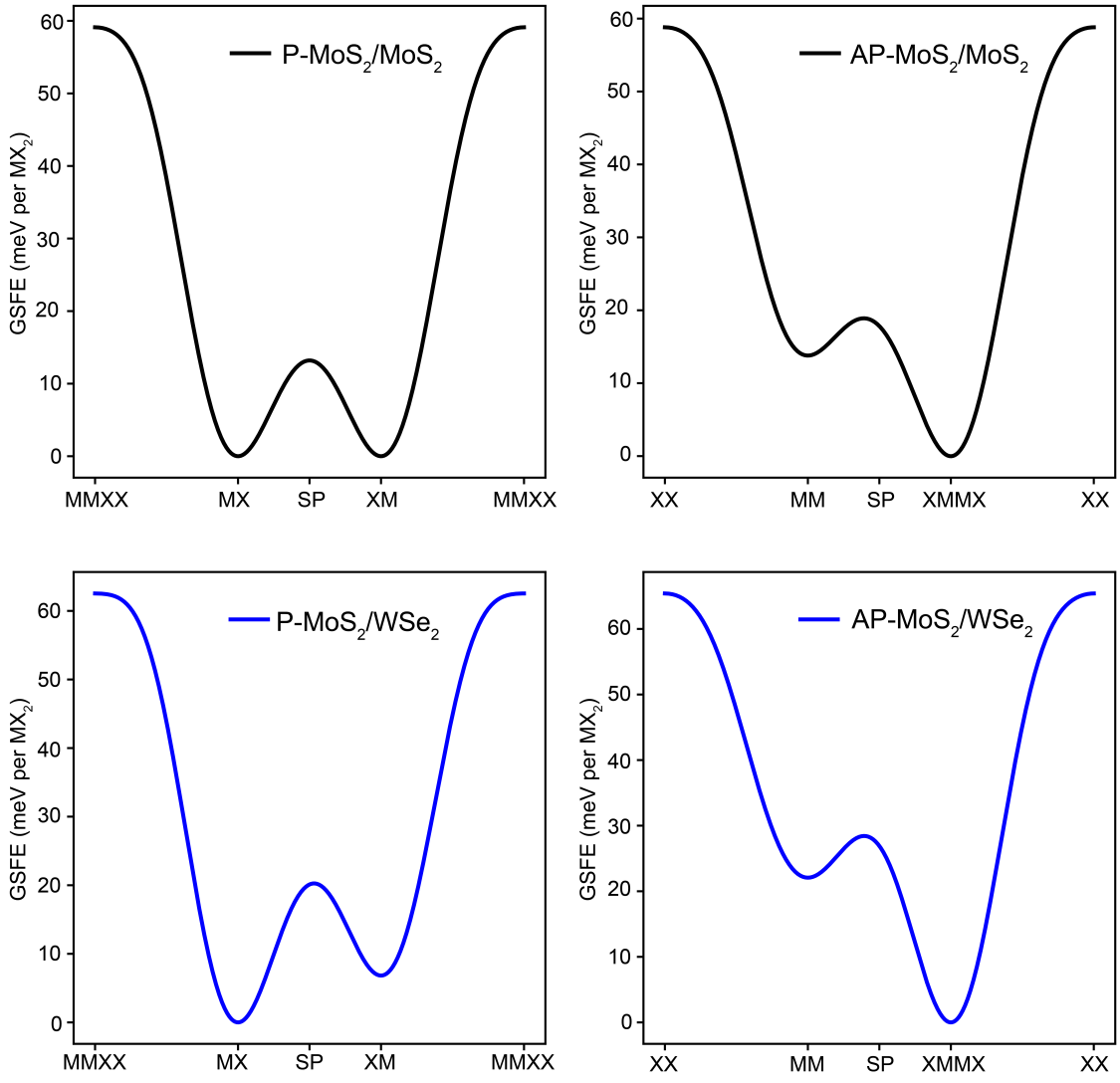

Figure A.24: Generalized stacking fault energies, V_{GSFE}, as given in Table A.5 plotted as a function of a normalized stacking parameter $v = w$. High symmetry stacking configurations are labeled.

A.13.2 Continuum elasticity model

The atomic relaxation of two layers is assumed to be smooth and periodic on the superlattice of the given moiré pattern. It is modeled by two vector fields, $\mathbf{u}_1(\mathbf{r})$ for the bottom layer and $\mathbf{u}_2(\mathbf{r})$ for the top layer, and where $\mathbf{r}$ is the location in the moiré pattern. Note that one can also perform this two-layer relaxation problem in the configuration basis, e.g. replace $\mathbf{r}$ with a pre-relaxation stacking reference $\mathbf{b}_0$, which

is the relative stacking configuration of layer 2 relative to layer 1 before any atomic relaxations occur ($u_l = 0$). For systems with only one unique moiré interface, these two approaches are identical, and are related by the linear map which transforms $\mathbf{r}$ to $\mathbf{b}_0$:

$$\mathbf{b}_0(\mathbf{r}) = A_1 A_{sc}^{-1} \mathbf{r} \tag{A.42}$$

where A_1 is the 2×2 matrix consisting of the unit-cell lattice vectors of the bottom layer, and A_{sc} are the lattice vectors of the moiré superlattice.

In fact, the optimization problem for a given collection of twist angles and heterostrain values is completely specified by just the moiré superlattice A_{sc} (and its angle relative to the unit-cell A_1). For clarity, we define the A_1 unit cell as:

$$A_1 = a_1 \begin{pmatrix} \sqrt{3}/2 & \sqrt{3}/2 \\ -1/2 & 1/2 \end{pmatrix} \tag{A.43}$$

where the primitive lattice vectors are given by the columns of A_1. For a unit cell A_2 defined relative to A_1 by a isotropic heterostrain (e.g. lattice constant difference) of α, a counter-clockwise twist of θ, and a shear heterostrain of magnitude β at an angle ϕ from the A_1 unit-cell, A_{sc} is given by:

$$\begin{aligned} A_{sc} &= (SR - I)^{-1} A_1, \\ R &= \begin{pmatrix} \cos\theta & \sin\theta \\ -\sin\theta & \cos\theta \end{pmatrix}, \\ S &= \begin{pmatrix} 1+\alpha+\beta_1 & \beta_2 \\ \beta_2 & 1+\alpha-\beta_1 \end{pmatrix}, \\ \beta_1 &= (\beta/2)\cos(2\phi + \pi/6 - \theta/2), \\ \beta_2 &= (\beta/2)\sin(2\phi + \pi/6 - \theta/2), \end{aligned} \tag{A.44}$$

with I the 2×2 identity matrix.

For the MoS_2 bilayers, we impose a relaxation symmetry assumption that $\mathbf{u}_2(\mathbf{r}) = -\mathbf{u}_1(\mathbf{r})$. That is to say, the relaxation of the two layers is equal and opposite at a given configuration, which ensures the effective change in the stacking, $\Delta\mathbf{u} = \mathbf{u}_2 - \mathbf{u}_1$, is evenly split between the two layers to minimize the strain energy. For the MoS_2/WSe_2 heterobilayer, we minimize both $\mathbf{u}_1$ and $\mathbf{u}_2$ independently, as the two layers do not have the same strain moduli.

The total energy is composed of two parts[180], the elastic strain of each layer and the interfacial energy between them:

$$\begin{aligned} E &= E_{\text{strain}} + E_{\text{GSFE}}, \\ E_{\text{strain}} &= \sum_{l=1}^{2} \int d\mathbf{r} \frac{1}{2} \mathcal{E}(\nabla \mathbf{u}_l(\mathbf{r})) C_l \mathcal{E}(\nabla \mathbf{u}_l(\mathbf{r})), \\ E_{\text{GSFE}} &= \int d\mathbf{r} V_{GSFE}\left(\mathbf{b}_0(\mathbf{r}) + \mathbf{u}_2(\mathbf{r}) - \mathbf{u}_1(\mathbf{r})\right). \end{aligned} \tag{A.45}$$

with C_l the rank-4 stiffness tensor (consisting of K_l and G_l), and $\mathcal{E}(M) = (M+M^T)/2$. This energy functional and its analytic gradient are implemented as functions which act on an $N \times N$ grid-sampling $\mathbf{u}_l$ over A_{sc}, with $N = 32$. The $\mathbf{u}_l$ are then optimized via the Julia OPTIM package[269], using the quasi-Newton solver L-BFGS.

Results for the MoS_2 moiré bilayer relaxations are shown in Fig. A.25–27. The reconstruction rotation maps and shear strain fields in Fig. A.25. align well with the experimental maps provided in Fig. 3.5 and 3.6 (Chapter 3). Fig. A.26 and A.27 demonstrate the effects of introducing a large heterostrain for P and AP moiré homobilayers, respectively. Similar to the data provided in Fig. 3.14 and 3.15, we observe that local rotations still dominate the reconstruction process when heterostrain is applied. Qualitative differences between the shear strain distributions in the simulated and experimental data can be attributed to differences in the direction of the applied heterostrain; in the simulations, heterostrain was applied at precisely 90°(Fig. A.26d–f and A.27d–f) or 0°(Fig. A.26g–i and A.27g–i) relative to the moiré unit cell, whereas the experimental data sets have a heterostrain angle that deviates from these values.

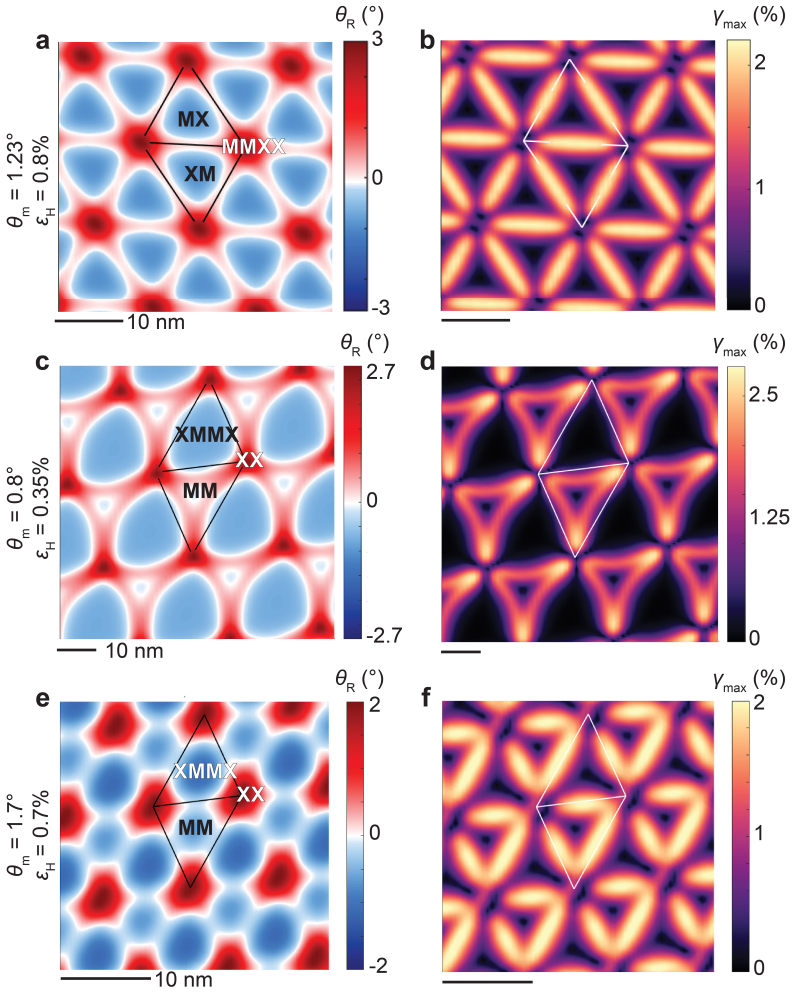

Figure A.25: Simulated maps of local reconstruction rotation (θ_R) and shear strain (γ_{max}) for **(a,b,)** P and **(c–f,)** AP MoS_2 moiré homobilayers. θ_m and ϵ indicate the moiré twist angle and heterostrain magnitude, respectively.

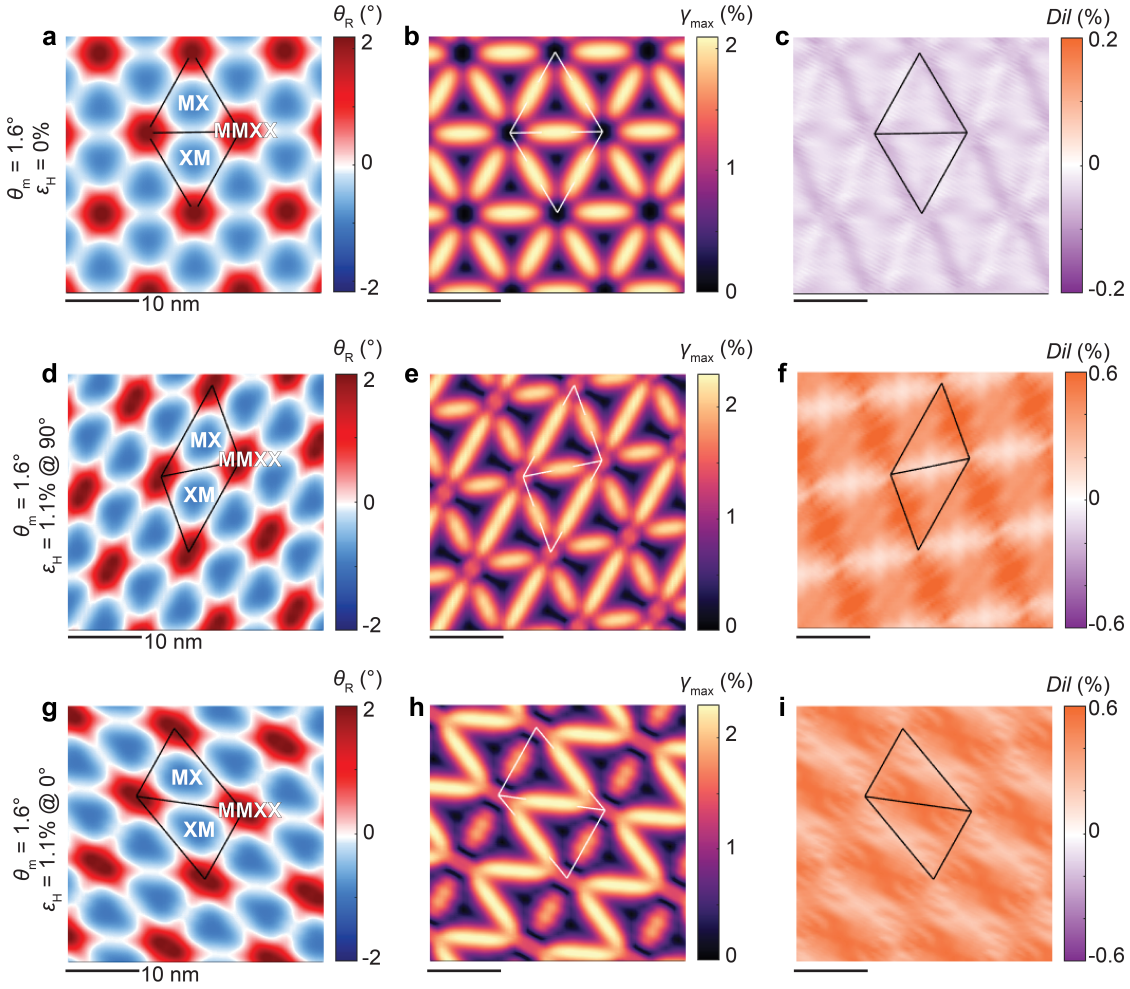

Figure A.26: Simulated maps of local reconstruction rotation (θ_R), shear strain (γ_{max}), and dilation (Dil) for P MoS_2 moiré homobilayers with varying amounts and directions of applied uniaxial heterostrain. θ_m and ϵ indicate the moiré twist angle and heterostrain magnitude, respectively. Maps are shown for cases of **(a–c,)** no heterostrain, **(d–f,)** heterostrain applied at 90° relative to the moiré, and **(g–i,)** heterostrain applied at 0° relative to the moiré.

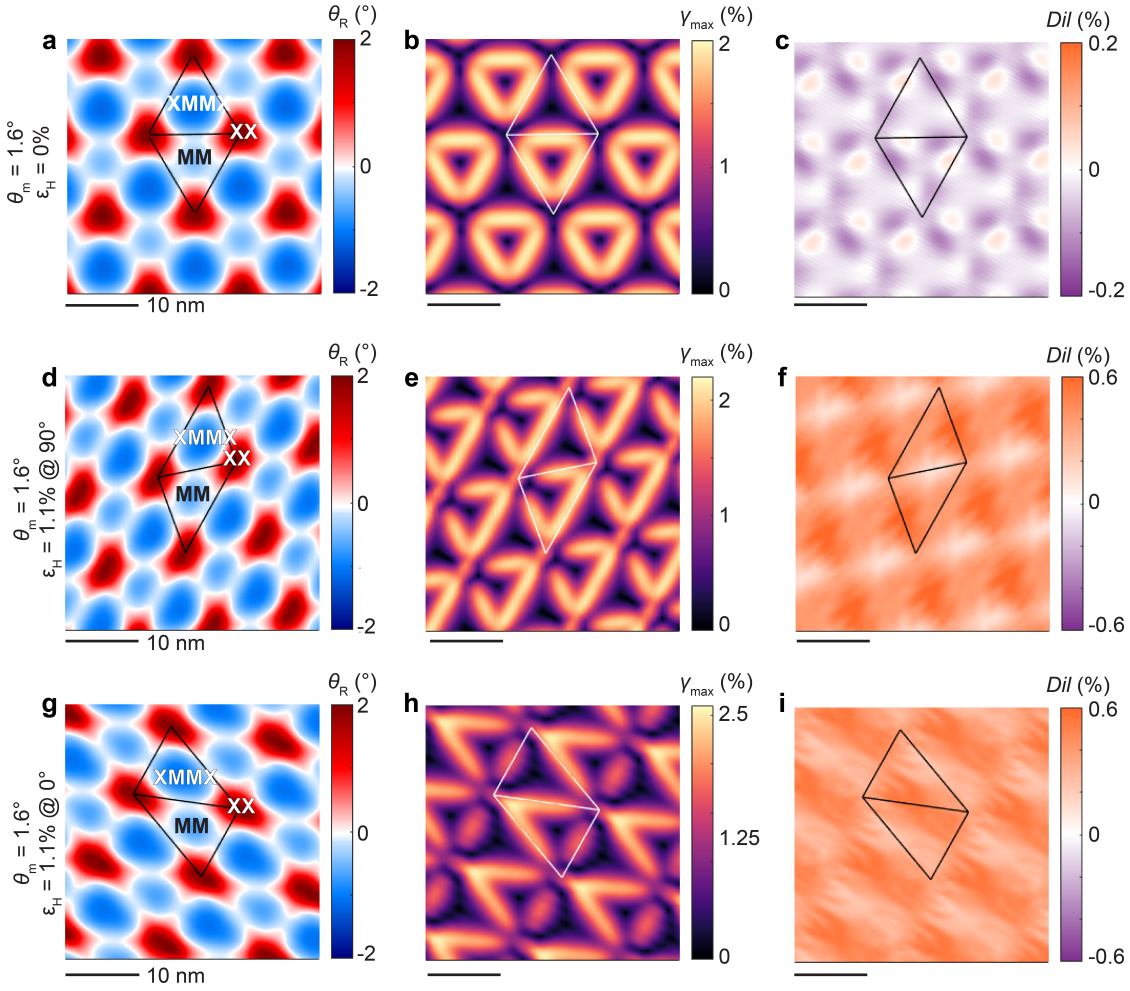

Figure A.27: Simulated maps of local reconstruction rotation (θ_R), shear strain (γ_{max}), and dilation (Dil) for AP MoS_2 moiré homobilayers with varying amounts and directions of applied uniaxial heterostrain. θ_m and ϵ indicate the moiré twist angle and heterostrain magnitude, respectively. Maps are shown for cases of **(a–c,)** no heterostrain, **(d–f,)** heterostrain applied at 90° relative to the moiré, and **(g–i,)** heterostrain applied at 0° relative to the moiré.

Relaxation simulations for the MoS_2/WSe_2 heterobilayers are shown in Fig. A.28–30. Since we extract values for interlayer displacement with the Bragg interferometry method, the experimental dilation and rotation values in Fig. 3.10–12 in Chapter 3 represent net values for the two TMDs in the heterobilayer. However, in contrast, the simulated results distinguish between the relaxation in layer 1 (MoS_2) and layer 2 (WSe_2) (Fig. A.28 and A.29). Based on the simulations, we find that the physical deformations from the relaxation process are partitioned nearly equally between the two layers, with relaxation in the WSe_2 layer being only 13% stronger than in the MoS_2 layer. To compare directly between the experimental and simulated results, we calculate the net local dilation and reconstruction rotation as $Dil_{net} = Dil_{layer2} - Dil_{layer1}$ and $\theta_{R,net} = \theta_{R,layer2} - \theta_{R,layer1}$ (Fig. A.30). Consistent with our measurements, the simulations indicate that a combination of reconstruction dilations and rotations are present when the interlayer twist angle is sufficiently large. The fact that there are periodic reconstruction rotations in the simulated P heterobilayer with a non-zero twist but not in our experimental data (Fig. 3.10i) may be attributed to the difference in twist angle between the two (1.2°_{sim} vs 0.80°_{exp}), indicating that the threshold for rotational reconstruction is above 0.80°, or to additional out-of-plane corrugations in the sample, as discussed in Chapter 3, Section 6.

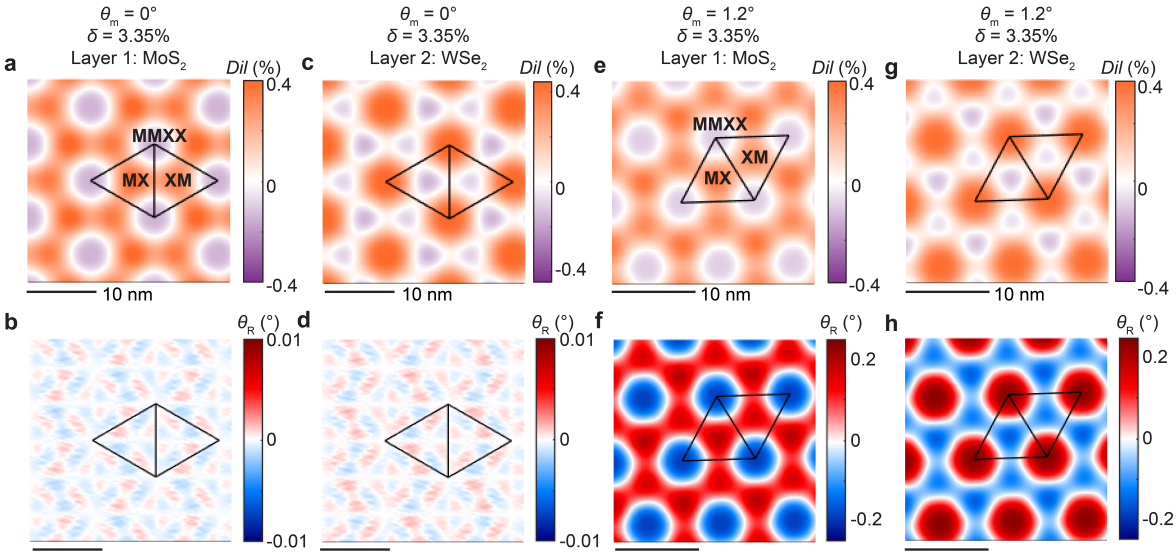

Figure A.28: Simulated maps of local dilation (Dil) and reconstruction rotation (θ_R) within each layer of a P MoS_2/WSe_2 heterobilayer using a lattice constant percent difference (δ) of 3.35% and a moiré twist angle of **(a–d,)** 0° and **(e–h,)** 1.2°.

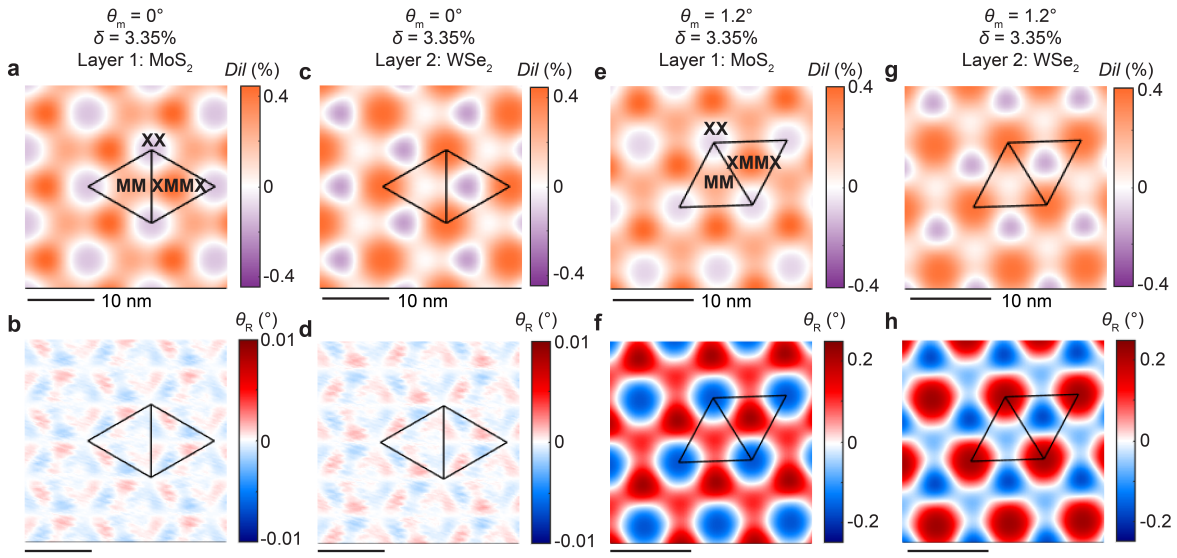

Figure A.29: Simulated maps of local dilation (Dil) and reconstruction rotation (θ_R) within each layer of an AP MoS_2/WSe_2 heterobilayer using a lattice constant percent difference (δ) of 3.35% and a moiré twist angle of **(a–d)** 0° and **(e–h)** 1.2°.

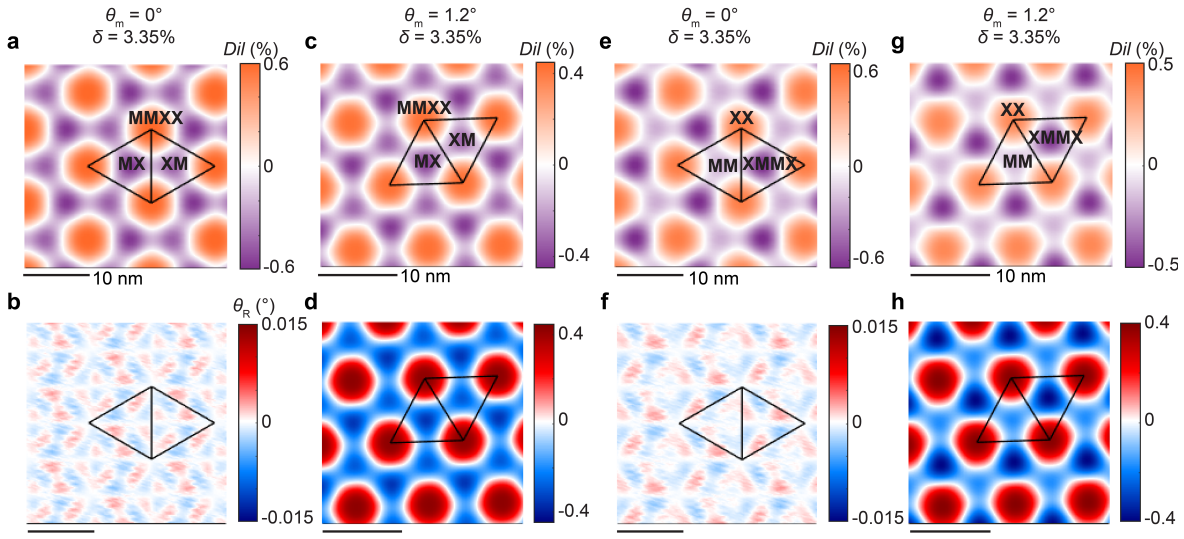

Figure A.30: Simulated maps of the net local dilation (Dil) and reconstruction rotation (θ_R) in **(a–d,)** P and **(e–h,)** AP MoS_2/WSe_2 heterobilayers. θ_m and δ indicate the moiré twist angle and lattice constant percent difference, respectively.

A.14 Effect of corrugations on volumetric strain

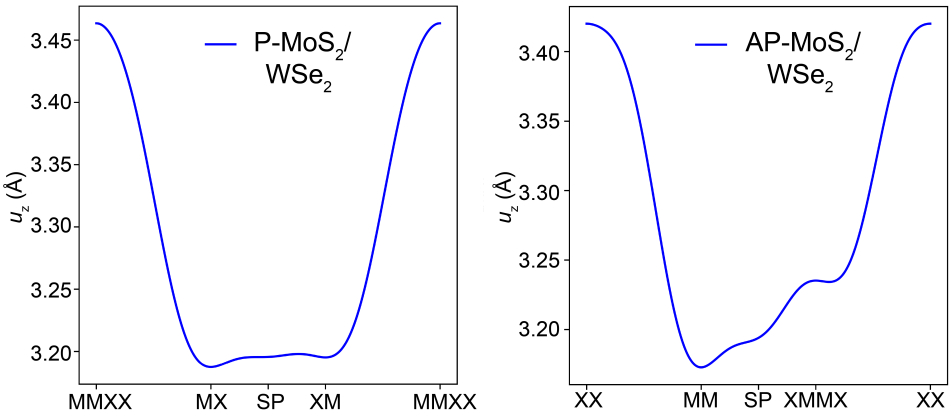

Figure A.31: Single layer displacement along the z-axis as a function of normalized stacking parameter for a P (left) and AP (right) moiré heterobilayer, excluding any in-plane relaxation.

To predict the relative effect of corrugations on the measured dilations, we use the interlayer distance functionals provided in Ref. [20] for MoS_2 and in Appendix, Section 13 for MoS_2/WSe_2. In both cases, we observe that the single layer displacement along the z-axis (u_z^{top}, Fig. A.31) varies on the order of 0.3Å (resulting in a total interlayer distance of 0.6Å, similar to previously reported values[21,22]) and has extrema at MX and MMXX regions (or MM and XX for AP bilayers). From the MoS_2/WSe_2 interlayer distance functional, we find that the steepest dependence of u_z^{top} on the in-plane displacement is $\partial u_z^{top}/\partial u_x^{top} \approx 0.51$ and occurs when the normalized stacking parameter (see Appendix, Section 13) is around 5.3 for P MoS_2/WSe_2. The z-axis displacement will then vary with probe location $\mathbf{r} = (x, y)$ through this dependence on in-plane displacement. We then expand to first order about the location of interest $\mathbf{r}_0$ where $v = 5.3$. Assuming the moiré is controlled only by lattice mismatch such that $\partial u_x^{top}/\partial y = \partial u_y^{top}/\partial x = 0$, this results in the following.

$$u_z^{top}(\mathbf{r}) \approx u_z^{top}(\mathbf{r}_0) + \frac{\partial u_z^{top}}{\partial u_y^{top}} \frac{\partial u_y^{top}}{\partial y} \Delta y + \frac{\partial u_z^{top}}{\partial u_x^{top}} \frac{\partial u_x^{top}}{\partial x} \Delta x \tag{A.46}$$

Around this location where out of plane displacements are expected to be greatest, local in-plane variations in $\mathbf{u}^{top}$ that correspond to a volumetric strain along the x-axis of $\partial u_x^{top}/\partial x$ will be accompanied by variations in u_z^{top} up to roughly half as large for P MoS_2/WSe_2. We can then define the effective lattice compression along the x-axis between the two layers associated with this change in height such that the intralayer displacement magnitude in the xz plane $|u^{top}|_{xz}$ is related to its in-plane projection

u_x^{top} via $|u^{top}|_{xz} = (1-\delta_x^{cor}/2)u_x^{top}$. An analagous analysis can be carried out to obtain the effective compression along the y-axis δ_y^{cor} expected to be on the same order of magnitude.

$$\delta_x^{cor}/2 = 1 - \left(1 + \left(\frac{\partial u_z^{top}}{\partial u_x^{top}}\right)^2\right)^{-1/2} \tag{A.47}$$

This corrugation-driven apparent lattice compression will decrease the effective interlayer lattice mismatch, $\delta = 1 - a_S/a_L$ (where a_S and a_L are the smaller and larger lattice constants respectively), by a factor of $1 - (\delta_x^{cor} + \delta_y^{cor})/2$, particularly in regions where the optimal interlayer height is most sensitive to stacking order. These compressions are therefore only expected in the narrow boundaries between XX and XMMX or MM regions for AP bilayers (or between MMXX and MX/XM stacking regions in P bilayers) as seen in Fig. 3.13b for the AP case. Measured dilations with a magnitude that is greater than the computed values suggest in-plane volumetric deformations in the underlying atomic lattices.

We note that this result is due to the fact that the dilation is measured in the sample with respect to a fixed rigid lattice constant. The corrugation-driven lattice compression will not change the percent lattice mismatch δ when both layers are assumed to deform by the same percent. This is because the corrugation will effectively compress both a_L and a_S by the same factor $(1 - (\delta_x^{cor} + \delta_y^{cor})/2$) leaving the lattice mismatch ($\delta = 1 - a_S/a_L$) and any strain measured relative to $(\delta_x^{cor} + \delta_y^{cor})/2)a_L$ unchanged. However since we measure strain relative to a uniform a_L reference, this effect leads to an apparent decrease in the displacement magnitudes within corrugated regions, manifesting in a smaller divergence and a perceived negative dilation.

A.15 Dark-field TEM imaging of twisted trilayer devices

All of the twisted WSe_2 trilayers studied in Chapter 4 were encapsulated between sheets of hBN and graphite to form functional devices. To view the WSe_2 moiré structure without influence from these colocalized hBN and graphite sheets, we performed transmission electron microscopy in dark-field mode (DF-TEM). To do so, we first viewed the selected area electron diffraction (SAED) pattern. We then placed a small objective aperture around a WSe_2 Bragg peak of interest in the back focal plane of the microscope and acquired the DF image using the electrons diffracted at that small range of angles. Example SAED patterns and DF-TEM images collected using various WSe_2 Bragg peaks are provided in Fig. A.32–34.

For 2D materials, Bragg peak intensities are sensitive to multiple factors including the local stacking order between layers and the sample tilt.[113,202] Both of these factors contribute to the observed contrast between domains within each DF-TEM image.

Variations in sample tilts, in particular, can lead to different stacking domain contrasts between different samples, as seen when comparing the images for the AtA′ samples in Fig. A.32 and A.33.

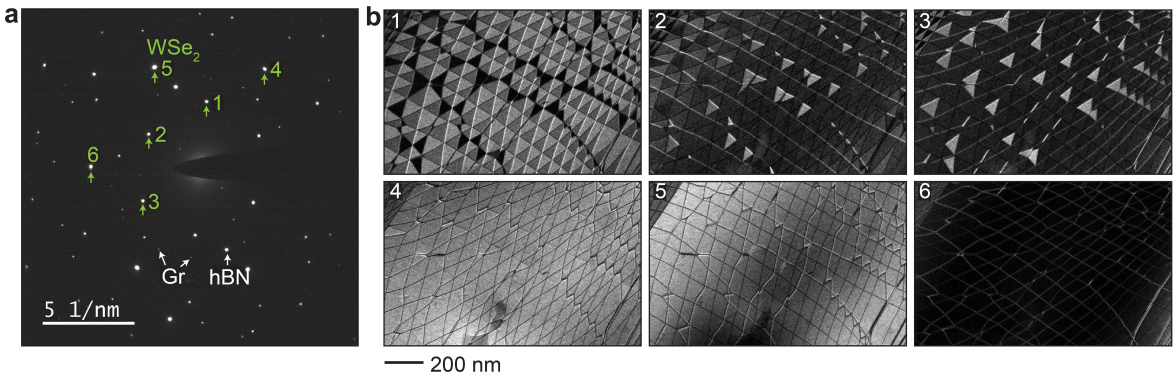

Figure A.32: **a,** Selected area electron diffraction pattern for AtA′ WSe_2 twisted trilayer (Device 2). WSe_2 Bragg peaks used for DF-TEM imaging are labeled with green numbers/arrows. **b,** Corresponding DF-TEM images at zero field.

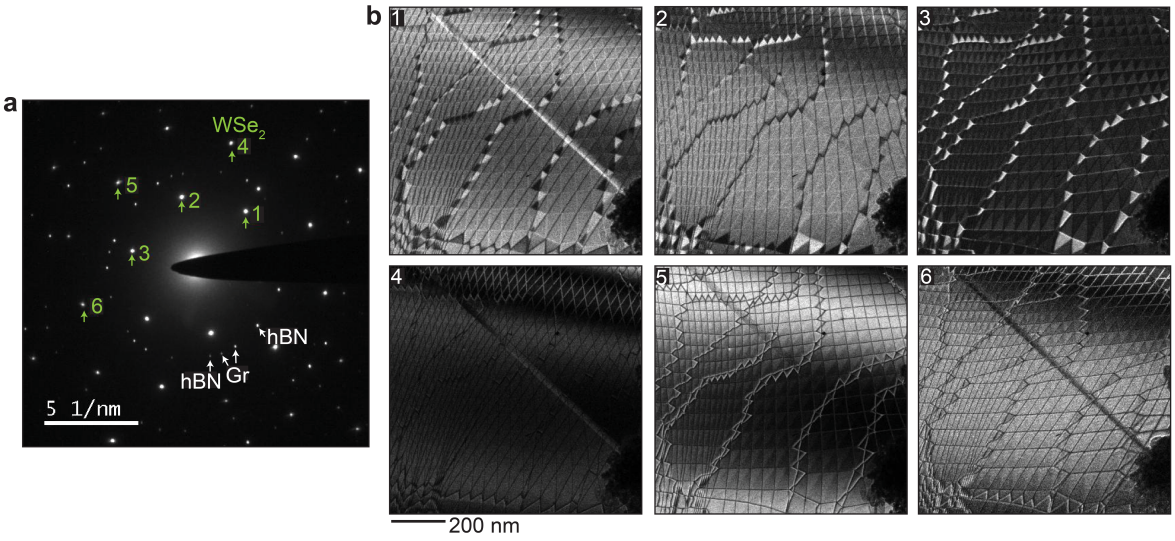

Figure A.33: **a,** Selected area electron diffraction pattern for AtA′ WSe_2 twisted trilayer with slight heterostrain between the top and bottom layers (Device 3). WSe_2 Bragg peaks used for DF-TEM imaging are labeled with green numbers/arrows. **b,** Corresponding DF-TEM images at zero field.

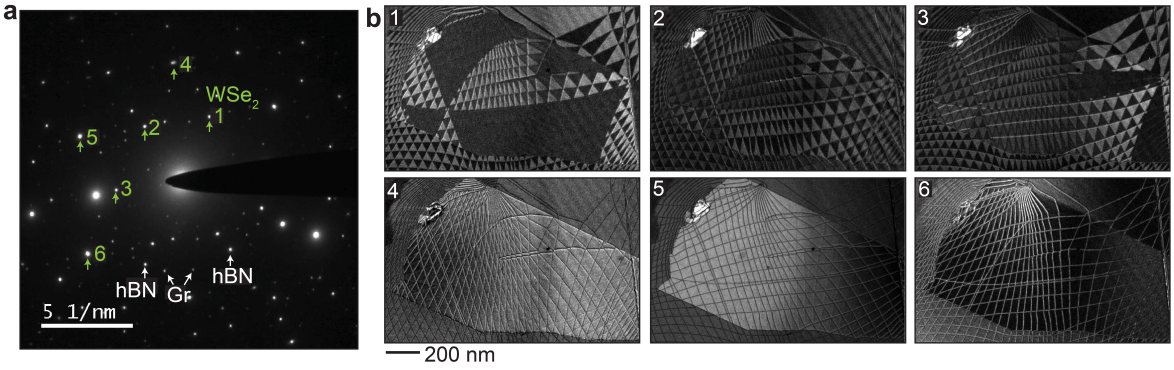

Figure A.34: **a,** Selected area electron diffraction pattern for tAB′ WSe_2 twisted trilayer (Device 4). WSe_2 Bragg peaks used for DF-TEM imaging are labeled with green numbers/arrows. **b,** Corresponding DF-TEM images at zero field.

A.16 Effects of sample tilt on Bragg disk intensities

Since sample tilt affects the measured Bragg disk intensities, regions used for 4D-STEM imaging were aligned onto the [0001] zone axis prior to data acquisition. We note that the experimental CBED patterns for the tAB' sample (Fig. 4.6e, f) do show a slight asymmetry in Bragg disk intensities, indicating that a small tilt was present in that sample when the 4D-STEM data pictured in Fig. 4.7d was collected. To assess the effect of this tilt on the subsequent stacking order assignment, we performed multislice simulations on several high-symmetry trilayer structures with various sample tilts (0–5° along the x- and y-axes). The resulting CBED patterns are shown in Fig. A.35a–d and A.36a–d. We then calculated the normalized cumulative first- and second-order Bragg disk intensities from these simulated patterns and plotted the results according to the bivariate color scheme used in Fig. 4.7b, as shown in Fig. A.35e and A.36e). From these results, it is evident that although sample tilt does have an effect on Bragg disk intensity across the full tilt range sampled, the effects are most dramatic when there is a tilt that exceeds 2°. Meanwhile, after normalization, the relative Bragg disk intensities and corresponding pixel color assignments for the sampled stacking orders are very similar for tilts in the 0–2° range. Based on comparison of the experimental CBED patterns for this sample (Fig. 4.6e, f) to these simulated patterns, we estimate that the tilt in this sample was $< 2°$ during 4D-STEM imaging and therefore does not impact the assignment of stacking order and identification of polar domains in the sample.

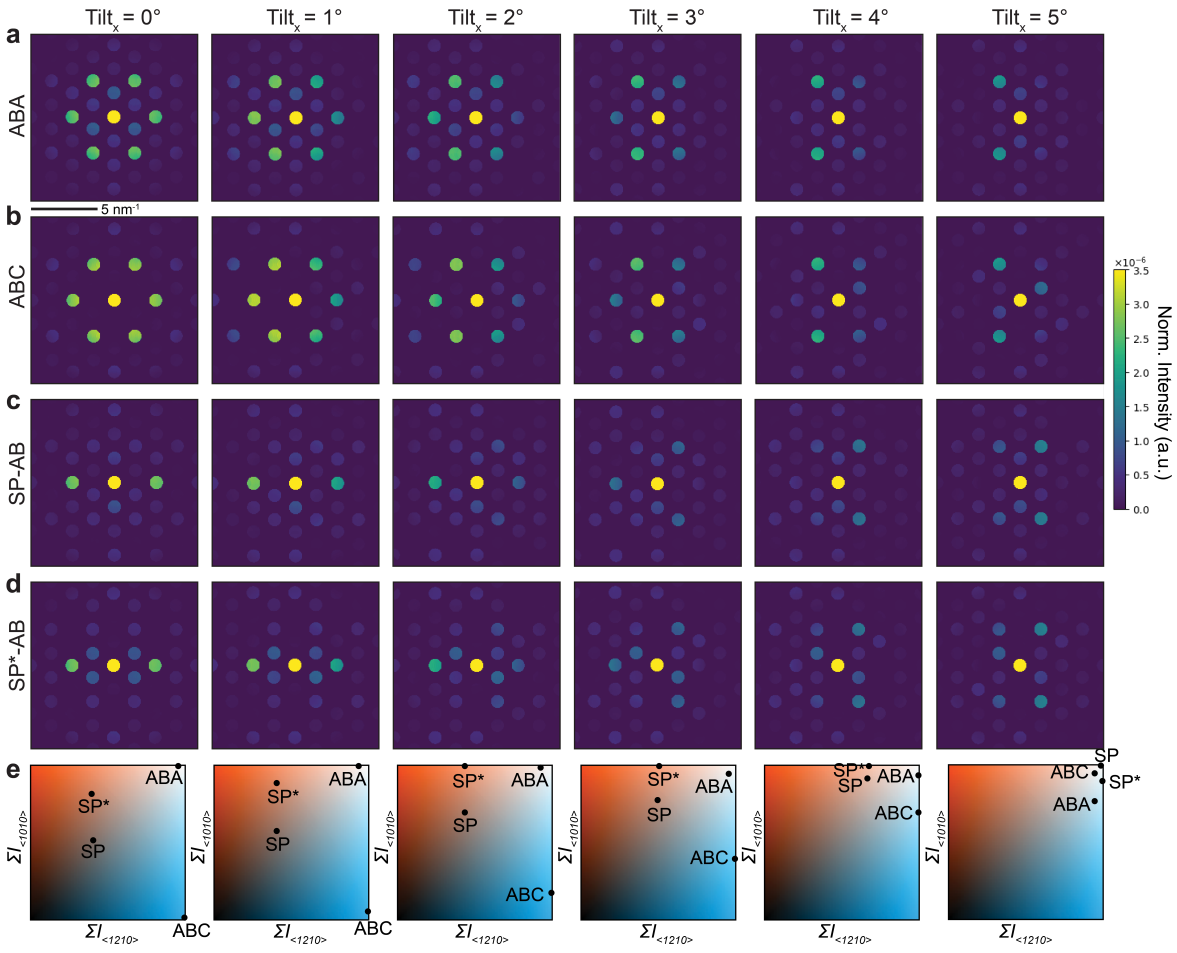

Figure A.35: a–d, Simulated CBED patterns for a series of high-symmetry stacking configurations with a sample tilt of 0–5° along the x-axis. **e,** Corresponding bivariate color legends relating pixel color to the normalized cumulative first and second order Bragg disk intensities ($\Sigma I_{\langle 1010\rangle}$ and $\Sigma I_{\langle 1210\rangle}$), as determined from the CBED patterns in **a–d**.

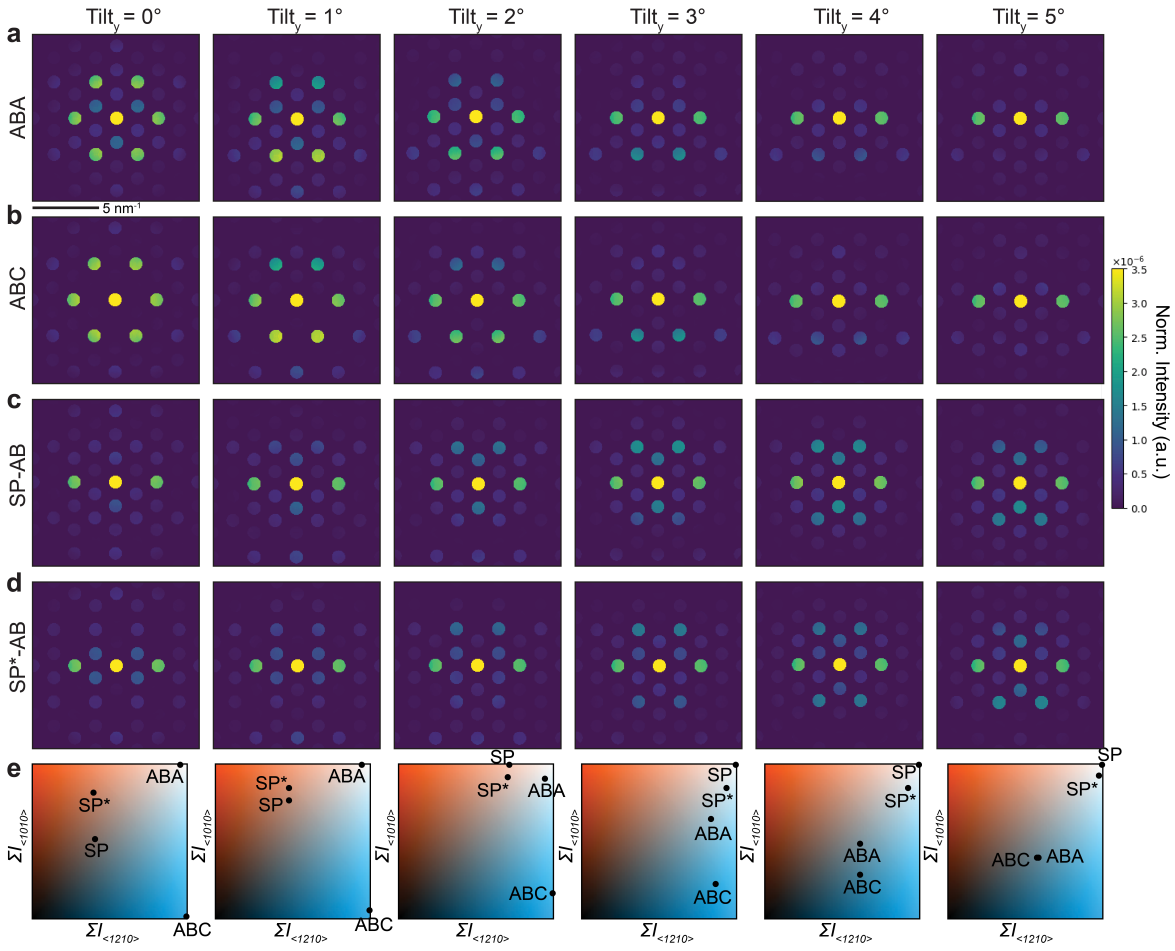

Figure A.36: a–d, Simulated CBED patterns for a series of high-symmetry stacking configurations with a sample tilt of 0–5° along the y-axis. **e,** Corresponding bivariate color legends relating pixel color to the normalized cumulative first and second order Bragg disk intensities ($\Sigma I_{\langle 1010 \rangle}$ and $\Sigma I_{\langle 1210 \rangle}$), as determined from the CBED patterns in **a**–**d**.